Author:
Clear, Chloe L E

Title:
Optical properties of solid state emitters in structured environments

Optical properties of solid state emitters in structured environments

By

CHLOE CLEAR

Department of Physics
UNIVERSITY OF BRISTOL

A dissertation submitted to the University of Bristol in accordance with the requirements of the degree of DOCTOR OF PHILOSOPHY in the Faculty of Physics.

SEPTEMBER 2021

Abstract

Single photon sources (SPS) are a promising component for many quantum information applications, where ideal properties include deterministic, highly efficient indistinguishable emission, as this allows for near perfect two–photon interference. This thesis uses open quantum systems theory to theoretically characterise solid state emitters; a class of single photon sources which are deterministic in nature.

The main focus of this thesis is on the single molecule SPS dibenzoterrylene (DBT), a photostable bright emitter when hosted in an anthracene nano–crystal. We present a theoretical analysis of the temperature dependent optical properties of DBT, including the emission spectra; where dephasing mechanisms which decohere emission and cause linewidth broadening are underpinned. All observed spectral features are accounted for including, a zero phonon line and discrete sharp peaks associated with transitions to local vibrational modes. Furthermore, the model includes a thermal phonon bath, which allows for the inclusion of broad phonon sidebands.

We present second order correlation function calculations for the DBT molecule where both Hanbury Brown and Twiss and Hong–Ou–Mandel interferometer set ups are considered under various driving regimes. In this work we present a novel method to extract photon indistinguishability with experimental verification from a continuous wave laser measurement and present results for driving the system with a pulsed laser.

We present a theoretical study of a DBT SPS coupled with different photonic structures. The structures considered are optical filters and cavities; where a cavity QED master equation model is developed which accounts for all DBT–anthracene spectral features. For both structures we show novel predictions of collection efficiency and photon indistinguishability.

Finally, we present calculations of a NV center coupled to an ultrasmall–mode–volume cavity. Where this work shows that indistinguishable photon extraction is possible at non–cryogenic temperatures and is readily applicable to other deterministic emitters.

Dedication and acknowledgements

First and foremost I would like to express my utmost gratitude and respect to my supervisor Dara P. S. McCutcheon. I feel very lucky to have had the opportunity to work with him and I will be forever grateful for the continued support and guidance he has provided throughout my PhD.

I would also like to extend my strong thanks to Alex S. Clark for his help along the way and who effortlessly kept me motivated with his enthusiasm for molecules. I would also like to pass great thanks to both Ross and Kyle for their vast experimental efforts, it has been a pleasure working with them.

Furthermore, I would also like to express thanks to Jake Iles–Smith who has been a great theoretical collaborator throughout my PhD. I have appreciated our interesting conversations regarding open quantum systems and the knowledge he has shared with me.

I thank Joe Smith for being wonderful to work with, and who gave me the interesting opportunity to turn my head from molecules for a substantial while and sharing his knowledge of NV centers. I would also like to express gratitude to all the people I have had the pleasure of getting to know during my doctoral training year in Bristol and Bath and within QET labs.

Additionally, I want to thank my close friends and wonderful family who have supported me immensely throughout my PhD and whom without this wouldn't of been possible. Finally, I would like to express my thanks to the surrounding rocks of the South West and the people I climb them with who made my time here so memorable and great.

AUTHOR'S DECLARATION

I declare that the work in this dissertation was carried out in accordance with the requirements of the University's Regulations and Code of Practice for Research Degree Programmes and that it has not been submitted for any other academic award. Except where indicated by specific reference in the text, the work is the candidate's own work. Work done in collaboration with, or with the assistance of, others, is indicated as such. Any views expressed in the dissertation are those of the author.

SIGNED:  DATE: 03/12/2021

Flow state. *An altered state of consciousness in which the mind functions at its peak, time may seem distorted, and a sense of happiness prevails. In such a state the individual feels truly alive and fully attentive to what is being done.*

Medical Dictionary, (2009), Farlex and Partners

Table of Contents

List of Figures

CHAPTER 1

MOTIVATIONS AND OVERVIEW

The search for an ideal on-demand efficient emitter of single photons has generated great research efforts over the past couple of decades [32]. This drive predominantly stemmed from E. Knill, R. Laflamme and G.J. Milburn, who proved in 2000, that quantum computing (QC) is possible using only single photons, single photon detectors and linear optics [60]. Other quantum information technologies that rely on single photons as the information carrier (or qubit) include, quantum communication, quantum sensing and quantum networks [22, 62, 68]. Motivations for using photons as qubits originate from their niche properties, such as, their ability to be easily manipulated with linear optics and weak interaction with their environment which leads to high coherence. Moreover, dealing with photons allows for trivial integration into fibre networks. A key requirement for several quantum information applications including optical computation and quantum networks is two–photon interference [20]. For near–perfect quantum interference to be achieved, an ideal source emits indistinguishable photons, which infers that the interfering photons are identical in every way, including, polarization, spatial mode and temporal profile [17, 59].

Single photon emitters can be classified into two subgroups, deterministic and probabilistic sources. An example of a probabilistic source is a crystal with a non–linearity which enables spontaneous parametric down conversion via non–linear processes [64]. For such crystals, the bulk system is excited with a pump laser and two single photons termed the signal and idler are emitted [12]. A benefit of these sources is the ability to herald photons which gives the user confirmation of an emission event. The major draw back of these sources however, is due to the probabilistic nature of single events, where if the source is driven too strongly multi–photon emission events can occur reducing the purity [32]. Conversely, a deterministic source can be thought of as a two–level system, where only one excitation can occur at any one time and the corresponding relaxation leads to the emission of a single photon with near–unity

efficiency. Examples of deterministic emitters include quantum dots (QDs) [116], defect centres in diamond [29], single molecules [112] and defects in two–dimensional materials such as hexagonal boron nitride [87]. It is important to note in practice, if collection efficiency isn't near unity and due to the inability to herald photons deterministic sources can hold probabilistic properties. For the purpose of this thesis however the latter described sources will still be termed 'deterministic' due to convention.

The focus of this thesis is on solid state deterministic quantum emitters and seeks to characterise their optical properties and viability for quantum information applications. Open quantum system techniques are used to model the emitters and their environments. The bulk of this thesis considers the single molecule emitter dibenzoterrylene (DBT). A model is developed which captures all spectral features and the origin of the phonon dephasing mechanisms are underpinned, where particular attention is paid towards the structure of the phonon environments. Research on the effect of exciting this molecule under different driving regimes is presented, including considerations of using either a continuous wave (cw) or pulsed laser. The well known Hong–Ou–Mandel experiment is simulated under these different regimes and a novel approach to extract the photon indistinguishability via a cw measurement is found and experimentally verified by collaborators, where this extraction technique is readily adaptable for other solid state emitters [104].

The final sections of this thesis are regarding coupling emitters to different photonic structures, starting with DBT. Structures include a waveguide filter and an optical micro–cavity. The motivation for this work is to investigate how the emission properties can be manipulated using such structures and calculate predictions of photon indistinguishability and efficiency for each case. The DBT cavity work detailed here supports the experimental efforts lead by Kyle D. Major, outlined in his thesis [72], who is working on developing an optical micro–cavity under Alex S. Clark's group at Imperial College London which enhances DBT molecule emission. In these calculations the parameter constraints for the optical micro–cavity are relaxed allowing for the calculation of optimal cavity parameters to maximise detection efficiency and indistinguishability over a wider cryogenic temperature range. This modification of the system parameters manipulates the model to reflect different photonic cavity structures.

Finally, original work on a different kind of solid state quantum emitter, a nitrogen vacancy defect centre in diamond (NV center) is presented. In this chapter calculations coupling a NV center to an ultrasmall–mode–volume cavity, reflecting recent developments in cavity engineering, are found [51]. Here, a cavity QED master equation model is developed, in which the NV center has been modelled with and without linear strain which causes a polarisation splitting of the excited states. It is important to capture this linear strain as it is known to arise from defects in the crystal structure [37]. The motivation of this work is to investigate if using these ultrasmall–mode–volume cavities allows for efficient indistinguishable emission from a

deterministic emitter at temperatures above the cryogenic limit at $\geq 200\,\mathrm{K}$, where this base temperature can be obtained with Peltier cooling.

CHAPTER 2

INTRODUCTORY THEORY

This chapter details the theoretical framework used throughout this thesis. Initially, density operator formalism is presented leading on to the description of closed and open quantum systems (OQS). To characterise the dynamics of open quantum systems the theory of master equations is then introduced. This chapter then presents the theory of harmonic oscillators and how they are commonly used to describe photonic and phonon environments coupled to an open quantum system. Finally, the system–environment interaction between an electron and lattice phonons is derived to first order with respect to lattice displacements following the reference [71]. This interaction is then taken to second order using a novel approach, where the motivation for capturing phonon anharmonicity arises from the desire to capture certain phonon mediated dephasing in single photon sources.

2.1 Closed and open quantum systems

A closed quantum system is one where there is no exchange of information (matter or energy) with another system or environment. To describe the dynamical behaviour of such systems, the following Schrödinger equation can be used, given by

$$i\hbar\partial_t \left|\Psi\right\rangle = H \left|\Psi\right\rangle , \tag{2.1}$$

where H is the time independent system Hamiltonian which is a Hermitian operator, and $\left|\Psi\right\rangle$ is the state vector of the system. Solving this partial differential equation gives

$$\left|\Psi(t)\right\rangle = U(t,t_0) \left|\Psi(t_0)\right\rangle , \tag{2.2}$$

where $U(t,t_0) = e^{-iH(t-t_0)/\hbar}$ is the unitary time evolution operator, which propagates the state from $t_0 \to t$. In nature it is rare that a system can be treated as closed due to interaction

with environmental degrees of freedom. To account for this one turns to the theory of open quantum systems (OQS). The theory of OQS seeks to describe the dynamical behaviour of the system which includes interactions from an environment. In OQS theory, the system can be described explicitly, whereas the environment cannot, and therefore it is desirable to describe the influence of the environment by a set of parameters. A well explored physical example of an open quantum system is a semiconductor quantum dot (QD). The QD system can be treated as a two–level quantum system, which interacts with a solid-state phonon lattice environment. The interaction between some sub-system and its environment leads to the inability to describe the subsystem as a state vector, and instead one must use density operators [15]. The dynamics of both closed and open quantum systems are outlined in following sections, which starts by detailing the properties of density operators.

2.1.1 Density operator

The density operator can be defined as a statistical mixture of pure quantum state vectors $\{ |\Psi_i\rangle \}$ [38], given by

$$\rho = \sum_i w_i \, |\Psi_i\rangle \, \langle \Psi_i| \, , \tag{2.3}$$

where the set of real numbers $\{w_i\}$ represent the state probabilities and satisfy the following conditions, $0 \leq w_i \leq 1$ and $\sum_i w_i = 1$. General properties of the density operator include, hermiticity $\rho = \rho^\dagger$, normalisation $\mathrm{Tr}(\rho) = 1$ and positivity $\rho \geq 0$ [33]. When all objects in an ensemble are in the same state one can define a pure state from $\rho_{\mathrm{PURE}} = |\Psi\rangle \, \langle \Psi|$. For a pure state the following normalisation condition holds $\mathrm{Tr}\big(\rho^2_{\mathrm{PURE}}\big) = 1$; where if $\mathrm{Tr}(\rho^2) < 1$ the state is mixed.

The expectation value for an operator A can be expressed as an ensemble average of the expectation values for each quantum state as

$$\langle A \rangle = \sum_i w_i \, \langle \Psi_i | A | \Psi_i \rangle \, . \tag{2.4}$$

Inserting the resolution of identity $\mathbb{1} = \sum_j |j\rangle\langle j|$ where, $\{ \, |j\rangle \, \}$ is a complete basis set, gives

$$\begin{aligned} \langle A \rangle &= \sum_{i,j} w_i \, \langle \Psi_i | A | j \rangle \, \langle j | \Psi_i \rangle \, , \\ &= \mathrm{Tr}\big(A \sum_i w_i \, |\Psi_i\rangle\langle\Psi_i| \, \big), \\ &= \mathrm{Tr}\big(A \rho \big). \end{aligned} \tag{2.5}$$

Where the definition of the trace has been used, which is

$$\mathrm{Tr}(Z) = \sum_j \, \langle j | Z | j \rangle \, . \tag{2.6}$$

2.1.2 Dynamics of closed quantum systems

For a closed system all of the states in the basis $\{ |\Psi_i\rangle \}$ evolve according to the Schrödinger equation, (2.1). One can differentiate the mixed state to form the von Neumann equation [15]

$$\begin{aligned} \partial_t \rho(t) &= \sum_i w_i \Big((\partial_t |\Psi_i(t)\rangle) \langle \Psi_i(t)| + |\Psi_i(t)\rangle (\partial_t \langle \Psi_i(t)|) \Big), \\ &= -\frac{i}{\hbar} \big[H(t), \rho(t) \big], \end{aligned} \tag{2.7}$$

where $\partial_t |\Psi_i(t)\rangle = -\frac{i}{\hbar} H(t) |\Psi_i(t)\rangle$ and $\partial_t \langle \Psi_i(t)| = \frac{i}{\hbar} \langle \Psi_i(t)| H(t)$ have been used. To propagate the density matrix in time from $(t_0 \to t)$ the unitary time evolution operators can be applied such that, $\rho(t) = U(t, t_0) \rho(t_0) U^\dagger(t, t_0)$. The equation in Eq. (2.7) is often expressed in the convenient form

$$\partial_t \rho(t) = \mathcal{L}(t) \rho(t), \tag{2.8}$$

where $\mathcal{L}(t)$ is the Liouvillian super–operator which maps operators to operators.

2.1.3 Dynamics of open quantum systems

When dealing with open quantum systems one has to consider mixed states, as at the very least the total system consists of two substates corresponding to the system and an environment. To work with mixed states it is useful to utilise the formalism of reduced density operators which will now be outlined. Reduced density operators allow one to explicitly write down the density operator for one part of the larger composite system. For example, consider a system (S), with basis $\{|s_i\rangle\}$ which acts only over the system sub space, and environment (E), with basis states $\{|e_j\rangle\}$ that act only in the environment space. The subsequent interacting composite system can be represented by the density operator ρ_{SE}. Now introducing the reduced density operator which describes the state of the system as

$$\rho_{\mathrm{S}} = \mathrm{Tr}_{\mathrm{E}}(\rho_{\mathrm{SE}}). \tag{2.9}$$

where $\mathrm{Tr}_{\mathrm{E}}(Z) = \sum_j \langle e_j | Z | e_j \rangle$ defines the partial trace over the environment, which acts only on the Hilbert space of E. This definition of reduced density operator can be used to find the expectation value for the operator A_{S}, which acts only on the subsystem S. First, representing this operator in the full Hilbert space as $\langle A \rangle = \mathrm{Tr}(A_{\mathrm{S}} \otimes \mathbb{1}_E \rho_{\mathrm{SE}})$, it can be written

$$\begin{aligned} \langle A \rangle &= \mathrm{Tr}(A_{\mathrm{S}} \otimes \mathbb{1}_E \rho_{\mathrm{SE}}), \\ &= \mathrm{Tr}_{\mathrm{S}}(A_{\mathrm{S}} \rho_{\mathrm{S}}). \end{aligned} \tag{2.10}$$

The reduced density operator ρ_{S} describes all measurements of the system, given that the environment is not observed. Conversely, to find the reduced density operator of the environment one has to take the trace of the composite density operator over the system subspace instead.

To reiterate, for closed quantum systems the state dynamics are governed by the Schrödinger equation, where the time evolution of a closed system is mediated with a unitary operator. In general this approach is not possible for open quantum systems due to classical improbability which arises from environment interference [15]. To model the dynamics for open quantum systems it is instead useful to describe the temporal evolution of the density matrix. The equation of motion used to describe this temporal evolution with respect to the density matrix is known as a quantum master equation. In other words, a master equation is a differential equation which describes the evolution of state probabilities [103]. In the following section a microscopic derivation of a quantum master equation is described using Born–Markov approximations. A Hamiltonian decomposition method is outlined which allows for evaluation of such a master equation with an arbitrary system and environment. Finally, the specialised case of a Markovian Lindblad master equation is detailed.

2.1.4 Master equations

Starting with the open quantum system described by the general Hamiltonian $H = H_{\mathrm{S}} + H_{\mathrm{E}} + H_{\mathrm{I}}$, where H_{S} and H_{E} represent the Hamiltonian of the system and environment, respectively. The interaction Hamiltonian is given by H_{I}, where this term captures the exchange of information between the system and the environment and is what makes the quantum system 'open'. It is desirable to find the continuous time evolution of the open quantum system, as was shown for the closed case in section (2.1.2). To do so a microscopic derivation of the master equation is first derived. The benefit of this approach is it allows for the derivation to be from first principles i.e. from the Hamiltonian of the complete open system.

2.1.4.1 Microscopic derivation

The microscopic derivation of master equation from first principles is possible for certain assumptions. For the purpose of this thesis the example of an OQS in the weak coupling limit is derived, as this is applicable to the physical systems explored.

To begin it is desirable to move into interaction picture, which requires the following unitary transformation,

$$\tilde{\rho}(t) = U_0^{\dagger}(t)\rho(t)U_0(t), \tag{2.11}$$

where $U_0(t) = U_{\mathrm{S}}(t)U_{\mathrm{E}}(t) = \exp[-i(H_{\mathrm{S}} + H_{\mathrm{E}})t/\hbar]$ [15]. Applying this unitary transformation on Eq. (2.7) gives the von Neumann equation in the interaction picture, as

$$\partial_t \tilde{\rho}(t) = -\frac{i}{\hbar}\Big[\tilde{H}_{\mathrm{I}}(t), \tilde{\rho}(t)\Big], \tag{2.12}$$

where the relation $\tilde{H}_{\mathrm{I}}(t) = U_0^{\dagger}(t)H_{\mathrm{I}}U_0(t)$ has been used. Integrating this expression to find

$$\tilde{\rho}(t) = \rho(0) - \frac{i}{\hbar}\int_0^t ds\Big[\tilde{H}_{\mathrm{I}}(s), \tilde{\rho}(s)\Big], \tag{2.13}$$

where it has been assumed that at an initial time of $t = 0$ the quantum states of the interaction and Schrödinger picture coincide, such that, $\tilde{\rho}(0) = \rho(0)$. Substituting this solution into Eq. (2.12) and taking the trace over the environment subspace we find

$$\partial_t \tilde{\rho}_{\mathrm{S}}(t) = -\frac{1}{\hbar^2}\int_0^t ds \mathrm{Tr}_{\mathrm{E}}\Big([\tilde{H}_{\mathrm{I}}(t), [\tilde{H}(s), \tilde{\rho}(s)]]\Big), \tag{2.14}$$

where

$$\mathrm{Tr}_{\mathrm{E}}\Big(\Big[\tilde{H}_{\mathrm{I}}(t), \rho(0)\Big]\Big) = 0, \tag{2.15}$$

has been assumed. To further simplify the above equation a few approximations are now made. The first being the *Born approximation*, which allows for the factorisation of the system and environment density reduced operators on the assumption of weak coupling, such that $\tilde{\rho}(t) = \tilde{\rho}_{\mathrm{S}}(t)\rho_{\mathrm{E}}$; where the time dependence of ρ_{E} is dropped due to the assumption the environment is in a steady state. Finally, the *Markovian approximation* is applied, which firstly involves, replacing $\tilde{\rho}_{\mathrm{S}}(s)$ with $\tilde{\rho}_{\mathrm{S}}(t)$ in the integral, as this ensures that the evolution of the system at time t is dependent only on the state at that instant and the initial state preparation; making the equation local in time. Additionally, making the substitution of variables $\tau = t - s$ and taking the limit of the integral to infinity leads to a Markovian master equation, given by

$$\partial_t \tilde{\rho}_{\mathrm{S}}(t) = -\frac{1}{\hbar^2}\int_0^\infty d\tau Tr_{\mathrm{E}}\Big([\tilde{H}_{\mathrm{I}}(t), [\tilde{H}(t-\tau), \tilde{\rho}_{\mathrm{S}}(t)\rho_{\mathrm{E}}]]\Big), \tag{2.16}$$

as the evolution no longer depends upon the initial state. Taking the limit to infinity here is justified so long as the integrand vanishes fast in the limit of τ being greater than the time in which the environment correlation functions decay, τ_E. These final assumptions capture the Markovian approximation, which ensures the evolution of the state of the system depends only on the state at that instant [44]. Finally, moving back to the Schrödinger picture by using the relation $\partial_t \rho_{\mathrm{S}}(t) = -i[H_{\mathrm{S}}, \rho_{\mathrm{S}}(t)] + U_{\mathrm{S}}(t)(\partial_t \tilde{\rho}_{\mathrm{S}}(t))U_{\mathrm{S}}^\dagger(t)$ gives the the following equation

$$\partial_t \rho_{\mathrm{S}}(t) = -\frac{i}{\hbar}[H_{\mathrm{S}}, \rho_{\mathrm{S}}(t)] - \frac{1}{\hbar^2}\int_0^\infty d\tau Tr_{\mathrm{E}}\Big([H_{\mathrm{I}}, [\tilde{H}_{\mathrm{I}}(-\tau), \rho_{\mathrm{S}}(t)\rho_{\mathrm{E}}]]\Big). \tag{2.17}$$

Where this equation is valid to second order with respect to the interaction Hamiltonian. Making the above approximations this equation is termed the second–order Born–Markov master equation and will be used throughout this thesis as a tool to describe the evolution of open quantum systems models.

2.1.4.2 Hamiltonian decomposition

To further this derivation a generalised decomposition of the open quantum system Hamiltonian can be substituted into the second order Born–Markov master equation. To begin one writes the interaction Hamiltonian as a decomposition of the general system operators A_i and environment operators B_i [19], giving

$$H_{\mathrm{I}} = \sum_i A_i \otimes B_i. \tag{2.18}$$

The time evolved interaction Hamiltonian can therefore be found from

$$\tilde{H}_{\mathrm{I}}(t) = \sum_i \tilde{A}_i(t) \otimes \tilde{B}_i(t), \tag{2.19}$$

where $\tilde{A}_i(t) = e^{iH_{\mathrm{S}}t/\hbar} A_i e^{-iH_{\mathrm{S}}t/\hbar}$ and $\tilde{B}_i(t) = e^{iH_{\mathrm{E}}t/\hbar} B_i e^{-iH_{\mathrm{E}}t/\hbar}$. Substituting this interaction Hamiltonian $\tilde{H}_{\mathrm{I}}(t)$ into the Born–Markov master equation shown in Eq. (2.17) we find

$$\partial_t \rho_{\mathrm{S}}(t) = -\frac{i}{\hbar}[H_{\mathrm{S}}, \rho_{\mathrm{S}}(t)] - \frac{1}{\hbar^2}\sum_{ij}\int_0^\infty d\tau \,\mathrm{Tr}_{\mathrm{E}}\Big([A_i \otimes B_i, [\tilde{A}_j(-\tau) \otimes \tilde{B}_j(-\tau), \rho_{\mathrm{S}}(t)\rho_{\mathrm{E}}]]\Big). \tag{2.20}$$

Factorising the system and environmental terms and using the cyclic property of a trace gives

$$\begin{aligned}\partial_t \rho_{\mathrm{S}}(t) = &-\frac{i}{\hbar}[H_{\mathrm{S}}, \rho_{\mathrm{S}}(t)] - \frac{1}{\hbar^2}\sum_{ij}\int_0^\infty d\tau \Big([A_i, \tilde{A}_j(-\tau)\rho_{\mathrm{S}}(t)]\,\mathrm{Tr}_{\mathrm{E}}\left(B_i \tilde{B}_j(-\tau)\rho_{\mathrm{E}}\right) \\ &+ [\rho_{\mathrm{S}}(t)\tilde{A}_j(-\tau), A_i]\,\mathrm{Tr}_{\mathrm{E}}\left(\tilde{B}_j(-\tau)B_i\rho_{\mathrm{E}}\right)\Big).\end{aligned} \tag{2.21}$$

Considering now the environmental terms by firstly defining the environment correlation functions with

$$C_{ij}(\tau) = \mathrm{Tr}_{\mathrm{E}}\left(B_i \tilde{B}_j(-\tau)\rho_{\mathrm{E}}\right). \tag{2.22}$$

Making use of Fourier decomposition to explicitly express the system operators time dependence as

$$\tilde{A}_i(\tau) = \sum_\nu e^{-i\nu\tau} A_i(\nu), \tag{2.23}$$

where $\nu = \lambda_m - \lambda_n$ is the difference in the system Hamiltonian eigenvalues and $A_i(\nu) = \sum_{n-m=\nu} |n\rangle\langle m| \, \langle n|A_i|m\rangle$ [15]. Combining decomposed system operators with the master equation shown in Eq. (2.21) to find

$$\begin{aligned}\partial_t \rho_{\mathrm{S}}(t) = &-\frac{i}{\hbar}[H_{\mathrm{S}}, \rho_{\mathrm{S}}(t)] - \frac{1}{\hbar^2}\sum_{ij}\sum_\nu \Big(K_{ij}(\nu)[A_i, A_j(\nu)\rho_{\mathrm{S}}(t)] \\ &+ K^*_{ji}(\nu)[\rho_{\mathrm{S}}(t)A_j^\dagger(\nu), A_i]\Big).\end{aligned} \tag{2.24}$$

Where $A_i^\dagger(\nu) = A_i(-\nu)$ and the environment response function has been introduced which absorbs the exponent as

$$K_{ij}(\nu) = \int_0^\infty d\tau C_{ij}(\tau) e^{i\nu\tau}, \tag{2.25}$$

noting that the Markovian approximation has been assumed here such that the upper integration limit has been taken to $t \to \infty$, which implies the evolution depends on only the systems present state [44]. To simply this model the response function can be split into its real and imaginary components, defining

$$K_{ij}(\nu) = \frac{1}{2}\gamma_{ij}(\nu) + iS_{ij}(\nu). \tag{2.26}$$

Substituting this into Eq. (2.24) along with the assumption that the decomposition operators are Hermitian $A_i(\tau) = A_i^\dagger(\tau)$, gives

$$\begin{aligned}\partial_t \rho_S(t) = &-\frac{i}{\hbar}[H_S, \rho_S(t)] - \frac{1}{\hbar^2}\sum_{ij}\sum_{\nu}\Big(\frac{1}{2}\gamma_{ij}(\nu)[A_i, A_j(\nu)\rho_S(t) - \rho_S(t)A_j^\dagger(\nu)] \\ &+ iS_{ji}^*(\nu)[A_i, \rho_S(t)A_j^\dagger(\nu) + A_j(\nu)\rho_S(t)]\Big),\end{aligned} \tag{2.27}$$

where the term multiplied by the imaginary part of the response function $S_i(\nu)$ is a Lamb shift which renormalises the system Hamiltonian by H_{LS} such that

$$\partial_t \rho_S(t) = -\frac{i}{\hbar}[H_S + H_{LS}, \rho_S(t)] - \frac{1}{2}\frac{1}{\hbar^2}\sum_{ij}\sum_{\nu}\gamma_{ij}(\nu)[A_i, A_j(\nu)\rho_S(t) - \rho_S(t)A_j^\dagger(\nu)]. \tag{2.28}$$

To define a general Lindblad master equation in its typical form, as the matrix of $\sum_{ij}\gamma_{ij}(\nu)$ is inherently positive [75], Eq. (2.28) can be diagonalised using an appropriate unitary operator P to find

$$P\gamma(\nu)P^\dagger = \begin{pmatrix} r_1(\nu) & 0 & \cdots & 0 \\ 0 & r_1(\nu) & \cdots & 0 \\ \vdots & \vdots & \ddots & 0 \\ 0 & 0 & 0 & r_N(\nu) \end{pmatrix}. \tag{2.29}$$

Where $r_i(\nu)$ are non–negative eigenvalues and the master equation can now be found in a diagonal form to find

$$\partial_t \rho_S(t) = -\frac{i}{\hbar}[H_S + H_{LS}, \rho_S(t)] - \frac{1}{\hbar^2}\sum_{i,\nu} r_i(\nu)\Big(L_i(\nu)\rho_S(t)L_i(\nu)^\dagger - \frac{1}{2}\{L_i(\nu)^\dagger L_i(\nu), \rho_S(t)\}\Big). \tag{2.30}$$

This equation contains the newly defined Lindblad operators $L_i(\nu)$, which can be found from $A_i(\nu) = \sum_k P_{ki}L_i(\nu)$. When considering physical dissipators the eigenvalues $r_i(\omega)$ will be revealed to represent the relaxation rates for the corresponding decay modes and depend on the environment correlation terms [15]. To go further in this analysis, it is necessary to consider some properties of the system–environment coupling to reveal the form of these relaxation rates.

2.2 Harmonic oscillator environments

The environments necessary to model solid–state single photon sources, the focus of this thesis, are photonic and phonon baths. A photonic bath describes the electromagnetic field and phonons are a quasi–particle arising from the quantisation of vibrations of atoms in a lattice [71]. Characterising a photonic bath is necessary to describe the emission from a single photon source. Phonons, on the other hand, mediate a vast amount of dephasing processes in solid–state single photon sources. Both the electromagnetic field and a phonon bath can

be well described by the harmonic oscillator model, which is first detailed in this section [71]. Different forms of bath correlation functions using bosonic operators are then derived which are necessary to find the decay rates present in master equation when considering photonic and phonon environments.

To model the influence on phonons in solid–state quantum emitters it is necessary to consider the interaction between electrons and phonons. In the latter part of this section the electron–phonon interaction Hamiltonian has been derived up to second order with respect to the atomic displacements of a regular crystal lattice. This derivation is a novel extension to that detailed in Many–Particle Physics by Gerald D. Mahan [71], which covers the linear interaction. The derivation of the quadratic electron–phonon interaction presented here has been published and can be found in the supplementary material of [23].

2.2.1 Harmonic oscillator

To describe bosonic systems such as phonons and photons, it is typical to use a harmonic oscillator model, which in second quantisation holds the following Hamiltonian [71],

$$H_{\mathrm{b}} = \hbar \sum_{\mathbf{k}} \omega_{\mathbf{k}} [b^{\dagger}_{\mathbf{k}} b_{\mathbf{k}} + \frac{1}{2}], \tag{2.31}$$

where $\hbar\omega_{\mathbf{k}}$ is the eigenenergy of a boson mode with wavevector $\mathbf{k}$. The boson creation $b^{\dagger}_{\mathbf{k}}$ and annihilation $b_{\mathbf{k}}$ operators act on the fock space as

$$b^{\dagger}_{\alpha} \left| n_1 \dots n_{\alpha}, \dots, n_N \right\rangle = \sqrt{n_{\alpha} + 1} \left| n_1 \dots (n_{\alpha} + 1), \dots, n_N \right\rangle, \tag{2.32}$$

and

$$b_{\alpha} \left| n_1 \dots n_{\alpha}, \dots, n_N \right\rangle = \sqrt{n_{\alpha}} \left| n_1 \dots (n_{\alpha} - 1), \dots, n_N \right\rangle, \tag{2.33}$$

where $\left| n_1, n_2, n_j \dots, n_N \right\rangle$ are Fock states with $n_j = 0, 1, 2 \dots$ for bosons (spin integer) and when acting on the vacuum state one finds $b_{\alpha} \left| 0 \right\rangle = 0$. From this the boson number operator can be defined as $N = \sum_{\mathbf{k}} b^{\dagger}_{\mathbf{k}} b_{\mathbf{k}}$. This formalism to describe phonons and photons will be used throughout this thesis.

2.2.2 Bosonic correlation functions

In this section two different bosonic bath correlation functions are derived. Both of these are necessary when evaluating the response functions in Eq. (2.25) present in the microscopic master equations developed throughout the bulk of this thesis.

2.2.2.1 Bosonic operators

First considering the bosonic annihilation (creation) operators b ($b^{\dagger}$) introduced in Eq. (2.32) and (2.33). We define the operators $B_2 = \sum_{\mathbf{k}} g_{\mathbf{k}} b_{\mathbf{k}}$ with $B_1 = B_2^{\dagger}$ which sums over the boson

modes with wavevector $\mathbf{k}$ and weighted constants $g_{\mathbf{k}}$, and the time evolved counterpart as $B_2(t) = \sum_{\mathbf{k}} g_{\mathbf{k}} b_{\mathbf{k}} e^{-i\omega_{\mathbf{k}} t}$ assuming $\omega_{\mathbf{k}}$ is the boson eigenenergy. Now considering the bath correlation function from Eq. (2.22) for these operators we find

$$\begin{aligned} C_{12}(\tau) &= \mathrm{Tr}_{\mathrm{E}}(B_1 B_2(-\tau)\rho_{\mathrm{E}}), \\ &= \sum_{k,k'} g_{\mathbf{k}} g_{\mathbf{k}'} \mathrm{Tr}_{\mathrm{E}}(b_{\mathbf{k}}^\dagger b_{\mathbf{k}'} \rho_{\mathrm{E}}) e^{i\omega_{\mathbf{k}}\tau}. \end{aligned} \tag{2.34}$$

Next we evaluate the trace in this equation using the following definition of the thermal Gibbs state [15], given by

$$\rho_E = \frac{e^{-\beta \sum_{\mathbf{k}} \omega_{\mathbf{k}} b_{\mathbf{k}}^\dagger b_{\mathbf{k}}}}{\mathrm{Tr}_{\mathrm{E}}\left(e^{-\beta \sum_{\mathbf{k}} \omega_{\mathbf{k}} b_{\mathbf{k}}^\dagger b_{\mathbf{k}}}\right)}, \tag{2.35}$$

with $\beta = 1/k_B T$. For the case where $\mathbf{k} \neq \mathbf{k}'$ this gives $\mathrm{Tr}_{\mathrm{E}}(b_{\mathbf{k}}^\dagger b_{\mathbf{k}'} \rho_{\mathrm{E}}) = 0$ and for $\mathbf{k} = \mathbf{k}'$ the following relation holds $\mathrm{Tr}_{\mathrm{E}}(b_{\mathbf{k}}^\dagger b_{\mathbf{k}} \rho_{E_{\mathbf{k}}}) = (e^{\beta\omega_{\mathbf{k}}} - 1)^{-1}$ [16]. Using these relations it can therefore be defined

$$\mathrm{Tr}_{\mathrm{E}}(b_{\mathbf{k}}^\dagger b_{\mathbf{k}'} \rho_{\mathrm{E}}) = \delta_{\mathbf{k}\mathbf{k}'} n(\omega_{\mathbf{k}}). \tag{2.36}$$

Substituting this trace back into Eq. (2.34) gives

$$\begin{aligned} C_{12}(\tau) &= \sum_k |g_{\mathbf{k}}|^2 n(\omega_{\mathbf{k}}) e^{i\omega_{\mathbf{k}}\tau}, \\ &= \int_0^\infty d\omega J(\omega) n(\omega) e^{\pm i\omega\tau}, \end{aligned} \tag{2.37}$$

where the continuum limit has been taken using $\sum_{\mathbf{k}} |g_{\mathbf{k}}|^2 \to \int_0^\infty d\omega J(\omega)$ with $J(\omega)$ the spectral density which can be defined generally as [65]

$$J(\omega) = \sum_{\mathbf{k}} |g_{\mathbf{k}}|^2 \delta(\omega - \omega_{\mathbf{k}}). \tag{2.38}$$

This function fully captures the coupling strength between the system and the bath, weighted by the bath density of states. To find the conjugate of this bath correlation function from $C_{21}(\tau) = \mathrm{Tr}_{\mathrm{E}}(B_2 B_1(-\tau)\rho_{\mathrm{E}})$ using $\mathrm{Tr}_{\mathrm{E}}(b_{\mathbf{k}} b_{\mathbf{k}'}^\dagger \rho_{\mathrm{E}}) = \delta_{\mathbf{k}\mathbf{k}'}(n(\omega_{\mathbf{k}}) + 1)$ to find

$$C_{21}(\tau) = \int_0^\infty d\omega J(\omega)(n(\omega) + 1) e^{\pm i\omega\tau}. \tag{2.39}$$

2.2.2.2 Displacement operators

The second bath correlation function considered here and used throughout this thesis is for the operators

$$B_\pm = e^{\pm \sum_{\mathbf{k}} \left(\frac{g_{\mathbf{k}}}{\omega_{\mathbf{k}}} b_{\mathbf{k}}^\dagger - \frac{g_{\mathbf{k}}^*}{\omega_{\mathbf{k}}} b_{\mathbf{k}}\right)}, \tag{2.40}$$

which are a product of displacement operators such that, $B_\pm = \prod_{\mathbf{k}} D(\pm h_{\mathbf{k}})$, with $D(\pm h_{\mathbf{k}}) = \exp\left[\pm(h_{\mathbf{k}} b_{\mathbf{k}}^\dagger - h_{\mathbf{k}}^* b_{\mathbf{k}})\right]$ where $h_{\mathbf{k}} = \frac{g_{\mathbf{k}}}{\omega_{\mathbf{k}}}$. The time evolution of these operators can be written as $B_\pm(\tau) = U_{\mathrm{E}}^\dagger(\tau) B_\pm U_{\mathrm{E}}(\tau) = \prod_{\mathbf{k}} D(\pm h_{\mathbf{k}} e^{i\omega_{\mathbf{k}}\tau})$ which gives

$$B_\pm(\tau) = e^{\pm \sum_{\mathbf{k}} h_{\mathbf{k}} (b_{\mathbf{k}}^\dagger e^{i\omega_{\mathbf{k}}\tau} - b_{\mathbf{k}} e^{-i\omega_{\mathbf{k}}\tau})}. \tag{2.41}$$

The subsequent correlation function of these operators can therefore be expressed as

$$\begin{aligned}\mathcal{G}(\tau) &= \mathrm{Tr}_{\mathrm{E}}(B_{-}(\tau)B_{+}\rho_{\mathrm{E}}),\\ &= \mathrm{Tr}_{\mathrm{E}}\Big(\prod_{\mathbf{k}} D(-h_{\mathbf{k}}e^{i\omega_{\mathbf{k}}\tau})\prod_{\mathbf{k}'} D(h_{\mathbf{k}'})\rho_{\mathrm{E}}\Big),\\ &= \mathrm{Tr}_{\mathrm{E}}\Big(\prod_{\mathbf{k}} D(-h_{k}e^{i\omega_{\mathbf{k}}\tau})D(h_{\mathbf{k}})\rho_{\mathrm{E}}\Big),\end{aligned} \tag{2.42}$$

where last line is justified as the creation and annihilation operators that belong to different modes $\mathbf{k}$ commute. Using the identity

$$\exp\big[\hat{A}\big]\exp\big[\hat{B}\big] = \exp\Big[\frac{1}{2}[\hat{A},\hat{B}]\Big]\exp\big[\hat{A}+\hat{B}\big], \tag{2.43}$$

which is valid as long as $[\hat{A},\hat{B}]$ is proportional to the identity [10], we find

$$\prod_{\mathbf{k}} D(-h_{\mathbf{k}}e^{i\omega_{\mathbf{k}}\tau})D(h_{\mathbf{k}}) = \prod_{\mathbf{k}} D(-h_{\mathbf{k}}e^{i\omega_{\mathbf{k}}\tau}+h_{\mathbf{k}})e^{\frac{1}{2}(h_{\mathbf{k}}^{*}e^{-i\omega_{\mathbf{k}}\tau}h_{\mathbf{k}}-h_{\mathbf{k}}e^{i\omega_{\mathbf{k}}\tau}h_{\mathbf{k}}^{*})}. \tag{2.44}$$

Substituting this back into the trace in Eq. (2.42) and evaluating gives $\mathrm{Tr}_{\mathrm{E}}(D(h_{\mathbf{k}}-h_{\mathbf{k}}e^{i\omega_{\mathbf{k}}\tau})\rho_{\mathrm{E}}) = \exp\big[-\frac{1}{2}|h_{\mathbf{k}}-h_{\mathbf{k}}e^{i\omega_{\mathbf{k}}\tau}|^2\coth(\beta\omega/2)\big]$ [83]. Substituting this into the correlation function in Eq. (2.42), we find

$$\mathcal{G}(\tau) = \exp\Big[\sum_{\mathbf{k}}|h_{\mathbf{k}}|^2(\cos(\omega\tau)-1)\coth(\beta\omega/2)\Big]\exp\Big[-\sum_{\mathbf{k}} i\sin(\omega\tau)|h_{\mathbf{k}}|^2\Big]. \tag{2.45}$$

where trigonometry identities have been used. Taking the continuum limit as before using $\sum_k |g_{\mathbf{k}}|^2/\omega_{\mathbf{k}}^2 \to \int_0^\infty d\omega J(\omega)/\omega^2$ and splitting the time (in)dependent terms we find

$$\mathcal{G}(\tau) = \exp\Big[\int_0^\infty d\omega\frac{J(\omega)}{\omega^2}(\cos(\omega\tau)-i\sin(\omega\tau))\Big]\exp\Big[-\int_0^\infty d\omega\frac{J(\omega)}{\omega^2}\coth(\beta\omega/2)\Big]. \tag{2.46}$$

which can be expressed as

$$\mathcal{G}(\tau) = \exp[\phi(\tau)]\,\langle B\rangle^2, \tag{2.47}$$

with $\phi(\tau) = \int_0^\infty d\omega\frac{J(\omega)}{\omega^2}(\coth(\beta\omega/2)\cos(\omega\tau)-i\sin(\omega\tau))$ and $\langle B\rangle^2 = e^{-\phi(0)}$.

2.2.3 Electron–phonon interaction

In this section the electron phonon interaction Hamiltonian is derived up to second order with respect to the atomic displacements of a crystal lattice. Taking this interaction to second order is not typically done [71], however as will be revealed in chapter 4 it is necessary to capture some of the temperature dephasing mechanisms of solid–state single photon sources [1, 23].

To begin the Hamiltonian describing a lattice of ions interacting with a single electron shown in Fig. 2.1 is defined as

$$H = H_{\mathrm{e}} + H_{\mathrm{p}} + H_{\mathrm{ei}}, \tag{2.48}$$

where H_e and H_p represent the electronic (system) and phonon (environment) parts of the Hamiltonian respectively. The final term H_{ei} is the electron–ion interaction Hamiltonian, where this term can be written as

$$H_{ei} = \sum_i V_{ei}(\mathbf{r} - \mathbf{R}_i). \tag{2.49}$$

Each ion subscripted i and has position $\mathbf{R}_i = \mathbf{R}_i^{(0)} + \mathbf{Q}_i$ where $\mathbf{R}_i^{(0)}$ is the equilibrium position of the ions and $\mathbf{Q}_i$ is a small displacement caused from the charge interaction with the electron. This small displacement of a single ion in real space can be represented in second quantisation (i.e. in terms of the bosonic creation (annihilation) operators $b_{\mathbf{k}}^\dagger$ ($b_{\mathbf{k}}$)) as

$$\mathbf{Q}_i = i \sum_{\mathbf{k}} \left(\frac{1}{2NM\omega_{\mathbf{k}}} \right)^{1/2} e^{i\mathbf{k}\cdot\mathbf{R}_i^{(0)}} (b_{\mathbf{k}} + b_{\mathbf{k}}^\dagger) \hat{\xi}_{\mathbf{k}}, \tag{2.50}$$

where this expression sums over all of the phonon modes with lattice wavevectors $\mathbf{k}$ [71]. The number of ions in the lattice is given by N, M is the ion mass and $\omega_{\mathbf{k}}$ is the eigenfrequency of the mode. The polarisation vector is given by $\hat{\xi}_{\mathbf{k}}$, which defines the direction of the quantised lattice vibration for each wavevector $\mathbf{k}$. Taking a Taylor expansion with respect to $\mathbf{Q}_i$ gives

$$\begin{aligned} V_{ei}(\mathbf{r} - \mathbf{R}_i^{(0)} - \mathbf{Q}_i) = V_{ei}(\mathbf{r} - \mathbf{R}_i^{(0)}) - \mathbf{Q}_i \cdot \nabla V_{ei}(\mathbf{r} - \mathbf{R}_i^{(0)}) \\ + \frac{1}{2} \mathbf{Q}_i \cdot \nabla\nabla V_{ei}(\mathbf{r} - \mathbf{R}_i^{(0)}) \cdot \mathbf{Q}_i + \mathcal{O}(Q^3). \end{aligned} \tag{2.51}$$

The first term in this expansion is constant and forms a periodic potential in the crystal lattice, the solution to this is called the Bloch states of the solid. The linear term describes a displacement of the potential well minimum or lattice deformation. The quadratic term, which captures the anharmonicity, is typically neglected for many systems [71], however, as mentioned in the introduction of this section it will be seen in chapter 4 for certain circumstances it is necessary in order to fully capture phonon mediated dephasing processes. This quadratic term results in fluctuations of the phonon occupancy numbers (change in phonon force constants) for the

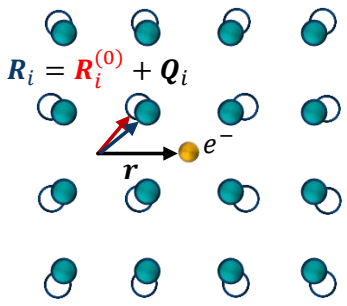

Figure 2.1: Lattice of ions with the indices i interacting with a single electron at position $\mathbf{r}$. The ions in their equilibrium positions (hollow circles) are at positions $\mathbf{R}_i^{(0)}$, whereas the ions displaced by the electron charge (opaque circles) are at positions $\mathbf{R}_i = \mathbf{R}_i^{(0)} + \mathbf{Q}_i$.

diagonal terms and phonon normal coordinate scrambling (Raman scattering processes) for the off–diagonal terms [1, 24]. In the next sections the linear and quadratic electron–phonon interaction terms are independently derived from Eq. (2.51).

2.2.3.1 Linear electron–phonon coupling

Defining the linear electron–phonon potential in terms of the electron–ion potential by summing over all ions gives

$$V_{\mathrm{ep}}^{(1)}(\mathbf{r}) = \sum_i \mathbf{Q_i} \cdot \nabla V_{\mathrm{ei}}(\mathbf{r} - \mathbf{R_i^{(0)}}). \tag{2.52}$$

To solve for the argument inside the sum of Eq. (2.52), first one expresses that the electron–ion potential possess a Fourier transform of the form

$$V_{\mathrm{ei}}(\mathbf{x}) = \frac{1}{N} \sum_{\mathbf{k}} V_{\mathrm{ei}}(\mathbf{k}) e^{i\mathbf{k}\cdot\mathbf{x}}. \tag{2.53}$$

Taking the derivative of this scalar field with respect to the real space variable $\mathbf{x}$, we find

$$\nabla V_{\mathrm{ei}}(\mathbf{x}) = \frac{i}{N} \sum_{\mathbf{k}} \mathbf{k} V_{\mathrm{ei}}(\mathbf{k}) e^{i\mathbf{k}\cdot\mathbf{x}}, \tag{2.54}$$

with $\nabla f(\mathbf{x}) = (\partial_{x_1} f(\mathbf{x}), \partial_{x_2} f(\mathbf{x}), \partial_{x_3} f(\mathbf{x}))$. Using this relationship to rewrite the linear electron–phonon potential in Eq. (2.52), to find

$$\begin{aligned} V_{\mathrm{ep}}^{(1)}(\mathbf{r}) &= \frac{i}{N} \sum_{\mathbf{q},\mathbf{i}} \mathbf{Q_i} \cdot \mathbf{k} V_{\mathrm{ei}}(\mathbf{k}) e^{i\mathbf{k}\cdot(\mathbf{r}-\mathbf{R_i^{(0)}})}, \\ &= \frac{i}{N} \sum_{\mathbf{q},\mathbf{i}} \mathbf{Q_i} e^{-i\mathbf{k}\cdot\mathbf{R_i^{(0)}}} \cdot \mathbf{k} V_{\mathrm{ei}}(\mathbf{k}) e^{i\mathbf{k}\cdot\mathbf{r}}. \end{aligned} \tag{2.55}$$

Transforming the second quantisation form of the lattice displacement shown in Eq. (2.50) into reciprocal space as

$$\begin{aligned} \frac{i}{N} \sum_{\mathbf{i}} \mathbf{Q}_i e^{-i\mathbf{k}\cdot\mathbf{R}_i^{(0)}} &= -\Big(\frac{1}{2NM\omega_{\mathbf{k}}}\Big)^{1/2} \hat{\xi}_{\mathbf{k}} (b_{\mathbf{k}} + b_{\mathbf{k}}^{\dagger}), \\ &= -\frac{1}{\sqrt{N}} \mathbf{Q}_{\mathbf{k}}, \end{aligned} \tag{2.56}$$

where it has been used that $\sum_i e^{i\mathbf{k}\cdot\mathbf{R}_i^{(0)}} e^{-i\mathbf{k}\cdot\mathbf{R}_i^{(0)}} = N$, and assuming the wavevector $\mathbf{k}$ goes only over the first Brillouin zone (BZ) which holds so long as one considers low energy excitations in the system [83]. Substituting Eq. (2.56) into the linear electron–phonon potential, it has been found

$$V_{\mathrm{ep}}^{(1)}(\mathbf{r}) = -\Big(\frac{1}{2NM\omega_{\mathbf{k}}}\Big)^{1/2} \sum_{\mathbf{k}} \hat{\xi}_{\mathbf{k}} \cdot \mathbf{k} V_{\mathrm{ei}}(\mathbf{k}) e^{i\mathbf{k}\cdot\mathbf{r}} (b_{\mathbf{k}} + b_{\mathbf{k}}^{\dagger}). \tag{2.57}$$

The Hamiltonian contribution for the linear electron–phonon coupling can be found from

$$H_{\mathrm{ep}}^{(1)} = \int d^3 r \rho(\mathbf{r}) V_{\mathrm{ep}}^{(1)}(\mathbf{r}), \tag{2.58}$$

where the fermion density operator has been introduced, given by

$$\rho(\mathbf{r}) = \sum_{\lambda,\eta} c_\lambda^\dagger c_\eta \psi_\lambda^*(\mathbf{r})\psi_\eta(\mathbf{r}), \tag{2.59}$$

$\psi_\lambda(\mathbf{r})$ is the electronic wavefunction with the annihilation (creation) operator c_λ ($c_\lambda^\dagger$) for the electronic state λ. Substituting in the linear electron–phonon potential shown in Eq. (2.57), it has been found

$$H_{\text{ep}}^{(1)} = \sum_{\mathbf{k}} \rho(\mathbf{k}) M^{(1)}(\mathbf{k})(b_{\mathbf{k}} + b_{\mathbf{k}}^\dagger), \tag{2.60}$$

where the electron–phonon linear matrix element is given by

$$M^{(1)}(\mathbf{k}) = -\Big(\frac{1}{2NM\omega_{\mathbf{k}}}\Big)^{1/2} \hat{\xi}_{\mathbf{k}} \cdot \mathbf{k} V_{\text{ei}}(\mathbf{k}). \tag{2.61}$$

Noting in Eq. (2.58) the fermion density operator here is represented in wavevector space by performing the Fourier transform $\rho(\mathbf{k}) = \int d^3 r e^{i\mathbf{k}\cdot\mathbf{r}} \rho(\mathbf{r})$.

2.2.3.2 Quadratic electron–phonon coupling

Finding the quadratic electron–phonon interaction Hamiltonian by first writing the quadratic potential as

$$V_{\text{ep}}^{(2)}(\mathbf{r}) = \frac{1}{2} \sum_i \mathbf{Q}_i \cdot \nabla\nabla V_{\text{ei}}(\mathbf{r} - \mathbf{R}_i^{(0)}) \cdot \mathbf{Q}_i. \tag{2.62}$$

Following the same methodology as for the linear case, it is assumed that the electron–ion potential possesses a Fourier transform in the form

$$V_{\text{ei}}(\mathbf{x}) = \frac{1}{N^2} \sum_{\mathbf{k},\mathbf{k}'} V_{\text{ei}}(\mathbf{k} + \mathbf{k}') e^{i(\mathbf{k}+\mathbf{k}')\cdot\mathbf{x}}, \tag{2.63}$$

where $\mathbf{k}$ and $\mathbf{k}'$ are the phonon mode wavevectors. The gradient of this function with respect to the real space variable can be expressed as

$$\nabla V_{\text{ei}}(\mathbf{x}) = \frac{i}{N^2} \sum_{\mathbf{k},\mathbf{k}'} (\mathbf{k} + \mathbf{k}') V_{\text{ei}}(\mathbf{k} + \mathbf{k}') e^{i(\mathbf{k}+\mathbf{k}')\cdot\mathbf{x}}, \tag{2.64}$$

which holds the form of a vector valued potential. Taking a second gradient again with respect to the real space variable, now gives a scalar valued potential

$$\nabla\nabla V_{\text{ei}}(\mathbf{x}) = -\frac{1}{N^2} \sum_{\mathbf{k},\mathbf{k}'} (\mathbf{k} + \mathbf{k}') \cdot (\mathbf{k} + \mathbf{k}') V_{\text{ei}}(\mathbf{k} + \mathbf{k}') e^{i(\mathbf{k}+\mathbf{k}')\cdot\mathbf{x}}. \tag{2.65}$$

Substituting in Eq. (2.65) into Eq. (2.62) to find the quadratic electron–photon potential as

$$V_{\text{ep}}^{(2)}(\mathbf{r}) = -\frac{1}{2N} \sum_{\mathbf{k},\mathbf{k}'} \mathbf{Q}_{\mathbf{k}} \cdot (\mathbf{k} + \mathbf{k}') \cdot (\mathbf{k} + \mathbf{k}') V_{\text{ei}}(\mathbf{k} + \mathbf{k}') e^{i(\mathbf{k}+\mathbf{k}')\cdot\mathbf{r}} \cdot \mathbf{Q}_{\mathbf{k}'}. \tag{2.66}$$

where Eq. (2.56) has been used to convert $\mathbf{Q}_i \rightarrow \mathbf{Q}_\mathbf{k}$ similar to the linear case. Finding the quadratic Hamiltonian contribution by first substituting in $\mathbf{Q}_\mathbf{k}$ from Eq. (2.56) and integrating over the charge density as shown in Eq. (2.59), gives

$$H_{\text{ep}}^{(2)} = \frac{1}{2}\sum_{\mathbf{k},\mathbf{k}'} \rho(\mathbf{k}+\mathbf{k}')M^{(2)}(\mathbf{k},\mathbf{k}')(b_\mathbf{k}+b_\mathbf{k}^\dagger)(b_{\mathbf{k}'}+b_{\mathbf{k}'}^\dagger), \tag{2.67}$$

where the electron–phonon second order matrix element is

$$M^{(2)}(\mathbf{k},\mathbf{k}') = \frac{1}{4NM\sqrt{\omega_\mathbf{k}\omega_{\mathbf{k}'}}}\hat{\xi}_\mathbf{k}\cdot(\mathbf{k}+\mathbf{k}')\cdot(\mathbf{k}+\mathbf{k}')\cdot\hat{\xi}_{\mathbf{k}'}V_{\text{ei}}(\mathbf{k}+\mathbf{k}'). \tag{2.68}$$

2.2.3.3 Electron–phonon matrix elements

It is advantageous to find an analytical form for the linear and quadratic form of these matrix elements, $M^{(1)}(\mathbf{k})$ and $M^{(2)}(\mathbf{k},\mathbf{k}')$. Moreover, we now consider an ideal two–level system with states $i = \{e, g\}$, assuming that transitions to higher order electronic states are neglected due to large energy splitting separations. Substituting in the resolution of identity over the two–dimensional system Hilbert space, the linear and quadratic interaction Hamiltonian can therefore be written as

$$H_{\text{ep}} = \hbar\sum_{i,j}|i\rangle\langle j|\sum_\mathbf{k} g_\mathbf{k}(b_\mathbf{k}+b_\mathbf{k}^\dagger) + \hbar\frac{1}{2}\sum_{i,j}|i\rangle\langle j|\sum_{\mathbf{k},\mathbf{k}'} f_{\mathbf{k},\mathbf{k}'}(b_\mathbf{k}+b_\mathbf{k}^\dagger)(b_{\mathbf{k}'}+b_{\mathbf{k}'}^\dagger), \tag{2.69}$$

with the linear and quadratic electron–phonon coupling strengths $g_\mathbf{k} = \langle i|M^{(1)}(\mathbf{k})\rho(\mathbf{k})|j\rangle$ and $f_{\mathbf{k},\mathbf{k}'} = \frac{1}{2}\langle i|M^{(2)}(\mathbf{k},\mathbf{k}')\rho(\mathbf{k}+\mathbf{k}')|j\rangle$, respectively. We can simplify this expression further by neglecting the off diagonal matrix elements $\langle e|\ldots|g\rangle$ and $\langle g|\ldots|e\rangle$, as typical longitudinal acoustic phonon energies ($\sim$ meV) are not sufficient to drive transitions between the ground and excited state ($\sim$ eV). Moreover, the ground state matrix elements are normalised to zero giving

$$H_{\text{ep}} = \hbar\,|e\rangle\langle e|\sum_\mathbf{k} g_\mathbf{k}(b_\mathbf{k}+b_\mathbf{k}^\dagger) + \hbar\frac{1}{2}\,|e\rangle\langle e|\sum_{\mathbf{k},\mathbf{k}'} f_{\mathbf{k},\mathbf{k}'}(b_\mathbf{k}+b_\mathbf{k}^\dagger)(b_{\mathbf{k}'}+b_{\mathbf{k}'}^\dagger), \tag{2.70}$$

with the strengths $g_\mathbf{k} = \langle e|M^{(1)}(\mathbf{k})\rho(\mathbf{k})|e\rangle$ and $f_{\mathbf{k},\mathbf{k}'} = \frac{1}{2}\langle e|M^{(2)}(\mathbf{k},\mathbf{k}')\rho(\mathbf{k}+\mathbf{k}')|e\rangle$, respectively. Substituting the electron density in reciprocal space $\rho(\mathbf{k}) = \int d^3r\sum_{\lambda,\eta} c_\lambda^\dagger c_\eta\psi_\lambda^\dagger(\mathbf{r})\psi_\eta(\mathbf{r})e^{i\mathbf{k}\cdot\mathbf{r}}$ where $\lambda,\eta = \{e,g\}$, into the linear and quadratic coupling strengths gives

$$g_\mathbf{k} = \sum_{\eta,\lambda}\int d^3r\psi_\eta^\dagger(\mathbf{r})\psi_\lambda(\mathbf{r})e^{i\mathbf{k}\cdot\mathbf{r}}\,\langle e|M^{(1)}(\mathbf{k})c_\eta^\dagger c_\lambda|e\rangle\,, \tag{2.71}$$

$$f_{\mathbf{k},\mathbf{k}'} = \frac{1}{2}\sum_{\eta,\lambda}\int d^3r\psi_\eta^\dagger(\mathbf{r})\psi_\lambda(\mathbf{r})e^{i(\mathbf{k}+\mathbf{k}')\cdot\mathbf{r}}\,\langle e|M^{(2)}(\mathbf{k},\mathbf{k}')c_\eta^\dagger c_\lambda|e\rangle\,. \tag{2.72}$$

Substituting in the equation for $M^{(1)}(\mathbf{k})$ and $M^{(2)}(\mathbf{k},\mathbf{k}')$ and assuming the electron–ion potential is equal to a constant deformation potential such that, $V_{\text{ei}}(\mathbf{k}) \rightarrow D_\alpha$ with $\alpha = \{e,g\}$, to find

$$g_\mathbf{k} = \Big(\frac{k^2}{2NM\omega_\mathbf{k}}\Big)^{1/2}\sum_\alpha D_\alpha\int d^3r|\psi_\alpha(\mathbf{r})|^2e^{i\mathbf{k}\cdot\mathbf{r}}, \tag{2.73}$$

$$f_{\mathbf{k},\mathbf{k}'} = \frac{1}{4NM\sqrt{\omega_{\mathbf{k}}\omega_{\mathbf{k}'}}}(k' + k\cos\theta_{kk'})(k + k'\cos\theta_{kk'})\sum_{\alpha} D_{\alpha}\int d^3r|\psi_{\alpha}(\mathbf{r})|^2 e^{i(\mathbf{k}+\mathbf{k}')\cdot\mathbf{r}}, \qquad (2.74)$$

where $\theta_{kk'}$ is the angle between $\mathbf{k}$ and $\mathbf{k}'$ wave vectors.

In the presented formulation the terms quadratic in the phonon displacements arise because the electron–phonon coupling is taken to second-order with respect to the atomic displacements of the crystal lattice. In this approach anharmonicity of the phonon modes is accounted for through their coupling to the electronic degrees of freedom. A different approach, typically used to characterise quantum dots, can give rise to similar quadratic terms. In this method the two–level electronic system assumption is relaxed, allowing for transitions to a higher lying electronic state, where the inclusion of this state gives rise to virtual phonon transitions between the first excited and higher order state which captures the phonon anharmonicity [81]. As will be seen in chapter 4 different platforms such as a single molecule require the derived approach displayed above to accurately account for these effects.

CHAPTER 3

OPTICAL PROPERTIES OF A QUANTUM EMITTER

This chapter reviews general optical properties of solid state quantum emitters covered through this thesis. Firstly, the dynamics of an ideal two–level system (TLS) coupled to a photonic environment capturing spontaneous emission is detailed and the corresponding emission spectrum is found. This generic TLS is then further coupled to a phonon environment, where the resultant effect on the emission is presented and discussed. The next optical property introduced in this section is the second order correlation measurement found from both a Hanbury Brown and Twiss (HBT) and Hong–Ou–Mandel (HOM) experiment. The emitter properties that can be revealed from these experiments are then discussed. Finally, the effect on spectral wandering of a quantum emitter is analysed where this work extends up on the reference given in [42] by including the effect from an emitter simultaneously undergoing pure dephasing.

3.1 Photonic environment

Deterministic quantum emitters in the most primitive sense can be modelled as a general optically active two–level electronic system (TLS), shown in Fig. 3.1. The ground $|g\rangle$ and excited state $|e\rangle$ are split with energy E_X. The excited state has lifetime T_1 and a spontaneous decay rate $\Gamma_1 = 1/T_1$. To model the optical properties corresponding to this TLS, this system is weakly coupled to a quantised vacuum electromagnetic (EM) field environment. Describing this photonic environment as a harmonic oscillator with annihilation (creation) operators $c_l(c_l^\dagger)$ for mode l, the following spontaneous emission (SE) Hamiltonian can be used

$$H_{\mathrm{SE}} = H_{\mathrm{S}} + H_{\mathrm{EM}} + H_{\mathrm{I}}^{\mathrm{EM-TLS}}, \tag{3.1}$$

where the system term describes the electronic two–level system $H_{\mathrm{S}} = E_X\sigma^\dagger\sigma$ and $\sigma = |g\rangle\langle e|$ is the dipole operator. The electromagnetic field environment term is given by $H_{\mathrm{EM}} = \hbar\sum_l \nu_l c_l^\dagger c_l$

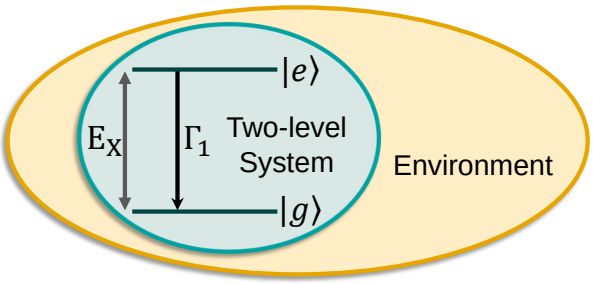

Figure 3.1: Two–level electronic system with a ground state $|g\rangle$ and excited state $|e\rangle$, split by energy E_X. The spontaneous decay rate from the excited state is given by Γ_1 and the system coupled to some arbitrary environment.

where ν_l is the frequency for electromagnetic mode l. The final term represents exciton–photon interaction which in its most general form is given by the Hamiltonian in the dipole approximation [110], as

$$H_{\mathrm{I}}^{\mathrm{EM-TLS}} = -\mathbf{d} \cdot \mathbf{E}_{EM}, \tag{3.2}$$

where $\mathbf{d}$ is the dipole dot operator which can be expressed in terms of the single emitter basis as $\mathbf{d} = \mathbf{d}_{ge}\sigma + \mathbf{d}_{eg}\sigma^{\dagger}$ with the dipole moment $\mathbf{d}_{ge} = \langle g|\mathbf{d}|e\rangle$ and $\mathbf{d}_{eg} = \mathbf{d}_{ge}^{\dagger}$. The vacuum photonic continuum field in Eq. (3.2) is given by

$$\mathbf{E}_{EM} = -\sum_{l} \mathbf{e}_l \sqrt{\frac{\hbar\nu_l}{2\epsilon_0 V}}\,(c_l^{\dagger} + c_l), \tag{3.3}$$

where $\mathbf{e}_l$ is a polarisation vector of the photon mode l, V is the quantisation volume and ϵ_0 is the permittivity of free space [39, 83]. Finding the interaction Hamiltonian from these vectors gives

$$H_{\mathrm{I}}^{\mathrm{EM-TLS}} = \hbar \sum_{l} (\sigma^{\dagger} + \sigma)(p_l^{*} c_l^{\dagger} + p_l c_l), \tag{3.4}$$

where the constants are wrapped into the linear coupling strength given by $p_l = -\sqrt{\frac{\hbar\nu_l}{2\epsilon_0 V}}\,\mathbf{e}_l \cdot \mathbf{d}_{ge}/\hbar$. Expanding the terms in Eq. (3.4) and moving into the interaction picture by

$$\tilde{H}_{\mathrm{I}}(-\tau) = U_0^{\dagger}(-\tau) H_{\mathrm{I}} U_0(-\tau), \tag{3.5}$$

with $U_0(t) = \exp[-i(H_{\mathrm{S}} + H_{\mathrm{EM}})t/\hbar]$, to find

$$\tilde{H}_{\mathrm{I}}^{\mathrm{EM-TLS}} = \hbar \sum_{l} (p_l^{*}\sigma^{\dagger} c_l^{\dagger} e^{i(\omega_{\mathrm{X}} + \nu_l)t} + p_l^{*}\sigma c_l^{\dagger} e^{i(\nu_l - \omega_{\mathrm{X}})t} + p_l \sigma^{\dagger} c_l e^{i(\omega_{\mathrm{X}} - \nu_l)t} + p_l \sigma c_l e^{-i(\nu_l + \omega_{\mathrm{X}})t}), \tag{3.6}$$

where $\omega_{\mathrm{X}} = E_{\mathrm{X}}/\hbar$ is the emission frequency of the TLS. To simplify this equation the rotating–wave approximation (RWA) can be invoked which allows for the removal of the fast oscillating terms. To make this approximation firstly it is assumed that dipole operators couple to the electromagnetic environmental modes close to resonance, where this allows for two different

timescales to be clearly identified. These different timescales correspond to the slow/fast oscillating terms dependent on $\pm(\nu_l - \omega_X)/\pm(\nu_l + \omega_X)$ in Eq. (3.6), respectively. For these fast oscillating terms, it is expected that they average to zero over the relevant timescale of the system relaxation time, allowing for their removal [15]. Safely neglecting these off–resonant terms and moving back into the standard frame leads to

$$H_{\mathrm{I}}^{\mathrm{EM-TLS}} = \hbar \sum_l p_l (\sigma c_l^\dagger + \sigma^\dagger c_l). \tag{3.7}$$

To find the emission spectrum for this Hamiltonian, a Born-Markov master equation is now derived.

3.1.1 Spontaneous emission master equation

In order to find a master equation that describes a TLS coupled to a photonic environment, first Eq. (2.17) needs to be evaluated. To solve this the interaction picture Hamiltonian from Eq. (3.5) needs to be found, giving

$$\tilde{H}_{\mathrm{S-EM}}(-\tau) = \hbar \sigma e^{-i\omega_X \tau} C^\dagger(-\tau) + \mathrm{h.c.}, \tag{3.8}$$

where $C(-\tau) = \sum_l p_l c_l e^{i\nu_l \tau}$. Inserting the expressions for $H_{\mathrm{S-EM}}$ and $\tilde{H}_{S-EM}(-\tau)$ into the integral shown in Eq. (2.17) gives

$$\partial_t \rho_{\mathrm{S}}(t) = -\frac{i}{\hbar}\big[H_{\mathrm{S}}, \rho_{\mathrm{S}}(t)\big] - \frac{1}{\hbar^2}\int_0^\infty d\tau \mathrm{Tr}_E\Big(\big[H_{\mathrm{S-EM}}, [\tilde{H}_{\mathrm{S-EM}}(-\tau), \rho_{\mathrm{S}}(t) \otimes \rho_E]\big]\Big). \tag{3.9}$$

To solve the integral in this equation the photonic environment correlation functions need to be evaluated. Drawing on the section on bosonic operators in (2.2.2.1) and as the photonic bath is assumed in vacuum the temperature of this environment is effectively 0 K, leading to the only non–zero correlation function to be

$$\begin{aligned} \mathrm{Tr}_E(CC^\dagger(-\tau)\rho_E) &= \int_0^\infty d\nu J_{EM}(\nu)(n(\nu)+1)e^{i\nu\tau} \\ &= \int_0^\infty d\nu J_{EM}(\nu)e^{i\nu\tau} = \chi(\tau), \end{aligned} \tag{3.10}$$

as $n(\nu) = (e^{-\beta\nu} - 1)^{-1}$ the Bose occupation number is zero for a vacuum continuum and $J_{EM}(\nu) = \sum_l |p_l|^2 \delta(\nu - \nu_l)$ is the photonic spectral density. Substituting the non–zero correlation function into Eq. (3.9) gives

$$\partial_t \rho_{\mathrm{S}}(t) = -\frac{i}{\hbar}\big[H_{\mathrm{S}}, \rho_{\mathrm{S}}(t)\big] - \Big(\int_0^\infty d\tau \chi(\tau) e^{-i\omega_X \tau}\Big(\sigma^\dagger \sigma(\text{-}\tau)\rho_{\mathrm{S}}(t) - \sigma(\text{-}\tau)\rho_{\mathrm{S}}(t)\sigma^\dagger\Big) + h.c.\Big) \tag{3.11}$$

Solving for the environment response function from Eq. (2.25) gives

$$\begin{aligned}\mathcal{K}(\omega_X) &= \int_0^\infty d\tau \chi(\tau) e^{-i\omega_X \tau}, \\ &= \int_0^\infty d\omega \int_0^\infty d\tau J_{EM}(\omega) e^{i(\omega-\omega_X)\tau}, \\ &= \int_0^\infty d\omega \pi J_{EM}(\omega)\delta(\omega-\omega_X) + i\mathcal{P}\int_0^\infty d\omega \frac{J_{EM}(\omega)}{\omega-\omega_X}, \\ &= \pi J_{EM}(\omega_X) + i\mathcal{P}\int_0^\infty d\omega \frac{J_{EM}(\omega)}{\omega-\omega_X}.\end{aligned} \tag{3.12}$$

Where the evaluation of this integral into its real and imaginary parts is found using the Sokhotski-Plemlj theorem [15], which in its general form for a function $f(\omega)$ is

$$\int_0^\infty d\omega \int_0^\infty d\tau f(\omega) e^{\pm i(\omega-\nu)\tau} = \int_0^\infty d\omega \pi f(\omega)\delta(\omega-\nu) \pm i\mathcal{P}\int_0^\infty d\omega \frac{f(\omega)}{\omega-\nu}, \tag{3.13}$$

where $\mathcal{P}$ is the Cauchy principal value. Substituting the response function in Eq. (3.12) back into the master equation in Eq. (3.11) to find

$$\partial_t \rho_S(t) = -\frac{i}{\hbar}[H_S, \rho_S(t)] + \Big(\pi J_{EM}(\omega_X) + i\mathcal{P}\int_0^\infty d\omega \frac{J_{EM}(\omega)}{\omega-\omega_X}\Big)\mathcal{L}_\sigma[\rho_S(t)], \tag{3.14}$$

where $\mathcal{L}_A[\rho(t)] = A\rho(t)A^\dagger - \frac{1}{2}\{A^\dagger A, \rho(t)\}$ is the Lindblad operator. The term multiplied by the imaginary contribution of the response function is known as a Lamb shift, as it acts to renormalise the system Hamiltonian by H_{LS} such that,

$$\partial_t \rho_S(t) = -\frac{i}{\hbar}[H_S + H_{LS}, \rho_S(t)] + \pi J_{EM}(\omega_X)\mathcal{L}_\sigma[\rho_S(t)], \tag{3.15}$$

where this term corresponds to vacuum fluctuations of the electromagnetic field induced by the system–photonic bath coupling [15]. For the case of a vacuum photonic field it is expected that the Lamb shift energy for atomic–like systems is negligible compared to the system energy splitting (which for typical quantum emitters gives $H_S \sim 1\,\text{eV}$). Moreover, when modelling a systems properties it can be advantageous to represent the master equation in a rotated frame with respect to this renormalised system Hamiltonian, rendering its absolute value inconsequential (in particular for the systems considered in this thesis, where the Lamb shift contributions negligible). This rotation can be performed using $\rho_R(t) = U_R(t)\rho_S(t)U_R^\dagger(t)$ with $U_R = \exp[i(H_S + H_{LS})t]$ where using $[H_S, H_{LS}] = 0$, gives

$$\partial_t \rho_R(t) = \pi J_{EM}(\omega_X)\mathcal{L}_\sigma[\rho_R(t)], \tag{3.16}$$

where this removes the commutator term and now the system energy is normalised to zero.

3.1.2 Emission spectrum

Now the master equation for this system is found, the one color emission spectrum can be evaluated, where this can be defined by [110]

$$S(\omega) = 2\,\text{Re}\Big[\int_0^\infty d\tau g^{(1)}(\tau) e^{-i\omega\tau}\Big], \tag{3.17}$$

which is the Fourier transform of the time averaged first order correlation function of the electric field operator given by

$$g^{(1)}(\tau) = \int_0^\infty dt \left\langle E^\dagger(t+\tau)E(t) \right\rangle. \tag{3.18}$$

Defining the positive frequency component of the electric field operator with $E(t) = \sum_l c_l(t)$, where to solve for $E(t)$ the following Heisenberg equations of motion can be evaluated

$$\dot{c_l}(t) = -i[H(t), c_l(t)], \tag{3.19}$$

which for this Hamiltonian gives [56]

$$\dot{c_l} = -i\nu_l c_l(t) - ip_l c_l \sigma(t). \tag{3.20}$$

Solving this equation of motion by first using the product rule we find

$$\frac{\partial}{\partial t}\{c_l(t)e^{i\nu t}\} = i\nu c_l(t)e^{i\nu t} + \frac{\partial c_l(t)}{\partial t}e^{i\nu t}. \tag{3.21}$$

Substituting in $\dot{c_l}(t)$ and using the Fourier variable $\tilde{c_l}(\nu) = \int_{-\infty}^{\infty} dt c_l(t)e^{i\nu t}$ to find

$$\frac{\partial}{\partial t}\{c_l(t)e^{i\nu t}\} = i(\nu - \nu_l)c_l(t)e^{i\nu t} - ip_l\sigma(t)e^{i\nu t}, \tag{3.22}$$

$$\int_{-\infty}^{\infty} \partial\{c_l(t)e^{i\nu t}\} = i\int_{-\infty}^{\infty} \partial t\big((\nu - \nu_l)c_l(t)e^{i\nu t} - p_l\sigma(t)e^{i\nu t}\big). \tag{3.23}$$

Solving the above integrals this can be rearranged to give

$$\tilde{c_l}(\nu) = \frac{p_l \int_{-\infty}^{\infty} dt\sigma(t)e^{i\nu t}}{(\nu - \nu_l)} = \frac{p_l \Xi(\nu)}{(\nu - \nu_l)}, \tag{3.24}$$

where $\Xi(\nu) = \int_{-\infty}^{\infty} dt\sigma(t)e^{i\nu t}$. Summing over the modes to find the electric field operator we find $\tilde{E}(\nu) = \sum_l \tilde{c_l}(\nu) = \sum_l \frac{p_l}{(\nu - \nu_l)}\Xi(\nu)$. Next taking the continuum limit such that $\sum_l \frac{p_l}{\nu - \nu_l} \rightarrow \int_{\infty}^{\infty} d\omega \frac{p(\omega)}{\nu - \omega}$. Solving this improper integral using the Cauchy principal value $\mathcal{P}$ and the *Kramers–Kronig* relations [9] to find

$$\mathcal{P}\int_{-\infty}^{\infty} d\omega \frac{p(\omega)}{(\nu - \omega)} = -i\pi p(\nu). \tag{3.25}$$

To evaluate the photonic spectral density at ω_X as required for the spontaneous emission dissipator, one assumes this is unchanging for a non–driven emitter allowing for the assumption

$$\begin{aligned} J_{\mathrm{EM}}(\omega_X) &= \pi^2 |p(\omega_X)|^2 \\ &= \frac{\Gamma_1}{(2\pi)}, \end{aligned} \tag{3.26}$$

where Γ_1 is the systems spontaneous decay rate. Now Fourier transforming back to the time domain to find

$$E(t) = E_0(t) + \sqrt{\Gamma_1/2\pi}\,\sigma(t), \tag{3.27}$$

where $E_0(t)$ is the free field vacuum contribution. Substituting in the electric field operators in to the first order correlation function to find

$$g^{(1)}(\tau) = \frac{\Gamma_1}{2\pi}\int_0^\infty dt \left\langle \sigma^\dagger(t+\tau)\sigma(t)\right\rangle, \tag{3.28}$$

where the expectation value of the free field vacuum contribution is zero.

3.1.2.1 Quantum regression theorem

To solve the first order correlation function in the integrand of Eq. (3.28) the quantum regression theorem can be used which is outlined in this section [48]. Expressing this equation in terms of the trace over the system and environmental degrees of freedom

$$\left\langle \sigma^\dagger(t+\tau)\sigma(t)\right\rangle = \frac{\Gamma_1}{2\pi}\mathrm{Tr}_{S+E}[U_0^\dagger(t+\tau)\sigma^\dagger U_0(t+\tau)U_0^\dagger(t)\sigma U_0(t)\rho_{SE}(0)], \tag{3.29}$$

where $\rho_{SE}(0)$ is the initial system-environment density operator. Inserting the resolution of identity, the factorisation $U(t+\tau) = U(t)U(\tau)$, and using the cyclic properties of the trace to find

$$\left\langle \sigma^\dagger(t+\tau)\sigma(t)\right\rangle = \frac{\Gamma_1}{2\pi}\mathrm{Tr}_{S+E}[\sigma^\dagger U_0(\tau)\sigma\rho_{S+E}(t)U_0^\dagger(\tau)], \tag{3.30}$$

Defining an effective density operator by partially tracing over the environmental degrees of freedom

$$\Lambda(\tau,t) = \mathrm{Tr}_E[U(\tau)\sigma\rho_{S+E}(t)U^\dagger(\tau)], \tag{3.31}$$

gives $\left\langle \sigma^\dagger(t+\tau)\sigma(t)\right\rangle = \frac{\Gamma_1}{2\pi}\mathrm{Tr}_S[\sigma^\dagger\Lambda(\tau,t)]$. Postulating the equation of motion for $\Lambda(\tau,t)$ as $\partial_\tau\Lambda(\tau,t) = \mathcal{L}\big(\Lambda(\tau,t)\big)$, which is analogous to a master equation $\partial_t\rho_S(t) = \mathcal{L}\big(\rho_S(t)\big)$, where $\Lambda(0,t) = \sigma\rho_S(t)$, the time evolution of the effective density operator is found to be $\Lambda(\tau,t) = e^{\mathcal{L}\tau}\Lambda(0,t)$, from which

$$\left\langle \sigma^\dagger(t+\tau)\sigma(t)\right\rangle = \frac{\Gamma_1}{2\pi}\mathrm{Tr}_S[\sigma^\dagger e^{\mathcal{L}\tau}\sigma e^{\mathcal{L}t}\rho_S(0)]. \tag{3.32}$$

For the TLS-photonic open quantum system in question this can be analytically evaluated to give

$$g^{(1)}(\tau,t) = \frac{\Gamma_1}{2\pi}e^{-\Gamma_1 t}e^{-(\Gamma_1/2)\tau}, \tag{3.33}$$

where $\rho_S(0)$ is initially in the excited state. Substituting this back into the equation for the emission spectrum in Eq. (3.17) to find

$$S(\omega) = \frac{2\Gamma_1}{\pi(\Gamma_1^2 + 4\omega^2)}. \tag{3.34}$$

Here it can be concluded that the emission spectrum from an atomic two–level system coupled to a Markovian photonic bath results in a Lorentzian function with full–width half maximum Γ_1. Using a master equation in a rotating frame with respect to the TLS energy, shown in Eq. (3.16), to evaluate $S(\omega)$ the Lorentizan is centered on zero detuning, see Fig. 3.2 to visualise this emission.

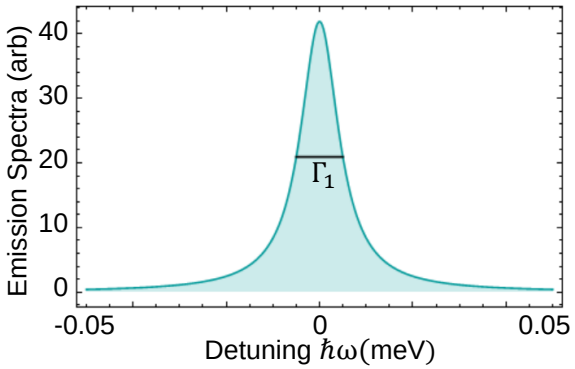

Figure 3.2: Emission spectrum of a two–level system as a function of energy splitting detuning. The spontaneous decay rate Γ_1 characterises the full–width half maximum of the Lorentizan function.

3.2 Phonon environment

For all solid state emitters the optically active electronic system is coupled to some lattice environment. To describe the interaction between a two–level system and some bosonic field the independent boson model can be utilised and is reviewed alongside the polaron transform in this section.

3.2.1 Independent boson model and polaron transform

The independent boson model couples a TLS to a bosonic harmonic oscillator environment (which is equivalent to a thermal phonon bath). To begin consider a Hamiltonian in the form

$$H_{\mathrm{IB}} = H_{\mathrm{S}} + H_{\mathrm{PH}} + H_{\mathrm{S-PH}}, \tag{3.35}$$

with the two–level system (TLS) term $H_{\mathrm{S}} = E_{\mathrm{X}}\sigma^{\dagger}\sigma$ as in Eq. (3.1). The phonon environment is $H_{\mathrm{PH}} = \hbar\sum_{\mathbf{k}} \omega_{\mathbf{k}} b_{\mathbf{k}}^{\dagger} b_{\mathbf{k}}$, where $b_{\mathbf{k}}^{\dagger}(b_{\mathbf{k}})$ are creation (annihilation) operators with wavevector $\mathbf{k}$ and frequency $\omega_{\mathbf{k}}$. The linear coupling term holds the form $H_{\mathrm{S-PH}} = \hbar\sigma^{\dagger}\sigma\sum_{\mathbf{k}} g_{\mathbf{k}}(b_{\mathbf{k}}^{\dagger} + b_{\mathbf{k}})$, with coupling strength $g_{\mathbf{k}}$.

An analytical solution to the independent boson model can be found using a variety of approaches [71]. In this section the polaron transform approach will be considered, as it will be revealed that performing this transformation has beneficial consequences for modelling phonon interactions. To move into the polaron frame, the following transform is acted on the Hamiltonian $H_{\mathrm{IB,P}} = U_{\mathrm{P}} H_{\mathrm{IB}} U_{\mathrm{P}}^{\dagger}$ where

$$U_{\mathrm{P}} = \sigma\sigma^{\dagger} + \sigma^{\dagger}\sigma B_{+}, \tag{3.36}$$

with the phonon bath displacement operator shown in Eq. (2.40). Performing this transform gives the polaron frame Hamiltonian to be

$$H_{\mathrm{IB,P}} = E'_{\mathrm{X}}\sigma^{\dagger}\sigma + H_{\mathrm{E}}, \tag{3.37}$$

where $E'_{\mathrm{X}} = E_{\mathrm{X}} - \hbar \sum_{\mathbf{k}} \frac{g_{\mathbf{k}}^2}{\omega_{\mathbf{k}}}$ is the polaron shifted TLS energy splitting. It can be seen that performing the polaron transform removes the interaction term $H_{\mathrm{S-PH}}$. To find the time dynamics of this system, the reduced system density operator needs to be evaluated from

$$\rho_{\mathrm{S}}(t) = \mathrm{Tr}_{\mathrm{E}}(U(t)\rho_{\mathrm{S}}(0)\rho_{\mathrm{E}}(0)U^{\dagger}(t))], \tag{3.38}$$

where $\rho_{\mathrm{S}}(0)\rho_{\mathrm{E}}(0)$ is factorised initial state complete density operator. The time evolution is governed by a unitary time evolution operator, by $U(t) = e^{-iH_{\mathrm{IB}}t}$ which in the polaron frame is $U(t) = U_{\mathrm{P}}^{\dagger} e^{-iH_{\mathrm{IB,P}}t} U_{\mathrm{P}}$ evaluating to [83]

$$U(t) = \sigma\sigma^{\dagger} e^{-iH_{\mathrm{E}}t} + \sigma^{\dagger}\sigma e^{-iE'_{\mathrm{X}}t} B_{-} e^{-iH_{\mathrm{E}}t} B_{+}. \tag{3.39}$$

Noting evolving the system with a unitary is only possible in the polaron frame as it gives a diagonal Hamiltonian by removing the interaction term. Evaluating Eq. (3.38) using the definition of the trace in Eq. (2.6) to sum over the environmental basis $|i\rangle = \{g, e\}$, in matrix notation gives

$$\rho_{\mathrm{S}}(t) = \begin{pmatrix} \rho_{ee}(0) & \rho_{eg}(0)e^{-iE'_{\mathrm{X}}t}\mathcal{G}^{*}(t) \\ \rho_{ge}(0)e^{iE'_{\mathrm{X}}t}\mathcal{G}(t) & \rho_{gg}(0) \end{pmatrix} \tag{3.40}$$

where $\mathcal{G}(t) = \mathrm{Tr}_{E}(B_{-}(\tau)B_{+}\rho_{E}(0))$ is the bosonic bath correlation function evaluated in Eq. (2.47). It can be seen that only the off–diagonal density terms hold time dependence. From performing this polaron transformation it can be seen that the phonon bath degrees of freedom are included in this description of the system operator. The consequence of performing this polaron transformation on the emission spectrum is now explored in the next section.

3.2.2 Phonon sideband emission

Considering now emission from a two–level system emitter coupled to both a photonic and thermal phonon bath environment. The resultant Hamiltonian to describe such a system is given by

$$H = H_{\mathrm{S}} + H_{\mathrm{E}} + H_{\mathrm{S-EM}} + H_{\mathrm{S-PH}}, \tag{3.41}$$

where all terms are from the Hamiltonians in Eq. (3.1) and Eq. (3.35) and the environment is given by $H_E = H_{\mathrm{PH}} + H_{\mathrm{EM}}$. This open quantum system well captures emission from a quantum dot coupled to its solid state lattice environment [55].

To find the optical dynamics of this system the Hamiltonian is subjected to a polaron transformation as performed in the previous section. Applying $H_{\mathrm{P}} = U_{\mathrm{P}} H U_{\mathrm{P}}^{\dagger}$ using Eq. (3.36), gives the transformed Hamiltonian is $H_{\mathrm{P}} = E'_{\mathrm{X}}\sigma^{\dagger}\sigma + H_E + H_{\mathrm{S-EM,P}}$ where

$$H_{\mathrm{S-EM,P}} = \sigma C^{\dagger} B_{-} + \sigma^{\dagger} C B_{+}, \tag{3.42}$$

where $C = \sum_l p_l c_l$ and terms $B_{\pm}$ are defined in Eq. (2.40). In the polaron frame, the interaction between the TLS and the thermal phonon environment has been rotated out and where the

influence of this phonon bath is now present in system–EM interaction term. The second order Born-Markov master equation for this system is equivalent to that written down in Eq. (3.14). The difference between the model shown in section (3.1), is that now the basis is in the polaron frame, where if this were to be moved back into the original frame the master equation would be non-Markovian.

To calculate the one color spectrum for this system the Fourier transform of the first order correlation function is required shown in Eq (3.17). To do so the electric field operator $E(t)$ which makes up $g^{(1)}(\tau, t)$ in Eq. (3.18) is needed. Solving the electric field operator from the Heisenberg equation of motion shown in Eq. (3.19), using the polaron transformed Hamiltonian, it has been found that [55]

$$\dot{c}_l = -i\nu_l c_l(t) - if_l c_l \sigma(t) B_-(t). \tag{3.43}$$

Solving this equation of motion using the Fourier variable $\tilde{c}(\nu) = \int dt c_l(t) e^{i\omega t}$, it has been found that [55]

$$E(t) = E_0(t) + \sqrt{\frac{\Gamma_1}{2\pi}}\,\sigma(t) B_-(t), \tag{3.44}$$

where $E_0(t)$ is the vacuum contribution which when taking expectation values can be neglected. Using this definition of the electric field operators, it has been found

$$\begin{aligned} g^{(1)}(\tau) &= \frac{\Gamma_1}{2\pi}\left\langle \sigma^\dagger(t+\tau) B_+(t+\tau)\sigma(t) B_-(t)\right\rangle, \\ &\approx \frac{\Gamma_1}{2\pi} g^{(1)}(\tau, t)\mathcal{G}(\tau), \end{aligned} \tag{3.45}$$

where $g^{(1)}(\tau, t) = \left\langle \sigma^\dagger(t+\tau)\sigma(t)\right\rangle$ is the photonic correlation function. The phonon correlation function is given by $\mathcal{G}(\tau) = \langle B_+(t+\tau) B_-(t)\rangle$ shown in Eq. (2.47). The factorisation of the trace can be performed as a consequence of the Born approximation as it is assumed that the system couples weakly to the phonon environment. Putting this in terms of the emission spectrum gives

$$S(\omega) = \frac{\Gamma_1}{\pi}\,\mathrm{Re}\Big[\int_0^\infty dt \int_0^\infty d\tau g^{(1)}(\tau, t)\mathcal{G}(\tau) e^{-i\omega\tau}\Big], \tag{3.46}$$

where the photonic correlation function can be computationally evaluated using the quantum regression theorem and the phonon correlation function can be found numerically. To simulate the emission spectrum for a two–level system coupled to a phonon bath, a typical quantum dot (QD) emitter has been chosen. The sideband functional form for a QD is characterised with the choice of the exciton–phonon spectral density $J_{PH}(\omega)$. For QDs it is typical to use a super Ohmic form to reflect the three–dimensional phonon bath and symmetric electronic wavefunction with

$$J_{PH}(\omega) = \sum_{\mathbf{k}} g_{\mathbf{k}}^2 \delta(\omega - \omega_{\mathbf{k}}) = \alpha\,\omega^3 \exp\left[-\omega^2/\xi^2\right]. \tag{3.47}$$

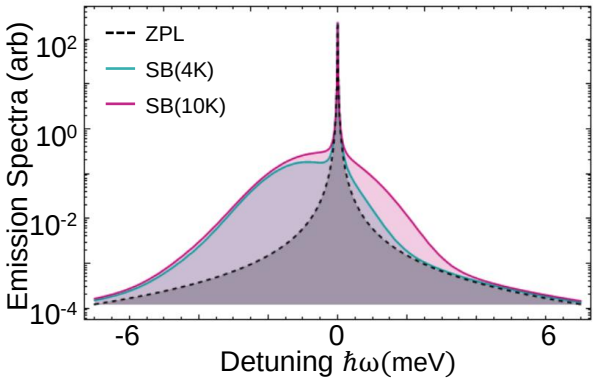

Figure 3.3: Emission spectrum of a two–level system coupled to a thermal phonon bath at 4 K and 10 K. Parameters used simulate linewidth limited quantum dot emission with $\Gamma_1 = 0.15\,\mathrm{ps}^{-1}$, and sideband parameters $\alpha = 0.03\,\mathrm{ps}^2$ and $\xi = 2.2\,\mathrm{ps}^{-1}$

Where α is the exciton–phonon coupling strength and ξ the high-frequency cut-off which is inversely proportional to the spacial extent of the ground and exciton wavefunction [83]; a detailed derivation for this functional form can be found in Appendix (A.1). This emission spectrum simulated at 4 K and 10 K is shown in Fig. 3.3, where the parameters used to simulate this system are taken from reference [55]. Comparing this spectrum to the ideal two–level system model in Fig. 3.2, one can observe the broad continuous phonon sideband which overlays the sharp Lorentzian peak also known as the zero phonon line (ZPL). The observed sideband originates from the polaron frame treatment, as this allows for the explicit capture of transitions to and from the phonon lattice bath. Emission into the negatively detuned sideband originates from the decay into a phonon mode coupled to the ground state and the positively detuned emission comes from an excitation into a phonon mode coupled to the excited state. When considering the phonon sideband however, as the temperature decreases a reduction in emission is observed as well as a shift to the negatively detuned frequency. This shift in the sideband is due to a lower thermal energy found from $k_B T$, which means fewer phonon modes from the lattice are excited.

3.3 Second order correlation functions

Until now only the emission spectrum has been considered to explore the optical properties of a single photon emitter, which is dependent on the first order correlation function. An alternative approach to this, is to directly probe the second order correlation function, which allows for two–photon interference effects to be explored. Second order correlation functions can be found experimentally by interfering photons on a beam splitter and measuring coincidence events with two detectors [59]. In this section two key experiments including, the Hanbury Brown and Twiss and Hong–Ou–Mandel experiments are introduced and discussed.

3.3.1 Hanbury Brown–Twiss experiment

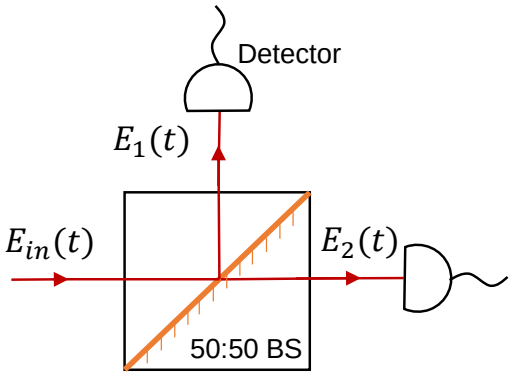

Figure 3.4: Hanbury Brown and Twiss experimental set up, where E_{in} is the positive input field and E_1 and E_2 are the positive fields detected by the detectors after passing through the $50:50$ beam splitter (BS). The vacuum electric field is incident on the bottom half of the BS.

The most straight forward method to measure a second order intensity correlation function is with a Hanbury Brown and Twiss (HBT) experiment, see figure 3.4. In this experiment there is one source which gets split at a $50:50$ beam splitter and the correlation between detection events is measured. The HBT experiment is used to verify if a source is emitting temporally separated single photons. If the source is a single photon emitter then there should be no coincidence events between the two output detectors at $\tau = 0$ leading to a signature dip to zero.

Evaluating the second order correlation function by first defining the general form as

$$G^{(2)}(t,\tau) = \left\langle E_1^\dagger(t) E_2^\dagger(t+\tau) E_2(t+\tau) E_1(t) \right\rangle . \tag{3.48}$$

where τ is the difference time in detection events. This measurement probes the probability of coincidence events between the two detectors. For the HBT set–up the detected electric fields can be related to the single input field for a $50:50$ beam splitter via the following matrix operation

$$\begin{pmatrix} E_1(t) \\ E_2(t) \end{pmatrix} = \frac{1}{\sqrt{2}} \begin{pmatrix} 1 & 1 \\ -1 & 1 \end{pmatrix} \begin{pmatrix} E_{in}(t) \\ E_0(t) \end{pmatrix}, \tag{3.49}$$

where $E_0(t)$ is the vacuum electric field incident on the bottom half of the beam splitter. Solving this equation to find $E_1(t) = \frac{1}{\sqrt{2}}(E_{in}(t) + E_0(t))$ and $E_2(t) = -\frac{1}{\sqrt{2}}(E_{in}(t) + E_0(t))$. Substituting the definitions of the output field into Eq. (3.48), where the expectation values of the free field values average to zero, as are assumed to be in the vacuum state, and dropping the 'in' subscripts to find

$$G^{(2)}_{HBT}(t,\tau) = \frac{1}{4} \left\langle E^\dagger(t) E^\dagger(t+\tau) E(t+\tau) E(t) \right\rangle . \tag{3.50}$$

Normalising this function with the uncorrelated expectation value to find

$$g^{(2)}_{HBT}(t,\tau) = \frac{\langle E^\dagger(t)E^\dagger(t+\tau)E(t+\tau)E(t)\rangle}{\langle E^\dagger(t)E(t)\rangle \langle E^\dagger(t+\tau)E(t+\tau)\rangle}. \tag{3.51}$$

3.3.2 Hong–Ou–Mandel experiment

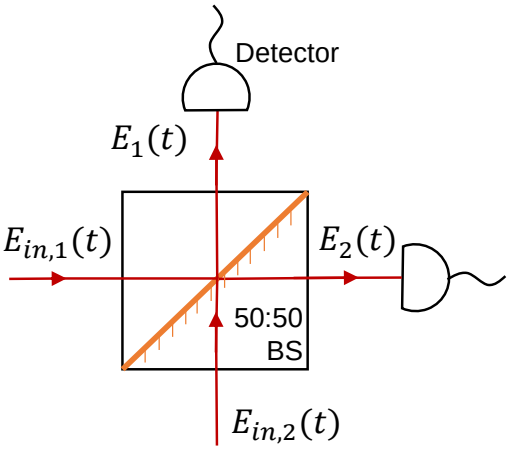

Figure 3.5: Hong–Ou–Mandel set up, where $E_{in,1}(t)$ and $E_{in,2}(t)$ are the positive input fields and $E_1(t)$ and $E_2(t)$ are the positive fields detected by the detectors after passing through the 50 : 50 beam splitter (BS).

Now considering the case where two separate photon streams are incident on either side of the beam splitter. This experimental setup is known as a Hong–Ou–Mandel (HOM) experiment, see Fig. 3.5. The HOM experiment is used to determine the indistinguishability of the two streams of incident photons, where indistinguishability describes to what degree are two photons quantum mechanically identical. The input fields in this experiment could either come from the same source emitting successive single photons with a variable time delay or from two different sources.

To find the second order correlating function for the HOM setup by first relating the detector fields to the input fields gives

$$\begin{pmatrix} E_1(t) \\ E_2(t) \end{pmatrix} = \frac{1}{\sqrt{2}} \begin{pmatrix} 1 & 1 \\ -1 & 1 \end{pmatrix} \begin{pmatrix} E_{in,1}(t) \\ E_{in,2}(t) \end{pmatrix}. \tag{3.52}$$

Solving this to find $E_1(t) = \frac{1}{\sqrt{2}}(E_{in,1}(t) + E_{in,2}(t))$ and $E_2(t) = \frac{1}{\sqrt{2}}(E_{in,2}(t) - E_{in,1}(t))$. Substituting the detected fields into the general second order correlation function shown in Eq. (3.48) gives

$$G^{(2)}_{HOM}(\tau,t) = \frac{1}{4}\Big\langle \big(E^\dagger_{in,1}(t) + E^\dagger_{in,2}(t)\big)\big(E^\dagger_{in,2}(t+\tau) - E^\dagger_{in,1}(t+\tau)\big) \\ \times \big(E_{in,2}(t+\tau) - E_{in,1}(t+\tau)\big)\big(E_{in,1}(t) + E_{in,2}(t)\big)\Big\rangle, \tag{3.53}$$

where to normalise this function the uncorrelated coincidence events can be used, from

$$\left\langle E_1^\dagger(t)E_1(t)\right\rangle \left\langle E_2^\dagger(t+\tau)E_2(t+\tau)\right\rangle = \frac{1}{4}\Big\langle \big(E_{in,1}^\dagger(t)+E_{in,2}^\dagger(t)\big)\big(E_{in,1}(t)+E_{in,2}(t)\big)\Big\rangle \times \Big\langle \big(E_{in,2}^\dagger(t+\tau)-E_{in,1}^\dagger(t+\tau)\big)\big(E_{in,2}(t)-E_{in,1}(t)\big)\Big\rangle. \quad (3.54)$$

To further simplify Eq. (3.53) the input fields $E_1(t)$ and $E_2(t)$ are assumed to originate from statistically independent sources which have identical emission properties. These assumptions allow for the factorisation of operators followed by the dropping of subscripts to give

$$G_{HOM}^{(2)}(t,\tau) = \frac{1}{2}\Big(4G_{HBT}^{(2)}(t+\tau) - \Big|\Big\langle E^\dagger(t)E(t+\tau)\Big\rangle\Big|^2 - \Big|\Big\langle E^\dagger(t)E^\dagger(t+\tau)\Big\rangle\Big|^2 + 2\,\mathrm{Re}\Big[\langle E(t)\rangle\Big\langle E^\dagger(t)E^\dagger(t+\tau)E(t+\tau)\Big\rangle - \langle E(t+\tau)\rangle\Big\langle E^\dagger(t)E^\dagger(t+\tau)E(t)\Big\rangle\Big)\Big] + \Big\langle E^\dagger(t)E(t)\Big\rangle\Big\langle E^\dagger(t+\tau)E(t+\tau)\Big\rangle\Big). \quad (3.55)$$

This equation can be used to capture having both input streams from the one source if there is sufficient delay between photons such that the photon streams can be approximated to be statistically independent.

3.3.2.1 Indistinguishability for a two–level system

This section will present how performing a Hong–Ou–Mandel interferometer experiment under non–resonant pulsed excitation allows for the measurement and calculation of full wavepacket photon indistinguishability. This pulsed excitation regime represents a very fast laser rapidly exciting the population to a higher lying state, which first undergoes a decay process to the first excited state, followed by decay to the ground state with the emission of a photon. To theoretically model this excitation regime, one can set the population to initially reside in the first excited state at time zero and time evolve capturing the final decay process. Using this approach the system can be modelled as two–level system with a ground and excited state which has a spontaneous decay rate Γ_1 and a phenomenological pure dephasing process is introduced with rate γ. This pure dephasing rate captures an effective jitter of the excited state electronic state energy which leads to a homogeneous broadening of the emission line. The dynamics of the reduced system operator $\rho_S(t)$ for this TLS can be described with the following second–order Born–Markov master equation

$$\partial_t\rho(t) = \Gamma_1\mathcal{L}_\sigma[\rho(t)] + 2\gamma\mathcal{L}_{\sigma^\dagger\sigma}[\rho(t)], \quad (3.56)$$

which is modified from Eq. (3.16) to include the phenomenological pure dephasing dissipator [55]. As presented in section (3.1) the input fields $E(t)$ and $E^\dagger(t)$ can be set to the dipole operators $\sigma(t)$ and $\sigma^\dagger(t)$ [59], where numerical factors are dropped and $\sigma = |g\rangle\langle e|$. To simplify Eq. (3.55) a few steps are taken. Firstly, the terms linear in $\langle E\rangle$ and the two terms in the form

$\langle EE \rangle$ all go to zero as expectation values linear in ladder operators are zero. Next, integrating over t to find the unnormalised ensemble average of coincidence events to find

$$G^{(2)}_{PUL}(\tau) = \frac{1}{2}\int_0^\infty dt\Big(\left\langle \sigma^\dagger(t)\sigma(t) \right\rangle \left\langle \sigma^\dagger(t+\tau)\sigma(t+\tau) \right\rangle - \left| \left\langle \sigma^\dagger(t+\tau)\sigma(t) \right\rangle \right|^2 \Big), \tag{3.57}$$

where the PUL subscript represents pulsed excitation under the HOM set-up. Under pulsed excitation $G^{(2)}_{HBT}(t,\tau) = 0$ for a single photon emitter as $\sigma^2 = 0$ [115]. The normalised second order correlation function can be found by dividing by the uncorrelated peak area $A = \int_0^\infty dt \int d\tau \left\langle \sigma^\dagger(t)\sigma(t) \right\rangle \left\langle \sigma^\dagger(t+\tau)\sigma(t+\tau) \right\rangle$ to find $g^{(2)}_{PUL}(\tau) = \frac{1}{A} G^{(2)}_{PUL}(\tau)$. To find the uncorrelated coincidence events, experimentally this corresponds to setting a perpendicular polarisation between interferometer arms, mathematically this relates to

$$G^{(2)}_{\perp_{PUL}}(\tau) = \frac{1}{2}\int_0^\infty dt \left\langle \sigma^\dagger(t)\sigma(t) \right\rangle \left\langle \sigma^\dagger(t+\tau)\sigma(t+\tau) \right\rangle, \tag{3.58}$$

where the interference term vanishes.

The indistinguishability of the single quantum emitter can be found from these correlation measurements by integrating over τ and finding the fraction [17, 58, 59]

$$\mathcal{I} = \frac{\int d\tau\, G^{(2)}_{PUL}(\tau) - \int d\tau\, G^{(2)}_{\perp_{PUL}}(\tau)}{\int d\tau\, G^{(2)}_{\perp_{PUL}}(\tau)}. \tag{3.59}$$

Substituting the functions for $G^{(2)}_{PUL}(\tau)$ and $G^{(2)}_{\perp_{PUL}}(\tau)$ into Eq. (3.59) to find [58]

$$\mathcal{I} = \frac{\int dt \int d\tau \left| \left\langle \sigma^\dagger(t+\tau)\sigma(t) \right\rangle \right|^2}{\int dt \int d\tau \left\langle \sigma^\dagger(t)\sigma(t) \right\rangle \left\langle \sigma^\dagger(t+\tau)\sigma(t+\tau) \right\rangle}. \tag{3.60}$$

Using the quantum regression theorem outlined in section (3.1.2.1) the correlation function in the numerator of Eq. (3.60) can be evaluated to give

$$\begin{aligned} \left| \left\langle \sigma^\dagger(t+\tau)\sigma(t) \right\rangle \right|^2 &= \left| \mathrm{Tr}_S\left(\sigma^\dagger e^{\mathcal{L}\tau}\sigma(e^{\mathcal{L}t}\rho_S(0))\right) \right|^2, \\ &= e^{-2\Gamma_1 t} e^{-(\Gamma_1+2\gamma)\tau}, \end{aligned} \tag{3.61}$$

where $\mathcal{L}$ is the Liouvillian super–operator. The integrand in the denominator is found using the same approach, giving $\left\langle \sigma^\dagger(t)\sigma(t) \right\rangle \left\langle \sigma^\dagger(t+\tau)\sigma(t+\tau) \right\rangle = e^{-\Gamma_1 t} e^{-\Gamma_1(t+\tau)}$. Integrating over both t and τ leads to the well documented equation for indistinguishability from a two–level system emitter with pure dephasing as

$$\mathcal{I}_{\text{pulsed}} = \frac{\Gamma_1}{2\Gamma_2}, \tag{3.62}$$

where $\Gamma_2 = \frac{\Gamma_1}{2} + \gamma$ [45, 115]. It can be seen from this relation that in order to achieve high indistinguishability it is crucial to minimise the pure dephasing rate. If the pure dephasing is thermal, one way to directly reduce γ is to reduce the temperature of the system, where both

the reasoning for this and the underlying mechanism of pure dephasing will be revealed in chapter 4. An alternative approach to increase indistinguishability would be to enhance the spontaneous emission rate, where this could be done via the means of coupling the TLS to a cavity, as will explored in chapters 6 and 7 [57].

3.4 Spectral wandering

So far only pure dephasing has been considered as a dephasing mechanism for a two–level system emitter. Another type of dephasing that is common amongst some solid state emitters is spectral wandering, also known as spectral diffusion or frequency jitter [28, 36, 50]. This process refers to the random wandering of central emission frequency, typically attributed to local fluctuations of the charge environment of the emitter. Spectral wandering leads to inhomogeneous broadening of the emission linewidth and is typically characterised by a Gaussian distribution. Pure dephasing on the other hand broadens the zero phonon line homogeneously and follows a Lorentzian profile. When an emitter exhibits both of these sources of dephasing the resultant spectral profile can be fit with a Voigt function [14]. In this section the spectral emission and indistinguishability of a spectrally wandered two–level system emitter, also dephased by some pure dephasing is derived. Different distribution functions for the spectral wandering are considered and a direct comparison of both dephasing mechanisms are presented.

3.4.1 Spectral wandering indistinguishability theory

Previous work to model a single photon emitter undergoing spectral wandering with *no* pure dephasing has been found in references [42, 58]. Here, both of these approaches include spectral wandering by performing a statistical average over the density operator with a Gaussian profile. Finding the emission spectrum of a spectrally broadened two–level system (TLS) emitter amounts to taking a convolution of the Lorentizan profile with a Gaussian noise function [14].

For this work a TLS single photon emitter which undergoes both spectral wandering and pure dephasing with rate γ_{PD}, is modelled. The starting point of this derivation is the second order Born-Markov master equation for a two–level system

$$\partial_t \rho(t) = -i[\delta\sigma^\dagger\sigma, \rho(t)] + \Gamma\mathcal{L}_\sigma[\rho(t)] + 2\gamma_{\mathrm{PD}}\mathcal{L}_{\sigma^\dagger\sigma}[\rho(t)], \tag{3.63}$$

where to model spectral wandering the stochastic detuning energy δ of the two–level system is explicitly included here, where in Eq. (3.16) $\delta = 0$. To model the jitter of the emission linewidth the detuning energy is statistically averaged over some general distribution function $f(\delta)$. To find the dynamics of the TLS with spectral wandering one considers the statistical averaging

of the first order correlation function $g^{(1)}(t,\tau) = \langle \sigma^\dagger(t+\tau)\sigma(t) \rangle$ with respect to δ giving

$$\begin{aligned} g^{(1)}_{\mathrm{SW}}(t,\tau) &= \Big\langle \Big\langle \sigma^\dagger(t+\tau)\sigma(t) \Big\rangle \Big\rangle_{\mathrm{SW}}, \\ &= \int d\delta f(\delta) g^{(1)}(t,\tau). \end{aligned} \tag{3.64}$$

Defining the first order correlation function for this spectral wandered systems allows for the calculation of the emission spectra following Eq. (3.17) to give

$$S(\omega) = 2\,\mathrm{Re}\Big[\int_0^\infty d\tau \int_0^\infty dt g^{(1)}_{\mathrm{SW}}(\tau,t) e^{-i\omega\tau} \Big]. \tag{3.65}$$

Note that this ensemble averaging method in one dimension is equivalent to convolving the spectral function with a distribution function [14, 47].

The emission spectra of a TLS undergoing spectral wandering is now directly compared to a TLS undergoing pure dephasing only. For the spectral wandering model, two different distribution functions are considered for the walk, a Lorentzian distribution in the form

$$f_L(\delta, \gamma_{\mathrm{SW}}) = \frac{1}{\pi} \frac{\gamma_{\mathrm{SW}}}{\delta^2 + \gamma^2_{\mathrm{SW}}}, \tag{3.66}$$

and a Gaussian distribution, given by

$$f_G(\delta, \sigma_{\mathrm{SW}}) = \frac{1}{\sigma_{\mathrm{SW}}\sqrt{2\pi}} \exp\left[\frac{-x^2}{2\sigma^2_{\mathrm{SW}}} \right]. \tag{3.67}$$

Using these distribution functions the spectral functions from Eq. (3.65) have been found. When assuming the random walk from spectral wandering follows a Lorentzian distribution, the resultant emission spectrum is

$$S_L(\omega) = \frac{2(2(\gamma_{\mathrm{SW}} + \gamma_{\mathrm{PD}}) + \Gamma_1)}{\pi(2(\gamma_{\mathrm{SW}} + \gamma_{\mathrm{PD}}) + \Gamma_1)^2 + 4\omega^2)}, \tag{3.68}$$

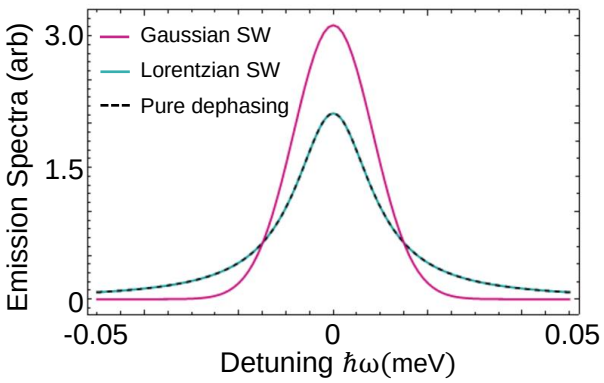

Figure 3.6: Spectral emission from a TLS comparing different dephasing mechanisms. Pure dephasing only shown in (dashed black) where, $2\gamma_{\mathrm{PD}} = 10/2\pi$ THz. Spectral wandering with no pure dephasing following a Lorentizan distribution with $2\gamma_{\mathrm{SW}} = 10/2\pi$ THz (solid blue) and a Gaussian distribution with $\sigma_{\mathrm{FWHM}} = 10/2\pi$ THz (solid pink).

which, for the case of no pure dephasing $\gamma_{\text{PD}} = 0$ is a spectral function that is equivalent to the pure dephasing model for $\gamma_{\text{SW}} = \gamma_{\text{PD}}$, see Fig 3.6. For the case of a Gaussian distribution the emission function is found to give

$$S_G(\omega) = \frac{\exp\left[\frac{(2\gamma_{\text{PD}}+\Gamma_1-2i\omega)^2}{8\sigma_{\text{SW}}^2}\right]\left(\text{Erfc}\left[\frac{2\gamma_{\text{PD}}+\Gamma_1-2i\omega}{2\sqrt{2}\sigma_{\text{SW}}}\right]+\exp\left[\frac{i(2\gamma_{\text{PD}}+\Gamma_1\omega)}{\sigma_{\text{SW}}^2}\right]\text{Erfc}\left[\frac{2\gamma_{\text{PD}}+\Gamma_1+2i\omega}{2\sqrt{2}\sigma_{\text{SW}}}\right]\right)}{2\sqrt{2\pi}\,\sigma_{\text{SW}}}, \tag{3.69}$$

noting that the full–width half–maximum (FWHM) is $\sigma_{\text{FWHM}} = 2\sqrt{2\ln 2}\,\sigma_{\text{SW}}$. To visualise these spectrally wandered emission spectrum see Fig. 3.6. It can be seen that when the FWHM are set to be equivalent for the Lorentzian and Gaussian spectral walk models, the Gaussian walk leads to emission which is less spectrally spread.

To find the indistinguishability for a spectrally wandered emitter one substitutes the ensemble average correlation functions into the definition of indistinguishability shown in Eq. (3.60) to find

$$I_{\text{SW}} = \frac{\int_0^\infty dt\int_0^\infty d\tau\left|\left\langle\left\langle\sigma^\dagger(t+\tau)\sigma(t)\right\rangle\right\rangle_{\text{SW}}\right|^2}{\int_0^\infty dt\int_0^\infty d\tau\left\langle\left\langle\sigma^\dagger(t)\sigma(t)\right\rangle\right\rangle_{\text{SW}}\left\langle\left\langle\sigma^\dagger(t+\tau)\sigma(t+\tau)\right\rangle\right\rangle_{\text{SW}}}, \tag{3.70}$$

where $\langle\langle\ldots\rangle\rangle_{\text{SW}}$ represents the ensemble averaging shown in Eq. (3.64). Evaluating the indistinguishability for a spectrally wandered emitter with firstly, a Gaussian distribution, by finding the numerator of the integrand in Eq. (3.70) gives

$$\left|\left\langle\left\langle\sigma^\dagger(t+\tau)\sigma(t)\right\rangle\right\rangle_{\text{SW,G}}\right|^2 = \exp\left[-(2\Gamma_1 t+(\Gamma_1+2\gamma_{\text{PD}}+\sigma_{\text{SW}}^2)\tau)\right]. \tag{3.71}$$

The statistically averaged excited state population with a Gaussian walk is found to be $\left\langle\left\langle\sigma^\dagger(t)\sigma(t)\right\rangle\right\rangle_{\text{SW,G}} = \exp[-\Gamma_1 t] = \left\langle\sigma^\dagger(t)\sigma(t)\right\rangle$, which is independent on the statistical averaging. Putting the evaluated integrands back into Eq. (3.70) and integrating over t and τ to find

$$I_{SW,G}(\sigma_{\text{SW}}) = \frac{\exp\left[\left(\frac{2\gamma_{\text{PD}}+\Gamma_1}{2\sigma_{\text{SW}}}\right)^2\right]\sqrt{\pi}\,\Gamma_1\text{Erfc}\left[\frac{2\gamma_{\text{PD}}+\Gamma_1}{2\sigma_{\text{SW}}}\right]}{2\sigma_{\text{SW}}}, \tag{3.72}$$

which for the case of no pure dephasing $\gamma_{\text{PD}} = 0$ the form found in reference [42] is recovered.

For the case of a Lorentzian distribution the numerator of the integrand in Eq. (3.70) has been evaluated to

$$\left|\left\langle\left\langle\sigma^\dagger(t+\tau)\sigma(t)\right\rangle\right\rangle_{\text{SW,L}}\right|^2 = \exp\left[-(2\Gamma_1 t+(\Gamma_1+2\gamma_{\text{PD}}+2\gamma_{\text{SW}})\tau)\right]. \tag{3.73}$$

The excited state population with a Lorentzian walk is again found to be independent on the distribution to give $\left\langle\left\langle\sigma^\dagger(t)\sigma(t)\right\rangle\right\rangle_{\text{SW,L}} = \exp[-\Gamma_1 t]$. Evaluating the integrals in Eq. (3.70) the indistinguishability for a Lorentzian walk has been found to be

$$I_{SW,L}(\gamma_{\text{SW}}) = \frac{\Gamma}{\Gamma+2(\gamma_{\text{SW}}+\gamma_{\text{PD}})}, \tag{3.74}$$

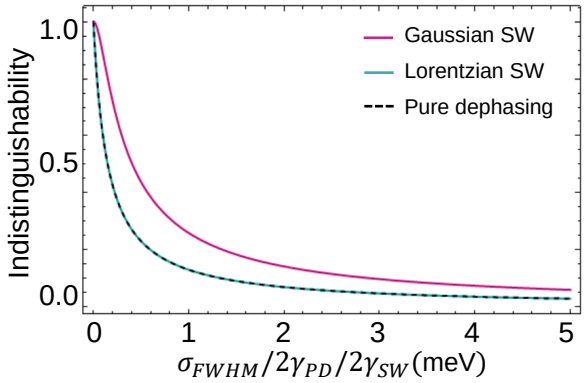

Figure 3.7: Indistinguishability vs $2\gamma_{\mathrm{PD}}/2\gamma_{\mathrm{SW}}$ for the pure dephasing model and the spectral wandering model with a Lorentz distribution, respectively. For the spectral wandering model with a Gaussian distribution the x–axis scales as the full width half maximum of the distribution σ_{SW}.

where this reiterates that spectral wandering under a Lorentzian walk is equivalent to the process of pure dephasing. To visualise the dependence on the analytical indistinguishability vs dephasing parameters, see Fig 3.7. To make the parameters for the Gaussian and Lorentzian walks comparable the distributions FWHM has been plotted on the horizontal axis, which is σ_{FWHM} and $2\gamma_{\mathrm{SW}}$, respectively. For all of these calculations $\Gamma_1 = 0.15\,\mathrm{ps}^{-1}$, which reflects a typical quantum dot emitter [55]. It can been seen that the indistinguishability for a spectrally wandering emitter with a Gaussian distribution is relatively higher when compared to a Lorentzian one. This is attributed to the reduction in spectral frequency distribution when considering a Gaussian profile as seen in Fig. 3.6, which reduces the distinguishability of emission.

In practicality no physical emitter will walk exactly like a distribution, as the fluctuations are random. Moreover, for solid state emitters the phonon sideband effects interfere with TLS emission and engulf the tails (as seen in Fig. 3.3) which mainly differentiate these distributions. Therefore in the literature, due to the increase in numerical complexity of dealing with the Gaussian walk, it is common to model spectral wandering using a Lorentzian profile [47, 115]. A final comment on spectral wandering is the ability to reduce it. Firstly, if the interfering photons have not had sufficient time to spectrally shift by ensuring short time delays between pulses, the effect of spectral wandering can be removed from indistinguishability measurements. However, as experiments get more complicated and include more optical elements, as well as the requirement for multi-photon interference; it will get increasingly difficult to interfere photons without directly addressing the effect of spectral wandering, if present. To get around this issue there has been a lot of experimental work aiming to reduce the random jitter of the emission energy, particularly on quantum dots [5]. Methods include, strong illumination which have been shown to increase crystal homogeneity [67] and electronic feedback loops

which has shown to increase emission frequency control [93].

CHAPTER 4

SINGLE MOLECULE QUANTUM EMITTER

In this chapter single molecules of Dibenzoterrylene (DBT), see fig. 4.1 are introduced and motivated as a suitable platform for single photon emitters with quantum information applications. Using the formalism of open quantum systems outlined in chapter 2, a theoretical model is developed which captures a single DBT coupled to a nano–crystal and photonic environment. From this model the temperature dependent optical dynamics for a DBT molecule are explored, including the emission spectra and second order correlation function measurements. Dephasing mechanisms from phonons which decohere the emission from DBT are are underpinned and characterised. This work directly reflects the publication given in reference [23]. The theoretical model developed in this work was completed in collaboration with Jake Iles–Smith. All the experimental aspects detailed in this chapter including measurements taken and crystal growth of the single photon emitter sample, were completed at Imperial College London lead by collaborator Alex S. Clark's group with Ross C. Schofield and Kyle D. Major.

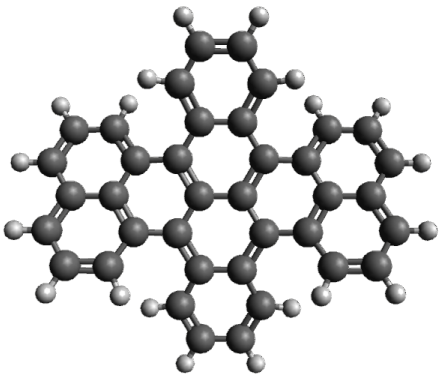

Figure 4.1: Ball and stick model of dibenzoterrylene, $C_{38}H_{20}$. Length and width of molecule are ~ 11.1 Å and ~ 9.7 Å, respectively. Carbon atoms are in dark grey and hydrogen is light grey.

4.1 Dibenzoterrylene

Deterministic sources of single photons are a key requirement for many quantum information applications [32, 60]. Single molecules of Dibenzoterrylene (DBT) are considered a promising platform for such a source due to a range of desirable characteristics, see Fig 4.1 [80]. The characteristic of consistent fluorescence wavelengths between $782 - 784\,\text{nm}$, which doesn't exhibit blinking or spectral wandering, leads to tunability across the whole inhomogeneous distribution [102]. This tunability is a direct advantage over other solid state sources such as quantum dots (QD) and nitrogen vacancy (NV) centres in diamond, for which is it difficult to identify two emitters with very similar emission characteristics [32, 111]. An additional characteristic of DBT is long term photo–stability, which is the ability to withstand photo bleaching. A DBT molecule can host up to 10^{12} excitations at room temperature before molecular bond degradation [70] and at cryogenic temperature can last indefinitely. To explore the other desirable characteristics of DBT which make it a promising a single photon source the electronic structure is next considered.

4.1.1 Electronic structure

A schematic energy diagram of a single DBT is given in figure 4.2a, where the purely electronic transition from the first excited state to the ground state is termed the zero phonon line (ZPL). At cryogenic temperatures ($\leq 3\,\text{K}$) DBT exhibits a very sharp bright [98] lifetime–limited zero phonon line [112] without the assistance from external control such as photonic cavities, electrical gating or plasmonic structures. It has been observed by J.-B. Trebbia et. al. at $2\,\text{K}$ the percentage of emission directly into the zero phonon line for a single molecule of DBT is

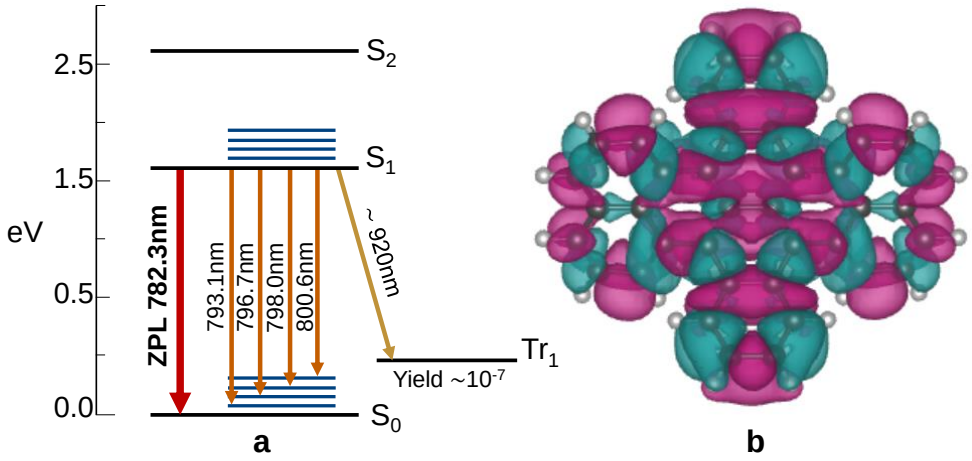

Figure 4.2: (a) Electronic structure of a DBT molecule showing the ground (S_0), first (S_1), and second (S_2) singlet states and the triplet (Tr_1) state. (b) Difference density between the ground (HOMO) and first excited state (LUMO) generated from ORCA.

33% [112]. This is a relatively high value when considering other sources such as NV centres which emit $2-5\%$ into their ZPL [29]. The lifetime of the first excited state for DBT is $\sim 4\,\text{ns}$. The second electronic excited state is well separated from the first by $\sim 1\,\text{eV}$. Moreover, the triplet state has a very low yield 10^{-7} with a relatively long lifetime of $\sim 70\,\mu\text{s}$ [72]. This large separation in electronic energy levels and high yield of the ZPL emission allow for the electronic states involved in single photon emission from a DBT molecule to be well described using a two–level system. As well as electronic levels, DBT hosts local vibrational modes which are associated with quantised movements of the molecule structure. Four of these local vibrational modes with the highest branching ratio are shown in blue on figure 4.2a [105].

To visualise the electronic orbitals the difference density between the ground S_0 and the first excited S_1 state has been calculated using the density functional theory computational package ORCA and is shown in figure 4.2b [84]. For these calculations time dependent density functional theory (TD-DFT) has been used which allows for the excited state calculation. The basis state used is the hybrid functional $B3LYP/G$, which is suitable for hydrocarbon molecules of this size.

4.1.2 DBT-Ac nano–crystal

The most promising environment to host DBT molecules are thin nano–crystals of anthracene (Ac) see fig. 4.3a [73, 85, 92]. In this nano–crystal structure DBT replaces three Ac molecules and causes little distortion to the structure [85]. Moreover, the molecules in the nano–crystal are bonded via van der Waal interactions which aids in the suppression of phonon dephasing due to the weak nature of the bonds [45]. See figure 4.3b for a photoluminescence spectra or emission spectra from a DBT molecule in Ac nano–crystal at 4.7K. The intensity of emission into the ZPL can be clearly seen when considering the linear scale in the inset of this figure and typically holds $30\% - 50\%$ of the total emission at cryogenic temperatures [117]. As well as a strong ZPL the emission spectra holds a rich structure of various features. The four sharp peaks

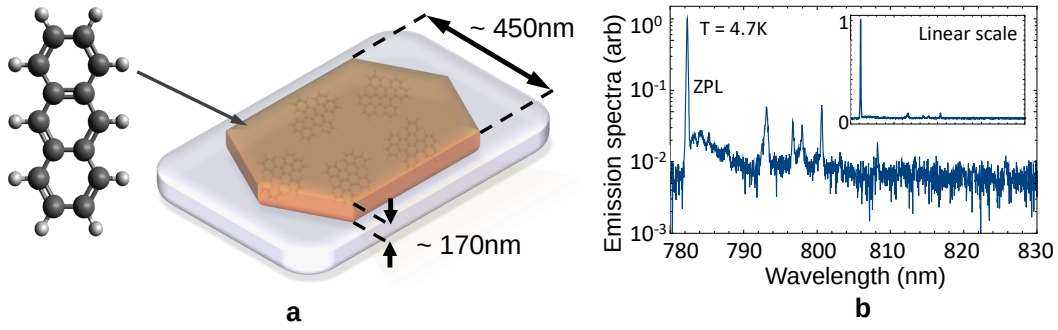

Figure 4.3: (a) Anthracene nano–crystal hosting DBT molecules, bonded via van der Waals. (b) Emission spectra collected from driving a DBT molecule embedded in an anthracene nano–crystal with a laser at 764.8 nm.

between $790 - 805$ nm are associated to the photon emission accompanied by one excitation of a localised vibrational mode of the molecule, where these modes are shown in figure 4.2a. Moreover, all distinct sharp peaks are overlaid with a broad sideband which is most prominent over the ZPL. This broad sideband originates from the simultaneous emission of a photon and a phonon into the Ac crystal.

The DBT doped nano–crystal of anthracene used to find all measurements presented in this chapter was grown using a re–precipitation technique at Imperial College London [90]. This involved mixing two solutions of 5 µL of 1 μMol DBT in toluene and 10 mL of 5 mMol zone-refined anthracene (Tokyo Chemical Industry UK) in acetone solution together. Sonication of 250 µL of this solution with 5 mL of distilled water at 37 kHz for 30 minuets was then followed by filtering through a syringe filter with 450 nm pore size. A 25 µL drop of this filtered solution was then pipetted onto a substrate of silica-on-silicon with a 150 nm gold coating (to improve collection of emission) and a 220 nm TiO_2 spacer layer (to protect against plasmonic losses), then left to dry via evaporation. Finally, the nano–crystal is spin–coated with a 150 nm poly–vinyl alcohol polymer layer for increased protection and cooled down in a closed cycle cryostat (Montana Cryostation) to a base temperature of 4.7 K.

4.2 Theoretical model

With all solid state emitters it is essential that temperature dependence and influence of phonon coupling and associated decoherence effects are well characterised and understood. The dominant dephasing mechanism for quantum dots is the coupling of excitons to a longitudinal acoustic phonon bath from the solid state environment. This coupling to phonons leads to an incoherent broad sideband which overlaps with the ZPL in the emission spectrum; as well as a homogeneous broadening to the ZPL at temperatures above $\sim$ 10 K [14, 42, 55, 56, 81, 96]. The aim for this chapter is to develop a theoretical model which fully captures all observed features from a single molecule single photon emitter, which allows for the uncovering of the underlying phonon coupling mechanisms. This theoretical work is aided with an experimental interrogation of the optical properties of a DBT–Ac nano–crystal at a range of cryogenic temperatures between 4.7 K and 40 K.

Inspired by the emission spectra in figure 4.3b the open quantum system model of a DBT–Ac nano–crystal is shown in Fig. 4.4. The model consists of an electronic two–level system (TLS) with ground and excited state $|g\rangle$ and $|e\rangle$ separated by energy E_X and coupled to N discrete localised vibrational modes (LVMs) both associated to the DBT molecule. Both the TLS and LVMs are treated within the system degrees of freedom leading to the explicit inclusion of all orders of interactions and interactions between them. Both the TLS and LVMs are coupled to a thermal phonon bath from the Ac nano–crystal. The TLS is separately coupled to an electromagnetic (EM) field which gives rise to spontaneous photon emission. The complete

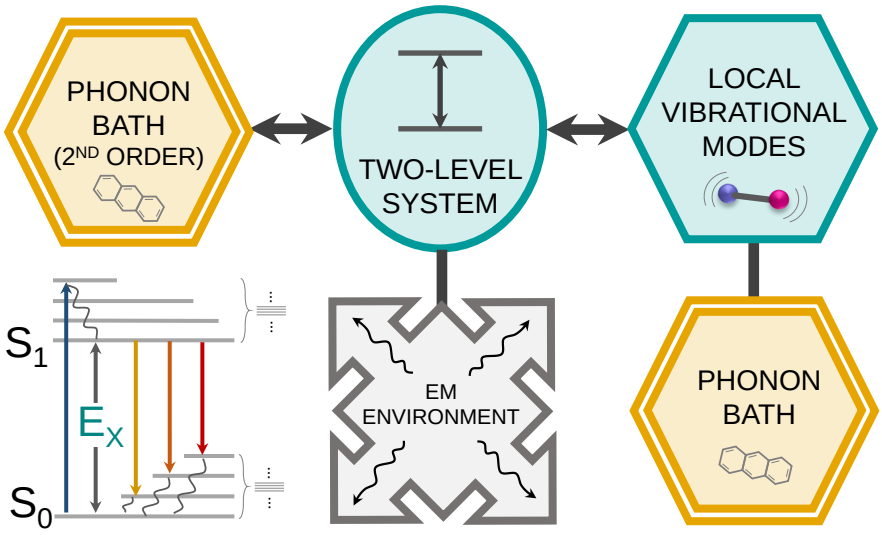

Figure 4.4: Open quantum system model of a single DBT molecule doped in an anthracene (Ac) nano–crystal environment. The system (blue) consists of a two–level electronic system (TLS) coupled to a discrete set of local vibrational modes (LVM) both associated with the DBT molecule. The TLS is coupled to a electromagnetic (EM) environment. A thermal phonon bath is coupled separately to the TLS and LVMs and originates from the nano–crystal environment. The double sided arrows represent the inclusion of non–Markovian feedback. The schematic energy level diagram (bottom left) shows the ground S_0 and first excited S_1 electronic singlet states split by the energy E_X, local vibrational modes and the thermal phonon environment.

Hamiltonian of the open quantum system is

$$H = H_{\mathrm{S}} + H_{\mathrm{E}} + H_{\mathrm{I}}^{\mathrm{EM-TLS}} + H_{\mathrm{I}}^{\mathrm{PH-TLS}} + H_{\mathrm{I}}^{\mathrm{PH-LV}}, \tag{4.1}$$

where the system Hamiltonian is $H_{\mathrm{S}} = E_X \sigma^\dagger \sigma + \hbar \sum_{i=1}^{N} [\Delta_i \alpha_i^\dagger \alpha_i + \eta_i \sigma^\dagger \sigma (\alpha_i^\dagger + \alpha_i)]$, with dipole operator $\sigma = |g\rangle\langle e|$. The N LVMs are modelled as harmonic oscillators with annihilation (creation) operators α_i ($\alpha_i^\dagger$) and separated in energy by Δ_i. The LVMs are coupled to the TLS with strengths η_i to first order with respect to lattice distortions. The term $H_{\mathrm{E}} = \hbar \sum_l \nu_l c_l^\dagger c_l + \hbar \sum_{\mathbf{k}} \omega_{\mathbf{k}} b_{\mathbf{k}}^\dagger b_{\mathbf{k}} + \hbar \sum_{\mathbf{q}} z_{\mathbf{q}} d_{\mathbf{q}}^\dagger d_{\mathbf{q}}$ describes the environment. It contains contributions from harmonic baths capturing the EM field with frequencies ν_l and annihilation (creation) operators c_l ($c_l^\dagger$) for mode l, and two thermal phonon baths which couple to the TLS and LVMs separately with frequencies $\omega_{\mathbf{k}}$ and $z_{\mathbf{q}}$ and annihilation operators $b_{\mathbf{k}}$ and $d_{\mathbf{q}}$ for wavevectors $\mathbf{k}$ and $\mathbf{q}$, respectively. The interaction Hamiltonian is split into three contributions, the EM environment–TLS term, derived in section (3.1) and given by $H_{\mathrm{I}}^{\mathrm{EM-TLS}} = \hbar \sum_l p_l (\sigma c_l^\dagger + \sigma^\dagger c_l)$, where this term is necessary to capture spontaneous photon emission and p_l is the coupling constant. The term $H_{\mathrm{I}}^{\mathrm{PH-TLS}} = H_{\mathrm{L}}^{\mathrm{PH}} + H_{\mathrm{Q}}^{\mathrm{PH}}$ couples the TLS to the thermal phonon bath, where this includes both linear

$$H_{\mathrm{L}}^{\mathrm{PH}} = \hbar \sigma^\dagger \sigma \sum_{\mathbf{k}} g_{\mathbf{k}} (b_{\mathbf{k}}^\dagger + b_{\mathbf{k}}), \tag{4.2}$$

and quadratic

$$H_{\mathrm{Q}}^{\mathrm{PH}} = \hbar\sigma^{\dagger}\sigma \sum_{\mathbf{k}\mathbf{k}'} f_{\mathbf{k}\mathbf{k}'}(b_{\mathbf{k}}^{\dagger} + b_{\mathbf{k}})(b_{\mathbf{k}'}^{\dagger} + b_{\mathbf{k}'}), \tag{4.3}$$

contributions, in respect to atomic displacements, where $g_{\mathbf{k}}$ ($f_{\mathbf{k}\mathbf{k}'}$) are the linear (quadratic) coupling constants, respectively [40, 120]. The derivation of these terms is found in section (2.2.3). The linear electron–phonon interaction describes a displacement of the phonon potential well minima. The quadratic term is a consequence of anharmonicity of the thermal phonon modes, resulting in a change of phonon force constants (diagonal) and Raman scattering processes (off–diagonal) [24]. It will be seen, that the quadratic interaction is crucial for capturing the temperature dependent homogeneous broadening of the zero phonon line [81]. The final interaction term couples the localised vibrational modes to the thermal phonon bath and is given by

$$H_{\mathrm{I}}^{\mathrm{PH-LV}} = \hbar \sum_{i,\mathbf{q}}^{N} h_{i,\mathbf{q}}(\alpha_i d_{\mathbf{q}}^{\dagger} + \alpha_i^{\dagger} d_{\mathbf{q}}), \tag{4.4}$$

where $h_{i,\mathbf{q}}$ is the real valued linear coupling strength and the derivation to this term is analogous to that of $H_{\mathrm{I}}^{\mathrm{EM-TLS}}$.

4.2.1 Polaron transformation

To model the optical dynamics of the single molecule emitter a master equation is developed using an extension to the polaron transformation approach detailed in section (3.2.1) [55, 78, 83, 101]. In this approach the Hamiltonian is subjected to two transformations which displace both the thermal phonon bath and the localised vibrational modes. The motivation for using these polaron transformations are to explicitly account for the phonon sideband present in the emission spectrum and to simplify the mathematics when dealing with the master equation, respectively.

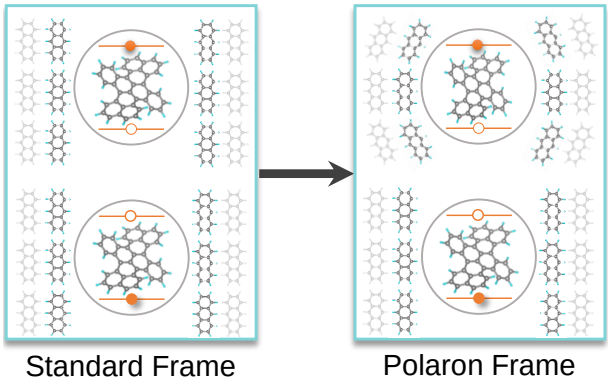

Figure 4.5: Visual representation (not to scale) of the polaron frame transformation between the two level system and the nano–crystal environment. The ground and excited state basis in the original frame is shown on the left. The right image shows the polaron frame basis; where the distortion in the crystal lattice in the excited state is accounted for.

4.2.1.1 Phonon bath polaron transform

The first of these transformations is mapped by $H_{\mathrm{P1}} = U_{\mathrm{P1}} H U_{\mathrm{P1}}^{\dagger}$ where $U_{\mathrm{P1}} = |g\rangle\langle g| + |e\rangle\langle e| B_{+}$ with the thermal phonon bath displacement operator $B_{\pm} = \exp[\pm \sum_{\mathbf{k}} \frac{g_{\mathbf{k}}}{\omega_{\mathbf{k}}}(b_{\mathbf{k}}^{\dagger} - b_{\mathbf{k}})]$. Performing this polaron transformation to the Hamiltonian terms dependent on $b_{\mathbf{k}}/b_{\mathbf{k}}^{\dagger}$ whilst using the relation in Eq. (2.43), gives

$$H_{\mathrm{L,P1}}^{\mathrm{PH}} = \hbar\sigma^{\dagger}\sigma\Big(\sum_{\mathbf{k}} g_{\mathbf{k}}(b_{\mathbf{k}}^{\dagger} + b_{\mathbf{k}}) - 2\sum_{\mathbf{k}} \frac{g_{\mathbf{k}}^{2}}{\omega_{\mathbf{k}}}\Big), \tag{4.5}$$

and

$$H_{\mathrm{Q,P1}}^{\mathrm{PH}} = \hbar\sigma^{\dagger}\sigma \sum_{\mathbf{k}\mathbf{k}'} f_{\mathbf{k}\mathbf{k}'}(b_{\mathbf{k}}^{\dagger} + b_{\mathbf{k}})(b_{\mathbf{k}'}^{\dagger} + b_{\mathbf{k}'}) \tag{4.6}$$

where residual linear terms $\propto \sum_{\mathbf{k}'} f_{\mathbf{k}\mathbf{k}'} \frac{g_{\mathbf{k}'}}{\omega_{\mathbf{k}'}}$ are not included as they sum to zero due to spherical symmetry [96]. The transformation to the environment term gives $H_{\mathrm{E,P_1}} = H_{\mathrm{E}} - \hbar\sigma^{\dagger}\sigma(\sum_{\mathbf{k}} g_{\mathbf{k}}(b_{\mathbf{k}}^{\dagger} + b_{\mathbf{k}}) + \sum_{\mathbf{k}} \frac{g_{\mathbf{k}}^{2}}{\omega_{\mathbf{k}}})$. Putting together $H_{\mathrm{L,P1}}^{\mathrm{PH}}$, $H_{\mathrm{Q,P1}}^{\mathrm{PH}}$ and $H_{\mathrm{E,P1}}$ results in the removal of the linear electron–phonon interaction $H_{\mathrm{L}}^{\mathrm{PH}}$ leaving the quadratic term $H_{\mathrm{Q}}^{\mathrm{PH}}$ and H_{E} unchanged, where the TLS energy is shifted such that $E_{\mathrm{X}} \rightarrow E_{\mathrm{X}} - \hbar\sum_{\mathbf{k}} \frac{g_{\mathbf{k}}^{2}}{\omega_{\mathbf{k}}}$. The final affected Hamiltonian component modified by this thermal phonon bath polaron transformation is $H_{\mathrm{I,P1}}^{\mathrm{EM-TLS}} = \hbar\sum_{l} p_{l}(\sigma B_{-} c_{l}^{\dagger} + \sigma^{\dagger} B_{+} c_{l})$, where the dipole operators are dressed in the phonon bath degrees of freedom. The consequence of this polaron transformation includes the distortion of the Ac lattice in response to the electronic excitation changing the basis, see Fig. 4.5. Moreover, when moving back into the original frame as the system is dressed with the phonon bath degrees of freedom non–Markovianity between the system and bath is accounted for in the model.

4.2.1.2 Local vibrational mode polaron transform

The second polaron transformation acts on the TLS and LVMs, and is defined through $H_{\mathrm{P}} = U_{\mathrm{P2}} H_{\mathrm{P1}} U_{\mathrm{P2}}^{\dagger}$ where $U_{\mathrm{P2}} = |g\rangle\langle g| + |e\rangle\langle e| \prod_{i} \mathcal{A}_{i}$ with $\mathcal{A}_{i} = \exp[\frac{\eta_{i}}{\Delta_{i}}(\alpha_{i}^{\dagger} - \alpha_{i})]$. The resultant transformed Hamiltonian is given by

$$H_{\mathrm{P}} = H_{0} + H_{\mathrm{I}}, \tag{4.7}$$

where $H_{0} = H_{\mathrm{S,P}} + H_{\mathrm{E}}$ and $H_{\mathrm{I}} = H_{\mathrm{I,P}}^{\mathrm{EM-TLS}} + H_{\mathrm{Q}}^{\mathrm{PH}} + H_{\mathrm{I,P}}^{\mathrm{PH-LV}}$, with the system term $H_{\mathrm{S,P}} = E_{\mathrm{P}}\sigma^{\dagger}\sigma + \hbar\sum_{i} \Delta_{i}\alpha_{i}^{\dagger}\alpha_{i}$, where $E_{\mathrm{P}} = E_{\mathrm{X}} - \hbar(\sum_{i} \eta_{i}^{2}/\Delta_{i} + \sum_{\mathbf{k}} g_{\mathbf{k}}^{2}/\omega_{\mathbf{k}})$ is the polaron shifted TLS energy splitting and the TLS-LVM interaction is rotated out. The elimination of the free system interaction term is useful as it removes issues of conflicting time scales (picoseconds for the local phonon mode and nano seconds for electronic decay) when solving integrals in the master equation derivation. The final polaron transformed interaction terms are

$$H_{\mathrm{I,P}}^{\mathrm{EM-TLS}} = \hbar\sum_{l} p_{l}\sigma_{\alpha} B_{-} c_{l}^{\dagger} + \mathrm{h.c.}, \tag{4.8}$$

where $\sigma_\alpha = \sigma \prod_i \mathcal{A}_i$ is the dressed dipole operator and

$$H_{\mathrm{I,P}}^{\mathrm{PH-LV}} = \hbar \sum_{i,\mathbf{q}} (\alpha_i^\dagger - \frac{\eta_i}{\Delta_i}\sigma^\dagger\sigma) h_{i\mathbf{q}} d_{\mathbf{q}} + \mathrm{h.c.}. \tag{4.9}$$

4.2.2 Molecule master equation

To model the dynamics of the system a Born-Markov master equation is derived in the polaron frame, where this begins in general form, derived in section (2.1.4), as

$$\partial_t \rho(t) = -\frac{i}{\hbar}[H_{\mathrm{S,P}}, \rho_{\mathrm{S}}(t)] - \Phi_{\mathrm{EM}}[\rho_{\mathrm{S}}(t)], \tag{4.10}$$

with the integral term

$$\Phi_{\mathrm{EM}}[\rho_{\mathrm{S}}(t)] = -\frac{1}{\hbar^2}\int_0^\infty d\tau \, \mathrm{Tr}_{\mathrm{E}} \Big([H_{\mathrm{I}}, [\tilde{H}_{\mathrm{I}}(-\tau), \rho_{\mathrm{S}}(t) \otimes \rho_{\mathrm{E}}]] \Big), \tag{4.11}$$

where $\rho(t)$ is the polaron frame reduced system density operator in the Schrödinger picture and $\tilde{H}_{\mathrm{I}}(-\tau) = \exp[-iH_0\tau/\hbar] H_{\mathrm{I}} \exp[iH_0\tau/\hbar]$ is the interaction picture interaction Hamiltonian. The Born approximation used here $\rho_{\mathrm{SE}} = \rho_{\mathrm{S}}(t) \otimes \rho_{\mathrm{E}}$ is justified as, the molecules in the DBT doped nano–crystal are bonded via van der Waals leading to a weak system–environment coupling. The polaron transformed Hamiltonian contains three interaction terms. The phonon and EM environment are assumed to hold no correlations between them and fluctuations experienced by the thermal phonon bath and each of the localised vibrational modes are uncorrelated. With these assumptions, terms with cross interactions vanish upon evaluation of the trace and therefore the three dissipators can be evaluated separately for each interaction Hamiltonian.

4.2.2.1 Spontaneous emission dissipator

To begin, the spontaneous emission dissipator is first evaluated, following steps similar to what was done in section (3.1) with the alteration of now working in the polaron frame. It is first required to find the EM-TLS interaction picture Hamiltonian from Eq. (3.5), which gives

$$\tilde{H}_{\mathrm{I,P}}^{\mathrm{EM-TLS}}(-\tau) = \hbar \sigma_\alpha(-\tau) B_-(-\tau) C^\dagger(-\tau) + \mathrm{h.c.}, \tag{4.12}$$

with $\sigma_\alpha(-\tau) = \sigma e^{-i\omega_{\mathrm{P}}\tau}\mathcal{A}(-\tau)$, where $\omega_{\mathrm{P}} = E_{\mathrm{P}}/\hbar$ is the polaron shifted TLS frequency and $\mathcal{A}(-\tau) = \exp\Big[-\sum_i \frac{\eta_i}{\Delta_i}(\alpha^\dagger e^{-i\Delta_i\tau} - \alpha e^{i\Delta_i\tau})\Big]$ is the time evolved dressed system operator. $B_\pm(-\tau) = \exp\Big[\pm\sum_k \frac{g_{\mathbf{k}}}{\omega_{\mathbf{k}}}(b_{\mathbf{k}}^\dagger e^{-i\omega_{\mathbf{k}}\tau} - b_{\mathbf{k}} e^{i\omega_{\mathbf{k}}\tau})\Big]$ and $C(-\tau) = \sum_l p_l c_l e^{i\nu_l\tau}$. Inserting the expressions for $H_{\mathrm{I,P}}^{EM-TLS}$ in Eq. (4.8) and $\tilde{H}_{I,P}^{EM}(-\tau)$ in Eq. (4.12) into the integral in Eq. (4.11) gives

$$\Phi_{\mathrm{EM}}[\rho_{\mathrm{S}}(t)] = -\frac{1}{\hbar^2}\int_0^\infty d\tau \mathrm{Tr}_E\big([H_{\mathrm{I,P}}^{EM-TLS}, [\tilde{H}_{\mathrm{I,P}}^{EM-TLS}(-\tau), \rho_{\mathrm{S}}(t) \otimes \rho_E]]\big). \tag{4.13}$$

To simplify this integral the evaluation of the EM and thermal phonon baths are required. Firstly, these correlation functions can be factorised such that

$$\mathrm{Tr}_E(B_- C^\dagger B_+(-\tau)C(-\tau)\rho_E) = \mathrm{Tr}_E(B_- B_+(-\tau)\rho_E)\mathrm{Tr}_E(C^\dagger C(-\tau)\rho_E), \tag{4.14}$$

as $B_\pm$ and C commute. Evaluation of the EM 0 K environment correlation function can be found in Eq. (3.10) given here for clarity $\mathrm{Tr}_E(CC^\dagger(-\tau)\rho_E) = \int_0^\infty d\omega J_{EM}(\omega)e^{i\omega\tau}$. The derivation for thermal phonon bath correlation functions are found in section (2.2.2.2), which finds $\mathcal{G}(\tau) = \mathrm{Tr}_E(B_- B_+(-\tau)\rho_E) = \langle B\rangle \exp[\phi(\tau)]$ where $\phi(\tau) = \int_0^\infty \frac{J_{\mathrm{PH}}(\omega)}{\omega^2} d\nu\big(\cos(\omega\tau)\coth\left(\frac{\beta\omega}{2}\right) - i\sin(\omega\tau)\big)$ and $\langle B\rangle = \exp\left[-\frac{1}{2}\phi(0)\right]$. Here, the exciton–phonon spectral density is introduced $J_{\mathrm{PH}}(\omega) = \sum_{\mathbf{k}} g_{\mathbf{k}}^2\delta(\omega-\omega_{\mathbf{k}})$ [55, 100]. Substituting these correlation functions into Eq. (4.13) gives

$$\Phi_{\mathrm{EM}}[\rho_{\mathrm{S}}(t)] = -\int_0^t d\tau\mathcal{G}(\tau)\chi(\tau)\Big(\sigma_\alpha^\dagger\sigma_\alpha(\text{-}\tau)\rho_{\mathrm{S}}(t) - \sigma_\alpha(\text{-}\tau)\rho_{\mathrm{S}}(t)\sigma_\alpha^\dagger\Big) + \mathcal{G}(\text{-}\tau)\chi(\text{-}\tau)\Big(\rho_{\mathrm{S}}(t)\sigma_\alpha^\dagger(\text{-}\tau)\sigma_\alpha\text{-}\sigma_\alpha\rho_{\mathrm{S}}(t)\sigma_\alpha^\dagger(\text{-}\tau)\Big). \tag{4.15}$$

where the commutation relation

$$[A,[B,C]] = ABC - BCA + h.c., \tag{4.16}$$

has been used.

It is now necessary to form the environment response functions by considering the time dependent integral in Eq. (4.15). To do so a unitary decomposition of the system operators is required as $e^{\pm i\Delta\tau}$ cannot be factored out of $\sigma_\alpha(\text{-}\tau)$. First, rewriting $\sigma_\alpha(-\tau) = \sigma e^{-i\omega_{\mathrm{P}}\tau}\mathcal{A}(-\frac{\eta_i}{\Delta_i},-\tau)$ where, $\mathcal{A}(-\frac{\eta_i}{\Delta_i},-\tau) = \exp\Big[-\sum_i \frac{\eta_i}{\Delta_i}(\alpha^\dagger e^{-i\Delta_i\tau} - \alpha e^{i\Delta_i\tau})\Big]$ is the time evolved local vibrational mode displacement operator. Expressing this time evolved operator in terms of system unitary operator $U_S(-\tau) = e^{i\sum_i \Delta_i\alpha_i^\dagger\alpha_i\tau}$, we find $\mathcal{A}(-\frac{\eta_i}{\Delta_i},-\tau) = U_S(-\tau)\mathcal{A}(-\frac{\eta_i}{\Delta_i})U_S^\dagger(-\tau)$ which gives $\mathcal{A}(-\frac{\eta_i}{\Delta_i},-\tau) = \sum_{n,m}\langle n|\mathcal{A}(-\frac{\eta_i}{\Delta_i})|m\rangle|n\rangle\langle m|e^{-i\sum_i\Delta_i(m-n)\tau}$, where the resolution of identity, $\mathbb{1} = \sum_n |n\rangle\langle n|$ has been inserted twice and the relation $\alpha^\dagger\alpha|n\rangle = n|n\rangle$ has been used. The time evolved dressed system operator $\sigma_\alpha(-\tau)$ can therefore be expressed as

$$\sigma_\alpha(-\tau) = \sigma\sum_{n,m}\mathcal{A}_{n,m}\big(-\frac{\eta_i}{\Delta_i}\big)e^{-i(\omega_{\mathrm{P}}+\sum_i\Delta_i(m-n))\tau}, \tag{4.17}$$

where $\mathcal{A}_{n,m}(\pm\frac{\eta_i}{\Delta_i}) = \langle n|\mathcal{A}(\pm\frac{\eta_i}{\Delta_i})|m\rangle|n\rangle\langle m|$ are the matrix elements of the system displacement operator.

Due to differing time scales between the EM field correlation timescale of a few femtoseconds and phonon relaxation (picoseconds) (for a TLS energy splitting of $E_{\mathrm{P}} = \hbar\omega_{\mathrm{P}} \approx 1.6\,\mathrm{eV}$), the phonon correlation function barely changes and therefore can be replaced by $\mathcal{G}(\tau) \to \mathcal{G}(0) = 1$ [79]. Now defining and evaluating the environment response function as was done

in section (2.1.4), it has been found

$$\begin{aligned}\mathcal{K}(\epsilon_{n,m}) &= \int_0^\infty d\tau \mathcal{G}(0)\chi(\tau)e^{-i\epsilon_{n,m}\tau}, \\ &= \int_0^\infty d\omega \int_0^\infty d\tau J_{EM}(\omega)e^{i(\omega-\epsilon_{n,m})\tau}, \\ &= \int_0^\infty d\omega \pi J_{EM}(\omega)\delta(\omega-\epsilon_{n,m}) + i\mathcal{P}\int_0^\infty d\omega \frac{J_{EM}(\omega)}{\omega-\epsilon_{n,m}}, \\ &= \pi J_{EM}(\epsilon_{n,m}) + iS_{EM},\end{aligned} \tag{4.18}$$

where $\epsilon_{n,m} = \omega_{\rm P} + \sum_i \Delta_i(m-n)$. Approximating the photonic spectral density to be flat over the relevant frequency scales with respect to the molecule emitter, to write $J(\epsilon_{n,m}) \approx \Gamma_1/\pi$. Substituting in this response function into Eq. (4.15) the spontaneous emission master equation integral becomes

$$\Phi_{EM}[\rho_{\rm S}(t)] = (\Gamma_1 + iS_{EM})\mathcal{L}_{\sigma_\alpha}[\rho(t)], \tag{4.19}$$

where $\mathcal{L}_A[\rho(t)] = A\rho(t)A^\dagger - \frac{1}{2}\{A^\dagger A, \rho(t)\}$ is the Lindblad operator. The imaginary term in this expression contributes to the Lamb shift and re–normalises the system Hamiltonian term such that $H_{\rm S,P} \to H_{\rm S,P} + H_{\rm LS}$. Moving the Lamb shift component to the commutator in Eq. (4.10) allows one to define the EM–TLS master equation dissipator as

$$\mathcal{D}_{EM}[\rho_{\rm S}(t)] = \Gamma_1 \mathcal{L}_{\sigma_\alpha}[\rho(t)], \tag{4.20}$$

4.2.2.2 Pure dephasing dissipator

Next the quadratic electron–phonon interaction term is considered, which leads to the homogeneous broadening or pure dephasing dissipator. Finding the interaction picture interaction Hamiltonian as $\tilde{H}_{\rm Q}^{\rm PH}(-\tau) = U_0^\dagger(-\tau)H_{\rm Q}^{\rm PH}U_0(-\tau)$ gives

$$\tilde{H}_{\rm Q}^{\rm PH}(-\tau) = \hbar\sigma^\dagger\sigma\sum_{\mathbf{k}\mathbf{k}'} f_{\mathbf{k}\mathbf{k}'}B_{\mathbf{k}}(-\tau)B_{\mathbf{k}'}(-\tau), \tag{4.21}$$

where $B_{\mathbf{k}}(-\tau) = (b_{\mathbf{k}}^\dagger e^{-i\hbar\omega_{\mathbf{k}}\tau} + b_{\mathbf{k}}e^{i\hbar\omega_{\mathbf{k}}\tau})$. Inserting $H_{\rm Q}^{\rm PH}$ and $\tilde{H}_{\rm Q}^{\rm PH}(-\tau)$ into Eq. (4.10) the integral takes the form

$$\begin{aligned}\Phi\rho_{\rm S}(t)] = -\int_0^t d\tau {\rm Tr}_E\Big(&\sigma^\dagger\sigma\big[\sum_{\mathbf{k}\mathbf{k}'} f_{\mathbf{k}\mathbf{k}'}B_{\mathbf{k}}B_{\mathbf{k}'}\big]\big[\sum_{\mathbf{k}\mathbf{k}'} f_{\mathbf{k}\mathbf{k}'}B_{\mathbf{k}}(-\tau)B_{\mathbf{k}'}(-\tau)\big]\rho_{\rm S}(t)\rho_E \\ &- \sigma^\dagger\sigma\big[\sum_{\mathbf{k}\mathbf{k}'} f_{\mathbf{k}\mathbf{k}'}B_{\mathbf{k}}(-\tau)B_{\mathbf{k}'}(-\tau)\big]\rho_{\rm S}(t)\rho_E\sigma^\dagger\sigma\big[\sum_{\mathbf{k}\mathbf{k}'} f_{\mathbf{k}\mathbf{k}'}B_{\mathbf{k}}B_{\mathbf{k}'}\big] + h.c.\Big).\end{aligned} \tag{4.22}$$

Considering the trace over the environment degrees of freedom we find

$$\begin{aligned}\Big\langle \big[\sum_{\mathbf{k}\mathbf{k}'} f_{\mathbf{k}\mathbf{k}'}B_{\mathbf{k}}B_{\mathbf{k}'}\big]\big[\sum_{\mathbf{k}\mathbf{k}'} f_{\mathbf{k}\mathbf{k}'}B_{\mathbf{k}}(-\tau)B_{\mathbf{k}'}(-\tau)\big]\Big\rangle &= \sum_{\mathbf{k}\mathbf{k}'}\sum_{\mathbf{l}\mathbf{l}'} f_{\mathbf{k}\mathbf{k}'}f_{\mathbf{l}\mathbf{l}'}\left\langle B_{\mathbf{k}}B_{\mathbf{k}'}B_{\mathbf{l}}(-\tau)B_{\mathbf{l}'}(-\tau)\right\rangle, \\ &= \sum_{\mathbf{k}\mathbf{k}'} |f_{\mathbf{k}\mathbf{k}'}|^2 \left\langle B_{\mathbf{k}}B_{\mathbf{k}}(-\tau)\right\rangle\left\langle B_{\mathbf{k}'}B_{\mathbf{k}'}(-\tau)\right\rangle.\end{aligned} \tag{4.23}$$

The factorisation of the correlation function above has been made based on the assumption that phonons do not scatter into the same mode i.e. $\mathbf{k} \neq \mathbf{k}'$ [96]. Simplifying this expression and again moving the Lamb shift term from the imaginary component of the response functions into the commutator gives the pure dephasing dissipator as

$$\mathcal{D}_{\mathrm{PD}}[\rho_{\mathrm{S}}(t)] = 2\gamma(T)\mathcal{L}_{\sigma^\dagger\sigma}[\rho(t)], \tag{4.24}$$

where the pure dephasing rate is

$$\gamma(T) = \mathrm{Re}\Big[\int_0^t d\tau \sum_{\mathbf{k}\mathbf{k}'} |f_{\mathbf{k}\mathbf{k}'}|^2 \left\langle B_{\mathbf{k}} B_{\mathbf{k}}(-\tau)\right\rangle \left\langle B_{\mathbf{k}'} B_{\mathbf{k}'}(-\tau)\right\rangle \Big]. \tag{4.25}$$

To evaluate the pure dephasing rate first the bath correlation functions need to be evaluated using section (2.2.2), which give

$$\begin{aligned}\left\langle B_{\mathbf{k}} B_{\mathbf{k}}(-\tau)\right\rangle &= \underbrace{\left\langle b_{\mathbf{k}}^\dagger b_{\mathbf{k}}^\dagger e^{-i\mathbf{k}\tau}\right\rangle}_{=0} + \left\langle b_{\mathbf{k}}^\dagger b_{\mathbf{k}} e^{i\mathbf{k}\tau}\right\rangle + \left\langle b_{\mathbf{k}} b_{\mathbf{k}}^\dagger e^{-i\mathbf{k}\tau}\right\rangle + \underbrace{\left\langle b_{\mathbf{k}} b_{\mathbf{k}} e^{i\mathbf{k}\tau}\right\rangle}_{=0}, \\ &= n(\nu_k)e^{i\nu_k\tau} + (n(\nu_k)+1)e^{-i\nu_k\tau}.\end{aligned} \tag{4.26}$$

Next taking the sum into the continuum limit $\sum_{\mathbf{k}\mathbf{k}'} \to \frac{V^2}{(2\pi)^6}\int_0^\infty d^3k \int_0^\infty d^3k'$, gives

$$\begin{aligned}\gamma(T) = \frac{V^2}{(2\pi)^6}\int_0^\infty d^3k \int_0^\infty d^3k' |f_{\mathbf{k}\mathbf{k}'}|^2 \Big(& n(\omega_{\mathbf{k}})(n(\omega_{\mathbf{k}'})+1) \\ & \times \delta(\omega_{\mathbf{k}} - \omega'_{\mathbf{k}}) + (n(\omega_{\mathbf{k}})+1)n(\omega_{\mathbf{k}'})\delta(\omega_{\mathbf{k}'} - \omega_{\mathbf{k}})\Big).\end{aligned} \tag{4.27}$$

Where the definition of a delta function $\delta(x-a) = \frac{1}{\pi}\,\mathrm{Re}\left[\int_0^\infty d\tau e^{i(x-a)\tau}\right]$ has been used and linear dispersion $\omega_{\mathbf{k}} = c|\mathbf{k}|$ where $|\mathbf{k}| = k$ is assumed, and c is the speed of sound in the nano–crystal. The presence of the delta functions result in only needing to evaluate the coupling constant $|f_{\mathbf{k}\mathbf{k}'}|^2$ for $k = k'$. Substituting in an isotropic Gaussian wave function into Eq. (2.74) $\psi_\alpha(\mathbf{r}) = (d_\alpha\sqrt{\pi})^{-3/2}e^{-r^2/2d_\alpha^2}$ where d_α is the confinement potential for the ground and excited states which is assumed to be equal, such that $d_\alpha \to d$, we find

$$|f_{\mathbf{k}\mathbf{k}'}|^2 = \Big(\frac{k}{4NMc}\Big)^2 (1+\cos\theta)^4 \sum_\alpha D_\alpha^2 e^{-k^2(1+\cos\theta)d^2}, \tag{4.28}$$

where $\mathbf{k}\cdot\mathbf{k}' = kk'\cos\theta$. Substituting this quadratic coupling constant and converting variables from wavevector magnitude into frequency, as well as defining the phonon cut off frequency $\xi = \sqrt{2}c/d$, the pure dephasing rate is found to be

$$\gamma(T) = \mu\int_0^\infty d\omega\omega^6 n(\omega)(n(\omega)+1)\int_0^\pi d\theta \sin(\theta)(1+\cos(\theta))^4 e^{-2\omega^2(1+\cos(\theta))/\xi^2}, \tag{4.29}$$

where $\mu = V^2\sum_\alpha D_\alpha^2/(128\pi^3(NM)^2c^8)$.

4.2.2.3 Local vibrational mode dissipator

To evaluate the dissipator arising from coupling to the thermal phonon bath, the master equation is evaluated in the interaction picture found in Eq. (6.23), where the interaction picture density operator is $\tilde{\rho}_{\rm S}(t) = e^{iH_{\rm S,P}t/\hbar}\rho_{\rm S}(t)e^{-iH_{\rm S,P}t/\hbar}$. Working in the interaction picture allows the secular approximation to be made which simplifies the algebra. Transforming $H_{\rm I,P}^{\rm PH-LV}$ into the interaction picture requires $\tilde{H}_{\rm I,P}^{\rm PH-LV}(t) = U_0^\dagger(t)H_{\rm I,P}^{\rm PH-LV}U_0(t)$ where $U_0(t) = e^{-i(H_{\rm S,P}+H_{\rm E})t/\hbar}$, this leads to the interaction Hamiltonian

$$\tilde{H}_{\rm I,P}^{\rm PH-LV}(t) = \hbar\sum_i(\alpha_i e^{-i\Delta_i t} - \frac{\eta_i}{\Delta_i}\sigma^\dagger\sigma)\sum_{\mathbf{q}} h_{i\mathbf{q}}d_{\mathbf{q}}^\dagger e^{iz_q t} + \text{h.c.} \tag{4.30}$$

Now, by writing $\tilde{H}_{\rm I,P}^{\rm PH-LV}(t) = \hbar\sum_{\alpha=1,2}\tilde{A}_\alpha(t)\tilde{B}_\alpha(t)$ where $\tilde{B}_1(t) = \sum_{\mathbf{q}} h_{\mathbf{q}}d_{\mathbf{q}}e^{-iz_q t}$ and $\tilde{B}_2(t) = \tilde{B}_1^\dagger(t)$, the correlation functions are calculated according to Eq. (2.22), finding

$$C_{12}(\tau) = \int_0^\infty d\nu J_{\rm PH-LV}(\nu)n(\nu)e^{i\nu\tau}, \tag{4.31}$$

$$C_{21}(\tau) = \int_0^\infty d\nu J_{\rm PH-LV}(\nu)(n(\nu)+1)e^{-i\nu\tau}, \tag{4.32}$$

where the local vibrational mode–phonon bath spectral density $J_{\rm PH-LV}(\nu) = \sum_q |h_q|^2\delta(z_q - \nu)$ has been introduced and the Bose occupancy number is $n(\nu) = (e^{\hbar\nu/k_B T} - 1)^{-1}$. Inserting Eq. (4.30) and the phonon correlation functions into the interaction picture master equation (6.23) gives

$$\begin{aligned}\partial_t\tilde{\rho}_S(t) = -\sum_i\int_0^\infty d\tau\Big(&C_{12}(\tau)[\alpha_i,\alpha_i^\dagger\tilde{\rho}_S(t)]e^{-i\Delta_i\tau} + C_{21}(-\tau)[\alpha_i^\dagger,\alpha_i\tilde{\rho}_S(t)]e^{i\Delta_i\tau}\\ &+\Big(\frac{\eta_i}{\Delta_i}\Big)^2\big(C_{12}(\tau)+C_{21}(-\tau)\big)[\sigma^\dagger\sigma,\sigma^\dagger\sigma\tilde{\rho}_S(t)] + \text{h.c.}\Big),\end{aligned} \tag{4.33}$$

where the secular (rotating–wave) approximation has been made, which involves neglecting as all terms with the factor $e^{\pm i\Delta t}$ as they are fast oscillating with respect to the time scale of the TLS relaxation [15]. Performing the time integrals and re-normalising the system Hamiltonian with the Lamb shift contribution, the master equation rotating back into the Schrödinger picture is

$$\partial_t\rho_{\rm S}(t) = \mathcal{D}_{\rm EM}[\rho_{\rm S}(t)] + \mathcal{D}_{\rm PH}[\rho_{\rm S}(t)] + \sum_i\Big(-i\Delta_i[\alpha_i^\dagger\alpha_i,\rho(t)] + \Gamma_{i,+}\mathcal{L}_{\alpha^\dagger}[\rho(t)] + \Gamma_{i,-}\mathcal{L}_a[\rho(t)]\Big). \tag{4.34}$$

Where this equation has been moved in the rotating frame to remove $E_{\rm P}\sigma^\dagger\sigma + H_{LS}$ from the system Hamiltonian in the commutor via the unitary $U_R(t) = e^{i(E_{\rm P}\sigma^\dagger\sigma+H_{LS})t}$. The local vibrational mode absorption and decay rates $\Gamma_{i,\pm}$ depend on $\kappa_i = \pi J_{\rm PH-LV}(\Delta_i)$. The local vibrational mode–phonon bath spectral density is assumed to take a super-Ohmic form $J_{\rm PH-LV}(\Delta_i) \propto \Delta_i^3\xi^{-2}e^{-\Delta_i/\xi}$, to reflect the three-dimensional and weak nature of the coupling, where ζ is the phonon bath cut-off frequency [18, 43, 86].

4.2.3 DBT–Ac emission spectra

We find the one color emission spectra detailed in section (3.1) by, first following Refs. [55, 56], solving the Heisenberg equations of motion $\dot{c}_l(t) = -i[H_{\rm P}, c_l(t)]$, in the polaron frame, which gives

$$\dot{c}_l = -i\nu_l c_l(t) - ip_l c_l \sigma_\alpha(t) B_-(t). \tag{4.35}$$

Solving this equation of motion using the Fourier variable $\tilde{c}(\nu) = \int dt c_l(t) e^{i\nu t}$ gives

$$E(t) = E_0(t) + \sqrt{\Gamma_1/2\pi}\,\sigma_\alpha(t) B_-(t) \tag{4.36}$$

where $E_0(t)$ is the free field, assumed to be in the vacuum. Note that the second source term contains both TLS and thermal phonon bath degrees of freedom. Substituting in the electric field operators in to the first order correlation function one finds

$$\begin{aligned} g^{(1)}(\tau) &= \int_0^\infty dt \frac{\Gamma_1}{2\pi} \left\langle \sigma_\alpha^\dagger(t+\tau) B_+(t+\tau) \sigma_\alpha(t) B_-(t) \right\rangle, \\ &\approx \frac{\Gamma_1}{2\pi} g_0^{(1)}(\tau) \mathcal{G}(\tau), \end{aligned} \tag{4.37}$$

where the correlation functions are $\mathcal{G}(\tau) = \langle B \rangle^2 \exp[\phi(\tau)]$ as previously defined in Eq. (2.47), while $g_0^{(1)}(\tau) = \int_0^\infty dt \left\langle \sigma_\alpha^\dagger(t+\tau)\sigma_\alpha(t) \right\rangle$, where this first order correlation function explicitly captures the LVMs via the dressed dipole operators. The factorisation of the correlation functions is taken using the Born approximation, where it is assumed that the coupling between the system and the phonon bath is weak. Substituting the first order correlation function into Eq. (3.17), the emission spectrum can be expressed as $S(\omega) \propto S_{\rm ZPL+LVM}(\omega) + S_{\rm SB}(\omega)$, where

$$S_{\rm ZPL+LVM}(\omega) = \frac{\Gamma_1}{\pi} \langle B \rangle^2 \,{\rm Re}\Big[\int_0^\infty d\tau g_0^{(1)}(\tau) e^{-i\omega\tau} \Big], \tag{4.38}$$

describes distinct absorption and emission peaks associated with the ZPL and localised vibrational modes, and

$$S_{\rm SB}(\omega) = \frac{\Gamma_1}{\pi} {\rm Re}\Big[\int_0^\infty d\tau g_0^{(1)}(\tau) (\mathcal{G}(\tau) - \langle B \rangle^2) e^{-i\omega\tau} \Big]. \tag{4.39}$$

describes a broad phonon sideband which overlaps each spectral peak. A key advantage of working in the polaron frame is that the correlation function $g_0^{(1)}(\tau)$ can be found using the (Markovian) quantum regression theorem shown in section (3.1.2.1) [48, 77], while non–Markovian interactions necessary to capture phonon sidebands are naturally captured by the phonon bath correlation function $\mathcal{G}(\tau)$ in Eq. (4.39). Furthermore, by writing the spectrum in this way it is immediately obvious that the Debye–Waller factor (fraction of light not emitted into sidebands) is given by $\int S_{\rm ZPL+LV}(\omega) d\omega / \int S(\omega) d\omega = \langle B \rangle^2$.

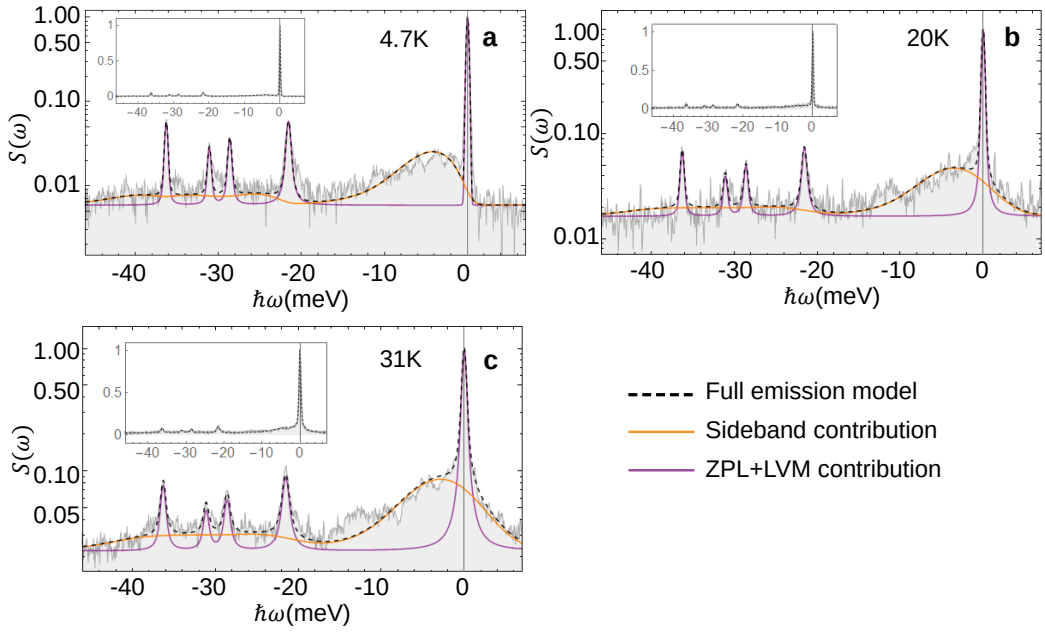

Figure 4.6: Single molecule of DBT emission spectra taken at 4.7 K (a), 20 K (b) and 31 K (c). Black-dashed lines show the full theoretical model and grey-solid lines show experimental data. The theoretical spectrum showing only the system features, zero phonon line (ZPL) and local vibrational modes is shown in purple, while the broad continuous phonon sideband contribution is shown in orange. The insets show the spectra on a linear scale to emphasize ZPL strength.

4.3 Emission spectra results and discussion

Predictions of the OQS model for three different temperatures between 4.7 K $-$ 31 K are shown by the dashed black lines in figure 4.6. The most prominent peak at zero detuning (or 782.32 nm) corresponds to the ZPL. While the other sharp peaks between -40 meV to -15 meV arise from excitation of local vibrational modes during the photon emission process [24, 45]. It has been found that to reproduce these emission features $N = 4$ separate DBT vibrational modes are required. The fitted vibrational mode energies $\hbar\Delta_i$ are consistent (to within 2%) with previous literature [27], and are listed in the Appendix (A.2), together with the fitted LVM coupling constants η_i. To achieve good spectral fits it is sufficient to account for only the ground and first excited state for each mode in our calculations, indicating that higher vibronic transitions contribute little to the observed spectra due to low transition probabilities.

The solid-purple lines in Fig. 4.6 show the calculated emission spectra including only the system features (ZPL and LVM peaks) using Eq. (4.38), while the solid-orange lines show the continuous phonon sideband contribution given in Eq. (4.39). The functional shape of the sideband depends on the form of the spectral density $J_{\mathrm{PH}}(\omega)$, as this characterises the frequency spectrum of the electron–phonon coupling. To model the molecule emission a super

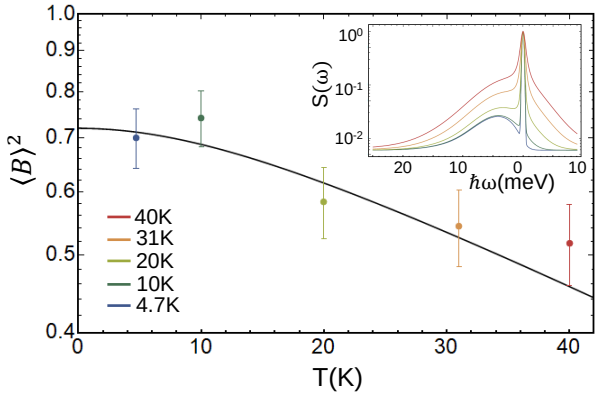

Figure 4.7: Debye–Waller factor given by $\langle B \rangle^2$, for varying temperature. The solid line shows the theoretical model. Points on the graph are extracted from experimental data using phenomenological fitting techniques. The inset shows the calculated spectrum of the ZPL and sideband at temperatures where the data was taken.

Ohmic form is chosen, such that

$$J_{\mathrm{PH}}(\omega) = \alpha\, \omega^3 \exp\left[-\omega^2/\xi^2\right], \tag{4.40}$$

where α captures the overall TLS–thermal phonon bath coupling strength, and $\xi = \sqrt{2}v/d$ is a high-frequency cut-off to reflect the suppression of coupling to phonons whose wavelengths are much smaller than the size of the DBT molecule d, where v is the speed of sound in anthracene. This spectral function is three-dimensional to reflect the bulk phonon density of states [18, 83]. These parameters are extracted from fitting the model to the experimental data and are shown in the appendix A.2. Due to the energy scale of the phonons involved the broad sideband they are assumed to be longitudinal acoustic phonons. This form for the spectral density is similar to that used to capture phonon sidebands and excitation-induced dephasing in semiconductor QDs [14, 55, 56, 78, 83, 96]. The derivation for the exciton–phonon spectral density is performed by approximating Gaussian wavefunctions for the electronic ground and excited states, further details of this derivation along with exploring other wavefunctions are given in the appendix (A.1).

The fraction of emission which goes into the ZPL and LVM peaks compared to the full emission is given by the Debye–Waller factor, from which as shown in section (2.2.2.2), can be readily found from $\langle B \rangle^2 = \exp[-\int_0^\infty J_{\mathrm{PH}}(\omega)\omega^{-2}\coth(\beta\omega/2)d\omega]$, which is the square of the phonon bath displacement operator expectation value. This function is plotted along side experimentally extracted values in Fig. 4.7. A motivation for a theoretical method to predict the Debye–Waller factor, is the high uncertainty involved in finding an extracted value from data. To extract these data points one can either look at the ratio between the ZPL and its sideband or fit all spectral lines (ZPL and LVMs) and compare this to the total emission spectra. The uncertainty in these extraction approaches are due several factors such as, high bandpass filtering upon collection dis-entangling overlapping spectral features and interference from

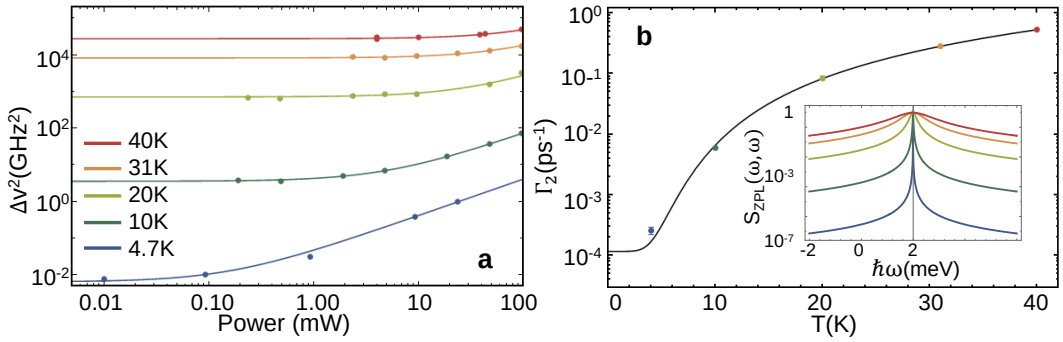

Figure 4.8: (a) Squared-linewidths extracted from fluorescence excitation spectra for varying power at different temperatures. Lines are fits to $\Delta\nu^2 = (\Gamma_2/\pi)^2(1+S)$. (b) Experimental values of Γ_2 found from the extrapolation in (a), plotted together with prediction from the theoretical model (solid line). The inset shows the calculated Lorentzian ZPL for temperatures at which the data was taken.

noise. To find the points shown in figure 4.7 both approaches were used and averaged to improve reliability. For this molecule the maximum ZPL fraction is found to be 72% (not considering LVMs). This value is lower than expected for DBT and therefore could in part account for the reduction from predictions in coupling observed for single molecules in open-access micro-cavities [116, 117]. Alternatively this slightly reduced fraction could be due to the close proximity of the nano–crystal surfaces used in the presented experiments [41], future work using co-sublimation grown crystals [73] may yield a different result.

Broadening of the spectral emission lines shown in Fig. 4.6 is captured by the dissipators in the master equation (4.34). Of particular interest is the temperature dependent homogeneous broadening associated with the ZPL. In the theoretical model developed this ZPL broadening follows

$$\Gamma_2(T) = \Gamma_1/2 + \gamma(T), \tag{4.41}$$

where $\gamma(T)$, is a phonon-induced pure dephasing rate. To compare this theoretical model against experiment, power–dependent line scans of fluorescence excitation spectra (FES) across the ZPL with power measured outside the cryostat before the objective lens are taken, which remove the influence of the resolution of the spectrometer. The width of the FES measured zero phonon lines can be expressed as

$$\Delta\nu = \frac{\Gamma_2(T)}{\pi}\sqrt{1+S}, \tag{4.42}$$

with saturation parameter S, where the temperature dependant results are shown in Fig. 4.8a. Finding this linewidth $\Delta\nu$ allow for $\Gamma_2(T)$ to be found by extrapolating the fits to zero power such that $\Delta\nu(S \to 0) = \Gamma_2(T)/\pi$ [45]. The extracted $\Gamma_2(T)$ values are shown in Fig. 4.8b, together with the theoretical model. The DBT molecule examined in this work was slightly broadened at the base temperature of 4.7 K predicting $\gamma(4.7) = 0.14\,\mathrm{ns}^{-1}$. This model predicts cooling below 3 K for this molecule would be sufficient to reach a lifetime–limited linewidth

$\Gamma_2(T) = \Gamma_1/2$. This homogeneous broadening originates from mixing between vibronic states induced by anharmonic effects, where the participation of two phonons from the residual bath is required. To capture this anharmonicity the inclusion of quadratic terms in the Hamiltonian need to be captured. Furthermore, this multi–phonon absorption process results in the strong temperature dependence of the ZPL broadening which matches measurement well.

4.4 Driving the molecule

To further demonstrate the adaptability of the theoretical model, time-domain dynamics of the DBT molecule are now investigated by considering the second-order intensity correlation function under continuously driven resonant excitation conditions [121].

4.4.1 Theoretical driving model

To account for continuous driving of the molecule the model must be revisited and an additional driving term is introduced into the system Hamiltonian defined in Eq. (4.1) such that,

$$H_{\mathrm{S,D}} = H_{\mathrm{S}} + \Omega\cos(\omega_d t)(\sigma + \sigma^\dagger), \tag{4.43}$$

with Rabi frequency Ω and driving laser frequency ω_{d}. Moving into a rotating frame with respect to the laser frequency such that $H' = U(t)HU^\dagger(t) - iU(t)\partial_t U^\dagger(t)$ with $U(t) = e^{i\hbar\omega_d\sigma^\dagger\sigma t}$. Applying this to the full pre-polaron transform driven Hamiltonian given in Eq. (4.1), modifies the system term to $H_{\mathrm{S,D}} = H_{\mathrm{S}} - \hbar\omega_{\mathrm{d}}\sigma^\dagger\sigma + \frac{\hbar\Omega}{2}(\sigma + \sigma^\dagger)$ and the EM-TLS interaction term to

$$H_{\mathrm{I,D}}^{\mathrm{EM-TLS}} = \hbar\sum_l p_l(e^{-i\hbar\omega_{\mathrm{d}}t}\sigma c_l^\dagger + e^{+i\hbar\omega_{\mathrm{d}}t}\sigma^\dagger c_l). \tag{4.44}$$

Where this transformation has been found using the relation $U(t) = e^{i\hbar\omega_d|e\rangle\langle e|t} = \mathbb{1} + i\hbar\omega_d t\,|e\rangle\langle e| + \ldots = |g\rangle\langle g| + |e\rangle\langle e|\,e^{i\hbar\omega_d t}$.

Performing now the two polaron transformations on this driven Hamiltonian as described in section (4.2.1) and considering only terms that differ from the non-driven case. Firstly, the driving term in the free–system Hamiltonian transforms to $\frac{\Omega}{2}(\sigma_\alpha B_- + \sigma_\alpha^\dagger B_+)$, which now reflects a system-environment interaction as it has a non-zero expectation value with respect to the thermal state ρ_E such that, $\mathrm{Tr}_E[\sigma_\alpha B_- + \sigma_\alpha^\dagger B_+] = \langle B\rangle\,(\sigma_\alpha + \sigma_\alpha^\dagger)$ [83]. Rearranging this term into separate system and interaction contributions using the following system operators $\underline{X} = (\sigma_\alpha + \sigma_\alpha^\dagger)$, $\underline{Y} = i(\sigma_\alpha - \sigma_\alpha^\dagger)$ and bath operators $B_x = \frac{1}{2}(B_+ + B_- - 2\langle B\rangle)$ and $B_y = \frac{i}{2}(B_+ - B_-)$, gives the polaron frame driven free system Hamiltonian

$$H_{\mathrm{S,D,P}} = \hbar\delta_{\mathrm{P}}\sigma^\dagger\sigma + \frac{\hbar\Omega}{2}\langle B\rangle\,\underline{X} + \hbar\sum_i \Delta_i\alpha_i^\dagger\alpha_i. \tag{4.45}$$

The case of resonant driving will be considered for these calculations such that $\delta_{\mathrm{P}} = E_{\mathrm{P}} - \hbar\omega_{\mathrm{d}} = 0$, where the previously defined polaron shifted TLS energy splitting $E_{\mathrm{P}} = E_{\mathrm{X}} -$

$\hbar(\sum_i \eta_i^2/\Delta_i + \sum_{\mathbf{k}} g_{\mathbf{k}}^2/\omega_{\mathbf{k}})$. The driving interaction term found from this rearrangement takes the form

$$H_{\mathrm{I}}^{\mathrm{DR}} = \frac{\hbar\Omega}{2}(\underline{X}B_x + \underline{Y}B_y). \tag{4.46}$$

Finally the driven EM-TLS polaron frame interaction term is

$$H_{\mathrm{I,P,D}}^{\mathrm{EM-TLS}} = \hbar \sum_l p_l e^{-i\hbar\omega_{\mathrm{d}}t}\sigma_\alpha B_- c_l^\dagger + \mathrm{h.c.}, \tag{4.47}$$

All other terms H_{E}, $H_{\mathrm{I,P}}^{\mathrm{PH-LV}}$ and $H_{\mathrm{Q}}^{\mathrm{PH}}$ are unchanged from the non-driven case shown in section (4.2.1.2).

4.4.1.1 Driven master equation

To find the master equation with this driven Hamiltonian the dissipator for the newly introduced interaction term $H_{\mathrm{I}}^{\mathrm{DR}}$, needs to be evaluated. To begin the driving-induced interaction Hamiltonian can be written as

$$H_{\mathrm{I}}^{\mathrm{DR}} = \frac{\hbar\Omega}{2}\underline{X} \otimes B_x + \frac{\hbar\Omega}{2}\underline{Y} \otimes B_y. \tag{4.48}$$

Following the derivation outlined in section (2.1.4.2) the system operators are moved to the interaction picture by using a Fourier decomposition, which gives $\underline{X}(-\tau) = \sum_\xi e^{i\xi\tau}\underline{X}(\xi)$ and $\underline{Y}(-\tau) = \sum_\xi e^{i\xi\tau}\underline{Y}(\xi)$. A unitary cannot be used in this case to time evolve the system operator as the free-system Hamiltonian doesn't commute with it. Finding the environment operators in the interaction picture gives $\tilde{B}_x(-\tau) = e^{-iH_{\mathrm{E}}\tau/\hbar}B_x e^{iH_{\mathrm{E}}\tau/\hbar}$ and similarly for $\tilde{B}_y(-\tau)$. Substituting in the environment operators into the correlation function defined in Eq. (2.22) and using section (2.2.2.2) gives

$$C_{xx}(\tau) = \frac{\langle B\rangle^2}{2}(e^{\phi(\tau)} + e^{-\phi(\tau)} - 2), \tag{4.49}$$

$$C_{yy}(\tau) = \frac{\langle B\rangle^2}{2}(e^{\phi(\tau)} - e^{-\phi(\tau)}), \tag{4.50}$$

and $C_{xy}(\tau) = C_{yx}(\tau) = 0$. Substituting the system operators along with the response functions $K_{xx}(\xi)$ and $K_{yy}(\xi)$ as found from Eq. (2.26) into the Eq. (2.17) gives the driving dissipator

$$\begin{aligned}\mathcal{D}_{\mathrm{DR}}[\rho_{\mathrm{S}}(t)] = &-\frac{1}{2}\Big(\frac{\Omega}{2}\Big)^2\sum_\xi \gamma_{xx}(\xi)[\underline{X}, \underline{X}(\xi)\rho_{\mathrm{S}}(t) - \rho_{\mathrm{S}}(t)\underline{X}^\dagger(\xi)] \\ &-\frac{1}{2}\Big(\frac{\Omega}{2}\Big)^2\sum_\xi \gamma_{yy}(\xi)[\underline{Y}, \underline{Y}(\xi)\rho_{\mathrm{S}}(t) - \rho_{\mathrm{S}}(t)\underline{Y}^\dagger(\xi)],\end{aligned} \tag{4.51}$$

where $\gamma_{xx}(\xi)$ and $\gamma_{yy}(\xi)$ are the real component of the response function and (ξ) is the eigenvalue difference. The Lamb shift terms originating from the imaginary component of the response function have been taken into the system Hamiltonian.

For all other dissipators besides the pure dephasing term moving into the interaction picture for the interaction Hamiltonian needs to be reconsidered due to commutation issues that arise from the additional driving term in the system. Firstly for the spontaneous emission dissipator the EM-TLS interaction term in the interaction picture is $\tilde{H}_{\mathrm{I,D}}^{\mathrm{EM-TLS}}(-\tau) = U_0^\dagger(-\tau) H_{\mathrm{D,I}}^{\mathrm{EM}} U_0(-\tau)$, which can be expressed as

$$\tilde{H}_{\mathrm{I,P}}^{\mathrm{EM-TLS}}(-\tau) = \hbar\sigma_\alpha(-\tau) e^{-i\omega_{\mathrm{d}}t} B_-(-\tau) \mathrm{C}^\dagger(-\tau) + \mathrm{h.c.}. \tag{4.52}$$

Using the approximation

$$\begin{aligned}\sigma_\alpha(-\tau)e^{-i\omega_{\mathrm{d}}t} &= \exp\Big[-i\big(\frac{\Omega\langle B\rangle}{2}\underline{X} + \sum_i \Delta_i\alpha_i^\dagger\alpha_i\big)\tau\Big]\sigma_\alpha \exp\Big[i\big(\frac{\Omega\langle B\rangle}{2}\underline{X} + \sum_i \Delta_i\alpha_i^\dagger\alpha_i\big)\tau\Big] e^{-i\omega_{\mathrm{d}}t}, \\ &\approx \sigma \exp\Big[-\sum_i \frac{\eta_i}{\Delta_i}\big(\alpha_i^\dagger e^{-i\Delta_i\tau} - \alpha_i e^{i\Delta_i\tau}\big)\Big] e^{-i\omega_{\mathrm{P}}t},\end{aligned} \tag{4.53}$$

where the last step uses the large difference in energy scales $\omega_{\mathrm{P}} \sim \omega_{\mathrm{d}} \sim 1.6\,\mathrm{eV}$ compared to $\Omega\langle B\rangle \approx 10\,\mathrm{meV}$. With this approximation this expression is now equivalent to the non-driven electromagnetic dissipator shown in Eq. (4.20).

When evaluating the local vibrational mode dissipator the following approximation can be made $e^{i(\frac{\Omega\langle B\rangle}{2}\underline{X} + \sum_i \Delta_i\alpha_i^\dagger\alpha_i)t}\alpha_j e^{-i(\frac{i\Omega\langle B\rangle}{2}\underline{X} + \sum_i \Delta_i\alpha_i^\dagger\alpha_i)t} \approx \alpha_j e^{-i\Delta_i t}$, which is valid as $\Omega\langle B\rangle\,(\sim 1\mu\mathrm{eV}) \ll \Delta_i(20-40\ \mathrm{meV})$ where these values are for a typical single molecule emitter and assuming that local vibrational mode fluctuations are uncorrelated. Similar to the spontaneous emission case with this approximation the local vibrational mode dissipator for the non-driven case is equivalent to that shown in Eq. (4.34). Putting these elements together the driven master equation is given by

$$\begin{aligned}\partial_t\rho_{\mathrm{S}}(t) = \mathcal{D}_{\mathrm{DR}}[\rho_{\mathrm{S}}(t)] + \mathcal{D}_{\mathrm{EM}}[\rho_{\mathrm{S}}(t)] + \mathcal{D}_{\mathrm{PH}}[\rho_{\mathrm{S}}(t)] \\ + \sum_i \Big(-i[\Delta_i\alpha_i^\dagger\alpha_i + \frac{\Omega}{2}\langle B\rangle\,\underline{X}, \rho(t)] + \Gamma_{i,+}\mathcal{L}_{\alpha^\dagger}[\rho(t)] + \Gamma_{i,-}\mathcal{L}_{\alpha}[\rho(t)]\Big).\end{aligned} \tag{4.54}$$

4.4.2 Second–order intensity correlation function

The steady state normalised second–order intensity correlation function from a Hanbury Brown and Twiss set up is

$$g^{(2)}(\tau) = \frac{\langle E^\dagger E^\dagger(\tau)E(\tau)E\rangle_{\mathrm{ss}}}{\langle E^\dagger E\rangle_{\mathrm{ss}}^2} \tag{4.55}$$

where τ is the time delay between detection events [45] and a derivation for this equation can be found in section (3.3.1). Substituting the definition of the electric field operators shown in Eq. (4.36) into equation (4.55) and simplifying gives

(4.56)

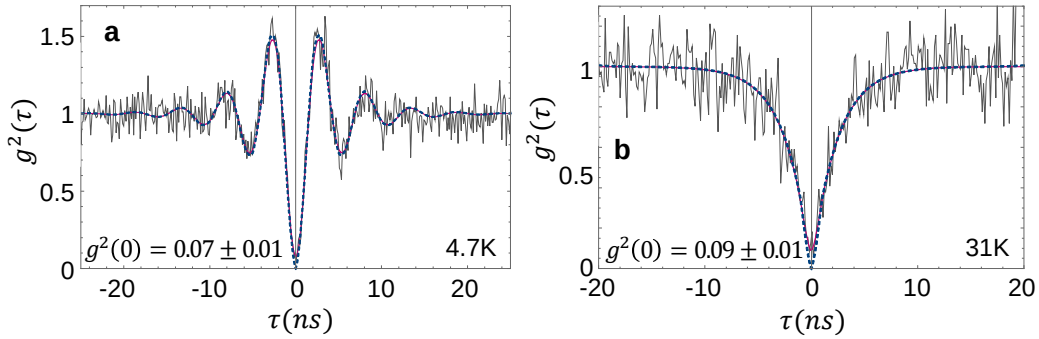

Figure 4.9: Measured $g^{(2)}(\tau)$ taken from a Hanbury Brown–Twiss experiment (grey solid line) for the DBT molecule at (a) 4.7 K and (b) 31 K. Purple solid lines show the theoretical model convolved with a Gaussian function to account for the detector timing jitter and blue dashed lines shows the model without convolution.

where influence of the bath displacement operators cancel out. Utilising the quantum regression theorem, see section (3.1.2.1), the second order correlation function can be readily evaluated to give

$$g^{(2)}(\tau) = \frac{\mathrm{Tr}_S(\sigma_\alpha^\dagger \sigma_\alpha e^{L\tau} \sigma_\alpha \rho_S(t \to \infty)\sigma_\alpha^\dagger)}{\langle \sigma_\alpha^\dagger \sigma_\alpha^2 \rangle_{\mathrm{ss}}}. \tag{4.57}$$

To calculate the normalisation factor shown in the denominator the inclusion of the upper half diagonal elements (all vibronic and electronic excited levels) of the 'steady state' density matrix are required.

The theoretically calculated $g^{(2)}(\tau)$ and experimental data from a Hanbury Brown–Twiss (HBT) set up are shown in Fig. 4.9, for temperatures of 4.7 K and 31 K. This HBT measurement probes the excited state population of the DBT molecule and is used to verify that the source is emitting single photons. For an ideal single photon emitter there should be no coincidence events between the two output detectors such that $\tilde{g}^{(2)}(0) \to 0$. The sharp dip observed at $\tau = 0$ in the data reflects the strong suppression of multi-photon emission events. At $T = 4.7$ K Rabi oscillations which represent the coherent exchange of excitations from the driving laser to the system, can be seen.

The parameters used to calculate $g^{(2)}(\tau)$ are taken from the fits of the DBT emission spectra, where the Rabi frequency Ω, is the only additional free parameter. Interestingly, to reproduce the experimentally observed Rabi frequency of the oscillations, when fitted phenomenologically, is the re-normalised Rabi frequency $\Omega_r = \Omega \langle B \rangle \prod_i \langle \mathcal{A}_i \rangle$ instead of the bare Rabi frequency Ω, which arises from both the local vibrational mode and thermal bath phonon coupling [79]. As temperatures increase thermal phonon interactions begin to suppress these Rabi oscillations, demonstrated in Fig. 4.9b.

4.5 Chapter summary

In this chapter firstly, single molecules of dibenzoterrylene have been motivated as promising single photon sources. Characteristic properties of DBT are presented and a suitable host for DBT molecules, a nano–crystal of anthracene (Ac) has been motivated and described. The growth of the DBT–Ac nano–crystal used to provide the results presented in this chapter has been detailed.

A theoretical model in the formalism of open quantum systems theory has been developed which comprehensively describes the optical properties of a single dibenzoterrylene molecule doped in an anthracene nano–crystal. The model successfully reproduces temperature dependent emission spectra measurements, where all spectral features are well captured. These features include, a zero phonon line (ZPL) at 782.3 nm, sharp peaks which arise from the excitation of four separate local vibrational modes (LVM) and a broad continuous longitudinal acoustic sideband associated with both the ZPL and LVMs. Additionally, the model captures the temperature dependent homogeneous ZPL broadening which arises from anharmonic effects of the thermal phonon bath by taking the electron–phonon interaction to second order with respect to lattice displacements. In the model an extension to polaron theory is developed which displaces both the thermal phonon bath and the localised vibrational modes. To model the dynamics a second–order Born–Markov master equation in the polaron frame is derived. Working in the polaron frame allows for the non–Markovian feedback between the system and the thermal bath which captures the observed broad sidebands. This model also holds versatility to alternative host environments, as its influence is captured by including a thermal phonon bath which is characterised by two free parameters, the exciton–phonon coupling strength and a high–frequency cut off (to capture a different host these parameters can be adapted). Moreover, this work could be extended in to capture other promising solid-state quantum emitters for which phonon coupling effects are important, such as two-dimensional materials [3].

CHAPTER 5

HONG–OU–MANDEL EXCITATION REGIMES

This chapter presents calculations of second order correlation function measurements $g^{(2)}(\tau)$ from a Hong–Ou–Mandel (HOM) interferometer set up under different driving regimes. For these calculations interference between successive single photons from a single quantum emitter separated with some time delay are considered. The main motivator of conducting a HOM experiment is the ability to observe and quantify two–photon interference effects, where this interference resides in the suppression of detected coincidence events, measured by $g^{(2)}(\tau)$.

The full–photon wavepacket indistinguishability $\mathcal{I} = \langle\psi_1|\psi_2\rangle$ of a quantum emitter under pulsed excitation can be determined from a HOM measurement, as shown in section (3.3.2).

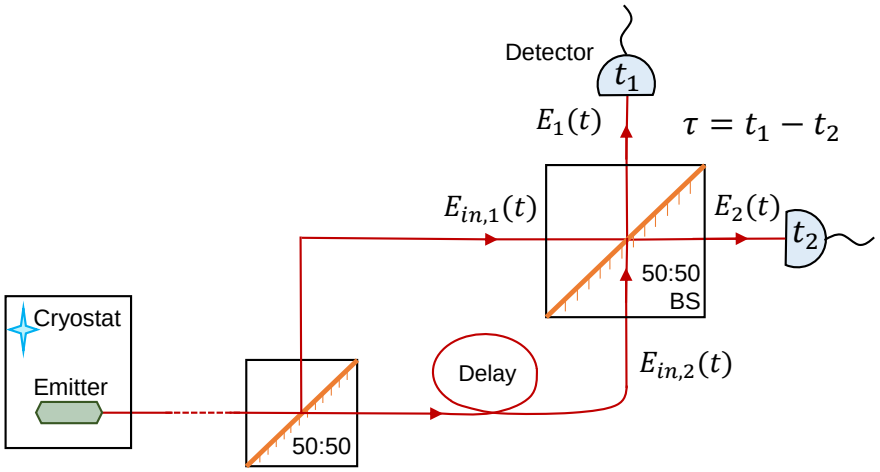

Figure 5.1: HOM set up with a single photon emitter as the source input split on a 50:50 beamsplitter (BS) followed by some delay, before interfering on another 50:50 beam splitter. The time difference between detector measurements is $\tau = t_1 - t_2$.

This indistinguishability indicates to what degree photons with the wavefunctions $|\psi_1\rangle$ and $|\psi_2\rangle$ are quantum mechanically identical and gives the amplitude of two–photon interference. Indistinguishability is a key requirement for many quantum information applications which rely on photonics such as linear optical quantum computing [60] or quantum networks which use spin–photon entanglement [11]. Other idealistic requirements for a single photon source with the above quantum applications include high efficiency and on-demand emission.

The first driving regime considered in this chapter is non–resonant pulsed excitation. From which full photon wave packet indistinguishability can be found from the normalised time-integrated difference between second order correlation measurements for input photons with perpendicular and parallel polarization alignment. This work extends upon the example shown in section (3.3.2) (which considers solely a two–level system), to include non-temporal decoherence effects such as a longitudinal acoustic phonon sideband and localised vibrational modes. Other regimes covered in this chapter are non–resonant and resonant continuous wave (cw) excitation. Measurements from cw excitation typically involve looking at the height of the HOM dip at $g^{(2)}(0)$, which depends highly on the temporal resolution of the detector. For the case of an ideal detectors the value of $g^{(2)}(0)$ tends to zero regardless of the incoming photon distinguishability [55, 94], as the measurement acts as a frequency filter. As photons get more distinguishable, the temporal detector resolution needs to increase to capture this suppression to zero. For the case of near–indistinguishable photons with realistic detectors, the $g^{(2)}(0)$ suppression should be resolved close to zero indicating two–photon interference effects, which is why this value is still quoted in literature [69, 88, 98, 113]. However, as the coincidence rate at zero time delay is highly sensitive on the detector resolution it is insufficient to quantitatively determine the true coherence properties of the incident photons. In this chapter a novel method is proposed from which the full wavepacket indistinguishability can be extracted from a non–resonant cw HOM experiment. Finally, the regime of resonant driving is considered which is of fundamental interest as it directly probes the exciton state. Within the resonant driving regime, Rabi oscillations are observed and the effect of a continuous phonon sideband is discussed.

The systems explored in this work are transferable across any deterministic solid state emitter, however, to support these calculations a single molecule DBT emitter is considered. The work presented in this chapter is based on this publication in [104]. All experimental aspects detailed in this chapter were completed at Imperial College London and lead by collaborator Alex S. Clark's group with Ross C. Schofield, Kyle D. Major and Rowan A. Hoggarth.

5.1 Pulsed excitation

The calculation of a non–resonantly pulsed ideal two–level system (TLS) emitter can be found in section (3.3.2). To model this regime the system is initially populated in the excited state,

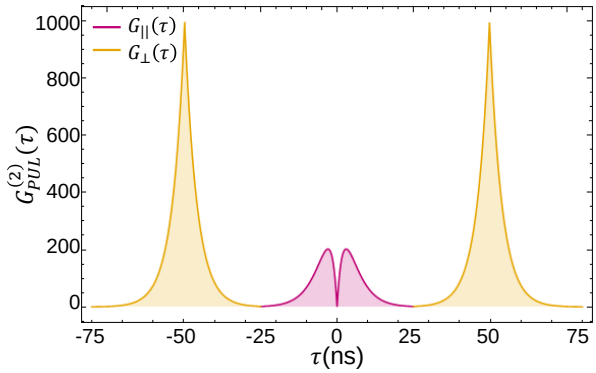

Figure 5.2: Calculation of the measurement taken from a pulsed HOM experiment accounting for the ZPL emission from a DBT molecule at $\Gamma_1 = 2\pi \times 40\,\text{MHz}$ and $\gamma = 2\pi \times 15\,\text{MHz}$, the time delay between pulses is simulated to $T = 12.5/\Gamma_1 \approx 50\,\text{ns}$. Yellow peaks represent the uncorrelated counts which can also be found from perpendicular polarisation between interferometer input arms, whereas the purple feature is the ensemble average of coincidence events, $G^{(2)}_{PUL}(t,\tau)$ found with parallel alignment.

such that $\rho(0) = |e\rangle\langle e|$; it is assumed that the population has already inverted from the fast laser pulse. Taking the parameters for the DBT molecule described in chapter 4, the coincidence detection rate of a pulsed single molecule has been found in Fig. 5.2. In this figure the ensemble average of unnormalised coincidence events $G^{(2)}_{PUL}(\tau)$ is shown in pink, along side the uncorrelated coincidence probability $G^{(2)}_{\perp_{PUL}}(\tau)$ with a pulse time delay of $T = 12.5/\Gamma_1 \approx 50\,\text{ns}$, chosen to avoid any peak overlap, in yellow.

It is already apparent from the work shown in chapter 4 that emission from a single molecule of DBT has a rich emission structure consisting of more than just a zero phonon line, including a longitudinal acoustic phonon sideband and sharp peaks originating from local vibrational modes. When considering key parameters such as the indistinguishability of an emitter, it is particularly important to characterise the effect of non-temporal decoherence from both the continuous phonon sideband and the localised vibrational modes. Noting that it is arguably more important to capture the effect of a continuous sideband as it directly overlaps with the ZPL, in comparison to the local modes which are well separated in frequency. To remove the vast majority of both of these decoherence effects a filter can be used. In this work the influence of both non-temporal decoherence effects are included in the modelling as it is of fundamental interest to investigate the arising physics.

5.1.1 Inclusion of a phonon sideband

We first consider the model of a two–level system with a phonon sideband by following the methodology set out in section (3.2.2). The positive component of the electric field operator, for this open quantum system is found to be $E(t) = \sqrt{\Gamma_1/2\pi}\,\sigma(t)B_-(t)$, negating the vacuum term. Substituting the field operator into Eq. (3.57) we find the unnormalised ensemble average

of coincidence events from a TLS with continuous phonon sideband as

$$G^{(2)}_{PULSB}(\tau) = \frac{\Gamma_1}{4\pi}\int_0^\infty dt\Big(\left\langle\sigma^\dagger(t)\sigma(t)\right\rangle\left\langle\sigma^\dagger(t+\tau)\sigma(t+\tau)\right\rangle - \left|\mathcal{G}(\tau)\left\langle\sigma^\dagger(t+\tau)\sigma(t)\right\rangle\right|^2\Big), \quad (5.1)$$

with the phonon bath correlation function $\mathcal{G}(\tau) = \langle B_-(t+\tau)B_+(t)\rangle$ detailed in Eq. (2.47). For the purpose of these calculations the parameters to capture the sideband are those found from the molecule characterised in chapter 4 which are $\xi = (8.6 \pm 0.6)\,\mathrm{ps}^{-1}$ for the frequency cut off and $\alpha = (0.009 \pm 0.001)\,\mathrm{ps}^2$ for the phonon coupling strength. See figure 5.3a for simulations of $G^{(2)}_{PULSB}(\tau)$ comparing the cases for the inclusion/exclusion of a phonon sideband with the pure dephasing fixed to $\gamma = 2\pi \times 15\,\mathrm{MHz}$ in dashed–yellow and solid–pink lines respectively and for the case of a sideband present but with $\gamma = 0$. It can be seen that the inclusion of the sideband introduces a significant bump around $(0.1 - 1)$ ps which then plateaus out before tapering off (on a log scale), where this feature directly reflects the presence of the phonon correlation function $|\mathcal{G}(\tau)|^2$ in Eq. (5.1), shown in the inset of Fig. 5.3a. The inclusion of the sideband significantly increases the area of the peak, where this reflects the increased decoherence of the emission, and as will be seen leads to a reduction in indistinguishability. For the case of an ideal two–level system with no pure dephasing ($\gamma = 0$) and some spontaneous decay, there is no chance of coincidence events due to purely coherent emission giving, $\int_0^\infty d\tau G^{(2)}_{PUL}(\tau) = 0$. Noting that for *any* single photon emitter under non–resonantly pulsed excitation $G^{(2)}_{PUL}(0) = 0$ holds as the terms in Eq. (5.1) cancel. The height of the dip at $G^{(2)}_{PUL}(0)$ depends on the de-

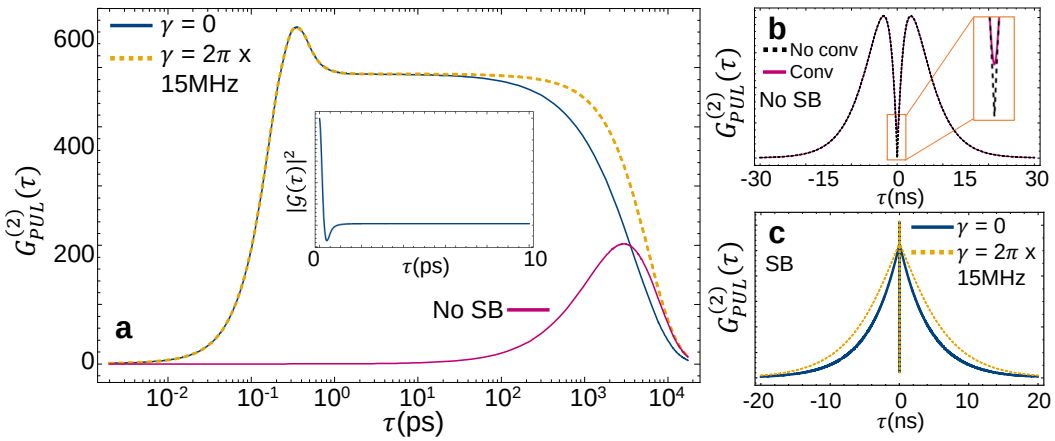

Figure 5.3: (a) Simulation of $G_{PUL}(\tau)$ from a DBT molecule on a log scale capturing the ZPL and continuous LA phonon sideband $\xi = (8.6 \pm 0.6)\,\mathrm{ps}^{-1}$ and $\alpha = (0.009 \pm 0.001)\,\mathrm{ps}^2$ taken from the analysis of the molecule in chapter 4. The ZPL has a pure dephasing rate of $\gamma = 2\pi \times 15\,\mathrm{MHz}$ (blue) and $\gamma = 0$ (dashed yellow), the omission of the sideband with pure dephasing rate fixed to $\gamma = 2\pi \times 15\,\mathrm{MHz}$ is shown in pink. (b) and (c) show the functions in (a) with linear scaling including a convolution with a Gaussian kernel to simulate detection jitter is shown in dashed black. Inset highlights the HOM dip.

tector timing resolution and can be captured in the model by a convolution with a Gaussian kernel $Gauss(\sigma_R) = \frac{1}{\sqrt{2\pi\sigma_R^2}} \exp\left[\frac{-x^2}{2\sigma_R^2}\right]$, with σ_R the standard deviation. To show this effect see Fig. 5.3b, for which the case of a TLS with pure dephasing has been convolved with a kernel of $\sigma_R = 0.3$ ns. Finally, a direct comparison of the model with a phonon sideband for the case of $\gamma = 2\pi \times 15$ MHz and $\gamma = 0$ is shown on a linear plot, where it is clear that the bump feature around $(0.1 - 1)$ ps is unlikely to be resolvable upon measurement due to detector jitter, unless the resolution is on the order of ~ 0.1 ps.

To find the indistinguishability of the molecule omitting the effects of the localised vibrational modes requires solving Eq. (3.59) which gives

$$\mathcal{I}_{ZPL+SB} = \frac{\int dt \int d\tau |\mathcal{G}(\tau)|^2 \left|\langle \sigma^\dagger(t+\tau)\sigma(t)\rangle\right|^2}{\int dt \int d\tau \, \langle \sigma^\dagger(t)\sigma(t)\rangle \, \langle \sigma^\dagger(t+\tau)\sigma(t+\tau)\rangle}. \tag{5.2}$$

To simplify this expression we assume that emission into the phonon sideband is completely incoherent [55], which leads to

$$\mathcal{I}_{ZPL+SB} \approx \langle B\rangle^4 \frac{\Gamma_1}{2\Gamma_2(T)}. \tag{5.3}$$

To explore the validity of this assumption both Eq. (5.2) and (5.3) have been found for varying temperatures, where the temperature dependent pure dephasing rate from Eq. (4.27) modifies the ZPL broadening and can be found in figure 5.4a. It can be seen that under 30 K the approximation of a purely incoherent sideband holds, however as the temperature increases above this, a small deviation in the two models can be seen (only with logarithmic scaling).

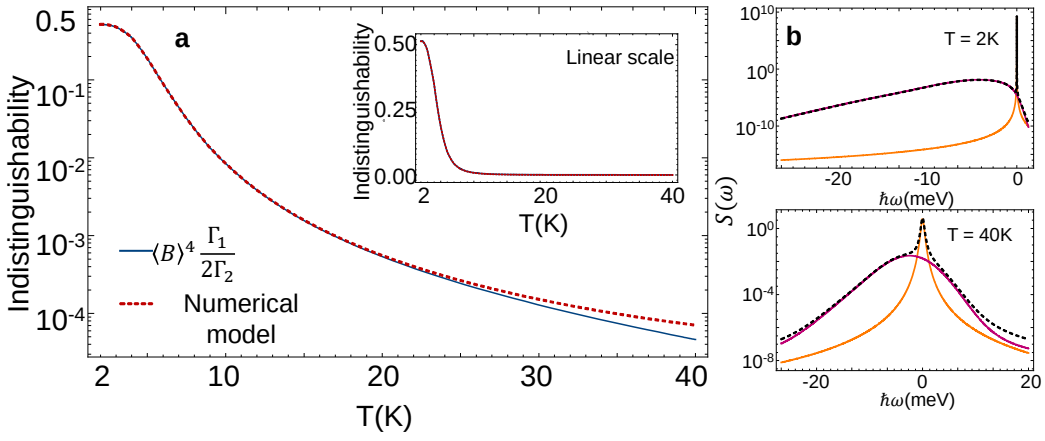

Figure 5.4: (a) Indistinguishability for a DBT molecule accounting for its ZPL and phonon sideband as a function of temperature. Comparing the case for assuming the sideband is fully incoherent (solid blue) and numerically finding the indistinguishability from Eq. (5.3) (dashed red). (b) Emission spectra for the molecule with a phonon sideband (SB) for 2 K (top) and 40 K (bottom) showing individual contribution to the zero phonon line and sideband and the combined spectra.

See Fig. 5.4b for the emission spectra for the lifetime limited case of $T = 2\,\mathrm{K}$ and for $T = 40\,\mathrm{K}$. The fraction of the sideband that is coherent is on the time scale of the ZPL lifetime which for DBT molecules is $\sim 4\,\mathrm{ns}$. For the lifetime limited case a very small fraction of the sideband directly overlaps with the ZPL which leads to the reasonable assumption of a purely incoherent sideband. However as the temperature increases it appears as though the sideband shifts, causing a higher fraction of the sideband to directly overlap with the ZPL peak leading to a relatively higher yet small coherent fraction.

5.1.2 Inclusion of local vibrational modes

Now considering the full model of a single DBT molecule with all its spectral features including the ZPL, phonon sideband and localised vibrational modes detailed in section (4.2) with the polaron frame master equation shown in Eq. (4.34). Substituting the electric field operator in Eq. (4.36) into Eq. (3.57) to find the unnormalised ensemble average of coincidence events from the full emission from a single DBT molecule as

$$G^{(2)}_{PUL_{SB+LV}}(\tau) = \frac{\Gamma_1}{4\pi}\int_0^\infty dt\Big(\left\langle\sigma_\alpha^\dagger(t)\sigma_\alpha(t)\right\rangle\left\langle\sigma_\alpha^\dagger(t+\tau)\sigma_\alpha(t+\tau)\right\rangle - \left|\mathcal{G}(\tau)\left\langle\sigma_\alpha^\dagger(t+\tau)\sigma_\alpha(t)\right\rangle\right|^2\Big). \quad (5.4)$$

For these calculations only one localised vibrational mode at 21.5 meV is included to demonstrate its influence on the function. Figure 5.5a shows simulations of $G^{(2)}_{PUL_{SB+LV}}(\tau)$ for the emission from a DBT emitter, comparing the cases for the inclusion/exclusion of a phonon sideband, with one localised vibrational mode and some pure dephasing set to $\gamma = 2\pi \times 15\,\mathrm{MHz}$

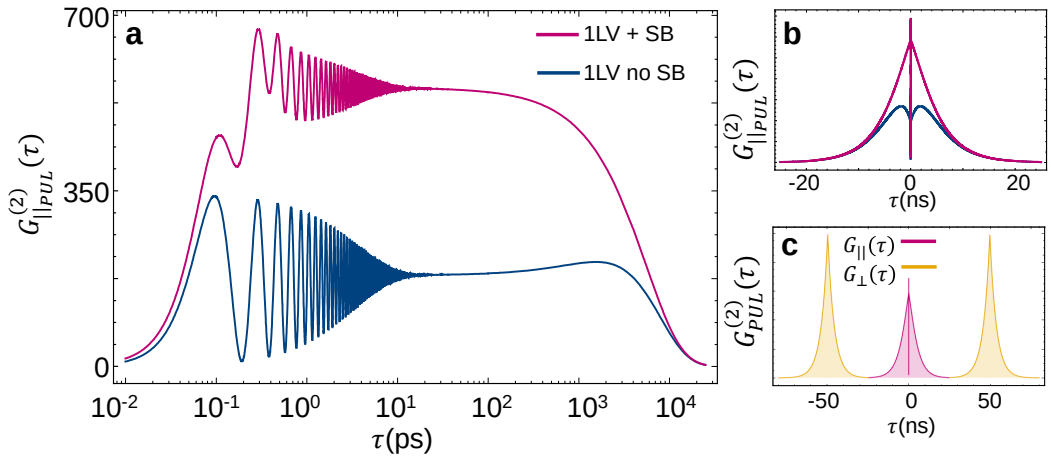

Figure 5.5: (a) Simulation of $G_{||_{\mathrm{PUL}}}(\tau)$ from a DBT molecule capturing the ZPL and one local vibrational mode (pink) shows the inclusion of the continuous LA phonon sideband and (blue) shows without (blue). (b) Shows the $G_{||_{\mathrm{PUL}}}(\tau)$ on a linear scale to visualise the parallel detection events. (c) shows the full $G_{\mathrm{PUL}}(\tau)$ profile with the inclusion of the sideband.

shown in the pink and blue lines, respectively. It can be seen that the inclusion of the local mode introduces an oscillation which has a period of $\sim (0.19 \pm 0.04)$ ps. The overall shape of the peak is also affected for these two scenarios which can be seen in figure. 5.5b, where a simulation of the full coincidence detection rate for a DBT emitter with the inclusion of the phonon sideband and the first localised vibrational mode is shown in 5.5c. Now assuming the emission into the localised vibrational modes is purely incoherent, justified as they are spectrally separated in frequency from the ZPL, the indistinguishability can be found from

$$\mathcal{I}_{SB+LV} \approx [\prod_i \langle \mathcal{A}_i \rangle^4] \langle B \rangle^4 \frac{\Gamma_1}{2\Gamma_2(T)}. \tag{5.5}$$

5.2 Continuous wave excitation

For the case of non–resonant cw driving the experimentally determined second-order correlation function takes on a different form; instead of measuring the ensemble average over coincidence events, we require the steady–state function found by taking $t \to \infty$, giving

$$G^{(2)}_{CW}(\tau) = \lim_{t\to\infty} \frac{1}{2}\Big(4G^{(2)}_{HBT}(t,\tau) - \Big|\Big\langle E^\dagger(t+\tau)E(t)\Big\rangle\Big|^2 + \Big\langle E^\dagger(t)E(t)\Big\rangle \Big\langle E^\dagger(t+\tau)E(t+\tau)\Big\rangle\Big). \tag{5.6}$$

In the following sections both non–resonant and resonant driving is considered.

5.2.1 Coherent non–resonant driving

To evaluate $G^{(2)}_{CW}(\tau)$ a three-level non–resonant coherent driving model shown in Fig. 5.6a is considered. This system captures the non–resonant driving to a higher vibrational level

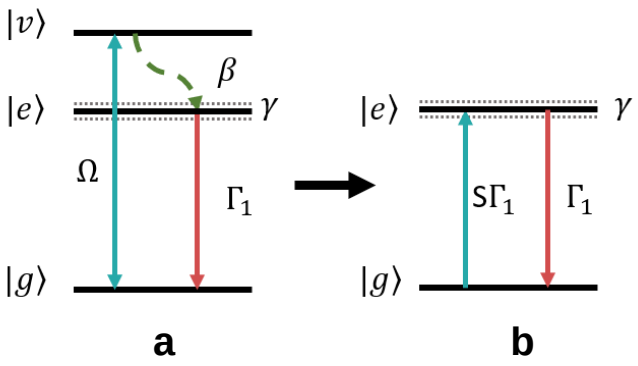

Figure 5.6: (a) Schematic diagram of non–resonant driving from the ground $|g\rangle$ to a higher vibrational level $|v\rangle$, modelled by coherent driving with the Rabi frequency Ω. The fast non-radiative decay rate from $|v\rangle \to |e\rangle$ is given by β. Spontaneous emission from the excited state $|e\rangle$ is given by Γ_1 and pure dephasing is given by γ. (b) Effective two level system by adiabatic elimination of the pump level, giving a driving rate $S\Gamma_1$ with the saturation parameter S.

with state $|v\rangle = (1,0,0)$ which then undergoes rapid non-radiative decay to the excited state $|e\rangle = (0,1,0)$ followed by radiative decay to the ground state $|g\rangle = (0,0,1)$. The transition operators are defined by $\sigma = |g\rangle\langle e|$, $\sigma_{vg} = |v\rangle\langle g|$ and $\sigma_{ev} = |e\rangle\langle v|$. The subsequent Born-Markov second-order master equation for this system is given by

$$\partial_t \rho(t) = -i[H_S, \rho] + \Gamma_1 \mathcal{L}_\sigma[\rho(t)] + \beta \mathcal{L}_{\sigma_{ev}}[\rho(t)] + 2\gamma \mathcal{L}_{\sigma^\dagger\sigma}[\rho(t)], \tag{5.7}$$

with system term $H_S = \frac{\Omega}{2}(\sigma_{vg} + \sigma_{vg}^\dagger)$ which represents the coherent driving with Rabi frequency Ω. Simplifying Eq. (5.6) by substituting in the positive electric field operator $E(t) \propto \sigma$ for this system and normalising with the excited steady state population $\langle \sigma^\dagger\sigma \rangle_{ss} = \lim_{t\to\infty} \langle \sigma^\dagger(t)\sigma(t) \rangle$, we find

$$g^{(2)}_{CW}(\tau) = \frac{1}{2\langle \sigma^\dagger\sigma \rangle^2_{ss}} \Big(\Big\langle \sigma^\dagger\sigma \Big\rangle^2_{ss} + \lim_{t\to\infty} \big(\Big\langle \sigma^\dagger(t)\sigma^\dagger(t+\tau)\sigma(t+\tau)\sigma(t) \Big\rangle - \Big| \Big\langle \sigma^\dagger(t+\tau)\sigma(t) \Big\rangle \Big|^2 \big) \Big), \tag{5.8}$$

which corresponds experimentally to parallel polarisation alignment to the interferometer input arms. To calculate the scenario of uncorrelated input fields, which corresponds to setting perpendicular polarisation alignment to the interferometer input arms, the interference term vanishes giving

$$g^{(2)}_{\perp_{CW}}(\tau) = \frac{1}{2\,\langle \sigma^\dagger\sigma \rangle^2_{ss}} \Big(\lim_{t\to\infty} \Big\langle \sigma^\dagger(t)\sigma^\dagger(t+\tau)\sigma(t+\tau)\sigma(t) \Big\rangle + \Big\langle \sigma^\dagger\sigma \Big\rangle^2_{ss} \Big). \tag{5.9}$$

To visualise these second order correlation function under continuous wave excitation see Fig. 5.7. In this figure $g^{(2)}(\tau)$ functions for both parallel and perpendicular alignment of the interferometer arms are shown, where at $\tau = 0$ anti–bunching is observed which takes the dip to 0.5 for both beam alignments. For the parallel case two–photon interference is observed and the dip goes to zero.

5.2.2 Indistinguishability from continuous excitation

It is evident that the methodology used to find the indistinguishability as shown in Eq. (3.60) cannot be used here as this gives a divergent result when integrating over τ. However, if the steady-state population squared (the normalisation factor) is subtracted, this results in convergent integrals and therefore it is postulated that the indistinguishability can be found from

$$\tilde{\mathcal{I}}(S) = \frac{\int d\tau (1 - g^{(2)}_{\parallel_{CW}}(\tau)) - \int d\tau (1 - g^{(2)}_{\perp_{CW}}(\tau))}{\int d\tau (1 - g^{(2)}_{\perp_{CW}}(\tau))}. \tag{5.10}$$

Substituting in the $g^{(2)}_{CW}(\tau)$ and $g^{(2)}_{\perp_{CW}}(\tau)$ into Eq. (5.10) we find

$$\tilde{\mathcal{I}}(S) = \frac{\int d\tau \lim_{t\to\infty} \Big| \langle \sigma^\dagger(t+\tau)\sigma(t) \rangle \Big|^2 / \langle \sigma^\dagger\sigma \rangle^2_{ss}}{\int d\tau\, 1 - \lim_{t\to\infty} \langle \sigma^\dagger(t)\sigma^\dagger(t+\tau)\sigma(t+\tau)\sigma(t) \rangle / \langle \sigma^\dagger\sigma \rangle^2_{ss}}. \tag{5.11}$$

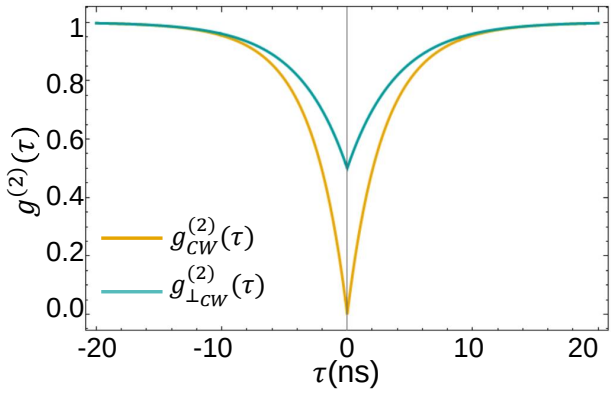

Figure 5.7: Simulation of a continuous wave second order correlation function measurement for the case of parallel (yellow) and perpendicular (blue) interferometer arm alignment. Model captures DBT molecule zero phonon line emission with parameters $\Gamma_1 = 2\pi \times 40 \pm 2\,\mathrm{MHz}$ and the dephasing rate $\Gamma_2 = 2\pi \times 35 \pm 4\,\mathrm{MHz}$.

This three level system Eq. (5.11) can only be evaluated numerically by invoking the quantum regression theorem. For a single DBT molecule the decay rate from the first localised vibrational mode is approximately $\beta \approx 2500 \times \Gamma_1$ [23]. The excited steady state population for this system is $\rho_{ee}(\infty) = \langle e|\rho(\infty)|e\rangle = \frac{\frac{\Omega^2}{\beta\Gamma_1}}{1+\frac{\Omega^2}{\beta\Gamma_1}+\frac{2\Omega^2}{\beta^2}}$. Setting driving strength saturation to $S = \frac{\Omega^2}{\beta\Gamma_1}$, as $\beta \gg \Gamma_1$, we find

$$\rho_{ee}(\infty) = \frac{S}{1+S(1+\frac{2\Gamma_1}{\beta})} \approx \frac{S}{1+S}, \tag{5.12}$$

which is valid as long as $\frac{2\Gamma_1}{\beta} \ll 1$, for typical DBT system parameters this relation is indeed valid as $\frac{2\Gamma_1}{\beta} \approx 10^{-3}$.

5.2.2.1 Adiabatic elimination of the pump level

It is advantageous to have an analytical form for $\tilde{\mathcal{I}}(S)$ as this allows for the extraction of indistinguishability from experiment. To do so an effective two-level system is now derived by adiabatically eliminating the higher order energy state, see Fig. 5.6. Starting with the optical Bloch equations for the three level non–resonantly driven system derived from Eq. (5.7), we find

$$\dot{\rho}_{vv}(t) = \frac{i\Omega}{2}(\rho_{vg}(t) - \rho_{gv}(t)) - \beta\rho_{vv}(t), \tag{5.13}$$

$$\dot{\rho}_{ee}(t) = -\Gamma_1\rho_{ee}(t) + \beta\rho_{vv}(t), \tag{5.14}$$

$$\dot{\rho}_{gg}(t) = -\frac{i\Omega}{2}(\rho_{vg}(t) - \rho_{gv}(t)) + \Gamma_1\rho_{ee}(t), \tag{5.15}$$

$$\dot{\rho}_{gv}(t) = \frac{i\Omega}{2}(\rho_{gg}(t) - \rho_{vv}(t)) - \frac{\beta}{2}\rho_{gv}(t), \tag{5.16}$$

$$\dot{\rho}_{ge}(t) = -\frac{i\Omega}{2}\rho_{ve}(t) - \frac{\Gamma_1}{2}\rho_{ge}(t) - \gamma\rho_{ge}(t), \tag{5.17}$$

$$\dot{\rho}_{ve}(t) = -\frac{i\Omega}{2}\rho_{ge}(t) - \frac{\Gamma_1}{2}\rho_{ve}(t) - \frac{\beta}{2}\rho_{ve}(t) - \gamma\rho_{ve}(t), \tag{5.18}$$

where $\rho_{XY}(t) = \langle X|\rho(t)|Y\rangle$ [25]. Solving firstly Eq. (5.16) with an integrating factor we find

$$\rho_{gv}(t) = \frac{i\Omega}{2}\int_0^t dt' e^{-\frac{\beta}{2}(t-t')}(\rho_{gg}(t') - \rho_{vv}(t')), \tag{5.19}$$

which can be solved for the case of $\beta \gg \Omega$ to give $\rho_{gv}(t) \approx \frac{i\Omega}{\beta}(\rho_{gg}(t) - \rho_{vv}(t))$, and by similar methodology $\rho_{vg}(t) \approx -\frac{i\Omega}{\beta}(\rho_{gg}(t) - \rho_{vv}(t))$. Using the forms for $\rho_{gv}(t)$ and $\rho_{vg}(t)$ and substituting into Eq. (5.13) gives

$$\dot{\rho}_{vv}(t) = -\frac{\Omega^2 + \beta^2}{\beta}\rho_{vv}(t) + \frac{\Omega^2}{\beta}\rho_{gg}(t). \tag{5.20}$$

Solving Eq. (5.20) using an integrating factor again we find

$$\begin{aligned}\rho_{vv}(t) &= \frac{\Omega^2}{\beta}\int_0^t e^{-\frac{\Omega^2+\beta^2}{\beta}(t-t')}\rho_{gg}(t')dt', \\ &\approx \frac{\Omega^2}{\Omega^2+\beta^2}\rho_{gg}(t).\end{aligned} \tag{5.21}$$

Finally, solving Eq. (5.18) using the same methodology as above we find

$$\begin{aligned}\rho_{ve}(t) &= -\frac{i\Omega}{2}\int_0^t e^{-(\frac{\Gamma_1+\beta}{2}+\gamma)(t-t')}\rho_{ge}(t')dt', \\ &\approx -i\frac{\Omega}{\beta+\Gamma_1+2\gamma}\rho_{ge}(t).\end{aligned} \tag{5.22}$$

Making a change of variables to the saturation parameter $S = \Omega^2/\beta\Gamma_1$ defined in the section on coherent non–resonant driving, to recover the ground and excited state optical Bloch equations for the effective two–level system, finding

$$\begin{aligned}\dot{\rho}_{ee}(t) &= -\Gamma_1\rho_{ee}(t) + \beta\frac{\Omega^2}{\Omega^2+\beta^2}\rho_{gg}(t), \\ &\approx -\Gamma_1\rho_{ee}(t) + S\Gamma_1\rho_{gg}(t),\end{aligned} \tag{5.23}$$

$$\dot{\rho}_{gg}(t) \approx \Gamma_1\rho_{ee}(t) - S\Gamma_1\rho_{gg}(t), \tag{5.24}$$

which holds as long as $\beta \gg \Omega$. Manipulating this equality further as $\Omega = \sqrt{S\Gamma_1\beta}$, leading to the constraint $\beta \gg S\Gamma_1$. The final optical Bloch equation to consider is the $\dot{\rho}_{ge}(t)$ contribution. This leads to an interesting pre–factor upon substitution of Eq. (5.22) into Eq. (5.17), finding

$$\dot{\rho}_{ge}(t) = -\frac{S\Gamma_1\beta}{2(\beta+2\Gamma_2)}\rho_{ge}(t) - \frac{\Gamma_1}{2}\rho_{ge}(t) - \gamma\rho_{ge}(t), \tag{5.25}$$

which for $\beta \gg \Gamma_2$ can be simplified to recover the two–level system optical Bloch equation

$$\dot{\rho}_{ge}(t) = -\frac{S\Gamma_1}{2}\rho_{ge}(t) - \frac{\Gamma_1}{2}\rho_{ge}(t) - \gamma\rho_{ge}(t). \tag{5.26}$$

5.2.3 Indistinguishability extraction results

Modelling the effective two–level system found from the adiabatic elimination above, using a second–order Born–Markov master equation, we find

$$\partial_t \rho(t) = \Gamma_1 \mathcal{L}_\sigma[\rho(t)] + \Gamma_1 S \mathcal{L}_{\sigma^\dagger}[\rho(t)] + 2\gamma \mathcal{L}_{\sigma^\dagger\sigma}[\rho(t)]. \tag{5.27}$$

The driving in this model is captured by the incoherent dissipator with rate $S\Gamma_1$, see Fig. 5.6. Using the quantum regression theorem the second-order perpendicular and parallel cw correlation functions in Eq. (5.8) and (5.9) can be analytically solved [48]. To evaluate these equations the constituent parts are independently found, firstly finding the excited steady state population $\langle \sigma^\dagger\sigma \rangle_{ss} = \lim_{t\to\infty} \mathrm{Tr}_S[\sigma^\dagger\sigma(e^{\mathcal{L}t}\rho_S(0))] = \frac{S}{1+S}$, where initially the system is populated is in the ground state. The first order correlation function present in $g^{(2)}_{\parallel_{CW}}(\tau)$ is found to be $\lim_{t\to\infty} \langle \sigma^\dagger(t+\tau)\sigma(t) \rangle = \lim_{t\to\infty} \mathrm{Tr}_S[\sigma^\dagger e^{\mathcal{L}\tau}\sigma(e^{\mathcal{L}t}\rho_S(0))] = \frac{S}{1+S} e^{-\frac{1}{2}(\Gamma_1(1+S)+2\gamma)|\tau|}$. Finding lastly, $\lim_{t\to\infty} \langle \sigma^\dagger(t)\sigma^\dagger(t+\tau)\sigma(t+\tau)\sigma(t) \rangle = \lim_{t\to\infty} \mathrm{Tr}_S[\sigma^\dagger\sigma e^{\mathcal{L}\tau}\sigma(e^{\mathcal{L}t}\rho_S(0))\sigma^\dagger] = \frac{S^2}{(1+S)^2}(1 - e^{-(1+S)\Gamma_1|\tau|})$. Putting these evaluated correlation functions together the parallel polarisation alignment second order correlation function is

$$g^{(2)}_{CW}(\tau) = \big(1 - \frac{1}{2}e^{-(1+S)\Gamma_1|\tau|} - \frac{1}{2}e^{-(\Gamma_1(1+S)+2\gamma)|\tau|}\big), \tag{5.28}$$

and the perpendicular measurement, corresponding to fully distinguishable photon inputs is

$$g^{(2)}_{\perp_{CW}}(\tau) = \big(1 - \frac{1}{2}e^{-(1+S)\Gamma_1|\tau|}\big). \tag{5.29}$$

Using these resultant correlation functions the numerator in Eq. (5.11) becomes

$$\int_0^\infty d\tau \lim_{t\to\infty} \left|\left\langle \sigma^\dagger(t+\tau)\sigma(t) \right\rangle\right|^2 / \left\langle \sigma^\dagger\sigma \right\rangle^2_{ss} = \frac{1}{\Gamma_1(1+S)+2\Gamma_1}. \tag{5.30}$$

Similarly, for the denominator of Eq. (5.11), we find

$$\int_0^\infty d\tau\, 1 - \lim_{t\to\infty} \left\langle \sigma^\dagger(t)\sigma^\dagger(t+\tau)\sigma(t+\tau)\sigma(t) \right\rangle / \left\langle \sigma^\dagger\sigma \right\rangle^2_{ss} = \frac{1}{\Gamma_1(1+S)}. \tag{5.31}$$

Substituting these into Eq. (5.11) we find for a two–level system

$$\tilde{\mathcal{I}}_{2LS}(S) = \frac{\Gamma_1(1+S)}{\Gamma_1(1+S)+2\gamma}. \tag{5.32}$$

In the limit of $S \to 0$ the full photon wavepacket indistinguishability found from the pulsed case $\tilde{\mathcal{I}}_{2LS}(S\to 0) = \frac{\Gamma_1}{\Gamma_1+2\gamma} = \mathcal{I}$ is recovered. Considering the case of differing driving strengths for measurements with the parallel (S_1) and perpendicular (S_2) alignment we find

$$\tilde{\mathcal{I}}_{2LS}(S_1, S_2) = \frac{\Gamma_1(1+S_2)}{\Gamma_1(1+S_1)+2\gamma} + \frac{S_2 - S_1}{1+S_1}. \tag{5.33}$$

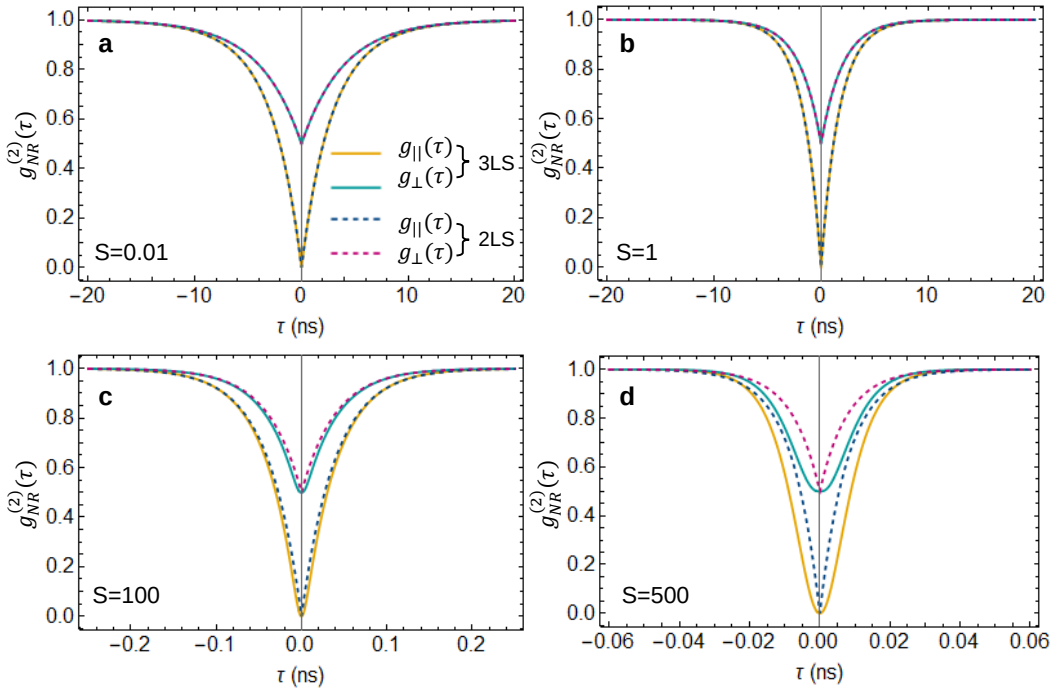

Figure 5.8: $g^{(2)}_{\perp/\|_{CW}}(\tau)$ calculations from the three–level system and effective two–level system models for varying driving strengths with saturation parameters, (a) $S = 0.01$, (b) $S = 1$, (c) $S = 100$, (d) $S = 500$. DBT dephasing parameters used to calculate these plots are $\Gamma_1 = 2\pi \times 40\,\text{MHz}$ and $\Gamma_2 = 2\pi \times 35\,\text{MHz}$.

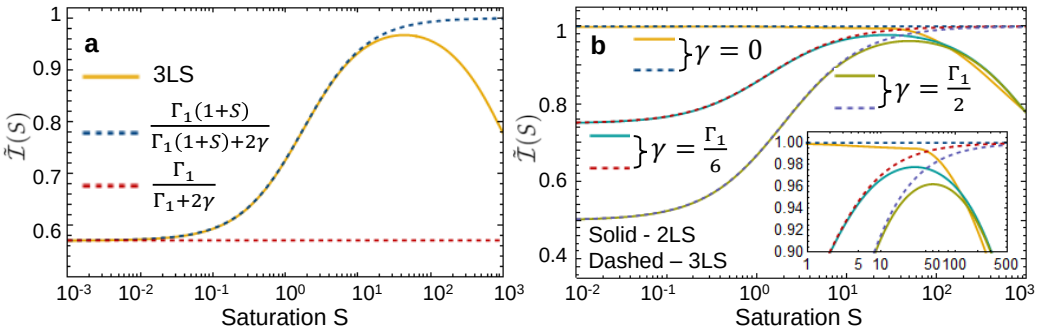

Figure 5.9: (a) Indistinguishability calculated from the three–level system coherent model (solid yellow line). The analytic form of $\tilde{\mathcal{I}}(S)$ from an effective non–resonantly driven two-level system dashed blue. Red line shows full photon wave packet indistinguishability using the parameters of the experimentally measured molecule giving $\mathcal{I} = 57\%$. (b) Calculation of $\tilde{\mathcal{I}}(S)$ for the coherently driven non–resonant three–level system and the effective incoherently driven two–level system for different pure dephasing parameters γ. Inset highlights the range where divergence between the two models occur.

Numerical calculations of $g^{(2)}_{\perp_{CW}}(\tau)$ and $g^{(2)}_{CW}(\tau)$ for both the two– and three–level system models are shown in Fig. 5.8, where the driving strength is varied from weak $S = 0.01$ to strong $S = 500$. The parameters for these calculations are the same as presented for the pulsed case above with, $\Gamma_1 = 2\pi \times 40\,\text{MHz}$ and the dephasing rate $\Gamma_2 = 2\pi \times 35\,\text{MHz}$. It can be seen that the models diverge for strong driving, which for our system parameters is around $S = 100$.

To compare calculations of $\mathcal{I}(S)$ for the two– and three–level system models to the indistinguishability of the TLS, see Fig. 5.9a. It can be seen that for strong driving the effective two–level system model breaks down by diverging from the three–level system and the analytical form for $\tilde{\mathcal{I}}_{2LS}(S)$ is no longer valid. To investigate for what S this break down occurs $\tilde{\mathcal{I}}(S)$ is plotted for varying $\mathcal{I}_{ZPL}$, see Fig 5.9b. For the case of maximum indistinguishability $\mathcal{I}_{ZPL} = 1$ the function $\tilde{\mathcal{I}}(S)$ deviates between the two level and three level system models by 0.5 % at $S = 23.3 \pm 0.1$, for the DBT system parameters. For decreasing $\mathcal{I}$, corresponding to an increase in pure dephasing, the break down value of S increases, where for $\mathcal{I} = 0.5$, a deviation of 0.5 % occurs at $S = 40.03 \pm 0.1$. The observed shift in the breakdown of the two-level system model can be explained by looking at Eq. (5.25), as when the excess pure dephasing becomes non-negligible this acts to suppress the saturation parameter present in this equation.

The origin for this deviation stems from including the pump level in the system. By driving to the pump level coherently the possibility for coherent exchange between the ground and pump level is captured in the model, which in turn acts to suppress $\tilde{\mathcal{I}}(S)$. To see how the states

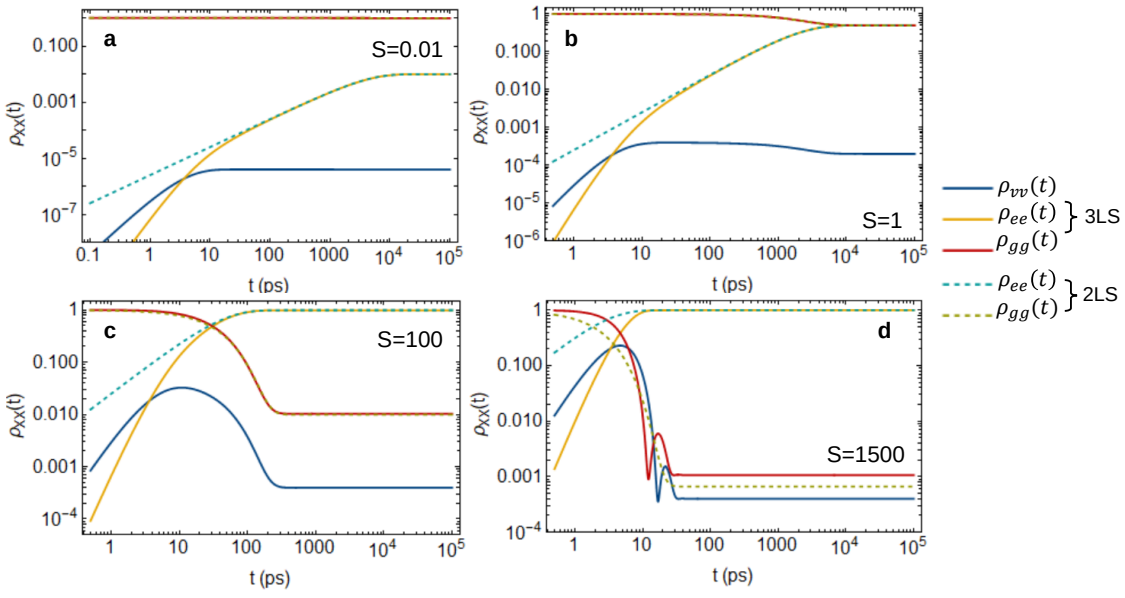

Figure 5.10: Evolution of the states given by $\rho_{XX}(t) = \langle X|\rho(t)|X\rangle$ for both the coherently driven three level system and the effective two level system model for various driving strengths, modified by the saturation parameter S. The initial offset for $t < 50$ ps between the two models for the excited state is due to some proportion of the population residing in the vibrational level for the three level system model.

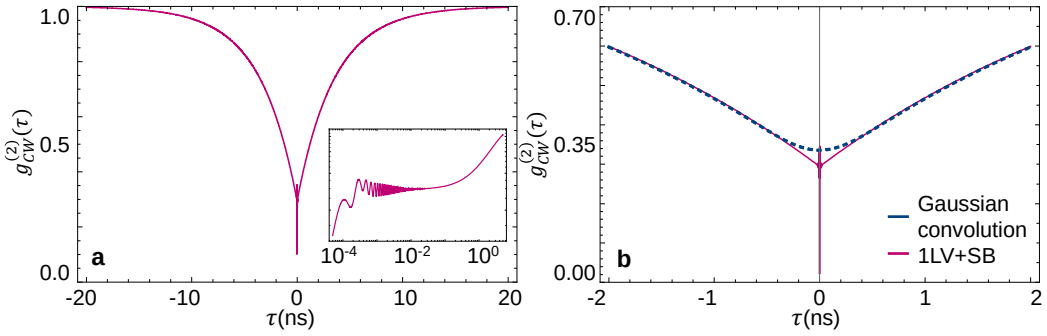

Figure 5.11: (a) Continuously driven $g^{(2)}_{CW}(\tau)$ with an emitter capturing a phonon sideband at 4.4 K and one local vibrational mode at detuning energy 21.5 meV with an indistinguishability of $\mathcal{I} = 0.27$. Inset shows log scale of feature around $\tau = 0$. (b) Convolution of $g^{(2)}_{CW}(\tau)$ with Gaussian kernel with standard deviation of 0.3 ns to model detector jitter in dashed blue, purple solid line shows unconvolved $g^{(2)}_{CW}(\tau)$.

evolve in the three– and two– levels systems models see Fig. 5.10, where this coherent exchange can been seen for strong driving with $S = 1000$. From this analysis it has been concluded that to extract the indistinguishability from a cw measurement using $\tilde{\mathcal{I}}_{2LS}(S)$ in Eq. (5.32) one must not pump too hard $S \lesssim 23$ for DBT parameters to ensure coherence effects between the ground and pump level can be neglected.

5.2.3.1 Inclusion of decoherence effects in cw

Until now we have neglected any effect from phonon sidebands or localised vibrational modes for a cw measurement. This methodology to find indistinguishability can be readily extended to capture the influence of both decoherence effects, similar to what was found for the pulsed case by substituting in either $E(t) \propto \sigma(t)B_-(t)$ or $E(t) \propto \sigma_\alpha(t)B_-(t)$. Taking the assumption that both the sideband and localised vibrational modes are purely decoherent gives

$$\tilde{\mathcal{I}}_{SB}(S) \approx \langle B \rangle^4 \frac{\int d\tau \lim_{t\to\infty} \left| \langle \sigma^\dagger(t+\tau)\sigma(t) \rangle \right|^2 / \langle \sigma^\dagger\sigma \rangle^2_{ss}}{\int d\tau (1 - \lim_{t\to\infty} \langle \sigma^\dagger(t)\sigma^\dagger(t+\tau)\sigma(t+\tau)\sigma(t) \rangle / \langle \sigma^\dagger\sigma \rangle^2_{ss})}, \tag{5.34}$$

and

$$\tilde{\mathcal{I}}_{SB+LV}(S) \approx \langle B \rangle^4 \left[\prod_i \langle \mathcal{A}_i \rangle^4 \right] \times \frac{\int d\tau \lim_{t\to\infty} \left| \langle \sigma^\dagger(t+\tau)\sigma(t) \rangle \right|^2 / \langle \sigma^\dagger\sigma \rangle^2_{ss}}{\int d\tau (1 - \lim_{t\to\infty} \langle \sigma^\dagger(t)\sigma^\dagger(t+\tau)\sigma(t+\tau)\sigma(t) \rangle / \langle \sigma^\dagger\sigma \rangle^2_{ss})}, \tag{5.35}$$

respectively. See Fig. 5.11 for calculation of Eq. (5.35) with one vibrational mode and a continuous phonon sideband, where the parameters are taken from the characterisation of the

molecule analysed in chapter 4 and shown in Appendix (A.2). The addition of the local vibrational mode creates an oscillation that can be seen in the inset of Fig. 5.11a similar to the pulsed case. Note that with a realistic detector the temporal resolution is unlikely to resolve this feature and therefore instead would raise the dip, to model this see Fig. 5.11b where the $g^{(2)}_{CW}(\tau)$ function is convolved with a Gaussian kernel of standard deviation 0.3 ns. The experimentally observed rising of the dip at $g^{(2)}_{CW}(0)$ does indeed reflect a drop in two–phonon interference, however it is important to note that the height of measured dip does not allow one to quantify indistinguishability.

5.2.4 Experimental details

Experimental characterisation of the DBT molecule examined in this work is taken out by Alex S. Clark's group at Imperial college London with Ross C. Schofield, Kyle D. Major and Rowan A. Hoggarth. The emission wavelength of this DBT molecule zero phonon line (ZPL) was found to be 784.45 nm from emission spectra measurements. In the experimental set up the emission from the DBT molecule is filtered with a 0.15 nm notch reflection filter, which at 4.7 K the proportion of emission into the ZPL is $\eta = 99.7\%$ removing the vast majority of the phonon sideband influence and all local vibrational modes. Power line scans were taken of across the ZPL, following the same methodology to the results presented in Fig. 4.8, gave the dephasing rate $\Gamma_2 = 2\pi \times 35 \pm 4$ MHz. The spontaneous decay rate was found from a Hanbury Brown and Twiss $g^{(2)}_{HBT}(\tau)$ measurement and to be $\Gamma_1 = 2\pi \times 40 \pm 2$ MHz, further details of the experimental characterisation of this molecule are shown in [104]. Negating

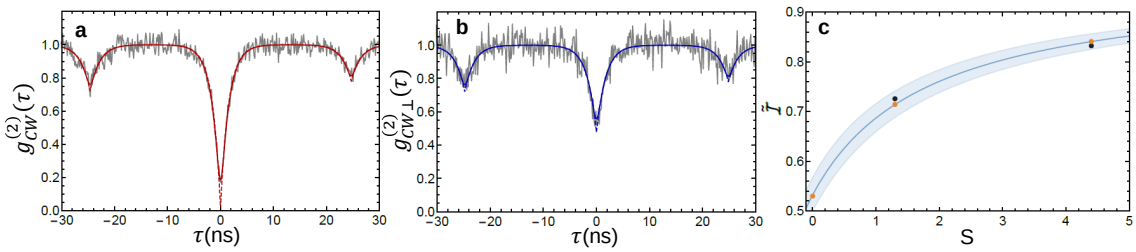

Figure 5.12: (a) Second order correlation measurement of a DBT molecule under non–resonant continuous wave (cw) excitation with parallel alignment between input arms. Raw data (grey) is shown overlaid with fitted model (dashed red line), and this convolved with the detector response function (solid red line). The features at $\tau = \pm 25$ ns are due to antibunching. (b) Second order correlation measurement with perpendicular alignment between input arms. Fitted model (dashed blue line) and convolved function (solid blue line). (c) Shows Eq. (5.10) as a function of saturation measurements (solid line), with the shaded region coming from uncertainties in the fit for Γ_1 and Γ_2 of the DBT molecule. Data points are from using measurements of $g^{(2)}_{CW}(\tau)/g^{(2)}_{CW_\perp}(\tau)$ to calculate Eq. (5.10) where, integration of the data is given by (black points) and fitted functions (orange points). The data point at $S = 0$ is from pulsed measurements shown in [104] and is $\mathcal{I} = 0.53 \pm 0.01$.

sideband decoherence effects the ZPL indistinguishability can be predicted from these decay rates from Eq. (3.62) to give $\mathcal{I}_{ZPL} = \Gamma_1/2\Gamma_2 = 0.57$. For the following calculations the both the spontaneous decay and pure dephasing rate, γ, are fixed to model this DBT molecule, where γ is extracted from $\gamma = \Gamma_2 - \frac{\Gamma_1}{2} = 2\pi \times 15\,\mathrm{MHz}$.

To experimentally verify this method to extract indistinguishability, measurements of non–resonant cw second order correlation function for parallel and perpendicular alignment have be taken, see figure. 5.12. The $g^{(2)}_{CW}(\tau)$ parallel measurement shows both anti–bunching and two–photon interference from the HOM dip at $\tau = 0$. For the perpendicular measurements only anti–bunching is observed as there is negligible interference. Fitting the cw parallel and perpendicular measurements by taking into account for the relative reflection/transmission (r/t) coefficients of two fibre 50:50 beam splitters that make up the interferometer in Fig. 5.1 with the equation

$$\begin{aligned} g^{(2)}_{||/\perp_{CW}}(\tau) = 1 - \frac{\mathcal{V}}{(r_1^2t_0^2 + r_0^2t_1^2)(r_0^2r_1^2 + t_0^2t_1^2)}\Big(& r_1^2t_1^2(r_0^4 + t_0^4)e^{(-\Gamma_1(1+S)|\tau|)} \\ &+ \mathcal{M}_{||/\perp} 2r_0^2r_1^2t_0^2t_1^2e^{(-(\Gamma_1(1+S)+2\gamma)|\tau|)} \\ &+ r_0^2r_1^4t_0^2e^{(-\Gamma_1(1+S)(|\tau - d\tau|))} \\ &+ r_0^2t_1^4t_0^2e^{(-\Gamma_1(1+S)(|\tau + d\tau|))}\Big), \end{aligned} \tag{5.36}$$

which is similar to that found in [98], however is adapted to include driving. The term for visibility $\mathcal{V}$ has been phenomenologically introduced, which takes account of the background and light from other emitters; in the prior formalism this is intrinsically 1 as only one emitter is considered. The term $\mathcal{M}$ is also introduced which is defined as the auxiliary modal overlap and accounts for non-temporal decoherence effects, such as an incoherent sideband and polarization drift. The subscripts 0 and 1 represent the first and second beam splitters, respectively, where an independent characterisation of the interferometer found, $t_0 = \sqrt{0.501(1)}$, $t_0 = \sqrt{0.499(1)}$, $r_1 = \sqrt{0.482(1)}$ and $t_1 = \sqrt{0.518(1)}$. The time difference between interferometer arms is $d\tau$ and can be found from the time difference in the side features giving 24.75 ns. Now looking at the the terms in Eq. (5.36), the first two terms correspond to the central dip around $\tau = 0$ contributing to the anti-bunching and indistinguishability, respectively, The final two terms corresponds to the anti-bunching features which arise from the time delay in one of the interferometer path around $\tau = \pm 25\,\mathrm{ns}$, noting for a HOM experiment with with two separate emitters the satellite dips would not present due to the lack of any time delay in the system.

Fig. 5.12c shows both calculation of $\tilde{\mathcal{I}}$ from integrating both the raw data (black points) and the fitted functions (orange points). For a known saturation S the indistinguishability from a non–resonant cw experiment can be found directly using Eq. (5.33). For the case of unknown S but known relative pump powers one can take multiple measurements of $g^{(2)}_{CW}(\tau)$ and $g^{(2)}_{\perp_{CW}}(\tau)$

and calculate $\tilde{\mathcal{I}}(S)$ from the the integrals of $\int_0^\infty d\tau(1 - g^{(2)}_{CW}(\tau))$ and $\int_0^\infty d\tau(1 - g^{(2)}_{\perp_{CW}}(\tau))$ in present in Eq. (5.10) and extrapolate back to ($S = 0$) leaving the true indistinguishability.

When undertaking a single source HOM experiment using either pulsed or non–resonant cw excitation, the indistinguishability measured is typically expected to decrease with an increasing optical delay line. This drop off in $\mathcal{I}$ is due to spectral wandering which is more commonly present in quantum dots and NV centers. For longer optical delay lines, the higher the optical depth leading to more time for spectral wandering to occur and decohere the interfering photons. This motivates keeping the optical delay line to a minimum. A direct advantage for cw measurement over pulsed excitation here, is that there is no longer a requirement for the interferometer delay to be set to match the laser repetition period. Finally, noting that for two separate interfering single photon emitters any spectral wandering is completely uncorrelated and no optical delay line is required for the experimental set up.

In contrast to pulsed excitation, determining indistinguishability from a non–resonant continuous driving regime requires multiple measurements at unknown pump powers, or a single measurement at a known S, due to the dependence of the correlation functions on the driving of the system. A benefit of having a method to extract $\mathcal{I}$ from a cw measurement is that it can be found from raw data - independent of the ratio of source lifetime to laser repetition rate. Moreover, cw excitation leads to higher count rates and greater spectral selectivity.

5.3 Resonant driving

Turning attention to finally the regime of resonant driving, which directly probes the exciton and results in fundamentally different physics compared to the non–resonant case. For weak resonant excitation one can achieve coherent scattering, whereas for strong driving a Mollow triplet can be seen in the emission spectra [35, 61]. Moreover, it has been found that driving on resonance can increase the coherence time of an emitter which can aid in reaching the radiative lifetime limit [49, 76].

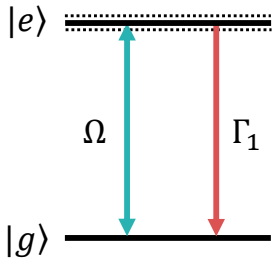

Figure 5.13: Schematic diagram of Resonant driving from the ground $|g\rangle$ to the first excited state $|e\rangle$, modelled by coherent driving with the Rabi frequency Ω. Spontaneous emission from the excited state $|e\rangle$ is given by Γ_1 and pure dephasing is given by γ.

To capture the regime of resonant driving we consider the second–order Born–Markov master equation for a resonantly driven two–level system given by

$$\partial_t \rho(t) = -i[H_S, \rho] + \Gamma_1 \mathcal{L}_\sigma[\rho(t)] + 2\gamma \mathcal{L}_{\sigma^\dagger\sigma}[\rho(t)], \tag{5.37}$$

with $H_S = \frac{\Omega}{2}(\sigma^\dagger + \sigma)$ the system driving term with Rabi frequency Ω. See Fig. 5.13 for visual representation of this system. Note that Eq. (5.37) is just a simplified version of the driven second–order master equation shown in Eq. (4.54) which accounts for both a longitudinal acoustic phonon sideband and N local vibrational modes.

Considering first the generalised case of a TLS with electric field operator $E(t) \propto \sigma(t)$, substituting this into Eq. (3.55) and taking $t \to \infty$ gives

$$\begin{aligned} G^{(2)}_{CW_{RES}}(\tau) = \frac{1}{2}\lim_{t\to\infty}\Big(&\left\langle \sigma^\dagger(t)\sigma^\dagger(t+\tau)\sigma(t+\tau)\sigma(t)\right\rangle - \left|\left\langle \sigma^\dagger(t)\sigma(t+\tau)\right\rangle\right|^2 \\ &+ 2\,\mathrm{Re}\Big[\langle\sigma\rangle_{ss}\left(\left\langle \sigma^\dagger(t)\sigma^\dagger(t+\tau)\sigma(t+\tau)\right\rangle - \left\langle \sigma^\dagger(t)\sigma^\dagger(t+\tau)\sigma(t)\right\rangle\right)\Big] \\ &- \left|\left\langle \sigma^\dagger(t)\sigma^\dagger(t+\tau)\right\rangle\right|^2 + \left\langle \sigma^\dagger\sigma\right\rangle^2_{ss}\Big). \end{aligned} \tag{5.38}$$

It can be seen that for this driving regime there are more terms that must be considered when comparing to the case of continuous wave non–resonant excitation. Normalising this function with $\left\langle E^\dagger(t)E(t)\right\rangle \left\langle E^\dagger(t+\tau)E(t+\tau)\right\rangle$ which for a driven HOM experiment gives

$$g^{(2)}_{CW_{RES}}(\tau) = \frac{G^{(2)}_{CW_{RES}}(t,\tau)}{\langle\sigma^\dagger\sigma\rangle^2_{ss} - |\langle\sigma_{ss}\rangle|^4}. \tag{5.39}$$

In an attempt to follow the same methodology to extract the indistinguishability as is been done from a continuous wave non–resonant excitation measurement we require the correlation function resulting from perpendicular alignment of the interferometer arms i.e. when input fields are orthogonal, which is

$$G^{(2)}_{CW_{RES,\perp}}(\tau) = \frac{1}{2}\lim_{t\to\infty}\Big(\left\langle \sigma^\dagger(t)\sigma^\dagger(t+\tau)\sigma(t+\tau)\sigma(t)\right\rangle + \left\langle \sigma^\dagger\sigma\right\rangle^2_{ss}\Big). \tag{5.40}$$

Normalising this function with orthogonal input fields by evaluating Eq. (3.54) gives

$$g^{(2)}_{CW_{RES,\perp}}(\tau) = \frac{G^{(2)}_{CW_{RES,\perp}}(t,\tau)}{\langle\sigma^\dagger\sigma\rangle^2_{ss}}. \tag{5.41}$$

Due to the presence of coherent driving in the system, even under very weak driving $\Omega = 5\times10^{-6}$ ps evaluating Eq. (5.10) gives $\tilde{\mathcal{I}} = 0.557$ which doesn't quite tend to $\mathcal{I} = 0.571$. For increasing driving strength the value of $\tilde{\mathcal{I}}$ increases and well surpasses 1, unlike the non–resonant case, where this increase is due to the coherent exchange present in the driven system. From this analysis it can be concluded that to extract the full photon wave packet indistinguishability from cw measurement, it is best to work under non–resonant excitation.

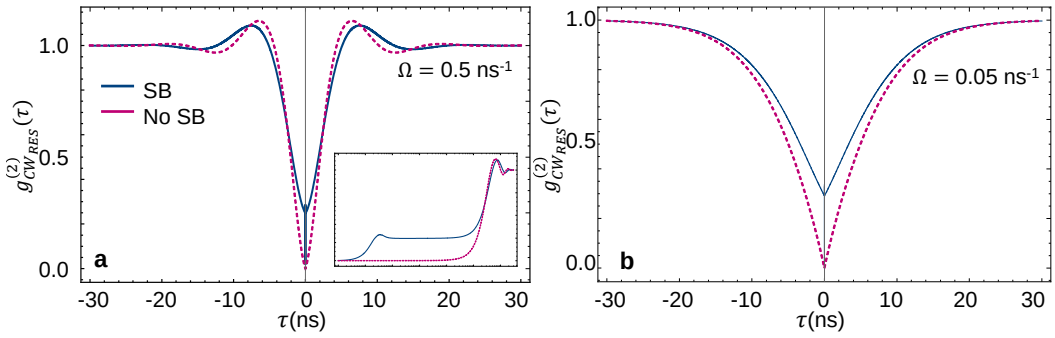

Figure 5.14: Resonant driving HOM calculation with (blue solid) and without (purple dashed) the LA continuous sideband, (a) strong driving with $\Omega = 0.5\,\mathrm{ns}^{-1}$ and (b) weak driving with $\Omega = 0.05\,\mathrm{ns}^{-1}$. Parameters for both simulations are $\Gamma_1 = 2\pi \times 40\,\mathrm{MHz}$ and $\gamma = 2\pi \times 15\,\mathrm{MHz}$, with sideband parameters taken from the analysis of the molecule in chapter 4, which are $\xi = (8.6 \pm 0.6)\,\mathrm{ps}^{-1}$ and $\alpha = (0.009 \pm 0.001)\,\mathrm{ps}^2$.

Including now the effects of coupling to a continuous thermal phonon bath, by firstly using the master equation model shown in Eq. (4.54) and removing any influence of the localised vibrational modes, as these can be filtered out. Substituting in $E(t) \propto \sigma(t)B_-(t)$ into Eq. (3.55), factorising the photonic and phonon correlation functions due to largely differing time scales and finding the steady state we find

$$\begin{aligned} G^{(2)}_{CW_{RES}}(\tau) = \frac{1}{2}\lim_{t\to\infty}\Big(&\left\langle \sigma^\dagger(t)\sigma^\dagger(t+\tau)\sigma(t+\tau)\sigma(t)\right\rangle - |\mathcal{G}(\tau)|^2\left|\left\langle \sigma^\dagger(t)\sigma(t+\tau)\right\rangle\right|^2 \\ &+ 2\,\mathrm{Re}\Big[\langle\sigma\rangle_{ss}\langle B\rangle^2\Big(\left\langle \sigma^\dagger(t)\sigma^\dagger(t+\tau)\sigma(t+\tau)\right\rangle - e^{2\,\mathrm{Im}[\phi(\tau)]}\left\langle \sigma^\dagger(t)\sigma^\dagger(t+\tau)\sigma(t)\right\rangle\Big)\Big] \\ &- \left|\langle B\rangle^2 e^{-\phi^*(\tau)}\right|^2\left|\left\langle \sigma^\dagger(t)\sigma^\dagger(t+\tau)\right\rangle\right|^2 + \left\langle \sigma^\dagger\sigma\right\rangle^2_{ss}\Big). \end{aligned} \tag{5.42}$$

where the phonon correlation functions, $\langle B_+B_+(\tau)\rangle = \langle B\rangle^2 e^{-\phi^*(\tau)}$, $\langle B_+B_+(\tau)B_-(\tau)\rangle = \langle B\rangle$ and $\langle B\rangle^{-1}\langle B_+B_+(\tau)B_-\rangle = e^{2\,\mathrm{Im}[\phi(\tau)]}$ which have been found using section (2.2.2.2), where the equation for $\phi(\tau)$ is found in Eq. (2.47). Normalising Eq. (5.42) in the usual way we find

$$g^{(2)}_{CW_{RES_{SB}}}(\tau) = \frac{G^{(2)}_{CW_{RES_{SB}}}(t,\tau)}{\langle\sigma^\dagger\sigma\rangle^2_{ss} - |\langle\sigma_{ss}\rangle|^4}. \tag{5.43}$$

A comparison of the TLS model with the inclusion/exclusion of the phonon sideband is shown in Fig. 5.14a and b, where both strong $\Omega = 0.5\,\mathrm{ns}^{-1}$ and weak $\Omega = 0.05\,\mathrm{ns}^{-1}$ driving strengths are simulated, respectively. For the strong driving case in Fig. 5.14a Rabi oscillations can be observed, similar to the results found for driven Hanbury Brown and Twiss intensity correlation functions in section (4.4), the inclusion of the sideband using the polaron frame approach renormalises the observed oscillation period by $\Omega_R = \langle B\rangle\,\Omega$, where this can be directly seen in the overlap of the two models. As previously discussed the HOM dip at zero time delay is dependent on the temporal detector resolution, where for a perfect

detector $g^{(2)}(0) = 0$ irrespective on the photon properties. For a realistic detector the HOM dip with indistinguishable photons should resolve the suppression close to zero however the resolution should be taken into consideration before making conclusions regarding photon properties. When considering the finite detector resolution, phonon relaxation processes such as the inclusion of continuous sideband or localised vibrational modes also act to increase the appearance of the dip at $\tau = 0$ as these occur on very short time scales (picoseconds). See the inset of Fig. 5.14a for a log–scale of the effect of the phonon sideband.

5.4 Chapter Summary

In this chapter calculations of second order correlation functions from a Hong–Ou–Mandel set up are found for differing driving regimes. The first regime considered is pulsed excitation, where calculations of full photon wavepacket indistinguishability are derived with the inclusion of non–temporal decoherence effects such as a continuous longitudinal acoustic sideband and localised vibrational modes.

In the theory presented, calculations of second order correlation functions of a single molecule emitter under continuous non–resonant coherent driving to a higher lying vibrational state is found using an open quantum systems model, where this is captured using a three–level system model. This higher energy state is then adiabatically eliminated to form an effective two–level system which allows for a novel derivation of an analytical expression to readily extract the photon indistinguishability; where a suitable parameter range for disregarding the coherent effects has been determined. The extraction method detailed in this chapter has been verified experimentally, using a single DBT emitter under cryogenic temperatures. This approach provides a tool for finding two–photon interference properties which is independent on the detector resolution, unlike the well referred HOM dip $g^{(2)}(0)$ value, or without the need for post-selecting on a given time window [49].

In the latter part of this chapter the regime of resonant cw driving has been explored which directly probes the exciton and holds interesting physics such as the observation of Rabi oscillations. It has been concluded that in order to extract indistinguishability only a non–resonant cw measurement is suitable. Moreover, the effect of including a continuous longitudinal sideband on the second order correlation measurement has been simulated.

Future work expanding on this research includes looking into interference effects from two separate quantum emitters, which has been experimentally demonstrated with diamond quantum dots [34, 89], defect centres [7, 107], and molecules [66]. The theory presented in this chapter could be straightforwardly modified to account for multiple sources and in doing so would include further parameters such as different central frequencies and differing dephasing rates of the two emitters. Moreover, this theoretical treatment could be readily expanded to considering the effects of optical cavities on photon emission as the derivations use a master

equation approach [55]. This model could be readily expanded to account for the affects of driving on these systems, and could include further parameters such as different central frequencies and dephasing rates of the two emitters used.

CHAPTER 6

SINGLE MOLECULES IN PHOTONIC STRUCTURES

Coherent single photon emission from solid–state platforms are predominately limited by temperature dependent phonon dephasing. For single molecules of dibenzoterrylene (DBT) doped in an anthracene (Ac) environment, this dephasing originates from both thermal bath phonons from the crystal environment and local vibrational modes from the DBT molecule. To enhance the indistinguishability of single photon emission from solid–state deterministic sources a few options are possible. The most straightforward measure is to cool down the source, as this suppresses the number of possible phonons modes that are excited. However, it has been found that by cooling alone, even taking the limit of 0 K, does not completely eliminate the possibility of phonon mode excitation leading to a phonon sideband, as it directly overlaps the zero phonon line [55]. Other approaches include, coupling the emission to a waveguide filter or directly filtering the emission, which can remove a fraction of the phonon sideband effects increasing the total coherent fraction [46, 70, 114]. Alternatively, the emitter can be coupled to a cavity, which can enhance the coherent fraction of emission and suppress emission outside cavity resonance [97, 116, 117]. In this chapter the latter two effects are explored, where two different filters are investigated and the corresponding indistinguishability and collection/detection efficiency are calculated. The filter transmission profiles presented in this chapter have been measured by collaborator Ross C. Schofield at Imperial College London. A derivation of a single DBT molecule coupled to a generic one–sided single moded cavity is detailed, where optimal cavity parameters are predicted which reflect an optical mirco–cavity and provide the maximum indistinguishability. In this work a novel numerical technique to efficiently calculate an emitters optical properties using matrix diagonalisation is developed, where this methodology has been adapted from Jake Iles–Smith's work.

6.1 Filtering molecule emission

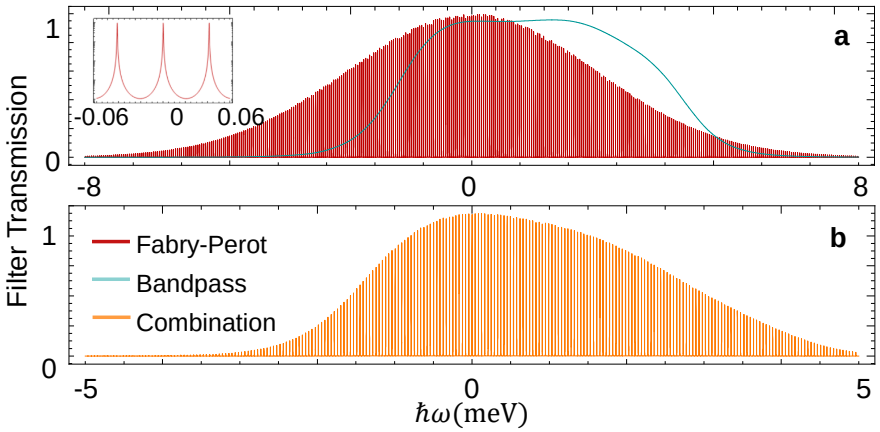

Figure 6.1: (a) The filter transmission of a $785 \pm 3nm$ bandpass filter and a Fabry-Perot filter with free spectral range (FSR) of 10GHz and width of 67MHz, which gives a finesse ($\mathcal{F}$) of 150. (b) Filter transmission profile of both the bandpass filter and Fabry–Perot filter.

In this section the effect on filtering molecule emission is explored. Two filters are modelled, the first is a 785 ± 3 nm bandpass filter (BP) with the measured transmission profile $f_{\mathrm{BP}}(\omega, \omega_0)$ and central frequency ω_0. The second is looking at the effect of combining this bandpass filter with a Fabry–Perot filter (FP) with a free spectral range (FSR) of 10 GHz, a width of ~ 67 MHz, giving a finesse ($\mathcal{F}$) of 150. The spectral profile of the Fabry-Perot filter is given by

$$f_{\mathrm{FP}}(\omega) = \exp\left[-\frac{\omega^2}{2\sigma^2}\right] \frac{1}{1 + (4\mathcal{F}^2/\pi^2)\sin[2\pi\omega/(2\mathrm{FSR})]^2}, \tag{6.1}$$

where the 'teeth' profile is tapered by a 3 nm Gaussian filter width given by the exponential function. Both filter profiles are shown in Fig. 6.1.

6.1.1 Filtering theory

All of the results presented in this section build upon the model presented in chapter 4, which includes a zero phonon line, pure dephasing and broad sideband, where the vibrational peaks are omitted as these are filtered out by the bandpass filter. To find the maximum indistinguishability achieved from these filters, first an investigation into the optimal alignment of the bandpass filter is completed as the measured transmission profile does not follow a Gaussian distribution. When considering the indistinguishability from a filtered quantum emitter it is advantageous to write it in terms of the emission spectra by taking the Fourier transform of Eq. (3.60) we find

$$\mathcal{I} = \frac{\int_{-\infty}^{\infty} d\omega \int_{-\infty}^{\infty} d\nu |S_{\mathrm{D}}(\omega, \nu)|^2}{\left(\int_{-\infty}^{\infty} d\omega S_{\mathrm{D}}(\omega, \omega)\right)^2}, \tag{6.2}$$

where the subscript D represents the detected emission which for the bandpass filtered emission is $S_{\mathrm{D}}(\omega,\nu) = f_{\mathrm{BP}}(\omega,\omega_0)f^*_{\mathrm{BP}}(\nu,\omega_0)S(\omega,\nu)$. This resultant filtered emission spectra has been found using the convolution theorem as it is in the frequency domain, using

$$\mathcal{F}[x * y] = \mathcal{F}[x]\mathcal{F}[y], \tag{6.3}$$

where $\mathcal{F}[\cdot]$ represents a Fourier transform. Noting that if this function were to be evaluated in the time domain the integrals would be much more involved due to the filtering functions [31]. The two–color unfiltered emission spectrum introduced here is given by $S(\omega,\nu) = s(\omega,\nu) + s^*(\nu,\omega)$ with

$$s(\omega,\nu) = \int_0^\infty dt \int_0^\infty d\tau \left\langle E^\dagger(t+\tau)E(t)\right\rangle e^{i\omega(t+\tau)}e^{-i\nu t}. \tag{6.4}$$

For the model in consideration the electric field operator is $E(t) = \sqrt{\frac{\Gamma_1}{2\pi}}\sigma(t)B_-(t)$; which has been derived in section (3.2.2). To calculate indistinguishability from Eq. (6.2) the quantum regression theorem is used to find the correlation functions and the integrals are found numerically. Varying the position of this bandpass filter and calculating $\mathcal{I}$, it has been found that a detuning of $\hbar\omega_0 = -1.58\,\mathrm{meV}$ gives the maximum indistinguishability, see Fig. 6.2a. The payoff for this maximum comes at the drop in collection efficiency. To compare this for the case where the BP filter transmission is close to its maximum, calculations for the filter centered on zero detuning are also found, see Fig. 6.1. By setting the bandpass filter detuning to zero, the drop in indistinguishability at 4.5 K is minimal at $\Delta\mathcal{I} = 0.02$, whereas a vast improvement in collection efficiency is found from $(\eta_f = 0.347 \rightarrow \eta_f = 0.703)$, using the relation

$$\eta_f = \frac{\mathrm{P_D}}{\mathrm{P}}, \tag{6.5}$$

where $\mathrm{P} = \int_{-\infty}^{\infty} d\omega S(\omega,\omega)$ is the power into the unfiltered emission spectra. To find the indistinguishability of the filtered emission with both the BP and FP filter, the required detected

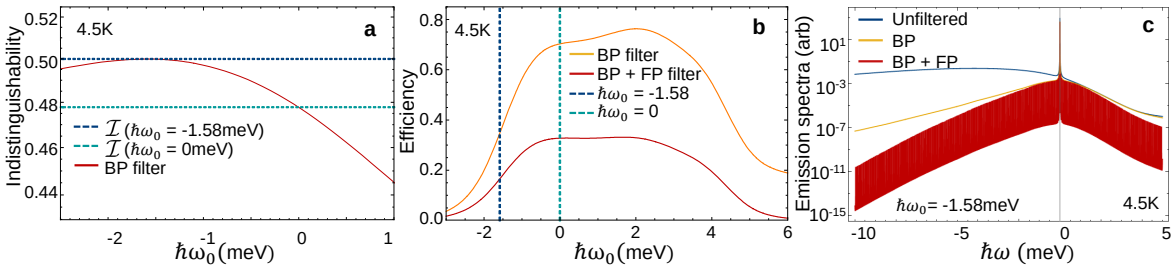

Figure 6.2: (a) Indistinguishability of emission at 4.5 K filtered by the bandpass filter as a function of its detuning position (blue solid line). The maximum indistinguishability is shown in dashed red. (b) Efficiency of the filtered emission with the bandpass filter (orange solid) and both bandpass and Fabry–Perot filter (red solid). The blue dashed line highlights the efficiency when choosing the detuning position which provides maximum indistinguishability. (c) Emission spectra for the unfiltered case and filtered case with the bandpass filter and both band pass filter and Fabry–Perot filter at 4.5 K.

emission is $S_D(\omega,\nu) = f_{FP}(\omega)f^*_{FP}(\nu)f_{BP}(\omega,\omega_0)f^*_{BP}(\nu,\omega_0)S(\omega,\nu)$. See Fig. 6.2b for efficiency of the filters as a function of the BP detuning offset. For simulations of the filtered emission spectra using the bandpass offset of $\hbar\omega_0 = -1.58\,\text{meV}$ see Fig. 6.2c.

6.1.2 Filtering results

The indistinguishability for the case of filtering the DBT emission with both the bandpass filter and the Fabry-Perot filter centered on the ZPL is shown in comparison to no filtering for various temperatures in Fig. 6.3a with different BP offsets. For calculations of collection efficiency for both filtering setups see Fig. 6.3b. For both results the dashed lines show a detuning of $\hbar\omega_0 = -1.58\,\text{meV}$, whereas the solid lines show the offset $\hbar\omega_0 = 0\,\text{meV}$. At 2.5 K an indistinguishability of $\mathcal{I} = 0.988$ is found with an filtering efficiency of $\eta_f = 0.435$, using the bandpass filter at zero offset. For the case of unfiltered emission with no local vibrational modes this is a significant improvement from $\mathcal{I} = 0.503$, where this dephasing predominately stems from the phonon sideband. Optimising the bandpass filter offset to achieve maximum indistinguishability using $\hbar\omega_0 = -1.58\,\text{meV}$, shows negligible improvement to $\mathcal{I}$ with the presented precision with the addition of the Fabry–Perot filter. At 2.5 K all offsetting the bandpass filter achieves is a drop in the filtering efficiency to $\eta_f = 0.220$. This confirmed when using a bandpass filter in conjunction with a fine tooth filter it is beneficial to maximise efficiency over indistinguishability.

When considering the unfiltered ZPL emission only the indistingusihability at 2.5 K is predicted to be $\mathcal{I}_{ZPL} = \frac{\Gamma_1}{2\Gamma_2} = 0.977$ where the temperature dependent pure dephasing relationship found in section (4.2.2.2) has been used. For the case of zero detuned bandpass filter at 4.5 K,

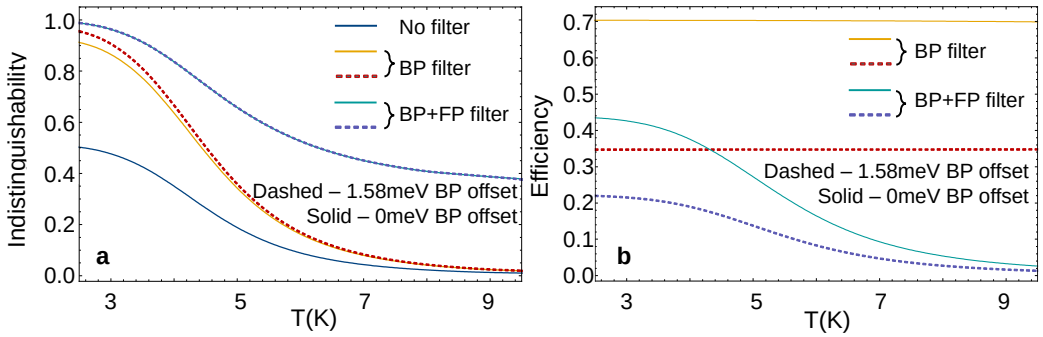

Figure 6.3: (a) Indistinguishability vs temperature for a DBT molecule unfiltered (solid dark blue), filtered with a bandpass filter (BP) (yellow and dashed red) centered with different offsets and finally, filtered with both the bandpass filter and a Fabry–Perot (FP) filter (turquoise and dashed purple). (b) Collection efficiency vs temperature with either the bandpass filter only (yellow and dashed red lines) or a combination with the Fabry–Perot filter (turquoise and dashed purple). For both plots solid lines show results for $\hbar\omega_0 = -0\,\text{meV}$ BP filter offset and dashed lines show $\hbar\omega_0 = -1.58\,\text{meV}$ BP offset.

the FP and BP filtered value drop to $\mathcal{I} = 0.745$, with an filtering efficiency of $\eta_f = 0.329$; where the decrease in efficiency is due to a larger fraction of emission going into the continuous sideband.

From this work it has been found that filtering a DBT emitter in the cryogenic limit alone can produce photons with close to unity indistinguishability. To capture the effects of a waveguide filter the calculations presented in this section can be directly used to model such structures. Modifications to this model involve changing the filter profile to match the waveguide in question, similar to what was done in reference [55]. In the next section a DBT molecule coupled to an optical cavity will be considered. The motivation for this work is to explore how a cavity can enhance and manipulate the molecules emitted electromagnetic field.

6.2 Cavity quantum electrodynamics

Now turning attention to a more involved approach to modify the emission from a quantum emitter, the optical cavity. In this section, calculations of indistinguishability and efficiency of a single molecule coupled to a single moded one–sided cavity with linewidth κ_c and frequency ω_c are detailed. This general description of a cavity can be used to capture various infrastructures, as different parameters model different architectures. The architecture that will be the focus of this work is an optical micro–cavity, which is an ideal candidate for DBT operating at low cryogenic temperatures in the lifetime limit, as it functions within the weak coupling limit yet hosts a sharp cavity linewidth which can suppresses the vast majority of the phonon sideband.

In the model presented for this work, the molecule is described as in chapter 4, which has a zero phonon line with temperature dependent pure dephasing, a broad phonon sideband and N local vibrational modes. This system is then coupled to a single sided single moded cavity and a master equation in the polaron picture is derived. Initially, calculations including one local vibrational mode are considered and the effect of setting the cavity resonance over this mode is qualitatively explored.

To predict values such as indistinguishability and efficiency of the cavity emission, all local modes are omitted from this model due the associated peaks sitting far from cavity resonance leading to their strong suppression. Finally, optimal values of the cavity are found for considering solely the DBT zero phonon line, due to a novel computational method which leads to high computational efficiencies.

6.2.1 Cavity model

To describe the interaction between a single emitter and a single mode cavity the following minimal coupling Hamiltonian under the dipole approximation [110], is required

$$H_{\mathrm{CAV-TLS}} = -\mathbf{d} \cdot \mathbf{E}_{CAV}, \tag{6.6}$$

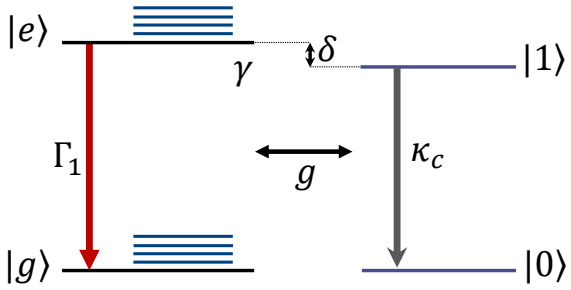

Figure 6.4: Schematic energy diagram of a single molecule with spontaneous decay rate Γ_1, localised vibrational modes (given in blue) and some pure dephasing defined by rate γ coupled to a single sided single moded cavity with coupling strength g and cavity linewidth κ_c. The energy difference between the cavity resonance and two–level system is given by δ.

where as in section (3.1) $\mathbf{d}$ is the dipole dot operator which in terms of the single emitter basis is $\mathbf{d} = \mathbf{d}_{ge}\sigma + \mathbf{d}_{eg}\sigma^\dagger$ with the dipole moment $\mathbf{d}_{ge} = \langle g|\mathbf{d}|e\rangle$, $\mathbf{d}_{eg} = \mathbf{d}_{ge}^\dagger$ and dipole operator $\sigma = |g\rangle\langle e|$. The single mode cavity field in this equation is given by

$$\mathbf{E}_{CAV} = -\mathbf{e}\Big(\frac{\hbar\omega_c}{\epsilon_0 V_M}\Big)^{1/2}(a^\dagger + a), \tag{6.7}$$

where $\mathbf{e}$ is a polarisation vector, V_M is the cavity mode volume and ϵ_0 is the permittivity of free space [39]. The cavity frequency is ω_c and the (creation) annihilation operators for the bosonic cavity mode are $(a^\dagger)a$. Finding this interaction Hamiltonian from these vectors gives

$$H_{\text{CAV}-\text{TLS}} = \hbar g(\sigma^\dagger + \sigma)(a + a^\dagger), \tag{6.8}$$

where the term g describes a coupling strength given by

$$g = \frac{1}{\hbar}\sqrt{\frac{\hbar\omega_c}{2\epsilon_0 V_M}}\, d_{ge}, \tag{6.9}$$

noting that $g \sim \sqrt{\frac{1}{V_M}}$, indicating that the smaller the cavity mode volume the stronger the coupling strength. Upon expansion of Eq. (6.8) the terms σa and $\sigma^\dagger a^\dagger$ are far off–resonance as they represent TLS relaxation with photon annihilation and TLS excitation with photon production, respectively. Neglecting these terms leads to

$$H_{\text{CAV}-\text{TLS}} = \hbar g(\sigma^\dagger a + \sigma a^\dagger). \tag{6.10}$$

This expression is valid below ultra–strong coupling: a regime in which the non–resonant terms cannot be neglected and where the coupling strength is comparable to either the TLS or cavity resonance frequencies [52]. In this thesis the ultra–strong regime is not of interest leading to the safe application of Eq. (6.10).

The emitter modelled in this section is a single molecule captured by a zero phonon line, continuous sideband and N local vibrational modes (LVM). Now defining the full Hamiltonian

to describe this single molecule emitter coupled to a single moded one sided cavity as [55],

$$H = H_{\mathrm{S}} + H_{\mathrm{I}}^{\mathrm{EM}} + H_{\mathrm{I}}^{\mathrm{PH-TLS}} + H_{\mathrm{I}}^{\mathrm{PH-LV}} + H_{\mathrm{E}}, \tag{6.11}$$

where the schematic state diagram corresponding to this system is shown in Fig. 6.4. The complete free–system term is given by

$$H_{\mathrm{S}} = E_{\mathrm{X}}\sigma^{\dagger}\sigma + \hbar\omega_c a^{\dagger}a + \hbar g(\sigma^{\dagger}a + \sigma a^{\dagger}) + \hbar\sum_{i=1}^{N}[\Delta_i \alpha_i^{\dagger}\alpha_i + \eta_i\sigma^{\dagger}\sigma(\alpha_i^{\dagger} + \alpha_i)], \tag{6.12}$$

where this term describes the TLS with energy splitting E_{X} coupled to the single cavity mode. The LVMs are described by the (creation) annihilation operators $(\alpha_i^{\dagger})\ \alpha_i$ with energy splitting Δ_i and coupling strength η_i. The phonon–TLS and phonon–LVM interaction terms are equivalent to that in section (4.2) with $H_{\mathrm{I}}^{\mathrm{PH-TLS}} = H_{\mathrm{L}}^{\mathrm{PH}} + H_{\mathrm{Q}}^{\mathrm{PH}}$ containing both linear and quadratic interaction terms and $H_{\mathrm{I}}^{\mathrm{PH-LV}} = \hbar\sum_{i,\mathbf{q}}^{N}(h_{i,\mathbf{q}}\alpha_i d_{\mathbf{q}}^{\dagger} + \mathrm{h.c.})$ which couples the localised vibrational modes to the thermal phonon bath with coupling strength $h_{i,\mathbf{q}}$. The electromagnetic interaction terms are given by

$$\begin{aligned} H_I^{EM} &= H_I^{EM-TLS} + H_I^{EM-CAV} \\ &= \hbar\sum_l (p_{l,\mathrm{L}}\sigma c_{l,\mathrm{L}}^{\dagger} + p_{l,\mathrm{L}}^{*}\sigma^{\dagger}c_{l,\mathrm{L}}) + \hbar\sum_l (p_{l,\mathrm{D}}a^{\dagger}c_{l,\mathrm{D}} + p_{l,\mathrm{D}}^{*}ac_{l,\mathrm{D}}^{\dagger}), \end{aligned} \tag{6.13}$$

which couples the EM field to both the cavity mode and the TLS which is described by the detected (D) and lost (L) modes. The final term is the environment Hamiltonian given by $H_{\mathrm{E}} = \hbar\sum_k \omega_k b_k^{\dagger}b_k + \hbar\sum_{l,\mu}\nu_{l,\mu}c_{l,\mu}^{\dagger}c_{l,\mu}$.

6.2.1.1 Polaron transformation

In the following section two successive polaron transformations, as detailed in section (4.2.1), are performed on this cavity QED master equation model. The first transformation is between the TLS and thermal phonon bath, which requires finding $H_{\mathrm{P1}} = U_{\mathrm{P1}}HU_{\mathrm{P1}}^{\dagger}$ with $U_{\mathrm{P1}} = \sigma\sigma^{\dagger} + \sigma^{\dagger}\sigma B_{+}$ and $B_{\pm} = e^{\pm\sum_{\mathbf{k}}\frac{g_{\mathbf{k}}}{\omega_{\mathbf{k}}}(b_{\mathbf{k}}^{\dagger} - b_{\mathbf{k}})}$. The second polaron transformation between the TLS and local vibrational modes requires $H_{\mathrm{P}} = U_{\mathrm{P2}}H_{\mathrm{P1}}U_{\mathrm{P2}}^{\dagger}$ where $U_{\mathrm{P2}} = |g\rangle\langle g| + |e\rangle\langle e|\prod_i \mathcal{A}_i$ with $\mathcal{A}_i = \exp[\frac{\eta_i}{\Delta_i}(\alpha_i^{\dagger} - \alpha_i)]$. Performing both transformations leads to the complete polaron frame Hamiltonian given by

$$\begin{aligned} H_{\mathrm{P}} = E_{\mathrm{P}}\sigma^{\dagger}\sigma + \hbar\omega_c a^{\dagger}a + \hbar g(\sigma^{\dagger}aB_{+} + \sigma a^{\dagger}B_{-}) + \hbar\sum_{i=1}^{N}\Delta_i\alpha_i^{\dagger}\alpha_i \\ + H_{\mathrm{I,P}}^{\mathrm{EM-TLS}} + H_{\mathrm{I}}^{\mathrm{CAV-EM}} + H_{\mathrm{Q}}^{\mathrm{PH}} + H_{\mathrm{E}}, \end{aligned} \tag{6.14}$$

where $E_{\mathrm{P}} = E_{\mathrm{X}} - \hbar(\sum_i^N \eta_i^2/\Delta_i + \sum_{\mathbf{k}} g_{\mathbf{k}}^2/\omega_{\mathbf{k}})$. We find the polaron frame EM–TLS term in the form

$$H_{\mathrm{I,P}}^{\mathrm{EM-TLS}} = \hbar\sum_l (p_{l,L}\sigma_{\alpha}c_{l,L}^{\dagger}B_{-} + p_{l,L}^{*}\sigma^{\dagger}c_{l,L}B_{+}), \tag{6.15}$$

where the linear electron–phonon interaction $H_{\mathrm{L}}^{\mathrm{PH}}$ has been rotated out. The final three terms in Eq. (6.14) are unchanged. The second polaron transformation between the TLS and LVMs dresses the dipole operators to give $\sigma_\alpha = \sigma \prod_i \mathcal{A}_i$ with $\mathcal{A}_i = \exp[\frac{\eta_i}{\Delta_i}(\alpha_i^\dagger - \alpha_i)]$.

Similar to the case of driving the emitter in section (4.4.1), the CAV–TLS interaction term from the system Hamiltonian reflects a system–environment interaction as it has a non–zero expectation value with respect to the thermal state ρ_{E} such that, $\mathrm{Tr}_E[\sigma a^\dagger B_- + \sigma^\dagger a B_+] = \langle B \rangle (\sigma a^\dagger + \sigma^\dagger a)$ [83]. To resolve this, the following change of variables is used $\mathcal{X} = (\sigma a^\dagger + \sigma^\dagger a)$, $\mathcal{Y} = i(\sigma a^\dagger - \sigma^\dagger a)$ and the terms $B_x = \frac{1}{2}(B_+ + B_- - 2\langle B \rangle)$ and $B_y = \frac{i}{2}(B_+ - B_-)$ are defined. Making these change of variables this gives the resultant system term to be

$$H_{\mathrm{S,P}} = E_{\mathrm{P}} \sigma^\dagger \sigma + \hbar g \langle B \rangle \mathcal{X} + \hbar \omega_c a^\dagger a + \hbar \sum_{i=1}^{N} \Delta_i \alpha_i^\dagger \alpha_i, \tag{6.16}$$

with an additional phonon–system interaction term in the form

$$H_{\mathrm{I}}^{\mathrm{PH-SYS}} = g(\mathcal{X} B_x + \mathcal{Y} B_y). \tag{6.17}$$

6.2.1.2 Cavity master equation

To investigate the dynamics from this model a second order Born–Markov master equation is derived following on from section (2.1.4); re-expressed here for clarity as

$$\partial_t \rho_{\mathrm{S}}(t) = -\frac{i}{\hbar}[H_S, \rho_{\mathrm{S}}(t)] - \Phi[\rho_{\mathrm{S}}(t)]. \tag{6.18}$$

with the integral

$$\Phi[\rho_{\mathrm{S}}(t)] = -\frac{1}{\hbar^2} \int_0^t d\tau Tr_E \Big([H_I, [\tilde{H}_I(-\tau), \rho_{\mathrm{S}}(t) \rho_{\mathrm{E}}]] \Big). \tag{6.19}$$

Now solving the dissipators for each Hamiltonian interaction terms.

6.2.1.3 Spontaneous emission dissipator

Firstly solving for the EM–TLS dissipator by moving $H_{\mathrm{I,P}}^{\mathrm{EM-TLS}}$ found in Eq. (6.13) into the interaction picture by

$$\begin{aligned} \tilde{H}_{I,P}^{EM-TLS}(-\tau) &= \exp\big[-iH_0\tau/\hbar\big]\sigma_\alpha \exp\big[iH_0\tau/\hbar\big] C_L^\dagger(-\tau) B^\dagger(-\tau) + h.c., \\ &\approx \sigma_\alpha(-\tau) C_L^\dagger(-\tau) B^\dagger(-\tau) + h.c., \end{aligned} \tag{6.20}$$

where $H_0 = H_{\mathrm{S,P}} + H_{\mathrm{E}}$. The time evolved dressed dipole operator in this equation is $\sigma_\alpha(-\tau) = \sigma e^{-i\omega_{\mathrm{P}}\tau} \mathcal{A}(-\tau)$, where $\omega_{\mathrm{P}} = E_{\mathrm{P}}/\hbar$ is the polaron shifted energy splitting and $\mathcal{A}(-\tau) = \exp\Big[-\sum_i \frac{\eta_i}{\Delta_i}(\alpha^\dagger e^{-i\Delta_i\tau} - \alpha e^{i\Delta_i\tau})\Big]$. This approximation to find the last line in Eq. (6.20) holds as long as $g\langle B \rangle < E_{\mathrm{P}} \sim 1.5\,\mathrm{eV}$. The time evolved environment terms $B(-\tau) = e^{\sum_k \frac{g_k}{\omega_k}(b_k^\dagger e^{-i\omega_k\tau} - b_k e^{i\omega_k\tau})}$

and $C_{\mathrm{L}}(-\tau) = \sum_l p_{l,\mathrm{L}} c_{l,\mathrm{L}} e^{i\nu_l \tau}$ have been introduced for clarity. Solving for Eq. (6.18), the result is equivalent to the to the dissipator solved in section (4.2.2.1), leading to

$$\mathcal{D}_{EM}[\rho_{\mathrm{S}}(t)] = \Gamma_1 \mathcal{L}_{\sigma_\alpha}[\rho_{\mathrm{S}}(t)], \tag{6.21}$$

with Γ_1, the spontaneous emission rate of the lost emission from the TLS, found from assuming a flat EM–TLS spectral density such that, $J_{\mathrm{EM,L}}(E_{\mathrm{P}}) \approx \Gamma_1/(2\pi)$ where $\mathrm{Tr}_E(C_{\mathrm{L}} C_{\mathrm{L}}^\dagger(-\tau)\rho_{\mathrm{E}}) = \int_0^\infty d\omega J_{\mathrm{EM,L}}(\omega) e^{i\omega\tau}$.

6.2.1.4 Cavity emission dissipator

Finding the EM–CAV dissipator by moving $H_{\mathrm{I}}^{\mathrm{EM-CAV}}$ found in Eq. (6.13) into the interaction picture gives

$$\begin{aligned} \tilde{H}_{\mathrm{I}}^{\mathrm{EM-CAV}}(-\tau) &= \exp\big[-iH_0\tau\big] a \exp\Big[iH_0\tau\Big] C_{\mathrm{D}}(-\tau) + h.c., \\ &\approx a e^{i\omega_c \tau} C_{\mathrm{D}}(-\tau) + h.c., \end{aligned} \tag{6.22}$$

with $C_{\mathrm{D}}(-\tau) = \sum_l p_{l,\mathrm{D}} c_{l,\mathrm{D}}^\dagger e^{i\nu_l\tau}$ and this approximation assumes renormalised cavity coupling strength is less than the cavity resonance such that $g\langle B\rangle < \omega_c$. Following the usual procedure by inserting the expressions for $H_{\mathrm{I}}^{\mathrm{EM-CAV}}$ and $\tilde{H}_{\mathrm{I}}^{\mathrm{EM-CAV}}(-\tau)$ into the master equation integral in Eq. (6.19), and applying the commutation relation from Eq. (4.16) we find

$$\begin{aligned} \mathrm{Re}\Big[\Phi_{CAV}[\rho_{\mathrm{S}}(t)]\Big] &= \mathrm{Re}\Big[\int_0^t d\tau Tr_E\Big([H_{\mathrm{I}}^{\mathrm{EM-CAV}}, [\tilde{H}_{\mathrm{I}}^{\mathrm{EM-CAV}}(-\tau), \rho_{\mathrm{S}}(t)\rho_{\mathrm{E}}]]\Big)\Big], \\ &= \int_0^t d\tau \chi_{\mathrm{D}}(\tau)(a^\dagger a \rho_{\mathrm{S}}(t) - a^\dagger \rho_{\mathrm{S}}(t) a) + h.c., \end{aligned} \tag{6.23}$$

where $\chi_{\mathrm{D}}(\tau) = \mathrm{Tr}_E(C_{\mathrm{D}} C_{\mathrm{D}}^\dagger(-\tau)\rho_{\mathrm{E}}) = \int_0^\infty J_{\mathrm{EM,D}}(\omega) e^{-i\omega\tau}$ is the photon correlation function for the detected cavity modes. Noting that only the real part of the integral has been explicitly evaluated as the imaginary part of this integral renormalises the system Hamiltonian and therefore resides in the commutator of Eq. (6.18). Similarly to the EM-TLS case we assume a flat EM-CAV spectral density such that, $J_{\mathrm{EM,D}}(\omega_c) \approx \kappa_c/(2\pi)$, where κ_c is the cavity decay rate. As the real part of $\Phi_{CAV}[\rho_{\mathrm{S}}(t)]$ is equal to the dissipator, we can write

$$\mathcal{D}_{CAV}[\rho_{\mathrm{S}}(t)] = \kappa_c \mathcal{L}_a[\rho_{\mathrm{S}}(t)]. \tag{6.24}$$

6.2.1.5 System–phonon dissipator

To solve the system–phonon dissipator the Hamiltonian decomposition method presented in section (2.1.4.2) is used, as the interaction Hamiltonian $H_{\mathrm{I}}^{\mathrm{PH-SYS}}$ cannot be moved into the interaction picture by unitary transformation. This method first involves first expressing the interaction Hamiltonian in the form

$$H_{\mathrm{I}}^{\mathrm{PH-SYS}} = g(\mathcal{X} \otimes B_x + \mathcal{Y} \otimes B_y). \tag{6.25}$$

Moving into the interaction picture, the system operators transform using a Fourier decomposition giving $\mathcal{X}(-\tau) = \sum_\xi e^{i\xi\tau}\mathcal{X}(\xi)$ and $\mathcal{Y}(-\tau) = \sum_\xi e^{i\xi\tau}\mathcal{Y}(\xi)$. In the interaction picture the environment operators transform to $\tilde{B}_{x\backslash y}(-\tau) = e^{-iH_E\tau/\hbar}B_{x\backslash y}e^{iH_E\tau/\hbar}$. Finding the environment correlation functions from Eq. (2.22) by substituting in the phonon operators to find

$$C_{xx}(\tau) = \frac{\langle B\rangle^2}{2}(e^{\phi(\tau)} + e^{-\phi(\tau)} - 2), \tag{6.26}$$

and

$$C_{yy}(\tau) = \frac{\langle B\rangle^2}{2}(e^{\phi(\tau)} - e^{-\phi(\tau)}), \tag{6.27}$$

with $C_{xy}(\tau) = C_{yx}(\tau) = 0$ as presented in section (4.4.1.1). Next evaluating the dissipator by forming the response functions from Eq. (2.25) giving, $K_{xx}(\xi)$ and $K_{yy}(\xi)$ using $C_{xx}(\tau)$ and $C_{yy}(\tau)$ and substituting these into Eq. (6.19) and taking the real part to give the driving dissipator

$$\begin{aligned}\mathrm{Re}\left[\Phi_{\mathrm{PH}}[\rho_{\mathrm{S}}(t)]\right] &= \mathcal{D}_{\mathrm{PH}}[\rho_{\mathrm{S}}(t)],\\ &= -\frac{1}{2}g^2\Big(\sum_\xi \gamma_{xx}(\xi)[\mathcal{X},\mathcal{X}(\xi)\rho_{\mathrm{S}}(t) - \rho_{\mathrm{S}}(t)\mathcal{X}^\dagger(\xi)]\\ &\quad - \sum_\xi \gamma_{yy}(\xi)[\mathcal{Y},\mathcal{Y}(\xi)\rho_{\mathrm{S}}(t) - \rho_{\mathrm{S}}(t)\mathcal{Y}^\dagger(\xi)]\Big),\end{aligned} \tag{6.28}$$

where the imaginary part of this integral is a Lamb shift term which further renormalises the system Hamiltonian.

The final two dissipators originate from the interaction terms $H_{\mathrm{I}}^{\mathrm{PH-LV}}$ and $H_{\mathrm{Q}}^{\mathrm{PH}}$, where the derivation of these dissipators can be found in sections (4.2.2.3) and (4.2.2.2). Putting together all of the dissipators the final cavity QED master equation is

$$\begin{aligned}\partial_t\rho_{\mathrm{S}}(t) = &-i[\delta a^\dagger a + g\langle B\rangle\mathcal{X},\rho_{\mathrm{S}}(t)] + \Gamma\mathcal{L}_\sigma[\rho_{\mathrm{S}}(t)] + \kappa_c\mathcal{L}_a[\rho_{\mathrm{S}}(t)] + \mathcal{D}_{\mathrm{PH}}[\tilde{\rho}(t)]\\ &+ 2\gamma(T)\mathcal{L}_{\sigma^\dagger\sigma}[\rho_{\mathrm{S}}(t)] + \sum_i\Big(-i\Delta_i[\alpha_i^\dagger\alpha_i,\rho(t)] + \Gamma_{i,+}\mathcal{L}_{\alpha^\dagger}[\rho(t)] + \Gamma_{i,-}\mathcal{L}_a[\rho(t)]\Big),\end{aligned} \tag{6.29}$$

where this form is in a rotating frame which removes the term $-i[E_{\mathrm{P}}\sigma^\dagger\sigma + H_{LS},\rho_{\mathrm{S}}(t)]$ and represents the system energy as a function of δ, the cavity detuning energy. The term H_{LS} is the final contribution from the Lamb shift energy which for atomic–like system can be neglected [15].

6.2.2 Cavity enhanced emission spectra

To find the emission spectrum from an emitter coupled to a cavity, it is important to consider both the emission into the detected cavity mode and the lost modes. In order to capture the continuous sideband this involves finding the solution to the Heisenberg equations of motion for both the lost and detected electric field operators as well as the cavity mode operator itself.

The electric field operator for the lost and detected modes are $E_\lambda(t) = \sum_l c_{l,\lambda}(t)$, where $c_{l,\lambda}(t)$ is the electric field annihilation operator in the Heisenberg picture with, $\lambda = \{\mathrm{L}, \mathrm{D}\}$. Expanding the Heisenberg equations of motion $\dot{c}_{l,\lambda}(t) = \frac{i}{\hbar}[H_\mathrm{P}(t), c_{l,\lambda}(t)]$, where $H_\mathrm{P}(t)$ is the time evolved full polaron transformed Hamiltonian. For the case of lost or detected electromagnetic modes we find

$$\dot{c}_{l,\mathrm{L}}(t) = -i\nu_l c_{l,\mathrm{L}}(t) - ip_{l,\mathrm{L}}\sigma_\alpha(t)B_-(t), \tag{6.30}$$

$$\dot{c}_{l,\mathrm{D}}(t) = -i\nu_l c_{l,\mathrm{D}}(t) - ip^*_{l,\mathrm{D}}a(t). \tag{6.31}$$

For the case of the cavity modes this requires finding $\dot{a}(t) = -i[H_\mathrm{P}(t), a(t)]$ which gives

$$\dot{a}(t) = -i\sum_l p_{l,\mathrm{D}}c_{l,\mathrm{D}}(t) - i\omega_c a(t) - ig\sigma_\alpha(t)B_-(t). \tag{6.32}$$

First solving the equation of motion for the lost modes in Eq. (6.30) by using the product rule and the Fourier variable $\tilde{c}_{l,\mathrm{L}}(\nu) = \int_{-\infty}^{\infty} dt c_{l,\mathrm{L}}(t)e^{i\omega t}$, as was done in section (3.1), we find

$$\tilde{c}_{l,\mathrm{L}}(\nu) = \frac{p_{l,\mathrm{L}}\Xi(\nu)}{(\nu - \nu_l)}, \tag{6.33}$$

where $\Xi(\nu) = \int_{-\infty}^{\infty} dt\sigma_\alpha(t)B_-(t)e^{i\nu t}$. Summing over the lost modes to find the electric field operator giving $\tilde{E}_\mathrm{L}(\nu) = \sum_l \tilde{c}_{l,\mathrm{L}}(\nu) = \sum_l \frac{p_{l,\mathrm{L}}}{(\nu-\nu_l)}\Xi(\nu)$. Next taking the continuum limit and invoking a relation from the *Kramers-Kronig* derivation $\rightarrow \mathcal{P}\int_{-\infty}^{\infty} d\omega \frac{p_\mathrm{L}(\omega)}{(\nu-\omega)} = -i\pi p_\mathrm{L}(\nu) \approx -i\sqrt{\frac{\Gamma_1}{2\pi}}$, where we have assumed the photonic spectral density to be flat such that $J_{\mathrm{EM,L}}(\nu) = \sum_l |p_{l,\mathrm{L}}|^2\delta(\nu - \nu_l) \approx \Gamma_1/(2\pi)$ and $J_{\mathrm{EM,L}}(\nu) = \pi^2|p_\mathrm{L}(\nu)|^2$. Now Fourier transforming back to the time domain to give $E_\mathrm{L}(t) = \sqrt{\Gamma_1/(2\pi)}\sigma_\alpha(t)B_-(t)$, where the vacuum contribution has been set to zero.

For the detected EM field using the Fourier variable methodology we find

$$\tilde{c}_{l,\mathrm{D}}(\nu) = \frac{p^*_{l,\mathrm{D}}\tilde{a}(\nu)}{(\nu - \nu_l)}, \tag{6.34}$$

where $\tilde{a}(\nu) = \int_{-\infty}^{\infty} dt a(t)e^{i\nu t}$. To find the cavity mode operator by first putting Eq. (6.34) into Eq. (6.32) and therefore requiring $\sum_l \frac{|p_{l,\mathrm{D}}|^2}{\nu-\nu_{l,\mathrm{D}}}$ to be evaluated, such that $\mathcal{P}\int_{-\infty}^{\infty} d\omega \frac{J_{\mathrm{EM,D}}(\nu)}{\omega-\nu} = -i\pi J_{\mathrm{EM,D}}(\omega) \approx -i\kappa_c/2$ as $J_{\mathrm{EM,D}}(\nu) \approx \kappa_c/(2\pi)$, putting this back into Eq. (6.32) to find

$$\tilde{a}(\nu) = \frac{ig\Xi(\nu)}{i(\nu - \omega_c) - \kappa_c/2}. \tag{6.35}$$

Finally, we find the detected electric field operator by substituting in $a(t)$ giving $\tilde{E}_\mathrm{D}(\nu) = \sum_l \tilde{c}_{l,\mathrm{D}}(\nu) = \sum_l \frac{p^*_{l,\mathrm{D}}}{(\nu-\nu_l)}\frac{ig\Xi(\nu)}{i(\nu-\omega_c)-\kappa_c/2}$. Taking the continuum limit and evaluating such that $\int_{-\infty}^{\infty} d\omega \frac{p^*_{l,\mathrm{D}}(\omega)}{(\nu-\omega)} = -i\pi p_\mathrm{D}(\nu) \approx -i\sqrt{\frac{\kappa_c}{2\pi}}$ as $J_{\mathrm{EM,D}}(\nu) = \pi^2|p_\mathrm{D}(\nu)|^2$. Putting this together to get the detected electric field operator in the frequency domain we find

$$\tilde{E}_\mathrm{D}(\nu) = \sqrt{\frac{4g^2}{\kappa_c\Gamma_1}}h_c(\nu)E_L(\nu), \tag{6.36}$$

where $h_c(\nu) = \frac{\kappa_c/2}{(i(\nu-\omega_c)-\kappa_c/2)}$ which resembles a Lorentizan filter function with detuning ω_c.

In order to calculate the detected cavity emission whilst capturing the phonon sideband it is not possible to directly use the cavity mode operator $\tilde{a}(\nu)$ when finding the first order correlation function. Instead the detected electric field operator $\tilde{E}_{\mathrm{D}}(\nu)$ can be used, which for the case of no phonon sideband effects and a single moded cavity the following correlation functions are equivalent as they can be exactly solved using quantum regression theorem giving the exact relationship

$$\frac{\kappa_c}{2\pi}\left\langle \tilde{a}^{\dagger}(\nu)\tilde{a}(\omega)\right\rangle = \frac{4g^2}{\kappa_c\Gamma_1}h_c^*(\omega)h_c(\nu)\frac{\Gamma_1}{2\pi}\left\langle \tilde{\sigma}_{\alpha}^{\dagger}(\nu)\tilde{\sigma}_{\alpha}(\omega)\right\rangle. \tag{6.37}$$

Here the pre–factor $F_{\mathrm{P}} = \frac{4g^2}{\kappa_c\Gamma_1}$ can be defined as a Purcell factor, which the regime of weak coupling this represents a measure of enhancement to the systems spontaneous decay rate, and in turn quantifies the enhancement/suppression of coherent emission. When considering the inclusion of the thermal phonon environment this relation becomes an approximation due to the phonon–system interaction dissipator in the master equation and therefore modelling the detected cavity emission in terms of the detected EM field $\tilde{E}_{\mathrm{D}}(\nu)$ is valid as long as the coupling to the phonon environment is weak [55].

6.2.2.1 Two–color emission

To calculate the indistinguishability and efficiency of the cavity enhanced emission, the emission spectrum for both the lost and detected modes is first required. To find these functions either $\tilde{E}_{\mathrm{L}}(t)$ or $\tilde{E}_{\mathrm{D}}(t)$ need to be substituted into Eq. (6.4) to find $S_{\mathrm{L/D}}(\omega,\nu) = s_{\mathrm{L/D}}(\omega,\nu) + s^*_{\mathrm{L/D}}(\nu,\omega)$ the full two–color lost/detected emission spectra. For the lost modes this gives

$$s_{\mathrm{L}}(\omega,\nu) = \frac{\Gamma_1}{2\pi}\int_0^{\infty}dt\int_0^{\infty}d\tau g^{(1)}(\tau,t)\mathcal{G}(\tau)e^{i\omega(t+\tau)}e^{-i\nu t}, \tag{6.38}$$

where $g^{(1)}(\tau,t) = \left\langle \sigma_{\alpha}^{\dagger}(t+\tau)\sigma_{\alpha}(t)\right\rangle$ is the first order correlation function of the dressed dipole system operators and $\mathcal{G}(\tau) = \langle B_+(t+\tau)B_-(t)\rangle$ is the phonon correlation function. The factorisation of these correlation functions is valid due to the varying time scales of the phonon relaxation ($\sim 1ps$) and photon emission ($\sim 1ns$). For the detected cavity emission it has been found

$$s_{\mathrm{D}}(\omega,\nu) = \frac{\Gamma_{\mathrm{D}}}{2\pi}h_c(\omega)^*h_c(\nu)\int_0^{\infty}dt\int_0^{\infty}d\tau g^{(1)}(\tau,t)\mathcal{G}(\tau)e^{i\omega(t+\tau)}e^{-i\nu t}, \tag{6.39}$$

where $\Gamma_{\mathrm{D}} = \frac{4g^2}{\kappa_c}$ has been defined.

To find the indistinguishability of the detected cavity emission Eq. (6.2) can be evaluated using Eq. (6.39), where the correlation function $g^{(1)}(\tau,t)$ can be numerically solved using quantum regression theorem as shown in section (3.1.2.1). For the cavity efficiency the fraction of power into the detected cavity mode over the total emission is required from

$$\eta_c = \frac{\mathrm{P_D}}{\mathrm{P_D}+\mathrm{P_L}}, \tag{6.40}$$

where $P_{\mathrm{L/D}} = \int_{\infty}^{\infty} d\omega S_{\mathrm{L/D}}(\omega, \omega)$.

6.2.2.2 Zero phonon line–cavity system

Simplifying the above theoretical model to consider a zero phonon line with some phenomenological pure dephasing coupled to the single moded one sided cavity the master equation in Eq. (6.29) becomes

$$\partial_t \rho_{\mathrm{S}}(t) = -ig[\mathcal{X}, \rho_{\mathrm{S}}(t)] + \Gamma \mathcal{L}_{\sigma}[\rho_{\mathrm{S}}(t)] + \kappa_c \mathcal{L}_a[\rho_{\mathrm{S}}(t)] + 2\gamma(T)\mathcal{L}_{\sigma^\dagger\sigma}[\rho_{\mathrm{S}}(t)]. \tag{6.41}$$

The other main difference in this simplified model is the derivation of the electric field operator for the lost and detected cavity emission; as all sideband effects are excluded from the system, the detected cavity emission can be directly found from the cavity annihilation/creation operators such that

$$s_{\mathrm{D}}(\omega, \nu) = \frac{\kappa_c}{2\pi} \int_0^{\infty} dt \int_0^{\infty} d\tau \left\langle a^\dagger(t+\tau)a(t) \right\rangle e^{i\omega(t+\tau)} e^{-i\nu t}. \tag{6.42}$$

The lost modes for the cavity–ZPL system are found from

$$s_{\mathrm{L}}(\omega, \nu) = \frac{\Gamma_1}{2\pi} \int_0^{\infty} dt \int_0^{\infty} d\tau g^{(1)}(\tau, t) e^{i\omega(t+\tau)} e^{-i\nu t}. \tag{6.43}$$

To find indistinguishability of this ZPL–cavity system it is no longer advantageous to calculate this value in the frequency domain as there are no effective filter functions present. Instead a matrix diagonalisation approach can be used which has been adapted from work originally developed by Jake Iles–Smith detailed below.

6.2.3 Correlation functions – diagonal method

In this section a method to solve a general first order correlation function using matrix diagonalisation is outlined. The development of this method is motivated by the increase computational complexity when dealing with large Hilbert space systems, such as, a cavity coupled emitter met with in this work. To begin, we define a general first order correlation function and its representation using the quantum regression theorem as

$$\begin{aligned} g^{(1)}(t, \tau) &= \left\langle O^\dagger(t+\tau)O(t) \right\rangle, \\ &= \mathrm{Tr}\left[O^\dagger e^{\mathcal{L}\tau} O e^{\mathcal{L}t} \rho(0) \right], \end{aligned} \tag{6.44}$$

with arbitrary Hilbert space system operator O with dimensions $d \times d$ and $\mathcal{L}$ is the Liouvillian master equation super operator with dimensions $d^2 \times d^2$. Moving now to Liouville space, with $|\cdot\rangle\rangle$ L-ket and L-bra $\langle\langle\cdot|$ notation defined as $\langle\langle A|B\rangle\rangle = \mathrm{Tr}\left[A^\dagger B\right]$ [82], where $\langle\langle A|$ is a vectorised form of the operator A with dimension d^2. Re-writing Eq. (6.44) in Liouville space gives

$$g^{(1)}(t, \tau) = \langle\langle O | e^{\mathcal{L}\tau} \tilde{O} e^{\mathcal{L}t} | \rho(0) \rangle\rangle, \tag{6.45}$$

where $\tilde{O} = O \otimes \mathbb{1}_d$. To diagonalise this function the diagonal form of the Liouvillian operator is first required from

$$\mathcal{L} = PDP^{-1}, \tag{6.46}$$

where P is a matrix of $\mathcal{L}$'s eigenvectors and D is a diagonal matrix of the corresponding eigenvalues. Substituting this equation into Eq. (6.45) we find

$$\begin{aligned} g^{(1)}(t,\tau) &= \langle\langle O|Pe^{D\tau}P^{-1}\tilde{O}Pe^{Dt}P^{-1}|\rho(0)\rangle\rangle, \\ &= \sum_{i,j} e^{(\lambda_i\tau+\lambda_j t)}A_{i,j}, \end{aligned} \tag{6.47}$$

with $A_{i,j} = \langle\langle O|P\mathcal{P}_iP^{-1}\tilde{O}P\mathcal{P}_jP^{-1}|\rho(0)\rangle\rangle$. To find the last line the relation $D = \sum_i \lambda_i |i\rangle \langle i| = \sum_i \lambda_i \mathcal{P}_i$ has been used where $\mathcal{P}_i = |i\rangle \langle i|$ is the projector of the eigenvectors and λ_i are the Liouvillian eigenvalues.

6.2.3.1 Emission properties

From this diagonal form of the first order correlation function the two–color emission spectra can be found from $S(\omega,\nu) = S(\omega,\nu) + S^*(\nu,\omega)$ where

$$\begin{aligned} S(\omega,\nu) &= \int_0^\infty dt \int_0^\infty d\tau g^{(1)}(t,\tau)e^{i\omega\tau}e^{i(\omega-\nu)t}, \\ &= \sum_{i,j} \frac{A_{i,j}}{(\lambda_i + i\omega)(\lambda_j + i(\omega-\nu))}. \end{aligned} \tag{6.48}$$

To simplify this further we can put this into matrix form, giving

$$S(\omega,\nu) = \mathbf{A}.\mathbf{M}(\omega,\nu) + \mathbf{A}^*.\mathbf{M}^*(\nu,\omega), \tag{6.49}$$

with $M_{i,j}(\omega,\nu) = \frac{1}{(\lambda_i+i\omega)(\lambda_j+i(\omega-\nu))}$.

To find the full–photon wavepacket indistinguishability in the time domain we require

$$\mathcal{I} = \frac{\int_0^\infty dt \int_0^\infty d\tau |\left\langle O^\dagger(t+\tau)O(t)\right\rangle|^2}{\int_0^\infty dt \int_0^\infty d\tau \left\langle O^\dagger(t+\tau)O(t+\tau)\right\rangle \left\langle O^\dagger(t)O(t)\right\rangle}. \tag{6.50}$$

Considering first the numerator and substituting in Eq. (6.47) we find

$$\begin{aligned} \int_0^\infty dt \int_0^\infty d\tau |\left\langle O^\dagger(t+\tau)O(t)\right\rangle|^2 &= \sum_{ijkl} A_{ij}A_{kl}^* \int_0^\infty dt e^{(\lambda_j+\lambda_l^*)t} \int_0^\infty d\tau e^{(\lambda_i+\lambda_k^*)\tau}, \\ &= \sum_{ijkl} A_{ij}A_{kl}^* \frac{1}{(\lambda_j+\lambda_l^*)} \frac{1}{(\lambda_i+\lambda_k^*)}. \end{aligned} \tag{6.51}$$

Simplifying this further by first, defining $L_{ij} = -\frac{1}{(\lambda_j+\lambda_i^*)}$, then using the following relations $\mathbf{C} = \mathbf{AB} \rightarrow c_{ij} = \sum_k a_{ik}b_{kj}$, and $\mathrm{Tr}[\mathbf{AB}] = \sum_{ij} a_{ji}b_{ij}$, we find

$$\begin{aligned}\int_0^\infty dt \int_0^\infty d\tau |\left\langle O^\dagger(t+\tau)O(t)\right\rangle|^2 &= \sum_{ijkl} A_{kl}^* L_{ki} A_{ij} L_{lj} \\ &= \sum_{il}[\sum_k A_{kl}^* L_{ki}][\sum_j A_{ij}L_{lj}], \\ &= \sum_{il}[\mathbf{A}^\dagger\mathbf{L}]_{li}[\mathbf{A}\mathbf{L}^\top]_{il} \\ &= \mathrm{Tr}[\mathbf{A}^\dagger\mathbf{L}\mathbf{A}\mathbf{L}^\top].\end{aligned} \tag{6.52}$$

For the denominator following a similar methodology gives

$$\begin{aligned}\int_0^\infty dt \int_0^\infty d\tau \left\langle O^\dagger(t+\tau)O(t+\tau)\right\rangle \left\langle O^\dagger(t)O(t)\right\rangle &= \sum_{ij} a_i a_j \int_0^\infty dt e^{(\lambda_i+\lambda_j)t} \int_0^\infty d\tau e^{\lambda_i \tau}, \\ &= \sum_{ij} a_i a_j \frac{1}{\lambda_i(\lambda_i+\lambda_j)}, \\ &= \sum_{ij} U_{ij}\Lambda_{ij}, \\ &= \mathrm{Tr}[\mathbf{U}^\top\mathbf{\Lambda}].\end{aligned} \tag{6.53}$$

where $a_i = \langle\langle O^\dagger O|P\mathcal{P}_i P^{-1}|\rho(0)\rangle\rangle$, $U_{ij} = a_i a_j$ and $\Lambda_{ij} = (\lambda_i(\lambda_i+\lambda_j))^{-1}$ have been introduced. Putting the numerator and denominator together to find a matrix representation of the indistinguishability we find

$$\mathcal{I} = \frac{\mathrm{Tr}\left[\mathbf{A}^\dagger\mathbf{L}\mathbf{A}\mathbf{L}^\top\right]}{\mathrm{Tr}[\mathbf{U}^\top\mathbf{\Lambda}]}. \tag{6.54}$$

This model can be further modified to directly include the influence of a phonon sideband when the system is in a polaron transformed basis such that $O(t) \approx \sigma(t)B_-(t)$, where $B_\pm = \exp\left[\pm\sum_{\mathbf{k}} \frac{g_{\mathbf{k}}}{\omega_{\mathbf{k}}}(b_{\mathbf{k}}^\dagger - b_{\mathbf{k}})\right]$, see Appendix (A.3) for details of this. When choosing to adopt this diagonal method to solve for a systems optical properties with the inclusion of a phonon sideband, it is important to note that this still requires solving the numerical integrals with the phonon correlation function $\mathcal{G}(\tau)$, which reduces the efficiency of this method. Moreover, this method is not a beneficial approach when filtering is involved due the requirement of working in the time domain, as the extra integrals required mix up the diagonalisation [31].

6.2.4 Cavity–molecule results

To calculate the results for this molecule–cavity system the parameters $\kappa_c = 2 \times 2\pi$ GHz and $g = 98 \times 2\pi$ MHz $= 0.41$ μeV were chosen to model a optical fibre mirco–cavity proposed by Kyle D. Major in Ref [72]; where the cavity linewidth κ_c has been decreased from $6.6 \times \pi$ GHz to reflect advancements in cavity design. For this choice in parameters the Purcell factor is

$F_P = 0.52$, indicating that there is no enhancement to the spontaneous decay rate for this mirco–cavity, only suppression from the sharp cavity linewidth. The parameters which describe the broad sideband and the local mode included in the model are taken from the analysis shown in appendix (A.2).

For simulations of the full DBT–cavity emission see Fig. 6.5a. For this simulation only one local vibrational mode was included in the model due to the large computational time for the simulations. To investigate the case for when the cavity is on resonance with either the ZPL or a local vibrational mode the cavity frequency detuning is set to to 0 meV or $\Delta_1 = 21$ meV in the system Hamiltonian, where there is a clear suppression around either feature the cavity is coupled to. This work lays the foundations to investigate into how coupling to a LVM modifies the lifetime of the vibrational state, which could in turn lead to an experimental measurement of the oscillations predicted due to local vibrational modes in second order correlation function measurements shown throughout chapter 5.

To highlight how the detected emission spectrum can be found from both the cavity modes and the cavity filtered dipole modes for the case of no phonon sideband effects, see Fig. 6.5b. To omit the phonon sideband influence from the calculations the interaction term H_L^{PH} is excluded and therefore the polaron transformation between the TLS and thermal phonon bath is not performed. Two separate localised vibrational modes were included in this calculation to give Fig. 6.5b. The peak appearing at 50.1 meV corresponds to a higher order mutli-phonon process whereby both localised modes are involved as this peak energy equals a summation of the local modes energy splitting. Higher order processes between the local modes are captured in this model due to their explicit treatment in the system degrees of freedom.

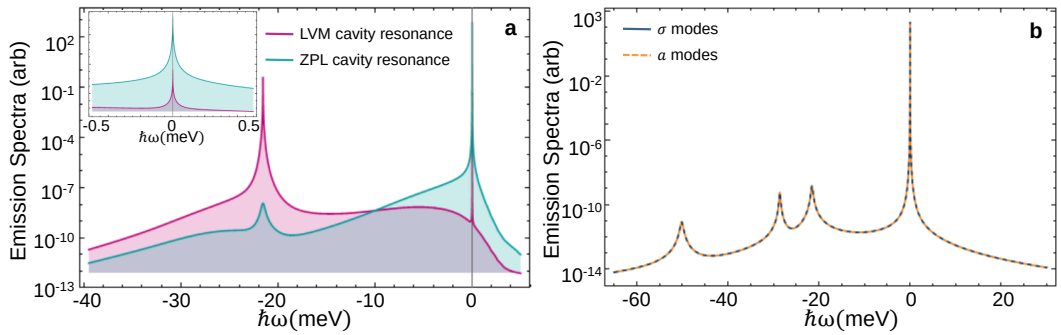

Figure 6.5: Detected cavity emission of a DBT molecule at 4.5 K using the cavity parameters $\kappa_c = 2 \times 2\pi$ GHz and $g = 98 \times 2\pi$ MHz. (a) Calculation for the cavity coupled to either the ZPL (blue) or one local vibrational mode (pink) with a continuous phonon sideband. Inset shows the ZPL over a shorter energy range, highlighting cavity suppression. (b) Calculations for a ZPL with two local vibrational modes coupled to a cavity without phonon sideband, emission spectra found with cavity modes $a^\dagger / a$ (solid blue) and filtered dipole operators $\sigma_\alpha^\dagger / \sigma_\alpha$ (dashed orange).

6.2.4.1 Cavity indistinguishability and efficiency

When considering indistingusihability calculations for this cavity system, to obtain the maximum possible value the cavity frequency should be on resonance with the zero phonon line. Considering this, for the following results all local modes are omitted from this model setting $N = 0$, due to them sitting far from cavity resonance leading to their strong suppression. To compare the emission spectra from the bare DBT molecule and the cavity see Fig. 6.6a. Here the choice in cavity parameters reflect an optical mirco–cavity with $\kappa_c < g$ and $g \sim 3\Gamma_1$, which captures the weak coupling regime whereby the enhancement to the spontaneous emission rate is minimal however the small cavity linewidth acts to suppress all sideband features. Finding the indistinguishability and efficiency for the cavity model considering solely a zero phonon line with and without a continuous phonon sideband is shown in Fig. 6.7. From Fig. 6.7 it is evident that the cavity linewidth sharpness at $\kappa_c = 2\pi$ GHz is sufficient to effectively eliminate the SB contribution over the considered temperature range. At 2.5 K an indistinguishability of $\mathcal{I} = 0.984$ is found with a respective cavity efficiency $\eta_c = 0.258$. Noting that these results indicate that filtering alone with a combination of the bandpass and Fabry–Perot filter leads to higher values of both $\mathcal{I}$ and efficiencies.

For the case of modelling the DBT zero phonon line coupled to the cavity, the diagonal method outlined in this chapter can be used to calculate indistinguishability in a highly efficient way. This allows for a full parameter sweep across both κ_c and g which enables for the optimisation of these parameters. See Fig. 6.8 for contour plots of indistinguishability for three different temperatures between 2.5 K and 10 K, with varying κ_c and g. On these plots the parameters $g = 98 \times 2\pi$ MHz with either $\kappa_c = 2 \times 2\pi$ GHz or $\kappa_c = 6.6 \times 2\pi$ GHz are highlighted with a pink and black cross, respectively, which represent the proposed parameters for the optical micro–cavity. From these points it is clear to see how the slight reduction in the cavity linewidth leads to an increase in indistinguishability due to the increase in suppression

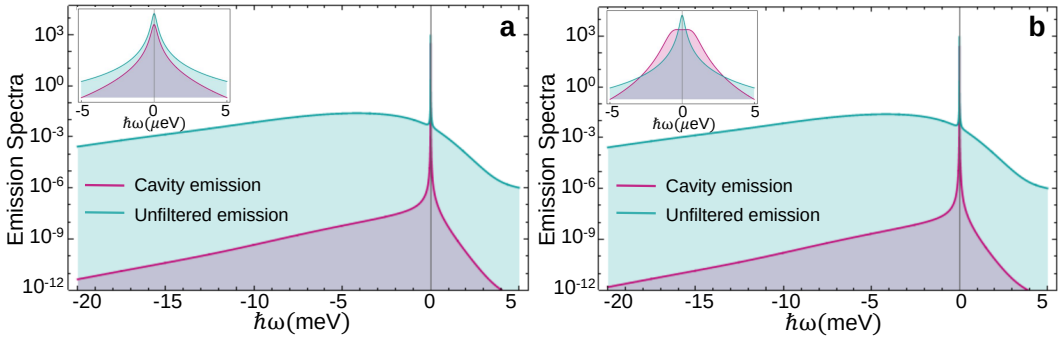

Figure 6.6: (a) Detected cavity emission compared to the bare emission of a DBT molecule at 4.5K using the cavity parameters $\kappa_c = 2 \times 2\pi$ GHz and $g = 98 \times 2\pi$ MHz. Inset shows the ZPL over a shorter energy range. (b) Cavity emission spectrum using optimised cavity parameters $\kappa_c = 0.52 \times 2\pi$ GHz and $g = 239 \times 2\pi$ MHz.

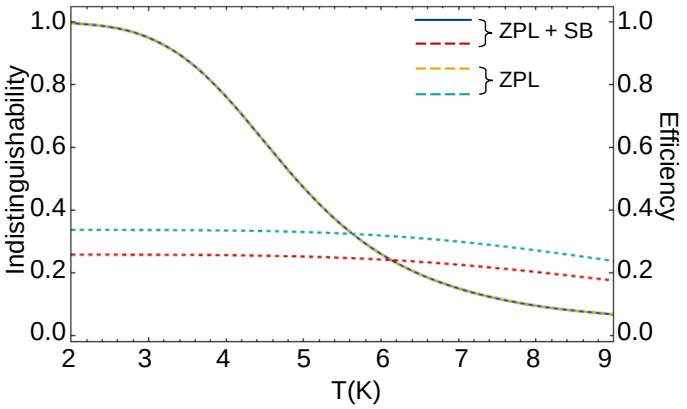

Figure 6.7: Indistinguishabilty and cavity efficiency of the molecule–cavity system looking at the model with just a zero phonon line (solid blue for $\mathcal{I}$, dashed red for η_c) and with a phonon sideband (dashed yellow for $\mathcal{I}$, dashed turquoise for η_c) for the mirco–cavity parameters $\kappa_c = 2 \times 2\pi$ GHz and $g = 98 \times 2\pi$ MHz.

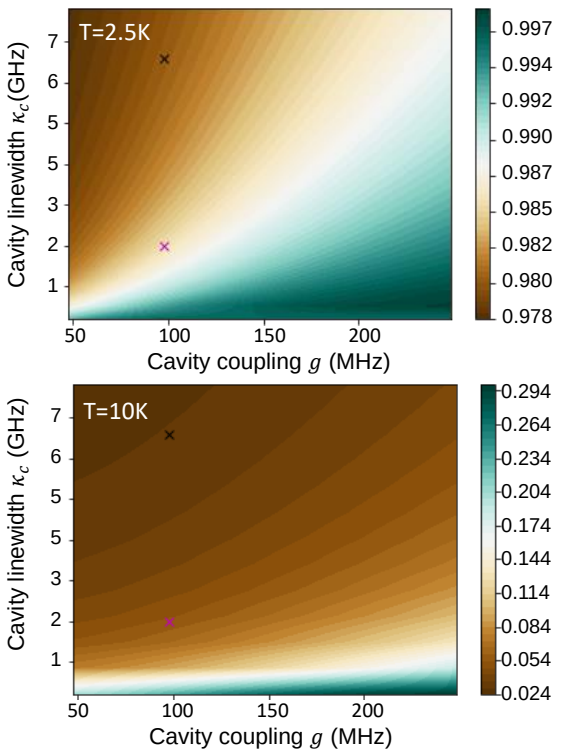

Temperature (K)	Cavity coupling (2π MHz)	Cavity linewidth (2π GHz)	$\mathcal{I}_{ZPL}$
2.5	98	2.00	0.985
	98	6.60	0.980
	239	0.52	0.998
4.5	98	2.00	0.637
	98	6.60	0.560
	239	0.52	0.929

Figure 6.8: 2D plots of indistinguishability as a function of both cavity linewidth and coupling strength for the cavity enhanced zero phonon line for a DBT molecule at temperatures 2.5 K, 4.5 K and 10 K. Black and pink crosses highlight the optical micro–cavity parameters. Table bottom right shows different values of indistinguishability for differing cavity parameters including the optimal values.

of the incoherent part of the emission including the sideband and a fraction of the ZPL that is homogeneously broadened. The highest region of indistinguishability on these plots is along the bottom right which hosts small linewidth and higher cavity coupling strengths. The optimal parameters values for the maximum indistinguishability are $g = 239 \times 2\pi$ MHz and $\kappa_c = 0.52 \times 2\pi$ GHz, and can be found along with the values of $\mathcal{I}_{\mathrm{ZPL}}$ in the table in Fig. 6.8. For these optimised parameters the resultant Purcell factor is $F_{\mathrm{P}} = 11.99$, from which it is expected that the spontaneous decay rate will experience enhancement, increasing the coherent fraction of emission. To visualise how these optimised values modify the cavity emission see Fig. 6.6b. The choice of a larger cavity coupling g leads to a visible Rabi vacuum splitting of the zero phonon line reflecting the dressed eigenstates of the cavity system, where the ZPL splits into two peaks separated by $2g = 196 \times 2\pi$ MHz$= 0.8\,\mu$eV. The predicted values of the indistinguishability and cavity efficiency for molecule emission with both the ZPL and phonon sideband are $\mathcal{I} = 0.998$ and $\eta_c(2.5\,\mathrm{K}) = 0.829$ at 2.5 K and $\mathcal{I} = 0.929$ with $\eta_c(4.5\,\mathrm{K}) = 0.824$ at 4.5 K; where there is no significant change in the values for $\mathcal{I}$ when accounting for the sideband over this temperature range. Moreover, it can be seen that having a stronger cavity coupling strength significantly increases the cavity efficiency along with the increased value of indistinguishability. To achieve a higher cavity coupling strength proposed in these optimisation calculations, a reduction in cavity mode volume is required.

6.3 Chapter summary

To summarise, in this chapter different enhancement techniques of two–photon interference from a single molecule of dibenzoterryene encased in a nano–crystal environment are investigated. The different techniques included filtering the photon emission where the effects of both a 3 nm bandpass filter and a Fabry–Perot filter are considered. Calculations of indistinguishability and collection efficiency for different combinations of these filters have been found for a range of cryogenic temperatures. The indistinguishability for a combination of both filters at 2.5 K is $\mathcal{I} = 0.988$ with a collection efficiency $\eta_f = 0.435$ where vast majority of the lost emission is from the sideband. Increasing the temperature to 4.5 K these values degrade to $\mathcal{I} = 0.745$ with a collection efficiency $\eta_f = 0.329$.

In the latter part of this chapter calculations of a DBT molecule coupled to a cavity are developed. For these cavity QED calculations a novel open quantum systems model using a master equation approach is detailed. This model captures the full molecule emission with a zero phonon line, localised vibrational modes and a continuous phonon sideband. Initially, cavity parameters selected are chosen to reflect an optical micro–cavity from which it is found that at 2.5 K the indistinguishability is $\mathcal{I} = 0.984$ with a cavity efficiency of $\eta_c = 0.258$. Simulations of cavity detected emission are found for this model considering the case of the cavity resonance set to match either the zero phonon line or a local vibrational mode. Finally,

the cavity parameters are optimised for the case of just considering the molecule's zero phonon line emission, as this is possible due to novel approach that decreases computational run time using matrix diagonalisation. It has been found that with an increased cavity coupling strength, mediated by a decrease in cavity volume and a decrease in the cavity leakage rate, the predicted indistinguishability of emission is $\mathcal{I} = 0.998$ and the cavity efficiency is $\eta_c = 0.829$ at 2.5 K. For these optimised parameters, high indistinguishability is better maintained for an increased temperature of 4.5 K giving $\mathcal{I} = 0.918$ with the cavity efficiency is $\eta_c = 0.824$. The significant improvement in efficiency compared to initial parameters is mediated by the increase in Purcell factor. These results demonstrate the applicability for single molecule in quantum information applications; whereby cooling to cryogenic temperatures and applying either a filter or coupling to a cavity near unity indistinguishability and high efficiencies can be achieved.

Further work could include exploring the quantitative effect on what happens to the system when coupling to one of the localised vibrational modes. It would be on fundamental interest to investigate the viability of measuring the exchange in population between one of the modes and the electronic system predicted in chapter 5, for the case of an enhanced local mode lifetime.

CHAPTER 7

NITROGEN-VACANCY CENTER

In this chapter the cavity QED formalism developed in chapter 6 will be used on a new system, a Nitrogen–Vacancy (NV) center in diamond. These sources are a popular candidate for quantum emitters due to their long–lived spin quantum state at room temperature and well-defined optical transitions [21]. Similar to other solid state emitters such as single molecules and quantum dots, limitations of NV centers arise from the strongly temperature dependent dephasing effects caused by phonon interactions. This phonon dephasing acts to suppress the indistinguishability of photon emission essential for quantum interference [122]. As well as phonon based dephasing, NV centers are susceptible to spectral wandering due to local charge fluctuations, where this effect is heightened when the emitters are close to the surface [99, 119].

This work investigates the viability of a deterministic single photon emitter operating at readily accessible temperatures without the need for cryogenics. The motivation for this works stems from the scalability issues that arise when using cryogenics, particularly outside a laboratory environment [8]. The temperatures considered for this work are 300 K and 200 K; where this temperature can be achievable using a Peltier cooling system [106]. To reduce the dephasing present in NV centers this work considers coupling such an emitter to an ultrasmall–mode–volume photonic crystal cavity in a silicon waveguide [51]. The work presented in this chapter was completed in collaboration with Joe A. Smith and other co–authors based at the University of Bristol in the published works found in reference [109].

To model this type of system, a cavity–QED master equation approach which is valid beyond weak coupling is used, where the resultant full–photon wavepacket indistinguishability and cavity efficiency are found. In previous cavity-QED studies the NV center is modelled as a two–level system with some excess dephasing to capture the homogeneous broadening of the zero phonon line [4, 118]. However, in this work, the possibility of a strain field is considered, where this effect is well documented in literature and originates from defects in the diamond

lattice [37]. To capture this strain the excited state of an NV center is treated as two orthogonally non-degenerate polarised dipoles.

Contrasting to the work developed for a DBT molecule in this thesis, the phonon based dephasing processes, including a broad phonon sideband which dominates the NV center emission spectra and zero phonon line pure dephasing are both treated phenomenologically here. The motivation for this phenomenological approach stems from the ability to explore more extreme cavity coupling strengths in a highly efficient frame work. Moreover, the focus of this work is to predominately to elucidate the role of an ultrasmall–mode–volume cavity rather then underpin dephasing mechanisms.

7.1 NV center emission properties

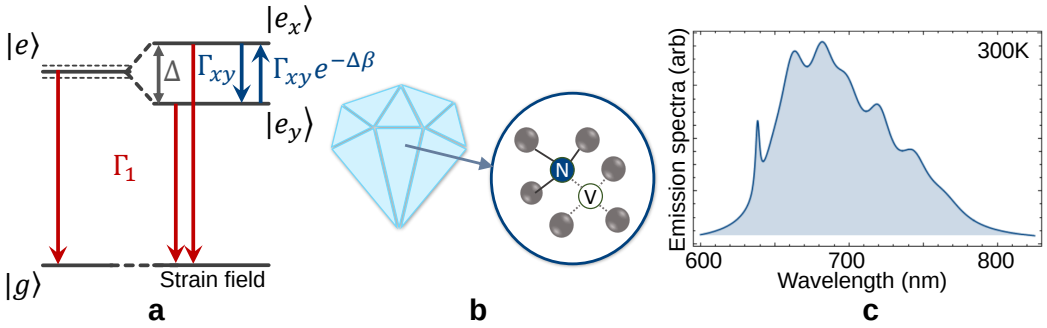

Figure 7.1: (a) Schematic energy diagram of a NV center in diamond with and without a strain field from defects in the crystal lattice. (b) Molecular diagram of the nitrogen vacancy center (c) Typical emission spectra from a NV center at 300 K.

NV centers have a rich electronic structure [91], however when considering the states involved in single photon emission only the electronic ground and excited state need to be considered [2]. The electronic energy diagram of an NV center along with a diagram of the molecular structure is shown in Fig. 7.1a and b. Emission from an NV center consists of two orthogonally polarised dipoles which are non-degenerate in the presence of linear strain fields caused by crystal defects [37, 74]. Under this linear strain the excited state splits from $|e\rangle$ to $|e_X\rangle$ and $|e_Y\rangle$ with splitting which is set to $\Delta = 0.1\,\mathrm{ps}^{-1}$ (which captures the upper bound to calculate the theoretical maximum degradation in $\mathcal{I}$) [37]. To capture the effect of a strain field the NV center is modelled as a three–level system shown in Fig. 7.1a. The polarisation relaxation rate from $|e_Y\rangle$ to $|e_X\rangle$ is given by Γ_{XY} which is $\Gamma_{XY} = 1/(2\pi)\ \mathrm{ps}^{-1}$ at 200 K and increases to $\Gamma_{XY} = 15.3/(2\pi)\ \mathrm{ps}^{-1}$ for 300 K [37].

NV centers are known to host vast phonon sidebands which have a large branching ratio $\sim 96 - 98\%$ [4, 6, 13]. A typical 300 K emission spectra of a NV center is shown in Fig. 7.1c, where the zero phonon line emission is modelled at 637 nm and the parameters used to model this emission are taken from [4]. The phonon sideband emission from a NV center can be

attributed to vibrational modes, local to deformations around the defect center [54], where these peaks which dominate the phonon sideband, can be well captured by seven separate Lorentizans [4]. Highlighting here, that the NV center phonon sideband originates from a different mechanism compared to quantum dots which host a continuous sideband from environmental lattice phonons. When considering the effect of linear strain on this phonon sideband, a re-normalisation of the peak energies is feasible due to the effect of the local defect which causes the strain on the crystal structure. Further work is needed to explore the scale of this re-normalisation effect, if any, on the sideband.

7.2 Ultrasmall–mode–volume cavity theory

Recent advancement in cavity fabrication has allowed for the possibility of ultrasmall–mode–volume photonic crystal cavity in silicon waveguides [51]. These cavities are also known as 'bow–tie' cavities due to their in–plane profile, where the bow–tie design allows for the ultrasmall–mode–volume due to confinement of the mode in the apex of the structure, see Fig 7.2a. The benefit of having an ultrasmall–mode–volume is high cavity coupling strengths g, due to the relationship $g \sim 1/\sqrt{V_M}$. Recent work from Hu et al. demonstrated such a photonic crystal cavity with a mode volume of $V_M \sim 0.001(\lambda_c/n)^3$, where λ_c is the resonance wavelength of the cavity and n is the cavity refractive index. For this work a planar nanodiamond–silicon nitride cavity is considered where the cavity wavelength is set to be on resonance with NV center emission at 637 nm and $n = 2.4$ [108]. This mode volume can be found from the normalised integral over the electrical energy density given by [51]

$$V_M = \frac{1}{\max(\varepsilon E^2)} \int \varepsilon E^2 dV, \tag{7.1}$$

where E is the electric field and ε is the permittivity. To visualise this mode volume for the bowtie cavity, see Fig. 7.2b and c, where two–dimensional planes of this structure are shown by plotting the electrical energy density. This cavity design is a vast improvement from the

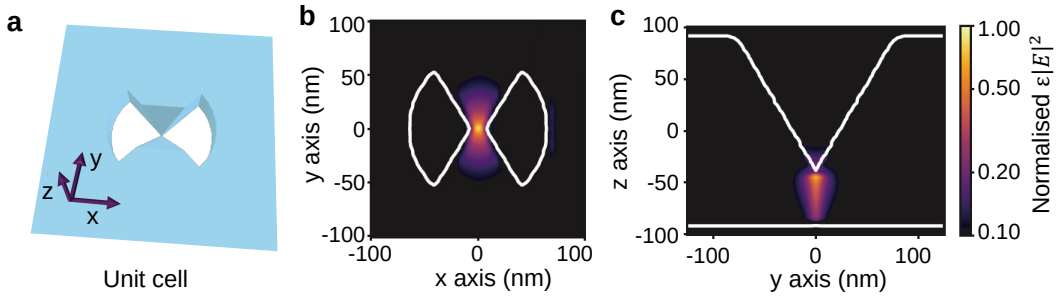

Figure 7.2: (a) Unit cell of bowtie in photonic crystal. Normalised electrical energy density for the two–dimensional bowtie plane (b) and the perpendicular plane (c) with respect to the dielectric at $x = 0$.

standard cylinder/rectangle cavity design which gives wavelength–scale mode volumes $V_M \sim (\lambda_c/n)^3$ [63, 95]. The increase in achievable cavity coupling strength motivates this work to simulate the possibility of extracting indistinguishable photons at non–cryogenic temperatures due to large Purcell enhancement. This work is focused on describing NV centers in nano–diamond encapsulated in silicon nitride films [108], however the theory in this chapter is readily extendable to other solid state single photon sources.

7.2.1 NV center pure dephasing model with zero strain

To begin the NV center is considered for the ideal case without linear strain, where this involves treating the emitter as an ideal two–level electronic system, see Fig. 7.3. The bow–tie cavity is modelled using a one sided single–moded cavity with annihilation (creation) operator $a(a^\dagger)$, following the same methodology presented in section (6.2.1). The cavity is parameterised by the linewidth κ_c and coupling strength g, where the choice of these parameters can be chosen to reflect the ultrasmall–mode properties of the bow–tie cavity. Firstly, describing the zero phonon line emission this of system with the second order Born–Markov master equation as shown in Eq. (6.41), re–displaying here for clarity as

$$\partial_t \rho_S(t) = -ig[\mathcal{X}, \rho_S(t)] + \Gamma_1 \mathcal{L}_\sigma[\rho_S(t)] + \kappa_c \mathcal{L}_a[\rho_S(t)] + 2\gamma \mathcal{L}_{\sigma^\dagger\sigma}[\rho_S(t)], \tag{7.2}$$

where the Lindblad operator is $\mathcal{L}_A[\rho(t)] = A\rho(t)A^\dagger - \frac{1}{2}\{A^\dagger A, \rho(t)\}$. The operator $\mathcal{X} = \sigma^\dagger a + \sigma a^\dagger$ describes the interaction between the cavity and two–level system. The spontaneous decay of the two-level system is $\Gamma_1 = 1/T_1$ where $T_1 = 20\,\text{ns}$ is the lifetime of a typical NV excited state [4]. The final dissipator of Eq. (7.2) contains the excess dephasing rate γ which captures the zero phonon line broadening and varies with temperature. The two color detected emission spectrum of the cavity enhanced NV center zero phonon line can be expressed using the cavity mode operators as $S_{\text{ZPL}}(\omega, \nu) = s_{\text{ZPL}}(\omega, \nu) + s_{\text{ZPL}}(\omega, \nu)^*$, with

$$s_{\text{ZPL}}(\omega, \nu) = \frac{\kappa_c}{2\pi} \int_0^\infty dt \int_0^\infty d\tau e^{i\omega(t+\tau)} e^{-i\nu t} \left\langle a^\dagger(t+\tau) a(t) \right\rangle. \tag{7.3}$$

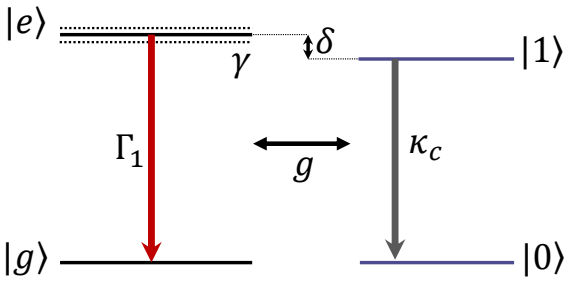

Figure 7.3: NV center with no linear strain field, modelled as a two–level system coupled to one sided single moded cavity with coupling strength g and decay rate κ_c, with cavity detuning from the TLS of δ.

The lost modes not detected from the cavity can be found from the dipole operators with

$$s_{\mathrm{ZPL}}^{LOST}(\omega,\nu) = \frac{\Gamma_1}{2\pi}\int_0^\infty dt \int_0^\infty d\tau e^{i\omega(t+\tau)}e^{-i\nu t}\left\langle \sigma^\dagger(t+\tau)\sigma(t))\right\rangle. \tag{7.4}$$

To find the efficiency of this cavity Eq. (6.40) can be used substituting in both the lost Eq. (7.4) and detected Eq. (7.3) emission spectra.

7.2.1.1 NV center sideband model

To capture emission into the broad phonon sideband $S_{\mathrm{SB}}(\omega)$, a summation of seven Lorentzian functions are used [4]. To model how this sideband emission is modified by the cavity, the convolution theorem can be used which allows for this function to be multiplied in the frequency domain by the cavity filter profile given by $h_c(\omega) = i\frac{\kappa_c}{2}/(i(\omega-\omega_0)-\frac{\kappa_c}{2})$, which gives

$$S_{\mathrm{SB}}(\omega) = N|h_c(\omega)|^2\sum_i \frac{A_i}{\pi}\frac{(\Gamma_i/2)}{(\omega-\omega_{0,i})^2+(\Gamma_i/2)^2}, \tag{7.5}$$

where A_i is the relative amplitude of the sideband peaks, $\omega_{0,i}$ are their relative peak positions and Γ_i are the full–width half–maxima. The normalisation factor N is chosen such that the Debye-Waller fraction (fraction into the ZPL) is $DW = 2.06\%$ for the bare emission (without cavity effects) of the NV center, where this is taken from [4]. To find and fix N in the calculations, the two color ZPL emission spectrum of the *bare* NV center is first required, given by $S_{\mathrm{ZPL}}^{(0)}(\omega,\nu) = s_{\mathrm{ZPL}}^{(0)}(\omega,\nu) + s_{\mathrm{ZPL}}^{(0)}(\omega,\nu)^*$, with

$$s_{\mathrm{ZPL}}^{(0)}(\omega,\nu) = \frac{\Gamma_1}{2\pi}\int_0^\infty dt \int_0^\infty d\tau e^{i\omega(t+\tau)}e^{-i\nu t}\left\langle \sigma^\dagger(t+\tau)\sigma(t))\right\rangle, \tag{7.6}$$

where to evaluate the correlation function in this equation the appropriate master equation required is $\partial_t\rho(t) = \Gamma_1\mathcal{L}_\sigma[\rho(t)] + 2\gamma\mathcal{L}_{\sigma^\dagger\sigma}[\rho(t)]$, which describes a two–level system with spontaneous decay and some pure dephasing. The bare sideband spectrum follows the form of Eq. (7.5) without filtering (i.e. setting $h_c(\omega) = 1$). Finding N to scale the sideband emission, such that $\mathcal{F}_{\mathrm{ZPL}}^{(0)}/(\mathcal{F}_{\mathrm{ZPL}}^{(0)}+\mathcal{F}_{\mathrm{SB}}^{(0)}) = DW = 2.06\%$ where $\mathcal{F}_{\mathrm{ZPL/SB}}^{(0)} = \int d\omega S_{\mathrm{ZPL/SB}}^{(0)}(\omega,\omega)$. The value found for N from the bare spectrum calculations is kept constant for the cavity calculations.

7.2.1.2 Indistinguishability calculations

The indistinguishability of NV–cavity system with sideband emission coupled to a cavity can be approximated by

$$\mathcal{I} = \frac{\int_{-\infty}^\infty d\omega\int_{-\infty}^\infty d\nu|S_{\mathrm{ZPL}}(\omega,\nu)|^2}{(\mathcal{F}_{\mathrm{ZPL}}+\mathcal{F}_{\mathrm{SB}})^2}, \tag{7.7}$$

where $\mathcal{F}_{\mathrm{ZPL}} = \int_{-\infty}^\infty d\omega S_{\mathrm{ZPL}}(\omega,\omega)$ and $\mathcal{F}_{\mathrm{SB}} = \int_{-\infty}^\infty d\omega|h_c(\omega)|^2 S_{\mathrm{SB}}(\omega)$ are the power into the ZPL and SB respectively. This equation is an approximation as the sideband contribution has

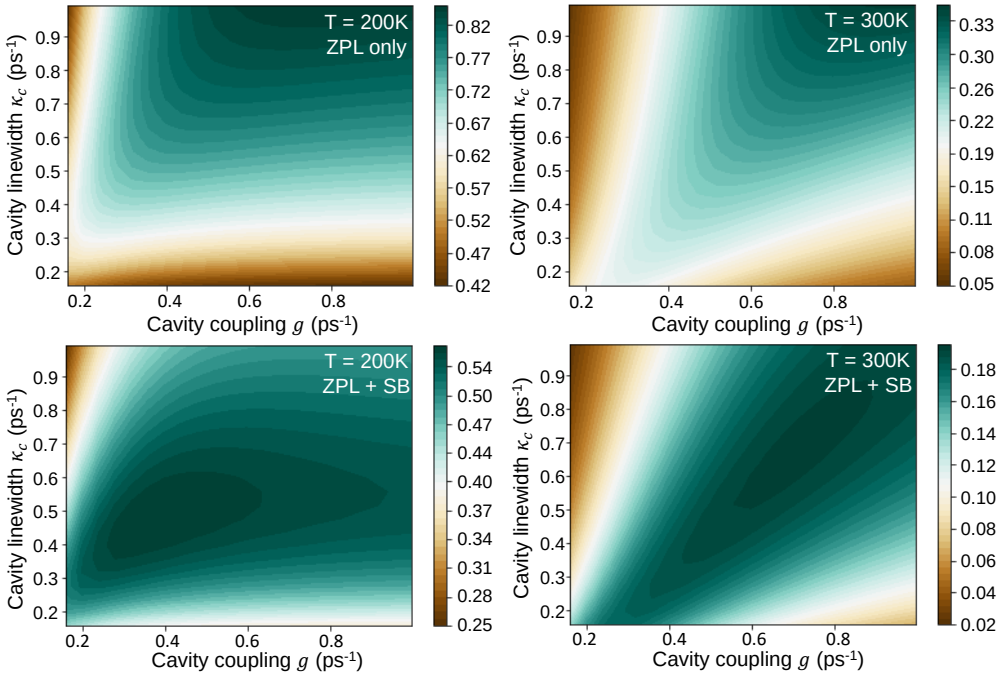

Figure 7.4: Indistinguishability calculations for a NV center coupled to a cavity with zero phonon line emission only (top) and the inclusion of SB (bottom) for the NV center modelled as an ideal two-level system. Cavity parameters found to optimise indistinguishability are $g = 0.38\,\mathrm{ps}^{-1}$ and $\kappa_c = 0.48\,\mathrm{ps}^{-1}$ for 200 K and $g = 0.71\,\mathrm{ps}^{-1}$ and $\kappa_c = 0.68\,\mathrm{ps}^{-1}$ for 300 K.

been neglected from from the numerator. This approximation assumes that the sideband is purely incoherent which is a reasonable assumption due to the resonance peaks that form the NV sideband being spectrally resolved from the ZPL emission. Factoring out the sideband contribution Eq. (7.7) can be rearranged to give

$$\mathcal{I} = \mathcal{I}_{\mathrm{ZPL}} \left(\frac{\mathcal{F}_{\mathrm{ZPL}}}{\mathcal{F}_{\mathrm{ZPL}} + \mathcal{F}_{\mathrm{SB}}} \right)^2, \tag{7.8}$$

where

$$\mathcal{I}_{\mathrm{ZPL}} = \int_{-\infty}^{\infty} d\omega \int_{-\infty}^{\infty} d\nu \frac{|S_{\mathrm{ZPL}}(\omega, \nu)|^2}{\mathcal{F}_{\mathrm{ZPL}}^2}, \tag{7.9}$$

is the indistinguishability of the ZPL only, which can be verified using the analytical model in [118] under weak coupling regimes.

7.2.2 NV center pure dephasing model results

To find the optimal cavity parameters for this NV center cavity system, calculations of both $\mathcal{I}_{\mathrm{ZPL}}$, considering just the ZPL emission and $\mathcal{I}$, considering the sideband contribution as well are found. Performing a full parameter sweep over both κ_c and g for 200 K and 300 K, see Fig. 7.4 for the plots. It can be seen that for calculations without a sideband emission the

maximum indistinguishability increases for both increasing coupling strength and linewidth for the parameter range considered. This increased indistinguishability is due to the enhanced spontaneous emission rate which causes a larger fraction of the emission to be coherent. For high coupling strength but decreased cavity linewidths (or increased quality factors as $\kappa_c = \omega_c/Q$), $\mathcal{I}_{\mathrm{ZPL}}$ decreases as the ZPL is split by g, leading to detected cavity emission resulting in the tails of the peaks which are mostly incoherent. Now looking at the results for both the ZPL and sideband emission in the bottom two plots of Fig. 7.4. It can be seen that including a sideband leads to a bounded region of high indistinguishability within the parameter range explored. This reduction in $\mathcal{I}$ for higher cavity line widths or lower quality factors is due to an increase sideband fraction included into the detected cavity emission. Moreover, the region of high $\mathcal{I}$ is bounded along a positive diagonal correlation, where this correlation is stronger for 300 K. This correlation arises from competition between the Rabi vacuum splitting of the ZPL, which increases for increasing g and the cavity linewidth which is inversely proportional to the cavity quality factor (Q). For a strongly split ZPL, a sharp cavity linewidth (high-Q) degrades the indistinguishability, as its the ZPL suppressed dip at zero detuning which is coupled into the detected cavity mode. For the region of low g and high κ_c (or low-Q) the Purcell enhancement of the spontaneous emission is not sufficient enough to achieve high $\mathcal{I}$. The optimal parameters found from these calculations are $g = 0.38\,\mathrm{ps}^{-1}$ and $\kappa_c = 0.48\,\mathrm{ps}^{-1}$ for 200 K from which an indistinguishability of $\mathcal{I} = 0.56$ is calculated. For 300 K the optimal values found are $g = 0.71\,\mathrm{ps}^{-1}$ and $\kappa_c = 0.68\,\mathrm{ps}^{-1}$ giving $\mathcal{I} = 0.20$. The Purcell factors ($F_{\mathrm{P}} = \frac{4g^2}{\Gamma_1 \kappa_c}$) for these parameters sets are $F_{\mathrm{P}}(200\,\mathrm{K}) = 24000$ and $F_{\mathrm{P}}(300\,\mathrm{K}) = 60000$. To visualise the emission spectra from both bare and cavity enhanced NV center see Fig. 7.5. For both temperatures it can be seen that the vast majority of the sideband is suppressed, where for the case of 200 K the ZPL emission is split where the difference in peak width is $2g$, indicating the system is in the critical/strong coupling regime.

Considering now the efficiency of this cavity system. For the case of the zero phonon line

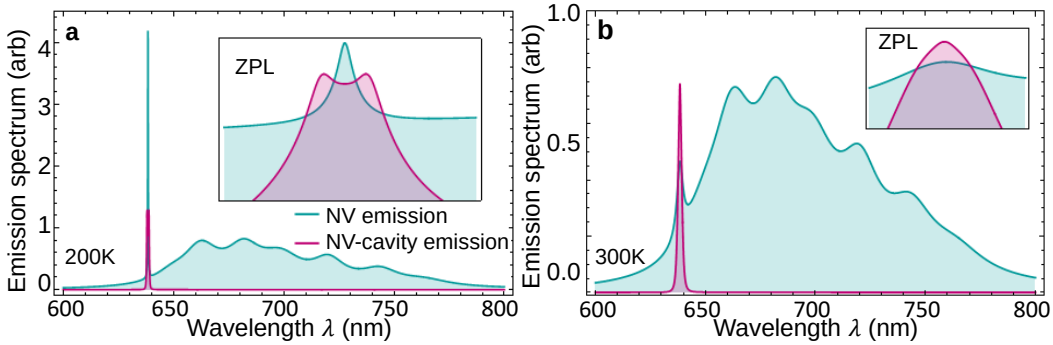

Figure 7.5: Emission from a bare NV center (blue) and cavity enhanced emission (pink) for 200 K (a) and 300 K (b) with parameters selected to optimise $\mathcal{I}$ found in Fig. 7.4. Insets show the zero phonon line over reduced wavelength range.

emission from a NV center *only* using Eq. (6.40), the cavity efficiency is $\eta_c(200\,\mathrm{K}) = 0.99984$ and $\eta_c(300\,\mathrm{K}) = 0.99996$, which both are close to unity. Noting that these fraction are very high due to the large Purcell factors that result from these cavity parameters. Furthermore, when considering the the fraction of sideband emission that couples into the detected cavity mode the total efficiency will decrease, where for these cavity parameters this coupled fraction is 0.30% for 200 K and 0.47% for 300 K.

7.2.2.1 Filtering NV–cavity emission

In this chapter calculations are simulated for temperatures $T \geq 200\,\mathrm{K}$ which is considered high when accounting for phonon effects; if indistinguishability is the main goal for a source the cavity enhanced emission can be post filtered to see extra enhancement in two–photon interference. In this section the cavity model formalism is extended to include the effects of a Lorentzian Fabry-Perot filter to the NV-cavity detected emission. The filter is assumed to be described by the frequency space Green's function in the form $h_f(\omega) = \frac{\kappa_f}{2}/(i(\omega-\omega_0)-\frac{\kappa_f}{2})$, which multiplies the positive frequency component of the detected electric field operator [55]. The expression for indistinguishability for this filtered cavity emission becomes

$$I_{filt} = \frac{\int_{-\infty}^{\infty} d\omega \int_{-\infty}^{\infty} d\nu |h_f(\omega)|^2 |h_f(\nu)|^2 |S_{\mathrm{ZPL}}(\omega,\nu)|^2}{\left(\int_{-\infty}^{\infty} d\omega |h_f(\omega)|^2 S_{\mathrm{ZPL}}(\omega,\omega) + |h_f(\omega)|^2 |h_c(\omega)|^2 S_{\mathrm{SB}}(\omega)\right)^2}. \tag{7.10}$$

Re–arranging to factor out the SB fraction again we find

$$I_{filt} = I_{\mathrm{ZPL}}^{filt}\left(\frac{\mathcal{F}_{\mathrm{ZPL}}^{filt}}{\mathcal{F}_{\mathrm{ZPL}}^{filt}+\mathcal{F}_{\mathrm{SB}}^{filt}}\right)^2, \tag{7.11}$$

where $\mathcal{F}_{\mathrm{ZPL}}^{filt} = \int_{-\infty}^{\infty} d\omega |h_f(\omega)|^2 S_{\mathrm{ZPL}}(\omega,\omega)$ and $\mathcal{F}_{\mathrm{SB}}^{filt} = \int_{-\infty}^{\infty} d\omega |h_f(\omega)|^2 |h_c(\omega)|^2 S_{\mathrm{SB}}(\omega)$ are the power after filtering in the ZPL and SB respectively. The indistinguishability of the filtered

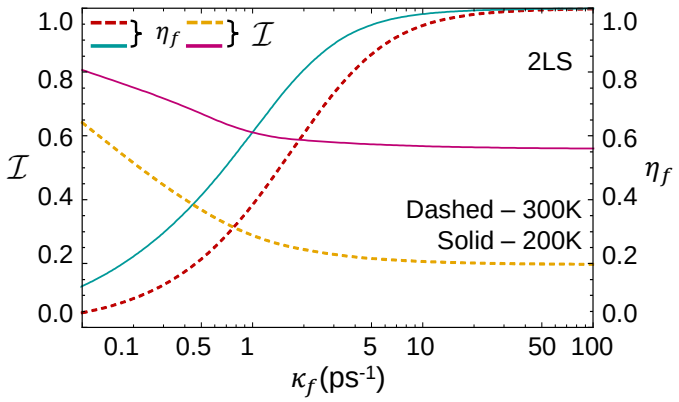

Figure 7.6: Indistinguishability and efficiency of a NV center with no linear strain for both 200 K (solid lines) and 300 K (dashed lines) as a function of post filtering cavity emission using the optimal parameters found from Fig. 7.4.

ZPL is

$$I_{\mathrm{ZPL}}^{filt} = \frac{\int_{-\infty}^{\infty} d\omega \int_{-\infty}^{\infty} d\nu |h_f(\omega)|^2 |h_f(\nu)|^2 |S_{\mathrm{ZPL}}(\omega,\nu)|^2}{(\mathcal{F}_{\mathrm{ZPL}}^{filt})^2}. \tag{7.12}$$

For calculations of indistinguishability and efficiency for the post filtered, detected cavity emission spectra see Fig. 7.6. The parameters used to simulate these results took the optimised cavity values found from Fig. 7.4. From these simulations it has been found that for a filter with width $\kappa_f = 0.3\,\mathrm{ps}^{-1}$ photon indistinguishability from an ultrasmall–mode–volume cavity is $\mathcal{I}(200\,\mathrm{K}) = 0.72$ and $\mathcal{I}(300\,\mathrm{K}) = 0.45$, with the filter efficiencies $\eta_f(200\,\mathrm{K}) = 0.30$ and $\eta_f(300\,\mathrm{K}) = 0.13$. In these predictions the sideband is assumed to be fully incoherent, it can be noted that under tight filter regimes these values may be a slight underestimation due the expectation of the sideband retaining some coherence [26].

7.2.3 NV center with linear strain

Considering now the presence of a strain field across the diamond emitter, which is common in diamond and therefore it is important to explore its impact [74]. It is known that the presence of a strain field splits the excited state into two non–degenerate orthogonally polarised levels [37, 74]. This effect is especially important when considering polarised cavities and will now be explored.

To model the NV center under a linear strain field the system is modelled as a three–level system with the excited state to split into the aforementioned non-degenerate orthogonally polarised orbitals $|e_x\rangle$ and $|e_y\rangle$ split by energy Δ, see Fig. 7.7 [74]. Coupling this three–level system to a single moded one sided cavity with coupling strength g, the following second order Born-Markov master equation is used to model the cavity enhanced zero phonon line (ZPL) emission [109]

$$\begin{aligned}\partial_t \rho(t) = &-ig[\chi(\theta), \rho(t)] + \Gamma_1 \mathcal{L}_{\sigma_x}[\rho(t)] + \Gamma_1 \mathcal{L}_{\sigma_y}[\rho(t)] + \Gamma_{xy} \mathcal{L}_{\sigma_{xy}}[\rho(t)] \\ &+ e^{-\Delta\beta} \Gamma_{xy} \mathcal{L}_{\sigma_{yx}}[\rho(t)] + \kappa_c \mathcal{L}_a[\rho(t)],\end{aligned} \tag{7.13}$$

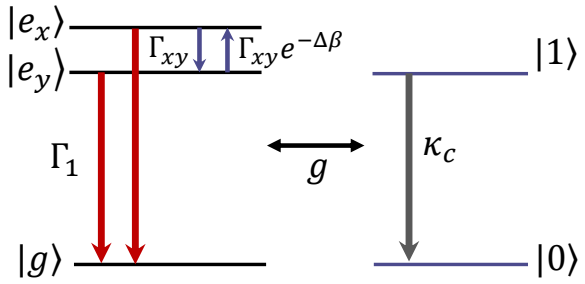

Figure 7.7: NV center with linear strain field, modelled as a three-level system coupled to one sided single moded cavity with coupling strength g and leakage rate or linewidth κ_c. Spontaneous decay from the excited state manifolds has the rate $\Gamma_1 = 0.05\,\mathrm{ns}^{-1}$. The two orthogonally polarised excited state manifolds split by $\Delta = 0.1\,\mathrm{ps}^{-1}$.

where σ_x and σ_y describe the decay from the corresponding excited state to the ground state and σ_{xy}/σ_{yx} describe the respective transitions between the two excited states. The first term contains the system Hamiltonian in a rotated frame which couples the three–level system to the cavity mode a, as

$$\chi(\theta) = g(\sigma_m(\theta)^\dagger a + \sigma_m(\theta)a^\dagger), \tag{7.14}$$

with $\sigma_m(\theta) = \sin(\theta)\sigma_x + \cos(\theta)\sigma_y$, where this term describes the alignment of the cavity mode with the excited state dipoles. The next four terms are Lindblad dissipators with $\mathcal{L}_A[\rho(t)] = A\rho(t)A^\dagger - \frac{1}{2}\{A^\dagger A, \rho(t)\}$. The second and third term in Eq. (7.13) describe spontaneous emission from each of the excited states $|e_x\rangle$ and $|e_y\rangle$ respectively with decay rate Γ_1. The fourth and fifth terms represent the decay/excitation between the two excited states with polarisation decay rates $\Gamma_{xy}/e^{\Delta\beta}\Gamma_{xy}$, respectively with $\beta = 1/k_BT$. The last term describes spontaneous emission from the cavity with leakage rate (linewidth) κ_c. For these calculations $\Delta = 100\,\text{GHz}$ which is an approximate upper bound on how large the energy splitting could be [37].

The two color ZPL detected emission from the NV–cavity system can be found from Eq. (7.3). The lost modes emitted from states e_x/e_y on the other hand are given by

$$s^{LOST}_{x\backslash y}(\omega,\nu) = \frac{\Gamma}{2\pi}\int_0^\infty dt \int_0^\infty d\tau e^{i\omega(t+\tau)}e^{-i\nu t}\left\langle \sigma^\dagger_{x\backslash y}(t+\tau)\sigma_{x\backslash y}(t))\right\rangle. \tag{7.15}$$

Similar to the case of no linear strain the phonon sideband emission is treated phenomenologically and is only introduced when final values of indistinguishability are calculated.

To find the efficiency of this cavity as a function of θ and different initial populations, Eq. (6.40) can be used where the power into the lost modes needs to be found as a sum of the excited state dipoles using $P_L = \int d\omega S^{LOST}_x(\omega,\omega) + S^{LOST}_y(\omega,\omega)$.

The indistinguishability of detected cavity emission with/without a sideband can be found from Eq. (7.8)/Eq. (7.9), which for this three–level system will depend upon the initial population and the cavity orientation angle θ. This initial state population could be experimentally controlled by varying the polarization of the pump laser to align to either the $|e_x\rangle$ or $|e_y\rangle$ state. To explore how both the indistinguishability and cavity efficiency varies as a function of both the initial population distribution and the coupling angle θ see Fig. 7.8.

7.2.4 NV center with strain results

It can be seen from Fig. 7.8 that both the cavity efficiency and indistinguishability exhibit an oscillatory profile as a function of cavity orientation with respect to the excited state dipoles. Here the maximum values correspond to the cavity aligning with the initial populated state. Moreover, it can be seen that there is drop in maximum indistinguishability and cavity efficiency compared to the two–level system (no strain); where the drop in efficiency is marginal (0.01%). To explain this non-negligible drop in indistinguishability it is advantageous to analyse

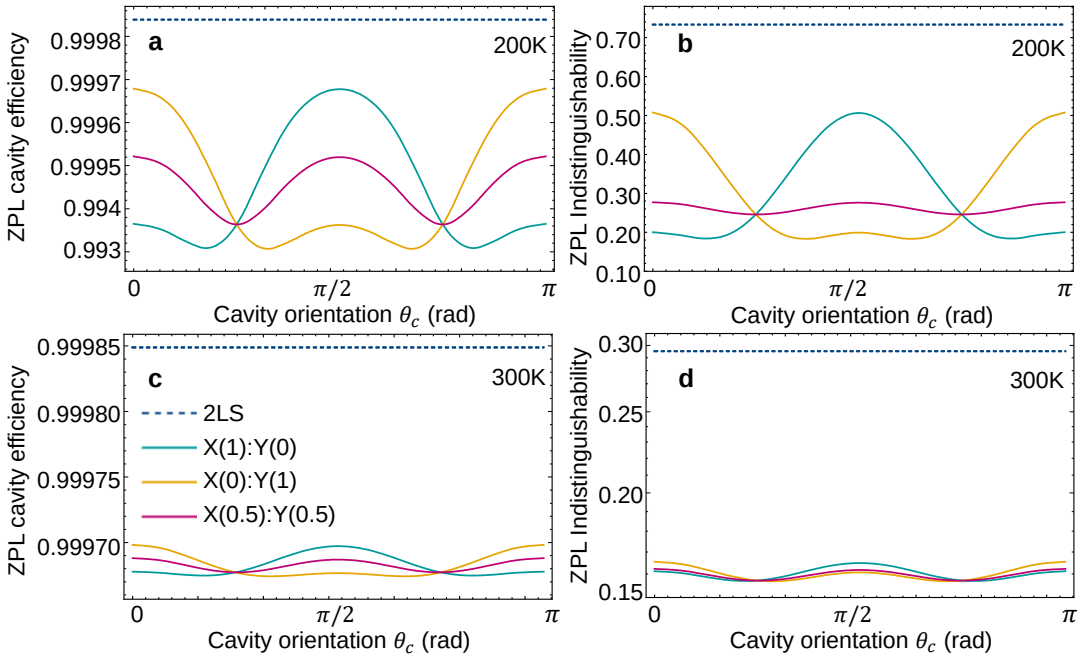

Figure 7.8: Calculations of NV center under linear strain with excited states split by $\Delta = 100\,\text{GHz}$, coupled to a bow–tie cavity with *no sideband*, showing the cavity efficiency and indistinguishability as a function of cavity orientation for 200 K (a)-(b) and 300 K (c)-(d), respectively. The (dashed) line shows the no strain (two–level system) case. The (solid) lines model different initial populations in solely $|e_x\rangle$, $|e_y\rangle$ and a 50 : 50 mixed state.

the evolution of the state population, see Fig. 7.9. For the case where the state population is initialised in $|e_x\rangle$ and the cavity is fully aligned to it (shown in 7.9a and c) the majority of photons rapidly exit the cavity, however as this is not instant, a fraction of the population can *decay* into $|e_y\rangle$, where this leads to dephasing of these photons and explains the drop in indistinguishability compared to the two–level system calculations. This dephasing also occurs for the state prepared and coupled to $|e_y\rangle$; however the origin of this dephasing differs, as it stems from a fraction of the population being *excited* to $|e_x\rangle$. As it is slight less probable that the population excites compared to decaying, between $|e_y\rangle$ and $|e_x\rangle$ the resultant indistinguishability for the case of coupling and initialising in the $|e_y\rangle$ state is slightly higher at $\mathcal{I} = 0.508$ compared to $\mathcal{I} = 0.506$ for $|e_x\rangle$. For the case where $|e_x\rangle$ is initially populated and $|e_y\rangle$ is enhanced by the cavity (see Fig. 7.9b and d) the photons rapidly exit the cavity before the populations are even fully mixed. This allows for photons to 'linger' in the state not enhanced by the cavity which leads to a much larger reduction in indistinguishability; for 200 K this goes from $\mathcal{I} = 0.51$ to $\mathcal{I} = 0.20$ for the system coupled and initialised in $|e_x\rangle$.

Finally, considering the effect on post filtering a NV center coupled to a bow–tie cavity under a linear strain field from crystal defects, see Fig. 7.8. For these calculations the initial population resides in $|e_y\rangle$ and the cavity is aligned into this state to the simulate optimal conditions.

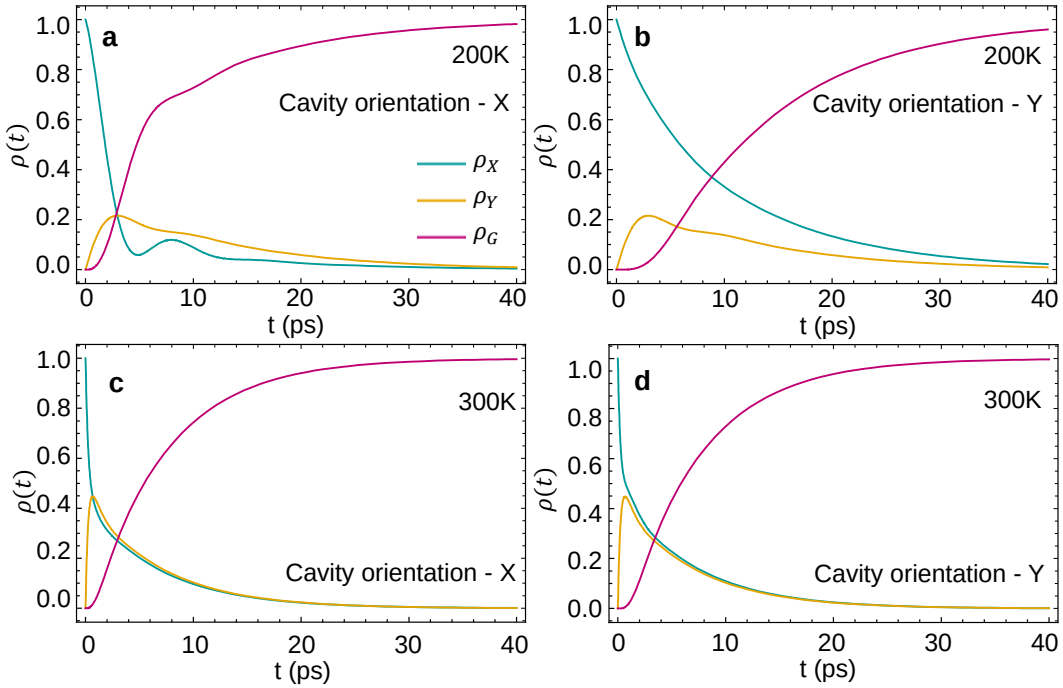

Figure 7.9: Population of the orthogonally polarised excited states $|e_x\rangle$ and $|e_y\rangle$ as well as the ground state. Plots show the cases for 200 K and 300 K with the initial population in $|e_x\rangle$ and the cavity oriented to couple to both dipole X (left) and Y (right).

It has been found that for a Lorentizan filter with $\kappa_f = 0.3\,\mathrm{ps}^{-1}$ the indistinguishability for the NV–cavity system under a linear strain goes up to $\mathcal{I}(200\,\mathrm{K}) = 0.53$ with $\eta_f(200\,\mathrm{K}) = 0.30$ and $\mathcal{I}(300\,\mathrm{K}) = 0.32$ with $\eta_f(300\,\mathrm{K}) = 0.13$.

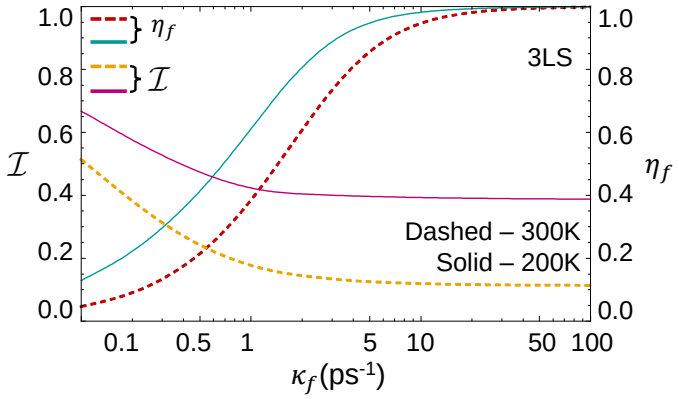

Figure 7.10: Post filtering of cavity enhanced emission for the optimal parameters $g = 0.38\,\mathrm{ps}^{-1}$ and $\kappa_c = 0.48\,\mathrm{ps}^{-1}$ for 200 K and $g = 0.71\,\mathrm{ps}^{-1}$ and $\kappa_c = 0.68\,\mathrm{ps}^{-1}$ for 300 K, using the three level system model to capture linear strain.

7.3 Chapter summary

In this chapter calculations of a NV center at non–cryogenic temperatures coupled to an ultrasmall–mode–volume cavity are performed. It has been found that by combining Peltier cooling down to 200 K with these ultrasmall 'bow–tie' cavities indistinguishability can be enhanced by nine orders of magnitude to $\mathcal{I} = 0.56$. It has been shown that further enhancement can be achieved by post filtering with a Lorentzian filter profile of width $\kappa_f = 0.3\,\mathrm{ps}^{-1}$ to find $\mathcal{I} = 0.72$, where this it at the payoff of collection efficiency $\eta_f = 0.30$. Higher values of $\mathcal{I}$ can be achieved with sharper filtering or reducing the temperature of the system by relaxing the Peltier cooling limit. The work presented in this chapter could be equally applied to other solid state single photon sources which exhibit lower phonon sideband branching ratios, where it would be interesting to investigate if this too would lead to indistinguishable emission at elevated temperatures.

In this work the inclusion of linear strain from crystal defects is accounted for by modeling the NV center as a three–level system. In this model the excited state is treated as two non–degenerate orthogonally polarised levels. It has been found that in the presence of a linear strain field the indistinguishability drops. This reduction in $\mathcal{I}$ is concluded to be mediated by dephasing between the two orthogonally polarised excited states. To ensure two–photon interference for a NV center with a strain field is at a maximum, it has been shown that the cavity orientation is very important and that it should be aligned to the emitter dipole.

Future work could include a non–phenomenological treatment of the phonon sideband, where in doing so the computational efficiency of these calculations would drop. However, by explicitly accounting for the sideband from the point of the Hamiltonian, it would be interesting see if this causes any changes to the predictions presented. From the method presented in this chapter, it is feasible that the value of $\mathcal{I}$ could very slightly increase, as this would capture the small fraction of the coherent sideband, neglected in this work.

CHAPTER 8

CONCLUSIONS AND OUTLOOK

The work presented in this thesis uses theoretical methods from open quantum systems theory to characterise the optical properties of solid state single photon sources, a promising component for quantum information applications. These quantum emitters are also a highly interesting platform to explore the quantum optics of isolated few–level systems. The main focus of this work looks at the single molecule dibenzoterrylene (DBT), a bright photostable single photon emitter. A secondary focus of this thesis looks at a nitrogen vacancy (NV) center in diamond, a well established single photon emitter.

To summarise, in chapter 3 an overview of different optical properties are explored including, the emission spectra of an ideal two–level system (TLS) and the result of coupling a TLS to a bath of thermal phonons, where the polaron transform is detailed as a key method used throughout this thesis. An additional optical property introduced in this chapter is second order correlation functions, specifically those from a Hanbury Brown and Twiss and Hong–Ou–Mandel interferometer setup. Finally, the effect of spectral wandering of an emitter is explored, where a novel method for the calculation of photon indistinguishability for an emitter undergoing both spectral wandering and pure dephasing is presented. A non–trivial result has been found from these calculations, which shows that the choice of the distribution function which describes the spectral walk results in a change in predicted indistinguishability.

Chapter 4 presents a novel open quantum systems model which captures all of the observable emission features of the promising single molecule, single photon source DBT hosted in a nano–crystal of anthracene (Ac). The model captures the zero phonon line (ZPL), four peaks associated with transitions to DBT's local vibrational modes and a broad temperature dependent phonon sideband associated with the Ac nano–crystal. This work reveals a temperature dependent homogeneously broadened ZPL which arises when anharmonic effects of the electron–phonon coupling are taken into account. This work constitutes as an important

starting point to study the effect of coupling these molecules to optical waveguides and cavities which is explored in chapter 6. Future work includes using the theoretical methods developed in this model to explore other promising solid state quantum emitters where phonon dephasing is prevalent such as two–dimensional defect material like hexagonal boron nitride.

Moving on to chapter 5, second order correlation function $g^{(2)}(\tau)$ calculations and measurements from a Hong–Ou–Mandel experimental setup are presented. Different laser driving regimes are explored and a novel approach to extract a measurement of indistinguishability from a continuous wave non–resonant laser is presented; which provides an alternative to the typical approach with a pulsed laser. Moreover, the calculations of $g^{(2)}(\tau)$ in this chapter are modified to include the effects of considering a DBT molecules phonon sideband and its local vibrational modes, which both lead to interesting results and hold consequences for indistinguishability measurements.

To capture the effect of the manipulation on the electromagnetic emission from a DBT quantum emitter, the effect of filtering emission and coupling the emitter to a cavity is explored in chapter 6. In this chapter it has been found that using a combination of a 3 nm bandpass and Fabry–Perot filter can lead to near–perfect indistinguishable extraction of photons from a DBT emitter in its lifetime limit below $\lesssim 3$ K. A novel cavity QED model which includes all observable features of DBT emission such as its phonon sideband and local vibrational modes is derived. The emission spectra of this DBT–cavity system is presented and coupling to either the ZPL or a local vibrational mode is compared to the bare spectrum. Parameters which reflect an optical mirco–cavity is first explored which again predicates near–indistinguishable detected photon emission for cryogenic temperatures, under the safe neglection of the local modes when coupling the cavity to the TLS resonance. By reducing the cavity mode volume a corresponding increase in detection cavity efficiency is predicted which reflects the increase in Purcell factor. Future work could look to explore further the effect of coupling to a local vibrational mode and incorporate these cavity calculations with the second order correlation function calculations presented in chapter 5.

Finally, chapter 7 considers a different emitter, the nitrogen vacancy center in diamond. In this work an ultrasmall–mode–volume cavity is coupled to a NV center at non–cryogenic temperatures. Using a 'bowtie' design developed by Hu et al. [51], the ultrasmall cavity mode volumes lead to high cavity coupling strength, which it has been found allows for the extraction of indistinguishable photons with $\mathcal{I} = 0.56$, for a Peltier cooled system at 200 K. It has been shown that further enhancement of $\mathcal{I}$ can be achieved by post filtering emission at the pay off of efficiency. Finally, in this chapter the effect of linear strain from crystal defects, known to occur in defect crystal centers, are accounted for by modelling the NV center as a three–level emitter with two orthogonally polarised non–degenerate excited state levels. From these calculations it has been found that it is essential both initially populate only one of the excited states and to align the cavity and emitter dipole for maximum $\mathcal{I}$ extraction as this can lead to

extra decoherence effects.

The work presented in the thesis emphasises the exciting promise that solid state emitters hold for both quantum information applications and fundamental research on isolated systems. It is known that solid state emitters host different drawbacks, a common attribute including, the phonon based dephasing explored in great detail in this thesis. However, with advancements in photonic infrastructures including cavity design, and the strong drive in development for a variety of platforms mentioned throughout this thesis, the outlook for these platforms is positive when considering different applications.

APPENDIX A

APPENDIX

A.1 Electron–phonon spectral density

In this appendix different functional forms of the exciton–phonon spectral density are derived using various forms for the electronic ground and excited state wavefunction. To begin the definition of the exciton–phonon spectral is given by

$$J_{PH}(\omega) = \sum_{\mathbf{k}} g_{\mathbf{k}}^2 \delta(\omega - \omega_{\mathbf{k}}), \tag{A.1}$$

where $g_{\mathbf{k}}$ is the product of the linear phonon matrix element and the charge density operator in reciprocal space given by

$$g_{\mathbf{k}} = -\frac{|\mathbf{k}|}{\sqrt{2NM\omega_{\mathbf{k}}}} \sum_j D_j \int \mathrm{d}^3 r |\psi_j(\mathbf{r})|^2 e^{i\mathbf{k}\cdot\mathbf{r}}, \tag{A.2}$$

where $k = |\mathbf{k}| = \sqrt{k_x^2 + k_y^2 + k_z^2}$, D_j is the constant deformation potential for the ground and excited state $j = \{g, e\}$ and the derivation for this can be found in section (2.2.3.1) [16, 83]. To find the phonon spectral density one can take the continuum limit using

$$\begin{aligned} \sum_{\mathbf{k}} g_{\mathbf{k}}^2 &\to \frac{V}{(2\pi)^3} \int \mathrm{d}\mathbf{k} g_{\mathbf{k}}^2, \\ &= \frac{V}{(2\pi)^3} \int_0^{\pi} \mathrm{d}\theta \sin\theta \int_0^{2\pi} \mathrm{d}\phi \int_{-\infty}^{\infty} \mathrm{d}k |\mathbf{k}|^2 g_{\mathbf{k}}^2, \\ &= \frac{V}{2\pi^2 c^3} \int_{-\infty}^{\infty} \mathrm{d}\omega_{\mathbf{k}} \omega_{\mathbf{k}}^2 g(\omega_{\mathbf{k}})^2, \end{aligned} \tag{A.3}$$

where the integral is taken over reciprocal space in spherical polar coordinates and linear dispersion has been assumed such that, $|\mathbf{k}| = \omega_{\mathbf{k}}/c$ and $\mathrm{d}|\mathbf{k}| = \mathrm{d}\omega_{\mathbf{k}}/c$, where c is the speed of

sound. Substituting this into the definition of the phonon spectral density shown in equation (A.1), the delta function causes only terms with $\omega = \omega_{\mathbf{k}}$ to be non-zero such that

$$J_{PH}(\omega) = \frac{V}{2\pi^2 c^3}\omega^2 g(\omega)^2. \tag{A.4}$$

Solving this function by first looking at Eq. (A.2) and writing $\sum_j D_j \int \mathrm{d}^3 r |\psi_j(\mathbf{r})|^2 e^{i\mathbf{k}\cdot\mathbf{r}} = (D_e\rho_e(\mathbf{k}) - D_g\rho_g(\mathbf{k}))$ where $\rho_j(\mathbf{k}) = \int \mathrm{d}^3 r e^{i\mathbf{k}\cdot\mathbf{r}}\rho_j(\mathbf{r})$ and $r^2 = |\mathbf{r}|^2 = x^2 + y^2 + z^2$. Expressing the linear coupling in terms of ω by assuming linear dispersion and setting $\omega = \omega_{\mathbf{k}}$ it has been found

$$g(\omega) = -\sqrt{\frac{\omega}{2NMc^2}}\,(D_e\rho_e(\mathbf{k}) - D_g\rho_g(\mathbf{k})). \tag{A.5}$$

Inserting this expression into eqn (A.1) to find the phonon spectral density as

$$J_{PH}(\omega) = \alpha\omega^3(D_e\rho_e(\mathbf{k}) - D_g\rho_g(\mathbf{k}))^2 \tag{A.6}$$

with the constant $\alpha = \frac{V}{4NM\pi^2c^5}$.

A.1.1 Gaussian wavefunction

To find a functional form for Eq. (A.6) the electronic wavefunction of the ground and excited state can be assumed. Where a common choice for a 3D harmonic oscillator bath is a isotropic Gaussian function [83], where this is typically chosen to accurately model quantum dots, for either the ground or excited state $j = \{g, e\}$ this is

$$\psi_j(\mathbf{r}) = \Big(\frac{1}{d_j\sqrt{\pi}}\Big)^{3/2} e^{-r^2/2d_j^2}, \tag{A.7}$$

where d_j is the confinement potential for the ground or excited states which is assumed the same in a symmetric potential approximation (allowing for the dropping of j as $d_e = d_g = d$ leading to $\rho_j(\mathbf{k}) \to \rho(\mathbf{k})$). Substituting this wavefunction into the expression for $\rho(\mathbf{k})$ to find

$$\begin{aligned}
\rho(\mathbf{k}) &= \int d^3 r |\psi(\mathbf{r})| e^{i\mathbf{k}\cdot\mathbf{r}}, \\
&= \Big(\frac{1}{d\sqrt{\pi}}\Big)^3 \int_{-\infty}^{\infty} d^3 r e^{i\mathbf{k}\cdot\mathbf{r}} e^{-r^2/d^2}, \\
&= \Big(\frac{1}{d\sqrt{\pi}}\Big)^3 \int_{-\infty}^{\infty} dx e^{iq_x x} e^{-x^2/d^2} \int_{-\infty}^{\infty} dy e^{iq_y y} e^{-y^2/d^2} \int_{-\infty}^{\infty} dz e^{iq_z z} e^{-z^2/d^2}.
\end{aligned} \tag{A.8}$$

Solving this using the relation $\int_{-\infty}^{\infty} dx e^{-a^2x^2} e^{ibx} = \frac{\sqrt{\pi}}{a} e^{-b^2/4a^2}$ to find

$$J_{PH}(\omega) = \alpha\omega^3 e^{-\omega^2/\omega_c^2} \tag{A.9}$$

where $\omega_c = \sqrt{2}\,c/d$ is the cut off frequency.

A.1.2 1s hydrogen wavefunction

The exciton–phonon spectral density can be found using a multitude of different electronic wavefunctions; where this is particularly useful when considering bath environments which aren't 3D in nature such as novel 2D materials like hexagonal Boron Nitride. To show an example using a different form, one can assume the electron wavefunction follows a 1s hydrogen orbital such that

$$\psi_j(\mathbf{r}) = \left(\frac{1}{\pi d^3}\right)^{1/2} e^{-r/d_j}. \tag{A.10}$$

where again it is assumed that the confinement potential d for the ground and excited states are the same taking a symmetric potential approximation. Substituting this wavefunction into the expression for the electron-phonon coupling strength again and evaluating the following integral

$$\begin{aligned}\rho(\mathbf{k}) &= \frac{1}{\pi d^3}\int_{-\infty}^{\infty} d^3 r e^{i(\mathbf{k})\cdot\mathbf{r}} e^{-2r/d}, \\ &= \frac{1}{\pi d^3}\int_0^{2\pi} d\phi \int_0^{\pi} d\theta sin\theta \int_0^{\infty} dr r^2 e^{iqr\cos\theta} e^{-2r/d}, \\ &= \frac{1}{(1+d^2q^2/4)^2}.\end{aligned} \tag{A.11}$$

Substituting this back into Eq. (A.6) to find

$$J_{PH}(\omega) = \alpha\omega^3 \frac{1}{(1+\omega^2/\omega_c^2)^2}. \tag{A.12}$$

A.2 DBT fitting parameters

For the open quantum systems model in chapter 4 fits for the local vibrational mode energies Δ_i and coupling constants η_i for each temperature are found from the emission spectra data and the resultant values are averaged. The vibrational mode energies are found to be $\hbar\Delta_1 = (21.55 \pm 0.01)$ meV, $\hbar\Delta_2 = (28.60 \pm 0.01)$ meV, $\hbar\Delta_3 = (31.10 \pm 0.02)$ meV and $\hbar\Delta_4 = (36.31 \pm 0.01)$ meV. These are in good agreement with values from the literature that are both calculated through Density Functional Theory, and measured in previous experiments [27]. The coupling constants found are $\hbar\eta_1 = (6.98 \pm 0.22)$ meV, $\hbar\eta_2 = (6.45 \pm 0.16)$ meV, $\hbar\eta_3 = (5.73 \pm 0.09)$ meV, and $\hbar\eta_4 = (9.30 \pm 0.14)$ meV.

To model the continuous phonon sideband the following parameters are required; an overall coupling strength between the TLS–phonon bath which is $\alpha = V\sum_\alpha D_\alpha^2/(4\pi^2 NMc^5)$, and a high-frequency cut-off $\xi = \sqrt{2}c/d$ to reflect the suppression of coupling to phonons whose wavelengths are much smaller than the size of the DBT molecule given by d, where c is the speed of sound in the anthracene nano-crystal. From fitting the temperature dependent emission spectra and taking the average to find $\xi = (8.6 \pm 0.6)\,\mathrm{ps}^{-1}$ and $\alpha = (0.009 \pm 0.001)\,\mathrm{ps}^2$. Knowing that the electronic wavefunction of the DBT molecule has a spatial extent of $\sim$

1.3 nm allows one to estimate the speed of sound in anthracene at cryogenic temperature to be $c \approx 1.3\,\mathrm{nm} * 8.6\,\mathrm{ps}^{-1}/\sqrt{2} \approx 7095\,\mathrm{m\,s}^{-1}$. This value is within a factor of two of the measured maximum value for the speed of sound in anthracene at room temperature ($\sim 3730\,\mathrm{m\,s}^{-1}$) [30, 53]. The discrepancy can be attributed to the crystal being stiffer at low temperature.

Finally, a function for the pure dephasing rate is required which relies upon the fitting parameter for the overall coupling strength $\mu = \alpha V/(32\pi(NM)c^3)$. From fitting the line-width data it has been found $\mu = 4.7 \times 10^{-7}\,\mathrm{ps}^5$.

A.3 Diagonal method with a phonon sideband

Upon the inclusion of a phonon sideband the system operator under the polaron transform is $O(t) \rightarrow O(t)B_-(t)$, where O represents some general system operator and $B_\pm = \exp\left[\pm\sum_{\mathbf{k}} \frac{g_{\mathbf{k}}}{\omega_{\mathbf{k}}}(b^\dagger_{\mathbf{k}} - b_{\mathbf{k}})\right]$ with $g_{\mathbf{k}}$ the electron phonon coupling constant. This leads to the first order correlation function $g^{(1)}(t+\tau,t) \approx \left\langle O^\dagger(t+\tau)O(t)\right\rangle \mathcal{G}(\tau)$, where $\mathcal{G}(\tau) = \langle B_+(\tau)B_-(0)\rangle$ is the phonon correlation function and the factorisation is justified due to differing time scales of phonon relaxation $\sim$ 1ps and photon emission $\sim$ 1ns. Evaluating the phonon correlation function one finds

$$\mathcal{G}(\tau) = \exp[-\Lambda(\tau)]\exp[-i\chi(\tau)], \tag{A.13}$$

where $\Lambda(\tau) = \int_0^\infty d\omega \frac{J_{PH}}{\omega^2}(1-\cos(\omega\tau))\coth(\beta\omega/2)$ and $\chi(\tau) = \int_0^\infty d\omega \frac{J_{PH}}{\omega^2}\sin(\omega\tau)$ where $J_{PH}(\omega)$ is electron-phonon spectral density. Finding the indistinguishability of this system from

$$\mathcal{I} = \frac{\int_0^\infty dt \int_0^\infty d\tau |\left\langle O^\dagger(t+\tau)O(t)\right\rangle|^2}{\int_0^\infty dt \int_0^\infty d\tau \left\langle O^\dagger(t+\tau)O(t+\tau)\right\rangle \left\langle O^\dagger(t)O(t)\right\rangle}. \tag{A.14}$$

by first finding the numerator by substituting in Eq. (6.47) giving

$$\begin{aligned}\int_0^\infty dt \int_0^\infty d\tau |\left\langle O^\dagger(t+\tau)O(t)\right\rangle \mathcal{G}(\tau)|^2 &= \sum_{ijkl} A_{ij}A^*_{kl}\int_0^\infty dt e^{(\lambda_j+\lambda_l^*)t}\int_0^\infty d\tau e^{(\lambda_i+\lambda_k^*)\tau}|\mathcal{G}(\tau)|^2, \\ &= \sum_{ijkl} A_{ij}A^*_{kl}\frac{-1}{(\lambda_j+\lambda_l^*)}\int_0^\infty d\tau e^{(\lambda_i+\lambda_k^*)\tau}|\mathcal{G}(\tau)|^2.\end{aligned} \tag{A.15}$$

Putting this in in terms of matrices and newly defining $G_{ki} = \int_0^\infty d\tau e^{(\lambda_i+\lambda_k^*)\tau}|\mathcal{G}(\tau)|^2$ it has been found

$$\begin{aligned}\int_0^\infty dt \int_0^\infty d\tau |\left\langle O^\dagger(t+\tau)O(t)\right\rangle \mathcal{G}(\tau)|^2 &= \sum_{ijkl} A^*_{kl}G_{ki}A_{ij}L_{lj} \\ &= \mathrm{Tr}[\mathbf{A}^\dagger\mathbf{G}\mathbf{A}\mathbf{L}^\top].\end{aligned} \tag{A.16}$$

Noting that the denominator is the same as in Eq. (6.53) in the main text as influence from the phonon correlation function cancels, this gives the final form

$$\mathcal{I} = \frac{\mathrm{Tr}\left[\mathbf{A}^{\dagger}\mathbf{G}\mathbf{A}\mathbf{L}^{\top}\right]}{\mathrm{Tr}[\mathbf{U}^{\top}\mathbf{\Lambda}]}, \tag{A.17}$$

where $a_i = \langle\langle O^{\dagger}O|P\mathcal{P}_i P^{-1}|\rho(0)\rangle\rangle$, $U_{ij} = a_i a_j$ and $\Lambda_{ij} = (\lambda_i(\lambda_i + \lambda_j))^{-1}$ are as introduce in the main text.

BIBLIOGRAPHY

[1] I. ABRAM, *Spectral characteristics of zero-phonon transitions in crystal impurities: A diagrammatic approach*, Chemical Physics, 25 (1977), pp. 87–102.

[2] T. A. ABTEW, Y. Y. SUN, B.-C. SHIH, P. DEV, S. B. ZHANG, AND P. ZHANG, *Dynamic jahn-teller effect in the* nv^- *center in diamond*, Phys. Rev. Lett., 107 (2011), p. 146403.

[3] I. AHARONOVICH, D. ENGLUND, AND M. TOTH, *Solid-state single-photon emitters*, Nature Photonics, 10 (2016), pp. 631–641.

[4] R. ALBRECHT, A. BOMMER, C. DEUTSCH, J. REICHEL, AND C. BECHER, *Coupling of a single nitrogen-vacancy center in diamond to a fiber-based microcavity*, Phys. Rev. Lett., 110 (2013), p. 243602.

[5] D. ARSENIJEVIĆ, M. KLEINERT, AND D. BIMBERG, *Phase noise and jitter reduction by optical feedback on passively mode-locked quantum-dot lasers*, Applied Physics Letters, 103 (2013), p. 231101.

[6] M. ATATÜRE, D. ENGLUND, N. VAMIVAKAS, S.-Y. LEE, AND J. WRACHTRUP, *Material platforms for spin-based photonic quantum technologies*, Nature Reviews Materials, 3 (2018), pp. 38–51.

[7] H. BERNIEN, L. CHILDRESS, L. ROBLEDO, M. MARKHAM, D. TWITCHEN, AND R. HANSON, *Two-photon quantum interference from separate nitrogen vacancy centers in diamond*, Physical Review Letters, 108 (2012), p. 043604.

[8] S. I. BOGDANOV, A. BOLTASSEVA, AND V. M. SHALAEV, *Overcoming quantum decoherence with plasmonics*, Science, 364 (2019), pp. 532–533.

[9] F. C. BOHREN AND R. D. HUFFMAN, *Classical Theories of Optical Constants*, John Wiley and Sons, Ltd, 1998, ch. 9, pp. 226–267.

[10] A. BONFIGLIOLI AND R. FULCI, *Topics in noncommutative algebra: the theorem of Campbell, Baker, Hausdorff and Dynkin*, vol. 2034, Springer Science & Business Media, 2011.

[11] J. BORREGAARD, A. S. SØRENSEN, AND P. LODAHL, *Quantum networks with deterministic spin–photon interfaces*, Advanced Quantum Technologies, 2 (2019), p. 1800091.

[12] R. BOYD AND D. PRATO, *Nonlinear Optics*, Elsevier Science, 2008.

[13] C. BRADAC, W. GAO, J. FORNERIS, M. TRUSHEIM, AND I. AHARONOVICH, *Quantum nanophotonics with group iv defects in diamond*, Nature Communications, 10 (2019), p. 5625.

[14] A. BRASH, J. ILES-SMITH, C. L. PHILLIPS, D. P. S. MCCUTCHEON, J. O'HARA, E. CLARKE, B. ROYALL, J. MØRK, M. S. SKOLNICK, A. M. FOX, AND A. NAZIR, *Light Scattering from Solid-State Quantum Emitters: Beyond the Atomic Picture*, Phys. Rev. Lett., 123 (2019), p. 167403.

[15] H. P. BREUER AND F. PETRUCCIONE, *The theory of open quantum systems*, Oxford University Press, 2002.

[16] H. BRUUS AND K. FLENSBERG, *Many-body Quantum Theory in Condensed Matter Physics: An Introduction*, Oxford graduate texts, Oxford University Press, 2004.

[17] J. BYLANDER, I. ROBERT-PHILIP, AND I. ABRAM, *Interference and correlation of two independent photons*, European Physical Journal D, 22 (2003), pp. 295–301.

[18] A. O. CALDEIRA AND A. J. LEGGETT, *Influence of Dissipation on Quantum Tunneling in Macroscopic Systems*, Phys. Rev. Lett., 46 (1981), pp. 211–214.

[19] H. J. CARMICHAEL AND M. O. SCULLY, *Statistical Methods in Quantum Optics 1: Master Equations and Fokker-Planck Equations* , vol. 53, 2000.

[20] S. CASTELLETTO, F. A. INAM, S. I. SATO, AND A. BORETTI, *Hexagonal boron nitride: A review of the emerging material platform for single-photon sources and the spin-photon interface*, Beilstein Journal of Nanotechnology, 11 (2020), pp. 740–769.

[21] L. CHILDRESS AND R. HANSON, *Diamond NV centers for quantum computing and quantum networks*, MRS Bulletin, 38 (2013), pp. 134–138.

[22] C. J. CHUNNILALL, I. P. DEGIOVANNI, S. KÜCK, I. MÜLLER, AND A. G. SINCLAIR, *Metrology of single-photon sources and detectors: a review*, Optical Engineering, 53 (2014), p. 081910.

[23] C. CLEAR, R. C. SCHOFIELD, K. D. MAJOR, J. ILES-SMITH, A. S. CLARK, AND D. P. MCCUTCHEON, *Phonon-Induced Optical Dephasing in Single Organic Molecules*, Physical Review Letters, 124 (2020), p. 153602.

[24] P. DE BREE AND D. A. WIERSMA, *Application of Redfield theory to optical dephasing and line shape of electronic transitions in molecular mixed crystals*, The Journal of Chemical Physics, 70 (1979), pp. 790–801.

[25] G. J. DE VALCÁRCEL, E. ROLDÁN, AND F. PRATI, *Semiclassical theory of amplification and lasing*, Revista Mexicana de Fisica E, 52 (2006), pp. 198–214.

[26] Y.-H. DENG, H. WANG, X. DING, Z.-C. DUAN, J. QIN, M.-C. CHEN, Y. HE, Y.-M. HE, J.-P. LI, Y.-H. LI, L.-C. PENG, E. S. MATEKOLE, T. BYRNES, C. SCHNEIDER, M. KAMP, D.-W. WANG, J. P. DOWLING, S. HÖFLING, C.-Y. LU, M. O. SCULLY, AND J.-W. PAN, *Quantum interference between light sources separated by 150 million kilometers*, Phys. Rev. Lett., 123 (2019), p. 080401.

[27] I. DEPERASIŃSKA, E. KARPIUK, M. BANASIEWICZ, A. MAKAREWICZ, AND B. KOZANKIEWICZ, *Single dibenzoterrylene molecules in naphthalene and 2,3-dimethylnaphthalene crystals: vibronic spectra*, Phys. Chem. Chem. Phys., 13 (2011), pp. 1872–1878.

[28] A. DIETRICH, M. W. DOHERTY, I. AHARONOVICH, AND A. KUBANEK, *Solid-state single photon source with Fourier transform limited lines at room temperature*, Physical Review B, 101 (2020), pp. 1–6.

[29] M. W. DOHERTY, N. B. MANSON, P. DELANEY, F. JELEZKO, J. WRACHTRUP, AND L. C. HOLLENBERG, *The nitrogen-vacancy colour centre in diamond*, Physics Reports, 528 (2013), pp. 1–45.
The nitrogen-vacancy colour centre in diamond.

[30] R. C. DYE AND C. J. ECKHARDT, *A complete set of elastic constants of crystalline anthracene by brillouin scattering*, J. Chem. Phys., 90 (1989), pp. 2090–2096.

[31] J. H. EBERLY AND K. WÓDKIEWICZ, *The time-dependent physical spectrum of light∗*, J. Opt. Soc. Am., 67 (1977), pp. 1252–1261.

[32] M. D. EISAMAN, J. FAN, A. MIGDALL, AND S. V. POLYAKOV, *Invited Review Article: Single-photon sources and detectors*, Review of Scientific Instruments, 82 (2011).

[33] U. FANO, *Description of states in quantum mechanics by density matrix and operator techniques*, Rev. Mod. Phys., 29 (1957), pp. 74–93.

[34] E. B. FLAGG, A. MULLER, S. V. POLYAKOV, A. LING, A. MIGDALL, AND G. S. SOLOMON, *Interference of single photons from two separate semiconductor quantum dots*, Physical Review Letters, 104 (2010), p. 137401.

[35] E. B. FLAGG, A. MULLER, J. W. ROBERTSON, S. FOUNTA, D. G. DEPPE, M. XIAO, W. MA, G. J. SALAMO, AND C. K. SHIH, *Resonantly driven coherent oscillations in a solid-state quantum emitter*, Nature Physics, 5 (2009), pp. 203–207.

[36] K.-M. C. FU, C. SANTORI, P. E. BARCLAY, AND R. G. BEAUSOLEIL, *Conversion of neutral nitrogen-vacancy centers to negatively charged nitrogen-vacancy centers through selective oxidation*, Applied Physics Letters, 96 (2010), p. 121907.

[37] K.-M. C. FU, C. SANTORI, P. E. BARCLAY, L. J. ROGERS, N. B. MANSON, AND R. G. BEAUSOLEIL, *Observation of the dynamic jahn-teller effect in the excited states of nitrogen-vacancy centers in diamond*, Phys. Rev. Lett., 103 (2009), p. 256404.

[38] J. C. GARRISON AND R. Y. CHIAO, *Quantum optics*, Oxford University Press Oxford ; New York, 2008.

[39] C. GERRY AND P. KNIGHT, *Introductory Quantum Optics*, Cambridge University Press, 2004.

[40] F. GIUSTINO, *Electron-phonon interactions from first principles*, Rev. Mod. Phys., 89 (2017), p. 15003.

[41] B. GMEINER, A. MASER, T. UTIKAL, S. GÖTZINGER, AND V. SANDOGHDAR, *Spectroscopy and microscopy of single molecules in nanoscopic channels: spectral behavior vs. confinement depth*, Phys. Chem. Chem. Phys., 18 (2016), pp. 19588–19594.

[42] P. GOLD, A. THOMA, S. MAIER, S. REITZENSTEIN, C. SCHNEIDER, S. HÖFLING, AND M. KAMP, *Two-photon interference from remote quantum dots with inhomogeneously broadened linewidths*, Phys. Rev. B, 89 (2014), p. 35313.

[43] F. GOTTWALD, S. IVANOV, AND O. KÜHN, *Vibrational spectroscopy via the caldeira-leggett model with anharmonic system potentials*, The Journal of Chemical Physics, 144 (2016).

[44] I. S. GRADSHTEYN AND I. M. RYZHIK, *Table of integrals, series, and products*, Elsevier/Academic Press, Amsterdam, seventh ed., 2007.

[45] S. GRANDI, K. D. MAJOR, C. POLISSENI, S. BOISSIER, A. S. CLARK, AND E. A. HINDS, *Quantum dynamics of a driven two-level molecule with variable dephasing*, Physical Review A, 94 (2016).

[46] S. GRANDI, M. P. NIELSEN, J. CAMBIASSO, S. BOISSIER, K. D. MAJOR, C. REARDON, T. F. KRAUSS, R. F. OULTON, E. A. HINDS, AND A. S. CLARK, *Hybrid plasmonic waveguide coupling of photons from a single molecule*, APL Photonics, 4 (2019), p. 86101.

[47] L. GREUTER, S. STAROSIELEC, A. V. KUHLMANN, AND R. J. WARBURTON, *Towards high-cooperativity strong coupling of a quantum dot in a tunable microcavity*, Phys. Rev. B, 92 (2015), p. 045302.

[48] G. GUARNIERI, A. SMIRNE, AND B. VACCHINI, *Quantum regression theorem and non-Markovianity of quantum dynamics*, Phys. Rev. A, 90 (2014), p. 22110.

[49] Y. M. He, Y. He, Y. J. Wei, D. Wu, M. Atatüre, C. Schneider, S. Höfling, M. Kamp, C. Y. Lu, and J. W. Pan, *On-demand semiconductor single-photon source with near-unity indistinguishability*, Nature Nanotechnology, 8 (2013), pp. 213–217.

[50] J. Houel, A. V. Kuhlmann, L. Greuter, F. Xue, M. Poggio, B. D. Gerardot, P. A. Dalgarno, A. Badolato, P. M. Petroff, A. Ludwig, D. Reuter, A. D. Wieck, and R. J. Warburton, *Probing single-charge fluctuations at a* GaAs/AlAs *interface using laser spectroscopy on a nearby ingaas quantum dot*, Phys. Rev. Lett., 108 (2012), p. 107401.

[51] S. Hu, M. Khater, R. Salas-Montiel, E. Kratschmer, S. Engelmann, W. M. Green, and S. M. Weiss, *Experimental realization of deep-subwavelength confinement in dielectric optical resonators*, Science advances, 4 (2018), p. eaat2355.

[52] J.-F. Huang, J.-Q. Liao, and L.-M. Kuang, *Ultrastrong jaynes-cummings model*, Phys. Rev. A, 101 (2020), p. 043835.

[53] H. B. Huntington, S. G. Gangoli, and J. L. Mills, *Ultrasonic measurement of the elastic constants of anthracene*, J. Chem. Phys., 50 (1969), pp. 3844–3849.

[54] V. Huxter, T. Oliver, D. Budker, and G. Fleming, *Vibrational and electronic dynamics of nitrogen–vacancy centres in diamond revealed by two-dimensional ultrafast spectroscopy*, Nature Physics, 9 (2013), p. 744.

[55] J. Iles-Smith, D. P. McCutcheon, A. Nazir, and J. Mørk, *Phonon scattering inhibits simultaneous near-unity efficiency and indistinguishability in semiconductor single-photon sources*, Nature Photonics, 11 (2017), pp. 521–526.

[56] J. Iles-Smith, D. P. S. McCutcheon, J. Mørk, and A. Nazir, *Limits to coherent scattering and photon coalescence from solid-state quantum emitters*, Phys. Rev. B, 95 (2017), pp. 201305–201310.

[57] P. Kaer, N. Gregersen, and J. Mork, *The role of phonon scattering in the indistinguishability of photons emitted from semiconductor cavity QED systems*, New Journal of Physics, 15 (2013).

[58] B. Kambs and C. Becher, *Limitations on the indistinguishability of photons from remote solid state sources*, New Journal of Physics, 20 (2018).

[59] A. Kiraz, M. Atatüre, and A. Imamo, *Quantum-dot single-photon sources: Prospects for applications in linear optics quantum-information processing*, Phys. Rev. A, 69 (2004), p. 32305.

[60] E. KNILL, R. LAFLAMME, AND G. MILBURN, *Efficient Linear Optics Quantum Computation*, Nature, 409 (2000), pp. 49–53.

[61] S. KREINBERG, T. GRBEŠIĆ, M. STRAUSS, A. CARMELE, M. EMMERLING, C. SCHNEIDER, S. HÖFLING, X. PORTE, AND S. REITZENSTEIN, *Quantum-optical spectroscopy of a two-level system using an electrically driven micropillar laser as a resonant excitation source*, Light: Science and Applications, 7 (2018).

[62] A. KUHN, M. HENNRICH, AND G. REMPE, *Deterministic Single-Photon Source for Distributed Quantum Networking*, Phys. Rev. Lett., 89 (2002).

[63] E. KURAMOCHI, H. TANIYAMA, T. TANABE, K. KAWASAKI, Y.-G. ROH, AND M. NOTOMI, *Ultrahigh-q one-dimensional photonic crystal nanocavities with modulated mode-gap barriers on sio2 claddings and on air claddings*, Opt. Express, 18 (2010), pp. 15859–15869.

[64] P. G. KWIAT, K. MATTLE, H. WEINFURTER, A. ZEILINGER, A. V. SERGIENKO, AND Y. SHIH, *New high-intensity source of polarization-entangled photon pairs*, Phys. Rev. Lett., 75 (1995), pp. 4337–4341.

[65] A. J. LEGGETT, S. CHAKRAVARTY, A. T. DORSEY, M. P. A. FISHER, A. GARG, AND W. ZWERGER, *Dynamics of the dissipative two-state system*, Rev. Mod. Phys., 59 (1987), pp. 1–85.

[66] R. LETTOW, Y. L. A. REZUS, A. RENN, G. ZUMOFEN, E. IKONEN, S. GÖTZINGER, AND V. SANDOGHDAR, *Quantum interference of tunably indistinguishable photons from remote organic molecules*, Physical Review Letters, 104 (2010), p. 123605.

[67] X. LIU, H. NAKAJIMA, Y. LI, S. ODASHIMA, I. SUEMUNE, AND H. KUMANO, *Optical control of spectral diffusion with single inas quantum dots in a silver-embedded nanocone*, Opt. Express, 25 (2017), pp. 8073–8084.

[68] H. K. LO, M. CURTY, AND K. TAMAKI, *Secure quantum key distribution*, Nature Photonics, 8 (2014), pp. 595–604.

[69] P. LOMBARDI, M. COLAUTTI, R. DUQUENNOY, G. MURTAZA, P. MAJUMDER, AND C. TONINELLI, *Indistinguishable photons on demand from an organic dye molecule*, Retrieved from http://arxiv.org/abs/2012.13055, (2021).

[70] P. LOMBARDI, A. P. OVVYAN, S. IPAZZAGLI, G. MAZZAMUTO, G. KEWES, O. NEITZKE, N. GRUHLER, O. BENSON, W. H. P. PERNICE, F. S. CATALIOTTI, AND C. TONINELLI, *Photostable Molecules on Chip: Integrated Sources of Nonclassical Light*, ACS Photonics, 5 (2018), pp. 126–132.

[71] G. D. MAHAN, *Many-Particle Physics*, Physics of Solids and Liquids, Springer US, 2013.

[72] K. D. MAJOR AND A. S. CLARK, *Coupling single molecules to cryogenic optical fibre microcavities*, Thesis, (2016).

[73] K. D. MAJOR, Y.-H. LIEN, C. POLISSENI, S. GRANDI, K. W. KHO, A. S. CLARK, J. HWANG, AND E. A. HINDS, *Growth of optical-quality anthracene crystals doped with dibenzoterrylene for controlled single photon production*, Review of Scientific Instruments, 86 (2015), p. 83106.

[74] N. B. MANSON, J. P. HARRISON, AND M. J. SELLARS, *Nitrogen-vacancy center in diamond: Model of the electronic structure and associated dynamics*, Phys. Rev. B, 74 (2006), p. 104303.

[75] D. MANZANO, *A short introduction to the Lindblad master equation*, AIP Advances, 10 (2020).

[76] C. MATTHIESEN, A. N. VAMIVAKAS, AND M. ATATÜRE, *Subnatural linewidth single photons from a quantum dot*, Phys. Rev. Lett., 108 (2012), p. 093602.

[77] D. P. S. MCCUTCHEON, *Optical signatures of non-markovian behavior in open quantum systems*, Phys. Rev. A, 93 (2016), p. 022119.

[78] D. P. S. MCCUTCHEON AND A. NAZIR, *Quantum dot Rabi rotations beyond the weak exciton–phonon coupling regime*, New J. Phys., 12 (2010), pp. 113042–113063.

[79] D. P. S. MCCUTCHEON AND A. NAZIR, *Model of the Optical Emission of a Driven Semiconductor Quantum Dot: Phonon-Enhanced Coherent Scattering and Off-Resonant Sideband Narrowing*, Phys. Rev. Lett., 110 (2013), p. 217401.

[80] W. E. MOERNER, *Single-photon sources based on single molecules in solids*, New Journal of Physics, 6 (2004), p. 88.

[81] E. A. MULJAROV AND R. ZIMMERMANN, *Dephasing in quantum dots: Quadratic coupling to acoustic phonons*, Phys. Rev. Lett., 93 (2004), p. 237401.

[82] Y. NAMBU AND K. NAKAMURA, *On the matrix representation of quantum operations*, arXiv: Quantum Physics, (2005).

[83] A. NAZIR AND D. P. MCCUTCHEON, *Modelling exciton-phonon interactions in optically driven quantum dots*, Journal of Physics Condensed Matter, 28 (2016), p. 103002.

[84] NEESE, F, *"the orca program system"*, Wiley Interdisciplinary Reviews: Computational Molecular Science, 2 (2012), p. 73–78.

[85] A. A. L. NICOLET, P. BORDAT, C. HOFMANN, M. A. KOL'CHENKO, B. KOZANKIEWICZ, R. BROWN, AND M. ORRIT, *Single Dibenzoterrylene Molecules in an Anthracene Crystal: Main Insertion Sites*, ChemPhysChem, 8 (2007), pp. 1929–1936.

[86] J. PAAVOLA, J. PIILO, K.-A. SUOMINEN, AND S. MANISCALCO, *Environment-dependent dissipation in quantum brownian motion*, Phys. Rev. A, 79 (2009), p. 052120.

[87] C. PALACIOS-BERRAQUERO, M. BARBONE, D. M. KARA, X. CHEN, I. GOYKHMAN, D. YOON, A. K. OTT, J. BEITNER, K. WATANABE, T. TANIGUCHI, A. C. FERRARI, AND M. ATATÜRE, *Atomically thin quantum light-emitting diodes*, Nature Communications, 7 (2016).

[88] R. B. PATEL, A. J. BENNETT, K. COOPER, P. ATKINSON, C. A. NICOLL, D. A. RITCHIE, AND A. J. SHIELDS, *Postselective two-photon interference from a continuous nonclassical stream of photons emitted by a quantum dot*, Physical Review Letters, 100 (2008), p. 207405.

[89] R. B. PATEL, A. J. BENNETT, I. FARRER, C. A. NICOLL, D. A. RITCHIE, AND A. J. SHIELDS, *Two-photon interference of the emission from electrically tunable remote quantum dots*, Nature Photonics, 4 (2010), pp. 632–635.

[90] S. PAZZAGLI, P. LOMBARDI, D. MARTELLA, M. COLAUTTI, B. TIRIBILLI, F. S. CATALIOTTI, AND C. TONINELLI, *Self-Assembled Nanocrystals of Polycyclic Aromatic Hydrocarbons Show Photostable Single-Photon Emission*, ACS Nano, 12 (2018), pp. 4295–4303.

[91] T. PLAKHOTNIK, M. W. DOHERTY, AND N. B. MANSON, *Electron-phonon processes of the nitrogen-vacancy center in diamond*, Phys. Rev. B, 92 (2015), p. 081203.

[92] C. POLISSENI, K. D. MAJOR, S. BOISSIER, S. GRANDI, A. S. CLARK, AND E. A. HINDS, *Stable, single-photon emitter in a thin organic crystal for application to quantum-photonic devices*, Opt. Express, 24 (2016), pp. 5615–5627.

[93] J. H. PRECHTEL, A. V. KUHLMANN, J. HOUEL, L. GREUTER, A. LUDWIG, D. REUTER, A. D. WIECK, AND R. J. WARBURTON, *Frequency-stabilized source of single photons from a solid-state qubit*, Phys. Rev. X, 3 (2013), p. 041006.

[94] R. PROUX, M. MARAGKOU, E. BAUDIN, C. VOISIN, P. ROUSSIGNOL, AND C. DIEDERICHS, *Measuring the photon coalescence time window in the continuous-wave regime for resonantly driven semiconductor quantum dots*, Phys. Rev. Lett., 114 (2015), p. 067401.

[95] Q. QUAN AND M. LONCAR, *Deterministic design of wavelength scale, ultra-high q photonic crystal nanobeam cavities*, Opt. Express, 19 (2011), pp. 18529–18542.

[96] A. REIGUE, J. ILES-SMITH, F. LUX, L. MONNIELLO, M. BERNARD, F. MARGAILLAN, A. LEMAITRE, A. MARTINEZ, D. P. S. MCCUTCHEON, J. MØRK, R. HOSTEIN, AND V. VOLIOTIS, *Probing Electron-Phonon Interaction through Two-Photon Interference in Resonantly Driven Semiconductor Quantum Dots*, Phys. Rev. Lett., 118 (2017), p. 233602.

[97] M. REITZ, C. SOMMER, AND C. GENES, *Langevin Approach to Quantum Optics with Molecules*, Phys. Rev. Lett., 122 (2019), p. 203602.

[98] M. REZAI, J. WRACHTRUP, AND I. GERHARDT, *Coherence Properties of Molecular Single Photons for Quantum Networks*, Physical Review X, 8 (2018), p. 31026.

[99] D. RIEDEL, I. SÖLLNER, B. J. SHIELDS, S. STAROSIELEC, P. APPEL, E. NEU, P. MALETINSKY, AND R. J. WARBURTON, *Deterministic enhancement of coherent photon generation from a nitrogen-vacancy center in ultrapure diamond*, Phys. Rev. X, 7 (2017), p. 031040.

[100] C. ROY AND S. JOHN, *Microscopic theory of multiple-phonon-mediated dephasing and relaxation of quantum dots near a photonic band gap*, Phys. Rev. A, 81 (2010), p. 023817.

[101] K. ROY-CHOUDHURY AND S. HUGHES, *Quantum theory of the emission spectrum from quantum dots coupled to structured photonic reservoirs and acoustic phonons*, Phys. Rev. B, 92 (2015), p. 205406.

[102] K. G. SCHÄDLER, C. CIANCICO, S. PAZZAGLI, P. LOMBARDI, A. BACHTOLD, C. TONINELLI, A. RESERBAT-PLANTEY, AND F. H. L. KOPPENS, *Electrical Control of Lifetime-Limited Quantum Emitters Using 2D Materials*, Nano Lett., 19 (2019), pp. 3789–3795.

[103] G. SCHALLER, *Open Quantum Systems Far from Equilibrium*, Lecture Notes in Physics, Springer International Publishing, 2014.

[104] R. C. SCHOFIELD, C. CLEAR, R. A. HOGGARTH, K. D. MAJOR, D. P. S. MCCUTCHEON, AND A. S. CLARK, *Photon indistinguishability measurements under pulsed and continuous excitation*, Phys. Rev. Research, 4 (2022), p. 013037.

[105] R. C. SCHOFIELD, K. D. MAJOR, S. GRANDI, S. BOISSIER, E. A. HINDS, AND A. S. CLARK, *Efficient excitation of dye molecules for single photon generation*, Journal of Physics Communications, 2 (2018), p. 115027.

[106] F. SCHREUDER AND J.-G. BIJ DE VAATE, *Localized LNA cooling in vacuum*, in THERMINIC 2006, Nice, France, Sept. 2006, TIMA Editions, pp. 175–179.
Submitted on behalf of EDA Publishing Association (http://irevues.inist.fr/handle/2042/5920).

[107] A. SIPAHIGIL, K. D. JAHNKE, L. J. ROGERS, T. TERAJI, J. ISOYA, A. S. ZIBROV, F. JELEZKO, AND M. D. LUKIN, *Indistinguishable photons from separated silicon-vacancy centers in diamond*, Physical Review Letters, 113 (2014), p. 113602.

[108] J. SMITH, J. MONROY-RUZ, J. G. RARITY, AND K. C. BALRAM, *Single photon emission and single spin coherence of a nitrogen vacancy center encapsulated in silicon nitride*, Applied Physics Letters, 116 (2020), p. 134001.

[109] J. A. SMITH, C. CLEAR, K. C. BALRAM, D. P. MCCUTCHEON, AND J. G. RARITY, *Nitrogen-vacancy center coupled to an ultrasmall-mode-volume cavity: A high-efficiency source of indistinguishable photons at 200 k*, Phys. Rev. Applied, 15 (2021), p. 034029.

[110] D. STECK, *Quantum and Atom Optics*, 2007.

[111] Y.-N. SUN, Y. ZOU, G. CHEN, J.-S. TANG, H.-Q. NI, M.-F. LI, G.-W. ZHA, Z.-C. NIU, Y.-J. HAN, C.-F. LI, AND G.-C. GUO, *Measurement of the inhomogeneous broadening of a bi-exciton state in a quantum dot using Franson-type nonlocal interference*, Opt. Express, 25 (2017), pp. 1778–1788.

[112] J.-B. TREBBIA, H. RUF, P. TAMARAT, AND B. LOUNIS, *Efficient generation of near infra-red single photons from the zero-phonon line of a single molecule*, Opt. Express, 17 (2009).

[113] J. B. TREBBIA, P. TAMARAT, AND B. LOUNIS, *Indistinguishable near-infrared single photons from an individual organic molecule*, Phys. Rev. A, 82 (2010), p. 063803.

[114] P. TÜRSCHMANN, N. ROTENBERG, J. RENGER, I. HARDER, O. LOHSE, T. UTIKAL, S. GÖTZINGER, AND V. SANDOGHDAR, *Chip-Based All-Optical Control of Single Molecules Coherently Coupled to a Nanoguide*, Nano Lett., 17 (2017), pp. 4941–4945.

[115] S. UNSLEBER, D. P. S. MCCUTCHEON, M. DAMBACH, M. LERMER, N. GREGERSEN, S. HÖFLING, J. MØRK, C. SCHNEIDER, AND M. KAMP, *Two-photon interference from a quantum dot microcavity: Persistent pure dephasing and suppression of time jitter*, Phys. Rev. B, 91 (2015), p. 075413.

[116] D. WANG, H. KELKAR, D. MARTIN-CANO, D. RATTENBACHER, A. SHKARIN, T. UTIKAL, S. GÖTZINGER, AND V. SANDOGHDAR, *Turning a molecule into a coherent two-level quantum system*, Nat. Phys., 15 (2019), pp. 483–489.

[117] D. WANG, H. KELKAR, D. MARTIN-CANO, T. UTIKAL, S. GÖTZINGER, AND V. SANDOGHDAR, *Coherent Coupling of a Single Molecule to a Scanning Fabry-Perot Microcavity*, Phys. Rev. X, 7 (2017), p. 21014.

[118] S. WEIN, N. LAUK, R. GHOBADI, AND C. SIMON, *Feasibility of efficient room-temperature solid-state sources of indistinguishable single photons using ultrasmall mode volume cavities*, Phys. Rev. B, 97 (2018), p. 205418.

[119] J. WOLTERS, N. SADZAK, A. W. SCHELL, T. SCHRÖDER, AND O. BENSON, *Measurement of the ultrafast spectral diffusion of the optical transition of nitrogen vacancy centers in nano-size diamond using correlation interferometry*, Phys. Rev. Lett., 110 (2013), p. 027401.

[120] L. M. WOODS AND G. D. MAHAN, *Nonlinear electron-phonon heat exchange*, Phys. Rev. B, 57 (1998), pp. 7679–7685.

[121] G. WRIGGE, I. GERHARDT, J. HWANG, G. ZUMOFEN, AND V. SANDOGHDAR, *Efficient coupling of photons to a single molecule and the observation of its resonance fluorescence*, Nature Physics, 4 (2008), pp. 60–66.

[122] A. ZAITSEV, *Optical Properties of Diamond: A data handbook*, Berlin: Springer, 2001.